Structure, Solubility and Crystallisation Behaviour of Bioactive Borosilicate Glasses

Dissertation

zur Erlangung des akademischen Grades Doktor-Ingenieur

(Dr.-Ing.)

FRIEDRICH-SCHILLER-
UNIVERSITÄT
JENA

vorgelegt dem Rat der Chemisch-Geowissenschaftlichen Fakultät der
Friedrich-Schiller-Universität Jena

von M. Sc. Juliane Brandt-Slowik

geboren am 02.04.1987 in Jena

Gutachter:

1. Prof. Dr. Delia S. Brauer, Jena

2. Assoc. Prof. Dr. Jonathan Massera, Tampere

(3. ……………………………………………..)

Tag der Verteidigung: 26.02.2020

Index

Register of Abbreviations

Abbreviation	**Meaning**
1D	one-dimensional
2D	two-dimensional
3D	three-dimensional
15Bc	heat-treated (partly-)crystallised glass 15B
25Bc	heat-treated (partly-)crystallised glass 25B
45S5c	heat-treated (partly-)crystallised glass 45S5
5Bc	heat-treated (partly-)crystallised glass 5B
Al^4 unit	AlO_4 tetrahedron with 4 bridging oxygen atoms
ATR	attenuated reflection mode
B^3 or B^4 unit	planar BO_3 unit with 3 bridging oxygen atoms or BO_4 tetrahedron with 4 bridging oxygen atoms
BAM	Bundesanstalt für Materialforschung und –prüfung
BO	bridging oxygen
DSC	differential scanning calorimetry
E_a	the activation energy of viscous flow (glass transition)
EAH	Ernst-Abbe-Hochschule Jena
E_c	the activation energy of crystallisation
$E_{c\alpha}$	the activation energy of crystallisation for a certain α (α is the fraction of glass crystallised)
EDX	energy dispersive X-ray analysis
FAp	fluorapatite
FP	floating point
FTIR	Fourier transform infrared spectroscopy
FSU	Friedrich-Schiller-Universität Jena
G	glass-forming units
GSP	glass stability parameters
HCP	half-cone point
HTM	heating microscopy
ICP-OES	inductively coupled plasma optical emission spectroscopy

IPHT	Leibniz-Institut für Photonische Technologien
ISA	index of surface activity
K_H	Hrüby parameter (a type of glass stability parameter)
K_{LL}	Lu & Liu parameter (type of glass stability parameter)
K_{SP}	Saad & Poulain parameter (a type of glass stability parameter)
K_W	Weinberg parameter (a type of glass stability parameter)
LM	light microscopy
MAS	magic angle spinning
MBP	minimum baseline point
n	JMA exponent (Johnson Mehl-Avrami exponent)
NBO	non-bridging oxygen
NC	network connectivity
NMR	nuclear magnetic resonance spectroscopy
OSIM	Otto-Schott-Institut für Materialforschung
pH-value	the numeric scale used to specify the acidity or basicity of an aqueous solution
PMMA	polymethyl methacrylate
q	heating rate
Q^n, $Q^{0,1\ldots}$ unit	SiO_4 tetrahedron with 0, 1, …bridging oxygen atoms (n)
Q^{xy}	Q^x connected to a Q^y unit, e.g. Q^{23}
Q_P^0	orthophosphate group
R	gas constant
R^2	coefficient of determination
rBA	regression bioactivity value
RN	reaction number
rpm	rounds per minute
rTg	regression glass transition temperature value
SBF	simulated body fluid
SDTA	simultaneous differential thermal analysis
SEM	scanning electron microscopy
SP	sintering point

SSD	the shaded surface display technique
TEM	transmission electron microscopy
T_g	glass transition temperature
TGA	thermogravimetric analysis
T_m	liquidus temperature
T_p	the temperature of crystallisation (maximum of exothermic peak)
$T_{p1,2\ldots}$	maximum of first, second… exothermic crystallisation peak (in case more than one exists)
Tris	Tris buffer solution
TTMS	Tris(trimethylsilyl)silane
T_x	the temperature of onset of crystallisation
WDXRF	wavelength dispersive X-ray fluorescence spectroscopy
XRD	X-ray diffraction
XRF	X-ray fluorescence spectroscopy
XRM	X-ray microscopy
α	thermal expansion coefficient or the fraction of glass crystallised
δ	chemical shift
ΔG_m	free energy of mixing
ΔH_m	enthalpy of mixing
ΔS_m	entropy of mixing
ΔT	working range: T_x-T_g
ΔT_{FWHM}	the full width at half maximum of the crystallisation peak

1. Introduction and Motivation

The increasing lifespan of the human population causes the demand for millions of implants, like prostheses and bone grafts to maintain the quality of life of the ageing individuals [1]. Biomaterials of the 1st generation are inert materials, whereas the materials of the 2nd generation are bioactive, that is forming a bond with host tissue [2]. Bioactive glasses are biomaterials of the 3rd generation. Those materials have gene activating properties, thereby inducing growth in the local tissue, which leads to tissue repair and regeneration [3].

The first material which was able to bond to bone was Bioglass® [2]. Larry Hench invented Bioglass®, bioactive glass 45S5, in the late 1960s [4] after he had been inspired by a Colonel of the US Army. The idea was to develop a material which can be used to fill bone defects, and which does not get rejected by the human body. The first successful clinical use of Bioglass® was in solid shape in a replacement of ossicles in a human middle ear [5]. Bioactive glass is advantageous in this application compared to other materials because it is not rejected or encapsulated, which would lead to a decrease in sound conduction. Furthermore, the use of bioactive glass was found to be successful in surgery, treating periodontal disease [6] and together with autologous bone in the reconstruction of bones after tumour removal or injury. Bioactive glasses are commercially used as particles or granules to treat bone defects and to support bone tissue regeneration [7]. Moreover, Bioglass® particles are utilised as air abrasion and air polishing reagent in oral healthcare and in toothpaste in the treatment of hypersensitive teeth.

At Åbo Akademi in Turku, Finland, during the 1990s, Andersson et al. [8] investigated 16 glasses in the system SiO_2-Na_2O-CaO-P_2O_5-Al_2O_3-B_2O_3 and Brink et al. [9] 26 glasses in the system Na_2O-K_2O-MgO-CaO-B_2O_3-P_2O_5-SiO_2 in *in-vivo* tests in the rabbit tibia. The composition of those glasses was chosen as a basis for statistical evaluation in order to correlate the influence of the oxides with the *in-vivo* performance [10]. This approach led to the discovery of glass S53P4 by Andersson et al., which is successfully used in the treatment of bone infections [7] and, which is commercially available since 2009 as Bonalive® [11] granules or putty. In both studies, models were developed to predict *in-vivo* performance as a function of the glass composition.

Typical bioactive glasses, like Bioglass® or Bonalive® exhibit a high tendency of crystallisation [12], which leads to a restricted field of application. Whereas particles or granules are easy to process, more complex structures which require glass forming at elevated temperatures are difficult to obtain. Furthermore, the bioactive glass Bonalive® does not dissolve completely even after 14 years in the human body [12], whereas a complete replacement by body tissue is favoured.

Boron is an interesting component in bioactive glasses because this element is known to play a role in the metabolism of healthy bones. [13-15]. Borosilicate glasses have shown to support cell growth [16], adhesion and differentiation in cell tests and to enhance bone formation [17] *in-vivo*. With an increasing amount of boron in the glass, a faster and more complete dissolution process enables an earlier formation of hydroxyapatite [18, 19], which is the inorganic substance of bones.

The objective of this thesis is to investigate systematically the impact of the boron content in bioactive glass has on the structure of these glasses, the solubility and on the crystallisation behaviour. Is it possible to control the solubility behaviour by the boron content of the glass? How is the influence of the boron substitution on the crystallisation tendency? Therefore, a glass series was designed by systematically substituting boron for silicon up to 25 % starting from Bioglass® 45S5.

As mentioned above, there are already extensive studies on boron-containing glasses. The study by Brink et al. [9] provides valuable in-vivo data, whereas a study by Fagerlund et al. [20] offers dynamic dissolution test results. Brink et al. and Fagerlund et al. worked with glass systems containing K_2O and MgO, which have the advantage to lead to a decreased crystallisation tendency in comparison to Bioglass® [10]. The investigation of the structure on their boron-containing glasses has been included in the study as an attempt to draw conclusions about the structure-property correlations in comparison to the systematical glass series.

2. Theoretical Background

2.1. Glass and Borosilicate Glass

Glass can be defined as a solid state, whose (1) atoms exhibit no periodic long-range order and (2) which shows a glass transition [21]. In contrast to crystalline solid states like ceramics, atoms in glasses exhibit only a near-range order. If you compare exemplarily crystalline silicates with silicate glasses, you can see that the fundamental unit is a SiO_4 tetrahedron in both materials, Figure 1. This illustration is a 2D projection leading to the fourth oxygen atom being positioned before or behind the image plane. However, for crystalline silicates in contrast to silicate glasses, the assembly of the atoms is periodically recurring and pre-established on long distances (1a).

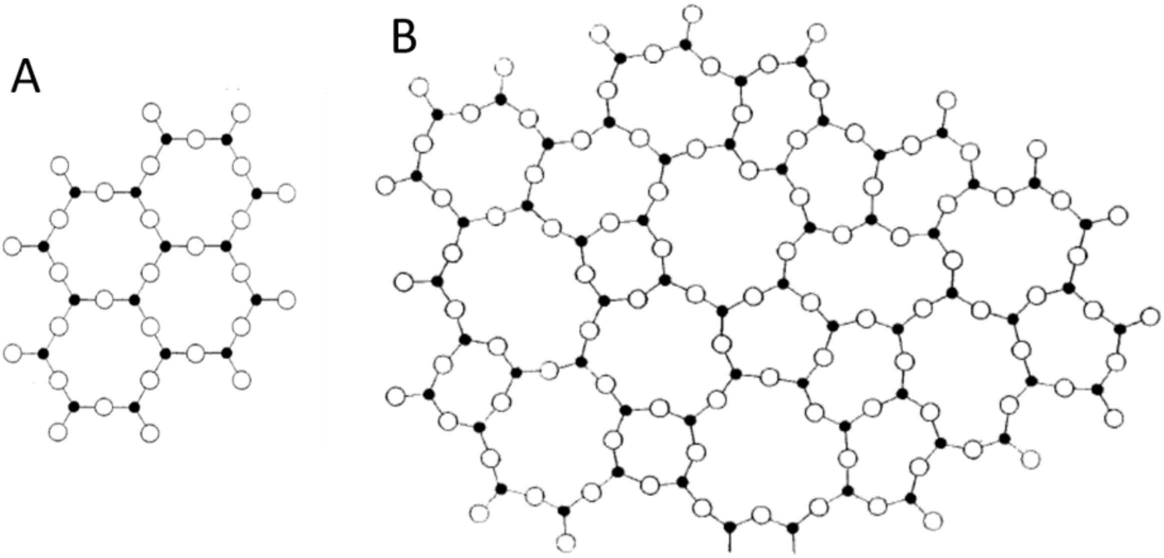

Figure 1: Schematic illustration of a) a crystalline silicate (quartz crystal) structure and b) a silicate glass structure [22]. Black: silicon atoms; white: oxygen atoms. Reprinted (adapted) with permission from Journal of the American Chemical Society, 54, W. H. Zachariasen, "The atomic arrangement in glass", 3841-3851, 10, Copyright (1932) American Chemical Society.

Due to the diverse structures, the properties of glasses and ceramics are different. The volume in dependence on the temperature is plotted exemplarily for a crystal and a glass in Figure 2. The volume of a glass melt changes gradually in opposite to the formation of a crystal from a melt whereby the volume declines suddenly reaching melting temperature T_m.

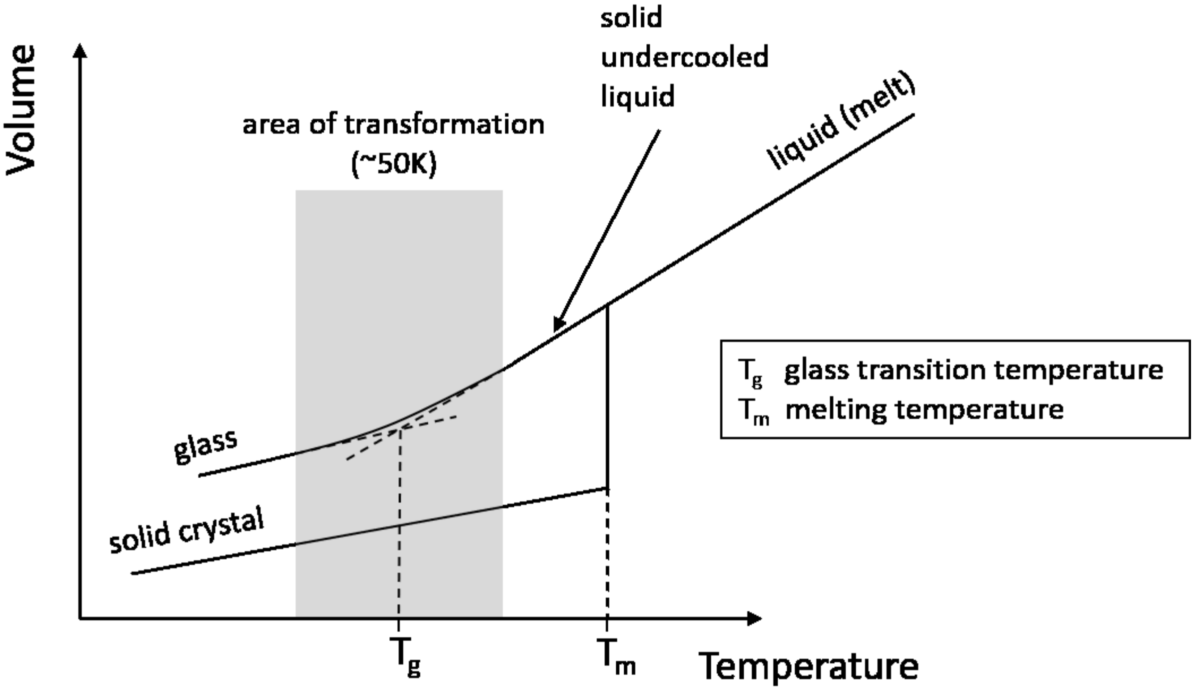

Figure 2: The volume in dependence on the temperature when cooling a liquid (melt).

When cooling a glass melt, there is a change in the slope in the area of transformation, Figure 2. This temperature is designated as glass transition temperature T_g. Below T_g, the glass is solid and behaves like a brittle-elastic solid state [21]. The glass transition is defined as “reversible change in an amorphous material or in amorphous regions if a partly crystalline material, from (or to) a viscous or rubbery condition to (or from) a hard and relatively brittle one” [23].

In a pure silicate glass, the four oxygen atoms at the corners of the tetrahedron are connected to other silicon atoms (bridging oxygen, BO). If network modifier like Na_2O and CaO are introduced in the system, negatively charged, non-bridging oxygen (NBO) atoms are formed, which are charge balanced with the positive network modifier ions, like Na^+ or Ca^{2+} [24].

Borosilicate glass systems provide the basis for many commercial glasses [21]. Most of them are phase-separated on a very fine scale (e.g. 5-20 nm), while they look transparent to the naked eye. Aluminium is one component of many commercially used borosilicate glasses, which leads to a depressed immiscibility temperature and consequently to a finer microstructure. Often borosilicate glasses are applied because they have better thermal shock resistance and improved chemical durability in comparison to soda lime glasses. The best-known phase-separated borosilicate glass is the glass Pyrex®, which contains about 81 wt% SiO_2, 13 wt% B_2O_3, 4 wt% Na_2O and 2 wt% Al_2O_3 leading to a silica-rich matrix with dispersed glass droplets containing the soda as well as the boric oxide. The chemical durability is close to the one of pure silica glass.

2.2. Bioactive Glass

The first synthetical material, which was able to bond to bone, was the ***bioactive glass Bioglass® 45S5***. Larry Hench, who is the inventor, tells in “The story of Bioglass®” [2] how he got inspired to work on the development of this fascinating material. In the summer of 1967, Hench was on his way to an U.S. Army Materials Research Conference. On the bus ride, he was talking to U.S. Army Colonel Klinker, who had just returned to the U.S. from Vietnam shortly before. Klinker asked Hench if he could make a material that would survive the exposure in the human body. The colonel said that the plastic and metallic implants available to the surgeons are rejected by the human body, leading to the necessity of numerous amputations. Klinker's statement “We need new materials that will not be rejected by the body” provided a delightful research topic to Hench. He prepared a proposal to the US Army [25]. In autumn 1969 the project was granted to test the hypothesis that “silicate-based glasses and glass-ceramics containing critical amounts of Ca and P ions would not be rejected by bone” [25]. Shortly after, Larry Hench prepared rectangles of Bioglass® 45S5 and Ted Greenlee, an Assistant Professor of Orthopaedic Surgery implanted them in the femur of rats. After six weeks Greenlee was very surprised about the performance of the material, as the samples did not come out of the bone. He pulled them, he pushed them, he cracked the bone, but the samples were still bonded in place [25]. Bioglass® has been in clinical use since 1985 [26].

In the Williams Dictionary of Biomaterials [27], there are two records for “bioglass”:

(I) glass based on SiO_2, which has a specific surface reactivity that enhances the interaction with surrounding tissue due to the action of additives, primarily alkali oxides

(II) trade name for series of bioactive glasses that have compositions in the range 40-55% wt% SiO_2, 12-25 wt% CaO, 19-25 wt% Na_2O and 6 wt% P_2O_5

Bioactivity implies an interaction between the implant and the surrounding living tissue leading to the formation of a bond [1]. Bioactive glasses can form this bond by developing a surface layer of apatite through the release of ions from the bulk material.

The ***composition of Bioglass®*** is similar to the one of soda lime glass, which is used as window and container glass, see Figure 3. The main components of both glasses are SiO_2, CaO and Na_2O.

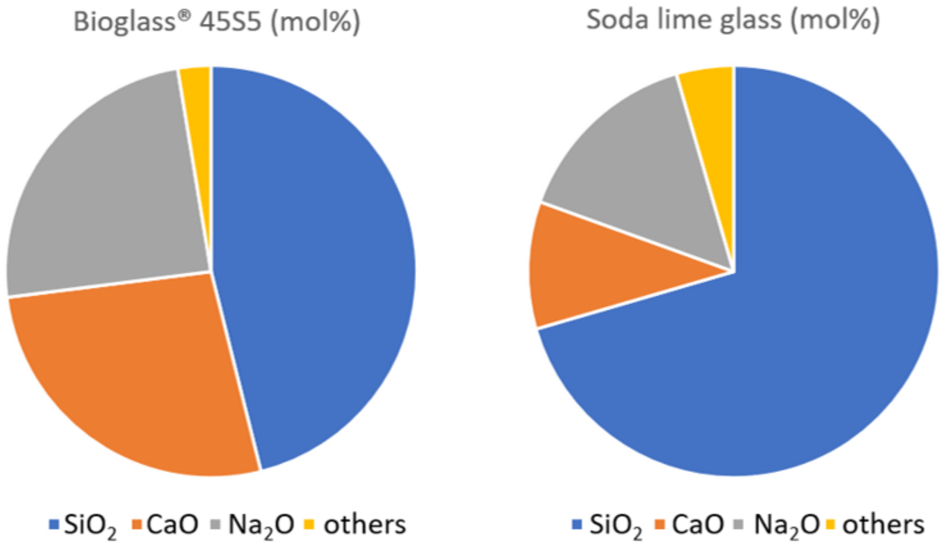

Figure 3: Components (mol%) of Bioglass® and soda lime glass. Data for the soda lime glass from Lohmeyer [28].

The network former in both glasses is silicon oxide. The amount of network modifiers in Bioglass® is high, with 26.9 mol% CaO and 24.4 mol% Na_2O, leading to the formation of many non-bridging oxygen atoms (NBO). For charge balance, NBO´s are surrounded by positive charged network modifier ions. Bioglass® exhibits a less cross-linked structure in comparison to conventional glasses [29], which contain a lower amount of network modifiers.

The structure of bioactive phospho-silicate glasses like Bioglass® is relatively well-understood [7, 26]. For individual glass compositions, the network connectivity (NC) can be calculated [4], see equation (2.1), which is the number of bridging oxygens per $[SiO_4]^{4-}$ tetrahedron.

$$\boldsymbol{NC = 2 + \frac{BO-NBO}{G}} \qquad (2.1)$$

Thereby, BO is the number of bridging oxygens, NBO the number of non-bridging oxygens and G the number of glass-forming units.

Phosphorus in melt-derived bioactive silicate glasses, like Bioglass® 45S5, is mainly present in the form of single orthophosphate groups (PO_4^{3-}) [4, 30, 31], see Figure 4 rather than participating in the glass network. For charge balance, it is surrounded by calcium ions and sodium ions [32].

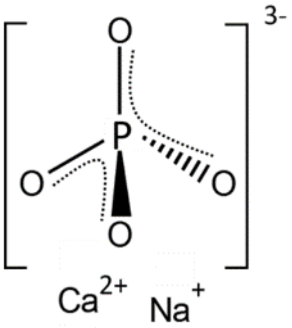

Figure 4: Orthophosphate group charge balanced with calcium ions and sodium ions

Application of equation (2.1) for Bioglass® with the composition (mol%) 46.1 SiO_2, 2.6 P_2O_5, 24.4 Na_2O and 26.9 CaO, gives a network connectivity of 2.11 [4].

$$NC_{45S5} = 2 + \frac{[2*SiO_2]-[(2*Na_2O)+(2*CaO)]+(2*P_2O_5*3)}{[SiO_2]} \qquad (2.2)$$

The network connectivity of 45S5 is very low in comparison to other glasses, with 2.11 which is caused by the high amount of network modifiers. Theoretically, 2.11 bridging oxygen atoms per silicon atom lead to a fragmented chain-like structure with a few crosslinks between the chains.

A schematic sketch of the Q^n nomenclature to illustrate the glass structure is shown in Figure 5.

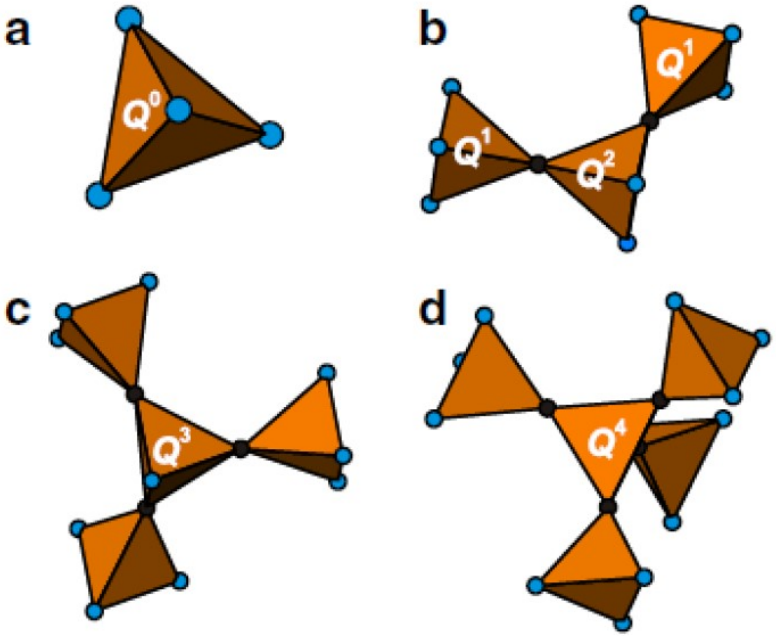

Figure 5: Schematic illustration of the Q^n nomenclature [33]. Reprinted from Journal of Non-Crystalline Solids, 357, M. Edén, "The split network analysis for exploring composition–structure correlations in multi-component glasses: I. Rationalizing bioactivity-composition trends of bioglasses", 1595-1602, 6, Copyright (2011), with permission from Elsevier. While a silicon atom is located in the centre of every tetrahedron, the blue circles represent NBO atoms and the black circles BO atoms.

While a silicon atom is located in the centre of every tetrahedron, the blue circles represent NBO atoms and the black circles BO atoms. The Q^n groups represent the possible building units in the glass structure, whereas n denotes the number of bridging oxygens per network former unit [21]. Every single SiO_4 tetrahedron (a) has zero bridging oxygen atoms and is therefore assigned as Q^0 unit. A SiO_4 tetrahedron, which is connected to other tetrahedrons along three corners is named a Q^3 unit (c). In Bioglass® 45S5, which is less connected, a high amount of Q^1, Q^2 and Q^3 groups are present.

When bioactive glasses get in contact with aqueous media, they start to dissolve [34]. Molecular dynamics simulations of a dry surface of Bioglass® 45S5 in interaction with a water molecule were carried out by Tilocca et al. [35]. The surface of bioactive silicate glasses is significantly rough and not homogeneous, which is caused by the low amount of silica in the glass. Preferred absorption sites of the water molecules on the glass are positions occupied by sodium and calcium cations. By these sites, the polar water molecules are enabled to penetrate under the surface of the glass. Furthermore, spontaneous dissociation of the water molecule occurs at strong sites [36]. According to Tilocca [36] strong sites are undercoordinated silicon atoms and non-bridging oxygens (NBOs) connected to undercoordinated and so reactive modifier cations.

An exchange reaction takes place: hydrogen ions from the aqueous environment inserted in the low connected glass structure react with the negatively charged non-bridging oxygen ions leading to the formation of silanol groups, Figure 6. Network modifier cations are leached out of the glass.

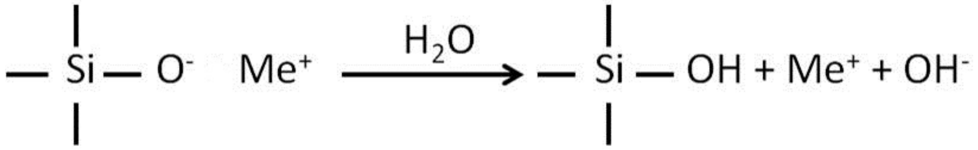

Figure 6: Due to the attack of water on the bioactive glass silanol groups are formed, positively charged network modifier cations are leached out of the glass and the pH-value in the surrounding media increases.

Molecular dynamic simulations by Tilocca [37] are dealing with the "early-stage alkali depletion and the SiO_2-rich gel formation in bioactive glasses". A model of Na^+/H^+ exchanged bioactive glass 45S5 was investigated. According to his study, the stable condition of a water molecule in Bioglass® 45S5 is the dissociated one. There is a high affinity between the OH^- present in the glass structure upon the dissolution process and the network modifier cations. This suggests that a large amount of OH^-, which entered the glass structure at first, is surrounded by network modifier cations rather than forming Si-OH or P-OH bonds.

Upon leaching of the network modifier ions, a silica-gel layer (ion-depleted layer) is formed. In that layer, there is an increase in the concentration of bridging oxygen atoms [37] in comparison to the Bioglass® structure. The study by Tilocca suggests that OH^- is stabilised by network modifier cations, while non-bridging oxygen atoms form cross-linking bridges with other silicon atoms, which thereby leads to an increase in the concentration of bridging oxygens. But for high exchange stages of Na^+/H^+, bond formation between the OH^- and the Si/P network formers take place.

Due to the remaining hydroxyl ions in the surrounding media the pH-value increases. The positively charged network modifier ions are leached out of the glass. The components of typical bioactive glasses like silicon, sodium, potassium, magnesium, oxygen, calcium and phosphorus are physiologically found in the human body [7]. Upon interaction with the surrounding solution, the concentration of these components does not reach levels high enough to disturb adjacent tissues.

As the water can penetrate deeply into the low connected glass structure a complete dissolution of the glass in the human body is possible in theory. Stronger connected glass networks with network connectivity of 2.4 or higher are more resistant in body fluid [4].

Hydroxyapatite ($Ca_5(PO_4)_3OH$) is the most stable calcium phosphate at physiological conditions (T = 37°C, pH-value= 7.4) [38]. Apatites are a group of calcium orthophosphates (e.g. hydroxyapatite) [26]. Various ion substitutions within the apatite structure are possible. Mineralised human tissue like dentin, enamel and bone is mainly composed of apatite. As bioactive glass provides the required ions, in case of supersaturation, apatite nucleation takes place [38]. The surface of the bioactive glass particle thereby often acts as a nucleus for crystallisation. An apatite layer is formed on the bioactive glass, which enables the bond to bone tissue [7, 26].

By inserting bioactive glass in the human body, bone defects can be cured. Ideally, the degradation of the bioactive glass should be as fast as the formation of the new bone in the body.

In comparison to other biomaterials, bioactive glasses have the advantage to form a ***strong interfacial bond to bone***. In Figure 7, SEM pictures and EDX profiles by Brink et al. [9] are presented after the 8-week implantation of glass cones in rabbit bone. Whereas in the left picture (A) the cross-section of the interphase inert glass-bone is shown, the right picture (B) presents the bond formation of bioactive glass to the bone.

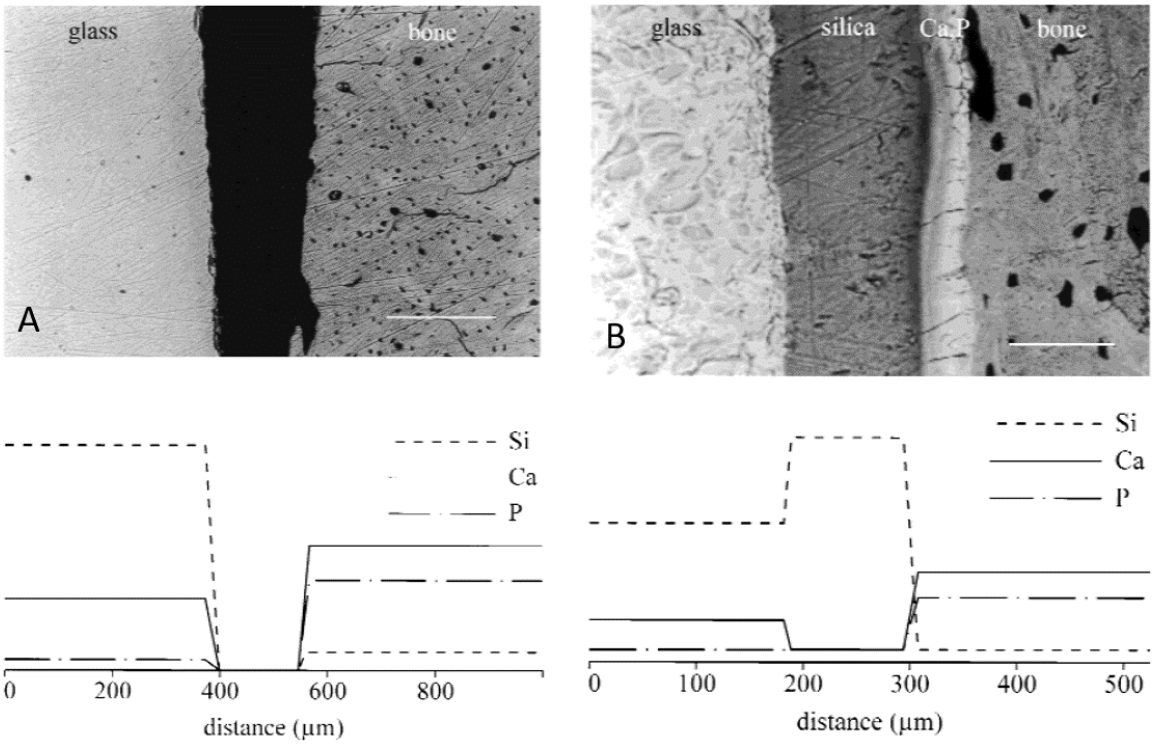

Figure 7: SEM pictures of cross-sections and schematic representation of the corresponding EDX profiles from the interface A) inert glass-bone and B) bioactive glass-bone after 8 weeks in rabbit tibia [9]. Reprinted from Journal of Biomedical Materials Research, 37, M. Brink, T. Turunen, R. Happonen, et al., Compositional dependence of bioactivity of glasses in the system Na_2O-K_2O-MgO-CaO-B_2O_3-P_2O_5-SiO_2, 114-121, 1, Copyright (1998), with permission from Wiley. A) A gap is visible between inert glass and bone. Bar = 200 µm. B) No gap is between bioactive glass and bone. Bar = 100 µm.

Between the inert glass and the bone is a gap (black), Figure 7A, which indicates no bond between the two materials. The bioactive glass bonded to the bone, Figure 7B. Between the bioactive glass and the bone, the silica layer (ion-depleted layer) and a layer rich in calcium and phosphorus (Ca,P) are present. In the schematic representation of EDX along both interfaces, the ratio of Ca to P in glass and bone is similar. Whereas the area of the gap exhibits no elements as expected, the silica-gel layer is very rich in silicon and low in calcium and phosphorus. The Ca,P layer exhibits an amount of silicon, calcium and phosphorus similar to the concentration of these elements in the bone.

Furthermore, the ***introduction of therapeutically active ions*** into the glass during manufacturing is possible [7], which enables flexible options adapted to the needs at the implant site.

Strontium-containing drugs are used in the treatment of osteoporosis. Osteoporosis is a disease, where the osteoblasts, the bone-forming cells, fail to produce enough new bone while the osteoclasts, bone-degrading cells, remove too much. Strontium-containing bioactive glasses have been shown to stimulate the osteoblasts while detaining the osteoclasts from resorbing too much bone [39].

Fluoride ions can be incorporated into apatite, leading to the formation of fluorapatite (FAp). The stability of FAp is higher in comparison to hydroxyapatite [38]. In the oral milieu, the FAp is more resistant against acidic attack than hydroxyapatite, as well. Therefore, the incorporation of fluoride is very interesting for dental applications.

Bioactive glasses do exhibit ***antibacterial properties***, which are associated with the increase in pH-value as well as in osmotic pressure [7], caused by the release of ions at the implant site.

Nowadays in clinical application, bioactive glass is used to treat small bone defects in non-load bearing regions of the body. An unmet challenge is the usage for structural, load-bearing bone defects [40]. The treatment of large bone defects due to cancer tumour removal or injury put high requirements on the used material. For example, three-dimensional porous scaffolds, ideally with adequate strength and toughness would be great to have to treat these large bone defects. Glass is a ***brittle*** material, which is a problem in the application of structural bone defect treatment [40]. One interesting option is the development of composite biomaterials, whereby the bioactive glass would be one component to serve clinical applications [1].

Bioactive silicate glasses exhibit a ***high crystallisation tendency*** [12], which makes the shaping of the glasses into 3-dimensional constructs at elevated temperatures very complex.

The further understanding of how the structure influences properties, like solubility and crystallisation tendency is of fundamental importance to tailor new bioactive glasses to meet the high demands in clinical applications.

2.3. Bioactive Borosilicate Glasses

Boron plays a role in the metabolism of healthy bones, which was known already in the 1990s [13-15]. It stands to reason to investigate the influence of boron in bioactive glasses. Exemplarily the time curve for the search item “bioactive borosilicate” (topic) in the database Web of Science carried out in July 2019 is plotted in Figure 8.

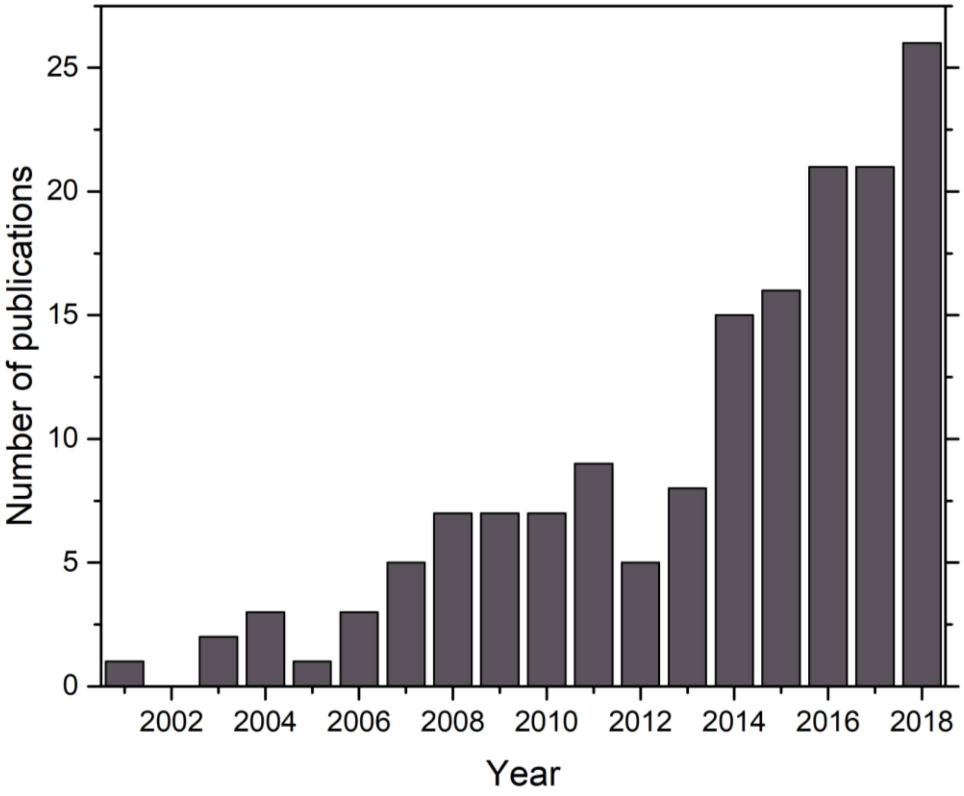

Figure 8: The number of publications per year during the timespan 2001-2018 for the search term “bioactive borosilicate” (topic) in the database Web of Science in July 2019.

For the time span from 2001 to 2018, 157 publications are listed in total. The research interest in this topic is growing: whereas in the year 2001 there was only one publication, over the course of time the number rose to 26 in 2018.

There are two interesting aspects regarding boron in bioactive glasses: (I) the chemical and (II) the biological point of view.

(I) Huang et al. [18] investigated the dissolution behaviour of glass 45S5, a borate glass and two intermediate borosilicate glass compositions in a phosphate solution. A higher content of B_2O_3 in the glass led to a faster conversion of the glass to hydroxyapatite. Yao et al. [19] carried out a similar study starting from a bioactive silicate glass, which did contain K_2O and MgO besides the components of glass 45S5: SiO_2, CaO, P_2O_5 and Na_2O. They found that the conversion rate to hydroxyapatite is depending on the ratio of B_2O_3/SiO_2 in the glass, as well. Furthermore, the glasses with a higher B_2O_3 content did react more completely in both studies. Thus, with increasing boron content, a ***faster and more complete dissolution process*** enables the ***earlier formation of hydroxyapatite***. The rate of glass degradation is tuneable and should be possible to match the bone regeneration rate in the body [41].

(II) Borosilicate glass has shown to ***support cell growth*** [16], ***adhesion*** and ***differentiation*** *in-vitro*, and in a rat model, tissue infiltration has been observed *in-vivo* after implantation for 6 weeks. The controlled release of boron ions has shown improved ***angiogenesis*** [42], which is the formation of new blood vessels. Borosilicate glass implanted in rat tibia bone led to an enhanced ***bone formation*** in comparison to glass 45S5 [17].

Yu & Eden [43] published a very interesting systematic investigation of two glass series in the system: SiO_2-B_2O_3-P_2O_5-CaO-Na_2O. ^{11}B, ^{29}Si, and ^{31}P MAS nuclear magnetic resonance (NMR) were used to examine the structure of these glasses. Orthophosphate is the present phosphorus species in all glasses. The amount of tetragonal boron increases and the polymerisation of the silicate network increases slightly with rising boron content.

2.4. Phase Separation, Glass Stability and Crystallisation

The liquids water and alcohol are completely miscible, stable in one homogeneous phase [21]. The combination of water together with oil in a container is, in contrast to the first example immiscible, called ***phase-separated***. After shaking the container, small droplets of the minor phase would appear in the matrix of the major phase. Because water and oil have a low viscosity, waiting would lead to the formation of two layers with the less dense phase (oil) on top of the denser layer (water).

Why do some liquids and melts separate in different phases while others stay homogeneous? If the free energy of mixing ΔG_m is lower for a homogeneous system, it will not separate [21]. But if ΔG_m is higher for the homogeneous state, phase separation will occur if possible. Kinetic considerations have to be taken into account. The free energy of mixing is given by the following expression (2.3):

$$\Delta G_m = \Delta H_m - T\Delta S_m \qquad (2.3)$$

where ΔH_m is the enthalpy of mixing and ΔS_m is the entropy of mixing. Above a critical temperature, the term $T\Delta S_m$ will be larger than the term ΔH_m, leading to a negative value of ΔG_m, indicating a homogeneous system.

In glass-forming melts liquid-liquid immiscibility is a widespread phenomenon [21]. Some commercial glass products, e.g. from the borosilicate system are based on phase-separating compositions.

How resistant a glass is against devitrification upon heating, is named its ***glass stability*** [44]. Usually, the glass stability is accessed by calculating the difference of T_x (onset of crystallisation) and T_g from a glass sample, which was heated up at a constant linear rate. Typically, DSC or DTA measurements are used and in case of multiple crystallisations, only the first one is considered for the calculations.

Crystallisation in a glass melt requires two processes: nucleation and crystal growth [21]. Nucleation can occur spontaneously in the bulk (homogeneous nucleation) or at a surface, e.g.at impurities in the glass (heterogeneous nucleation). Crystal growth can only start if a nucleus was formed beforehand.

The classical ***nucleation*** theory deals with homogeneous nucleation, which occurs spontaneously in the bulk [21]. Nucleation is the formation of a small unit, called "embryo", due to thermal fluctuations in a melt [24]. These embryos form and dissolve naturally.

There are two barriers regarding the formation of homogeneous nuclei [21]. (I) The thermodynamic barrier: change of the free energy in the system upon formation of a nucleus. (II) The kinetic barrier: rearrangement of mass to enable the growth of an organised particle.

The nucleation process can be described by (2.4) [21], whereby A can be expressed by formula (2.5):

$$I = A \exp\left[-\frac{W^{*}+\Delta G_D}{kT}\right] \qquad (2.4)$$

$$A = n_v\left(\frac{kT}{h}\right) \qquad (2.5)$$

where n_v is the number of formula units of the crystallising component phase per unit volume of the melt, k is the Boltzmann constant, T the absolute temperature in Kelvin and h is Planck´s constant. W^{*} is the thermodynamic energy barrier, in detail, the work required to form a nucleus of critical size. A nucleus, which reached the critical size will grow instead of redissolve. $\Delta G_D$is the kinetic free energy barrier to nucleation.

The ***thermodynamic barrier*** involves two influences, whereas the overall change in energy W upon the formation of a spherical nucleus is given by (2.6) [21]:

$$W = \frac{4}{3}\pi r^3 \Delta G_v + 4\pi r^2 \gamma \qquad (2.6)$$

where r is the radius of the forming nucleus, ΔG_v is the change in volume free energy per unit volume and γ is the crystal-melt interfacial free energy per unit area. The formation of a nucleus is accompanied by two changes in the energy of the system. (I) Upon formation of a crystalline nucleus, the volume free energy will decrease because the crystalline state has a lower volume free energy in comparison to the amorphous one. (II) The surface energy increases due to the formation of a new interface between the crystalline and the amorphous phase. Below the melting point of the crystal, T_m, the terms $\frac{4}{3}\pi r^3 \Delta G_v$ and $4\pi r^2 \gamma$ have opposite signs as the ΔG_v is negative. First, when the nucleus is little, the (positive) surface term dominates, leading to a nucleus, which is not stable. In case the nucleus grows further, starting from the critical radius r*, the volume term dominates, resulting in the presence of a stable nucleus.

The ***kinetic barrier*** for nucleation can be expressed in terms of the effective diffusion coefficient D, as calculated by (2.7) [21]:

$$D = \frac{kT\lambda^2}{h} \exp\left(\frac{-\Delta G_D}{kT}\right) \qquad (2.7)$$

where λ is the atomic jump distance.

According to the Stoke-Einstein relation (2.8) [21], the diffusion coefficient is dependent on the viscosity η.

$$D = \frac{kT}{3\pi\lambda\eta} \qquad (2.8)$$

Introducing (2.7) and (2.8) in the original formula (2.4), gives the following equation (2.9).

$$I = \frac{Ah}{3\pi\lambda^3\eta} \exp\left[-\frac{W^*}{kT}\right] \qquad (2.9)$$

The ***crystal growth*** is determined by a kinetic and a thermodynamic part [21]. The crystal growth rate U is given by the following expression (2.10) [21]:

$$U = a_0 \nu \exp\left(\frac{-\Delta E}{kT}\right) \left[1 - \exp\left(\frac{\Delta G}{kT}\right)\right] \qquad (2.10)$$

where a_0 is the interatomic separation distance, ν is the vibrational frequency, ΔE and ΔG the kinetic and the thermodynamic barriers.

Introducing (2.7) and (2.8) in equation (2.10), leads to equation (2.11).

$$U = \left(\frac{kT}{3\pi a_0^2 \eta}\right)\left[1 - \exp\left(\frac{\Delta G}{kT}\right)\right] \qquad (2.11)$$

If a nucleus is available, crystal growth can occur at any temperature below the melting temperature of the crystalline phase, T_m [21]. At high temperatures, the viscosity of a material is relatively low. Equation 2.11 shows that at high temperatures the crystal growth is limited by the thermodynamic term only. For lower temperatures, the viscosity increases, which leads to a decreasing crystal growth rate due to a decreased diffusion.

The Johnson-Mehl Avrami (JMA) exponent n provides information on the crystal growth behaviour of the investigated system [45]. Whereas a JMA exponent value of 1 is associated with surface crystallisation, 2 is assigned to volume crystallisation in 1D (one dimension; e.g. needles), 3 to volume crystallisation in 2D (two dimensions, e.g. small discs) and 4 to an interface correlated volume crystallisation in 3D (three dimensions, e.g. spheres) [46, 47]. A JMA exponent of >4 is associated with a complex crystallisation in 3D [47].

2.5. Mathematical Models

According to Hupa & Karlsson [10] the properties of a homogeneous material, like a silicate glass are determined by the amount of its components, e.g. oxides. ***Linear*** functions can be used as simple property-composition ***models*** (2.12), where x is a property-value, in brackets is the concentration of the different components together with factors, like a_0.

$$x = a_0 + a_1 * [Na_2O] + a_2 * [CaO] + \cdots a_n * [SiO_2] \qquad (2.12)$$

Andersson et al. [8] developed a phenomenological model to estimate the bioactivity of a glass according to its composition in the system SiO_2-Na_2O-CaO-P_2O_5-Al_2O_3-B_2O_3, see equation (2.13). The glass compositions were chosen statistically and regression analyses were used for the development of the model [10]. The bone bonding after 8 weeks implantation in rabbit tibia was investigated via scanning electron microscopy (SEM) in combination with energy-dispersive X-ray analysis (EDX). The property bioactivity (bonding to bone) was analysed using reaction numbers (RN), whereas the values in brackets, e.g. [SiO_2] are the concentrations of the components in wt%.

$$RN = 88.3875 - 0.0116272[SiO_2]^2 + 0.980188[Na_2O] - 1.12306[CaO] - \\ 1.20556[P_2O_5] - 0.560527[B_2O_3]^2 - 2.08689[Al_2O_3] \quad (2.13)$$

Brink [48] modified this model with the following assumptions: K_2O behaves like Na_2O, so the amount of Na_2O is substituted by Na_2O + K_2O in the model and MgO behaves like CaO, so the amount of CaO is substituted by CaO + MgO in the model. This model will be referred from now on as the "***modified Andersson model***". The assignment of the reaction numbers (RN) is plotted in Table 1 and the validity range of the model is given in Table A 1 (appendix).

Table 1: Assignment of the reaction numbers from the Andersson model [8]. Information in () is taken from Hupa & Karlsson [10]

Morphology	Reaction numbers (RN)
nearly inert glasses, only small changes in the surface composition and hardly any bone contact (inert composition leading to gap formation)	1/A
fairly high solubility, bone contact but no bonding, formation of a silica-rich layer but no accumulation of calcium and phosphorus (poor contact)	2/B
fairly high solubility, bone contact but no bonding, formation of a silica-rich or sodium-depleted layer	3/C
fairly high solubility, the formation of calcium and a phosphorus-rich surface layer, but no bone-bonding (good bone contact)	4/D
bioactive glasses, the formation of calcium- and phosphorus-rich surface layer and bone-bonding	6/E

Brink et al. [9] investigated the in-vivo behaviour of statistically chosen [10] glasses containing K_2O and MgO. The addition of these two components reduces the crystallisation tendency of bioactive glasses, which contain high concentrations of Na_2O and CaO in combination with a low amount of SiO_2 [10]. Surface reaction layers were investigated at the implanted glass after 8 weeks in rabbit tibia via SEM and EDX. The ***Index of surface activity model (ISA)*** is a model, which was developed by Brink et al. [9] (2.14) to access the relative in-vivo bioactivity in the glass system SiO_2-Na_2O-K_2O-MgO-CaO-B_2O_3-P_2O_5.

$$ISA = -8.4 + 79.0\frac{[Na_2O]+[K_2O]}{[SiO_2]} - 1.8\frac{([Na_2O]+[K_2O])^2}{[SiO_2]} - 11.6\frac{[MgO]}{[SiO_2]} - 9.2\frac{[CaO]}{[SiO_2]} - 84.8\frac{[B_2O_3]}{[SiO_2]} + 24.1\frac{([B_2O_3])^2}{[SiO_2]} + 21.9\frac{[P_2O_5]}{[SiO_2]} - 4.5\frac{([P_2O_5])^2}{[SiO_2]} \quad (2.14)$$

The assignment of the values in the ISA model are plotted in Table 2 and the validity range is given in Table A 2 (appendix).

Table 2: Assignment of the values in the ISA model by Brink et al. [9].

Morphology	ISA value
inert	ISA 1
silica layer	ISA 2
layered structure	ISA 3
bioactive	ISA 4

Pearson´s coefficient of correlation [49] r is a measure of the correlation between two (random) variables X and Y. It is calculated by dividing the covariance by the product of both standard deviations, see equation (2.15).

$$r = \frac{\sum_{i=1}^{n}(X_i-\bar{x})(Y_i-\bar{Y})}{\sqrt{\sum_{i=1}^{n}(X_i-\bar{x})^2}\sqrt{\sum_{i=1}^{n}(Y_i-\bar{Y})^2}} \quad (2.15)$$

The correlation coefficient r between the two variables X and Y is a value between 1 and -1, whereby 1 (-1) indicates a perfect positive (negative) correlation.

Fisher discriminant ratio [50] f_i is a measure for the separability of samples between two groups, see equation (2.16), where $\mu_{i,*}$are the means and $\sigma_{i,*}^2$ the variances of a random variable in two given groups.

$$f_i = \frac{(\mu_{i,1} - \mu_{i,2})^2}{\sigma_{i,1}^2 + \sigma_{i,2}^2} \quad (2.16)$$

A Fisher discriminant ratio of zero indicates no difference between the groups regarding the random variable, e.g. measured value.

3. Experimental Procedure

3.1. Glass series 45S5-B

3.1.1. Glass Composition & Glass Preparation

Glasses with the composition shown in Table 3 were prepared by a melt-quench route. The calculation for the glass preparation is shown in Table A 3 to Table A 5 in the appendix.

Table 3: Composition of the glasses of the 45S5-B series in mol%.

Glass name	B for Si substitution (%)	SiO_2	P_2O_5	CaO	Na_2O	B_2O_3
45S5	0	46.1	2.6	26.9	24.4	0.0
45S5-0.5B (0.5B)	0.5	46.0	2.6	26.9	24.4	0.1
45S5-1B (1B)	1	45.8	2.6	27.0	24.4	0.2
45S5-2.5B (2.5B)	2.5	45.2	2.6	27.1	24.5	0.6
45S5-5B (5B)	5	44.3	2.6	27.2	24.6	1.2
45S5-10B (10B)	10	42.5	2.7	27.5	24.9	2.4
45S5-15B (15B)	15	40.6	2.7	27.9	25.2	3.6
45S5-20B (20B)	20	38.7	2.7	28.2	25.5	4.8
45S5-25B (25B)	25	36.7	2.8	28.6	25.8	6.1

Batch components SiO_2 (Karl Roth, Karlsruhe, Germany), $(NaPO_3)_n$ (Chemische Fabrik Budenheim, Budenheim, Germany), $CaCO_3$ (Merck, Darmstadt, Germany), Na_2CO_3 (Karl Roth, Karlsruhe, Germany) and H_3BO_3 (Sigma Aldrich, Seelze, Germany) were mixed together with a ceramic ball via shaking by hand in a polypropylene container. Afterwards, the batch components were melted in a furnace with SiC heating elements in platinum crucibles between 1200 and 1350°C and the glass was cast as blocks (~150 g) into brass moulds. The glass blocks were annealed for a minimum of 2 hours at an adjusted temperature of 30 K above the onset of T_g and subsequently cooled down slowly to room temperature in the annealing furnace.

The glass composition of glasses 5B, 15B and 25B was investigated using wavelength dispersive ***X-ray fluorescence spectroscopy*** (WDXRF; Thailand Centre of Excellence for Glass, Department of Science Service, Ministry of Science and Technology, Bangkok, Thailand; S8 Tiger, Bruker AXS GmbH, Karlsruhe, Germany). As pressed powder method was applied, 10 g of glass particles 125-250 µm in size were prepared using stainless-steel mortar and sieves. The glass was ground in a tungsten carbide mortar grinder (Thailand Centre of Excellence for Glass, Department of Science Service, Ministry of Science and Technology, Bangkok, Thailand; RM100, Retsch, Haan, Germany) for 30 s, mixed with grinding aid wax tablets in a ratio of 5:1 and pressed hydraulically with a force of 20 tons for 20 s to form a stable pellet.

3.1.2. Investigation of Glass Structure and Density

To verify the amorphous state of the glasses X-ray diffraction (XRD; workgroup Prof. Wondraczek and workgroup Prof. Rüssel, OSIM, FSU Jena; miniFlex, Rigaku, Japan, CuKα measurements performed at room temperature) was carried out on glass powder which had been prepared using a stainless-steel mortar and subsequent milling for 20 min using an agate ball mill (OSIM, FSU Jena; KM1, MLW Janetzki, VEB Spezialmaschinenbau, Lutherstadt Wittenberg, Germany).

To examine potential phase separation of the glasses, the ***replica technique*** was carried out comprising the following steps:

1) A glass disc (thickness ~3 mm) is bent using tongs and finally broken to generate a new fracture plane.
2) Etching the fractured plane either for 10 s in a 1:1 mixture (by volume) of H_2O and 96% ethanol applied for glass 25B or for 5 s in 1 N HNO_3 (for glass 5B, 10B, 15B and 20B), followed by cleaning in H_2O and ethanol in a row.
3) Rinsing the disc in acetone and applying a cellit (cellulose acetate) foil on the etched surface.
4) Remove the cellit foil from the etched surface after drying to clean the surface thoroughly.
5) Coating the etched surface in a 30° angle with a Pt-Ir-C layer [51].
6) Removing the replica film (Pt-Ir-C membrane) from the glass by dipping the coated surface slowly into 40% NH_4F solution.
7) Rinse replica film twice in deionised water, followed by placing it on a copper mesh microscope slide.

The replica films were investigated in a transmission electron microscope (TEM; workgroup Prof. Rüssel, OSIM, FSU Jena; H8100, Hitachi, Tokyo, Japan) with an acceleration voltage of 200 kV.

^{29}Si MAS ***nuclear magnetic resonance spectroscopy*** (NMR) was examined for glass powders 45S5, 1B, 10B and 25B. A small amount of $CuCO_3$ (<0.005 g/100 g glass) was mixed with glass powder of glass 1B, 10B and 25B and remelted in the glasses to decrease the relaxation times. ^{29}Si MAS NMR was carried out at a 400 MHz (9.4 T) spectrometer (Avance III, HD 400, Bruker, Billerica, MA, USA) with a resonance frequency of 79.5 MHz at 12.5 kHz with the following d1 values: 3000 s (glass 45S5), 4500 s (glass 1B), 3800 s (glass 10B), and 4000 s (glass 25B). A Bruker 4 mm probe was used. Pulse length was 3 µs for 45S5, 1.5 µs for glass 1B and 10B and 1.25 µs for glass 25B. The number of scans was 64 for all examined glasses. The reference substance used was tris(trimethylsilyl)silane (TTMSS). The ^{29}Si MAS NMR spectra were normalised to the maximum.

^{31}P MAS NMR and ^{11}B MAS NMR were investigated for glasses 0.5B, 1B, 2.5B, 10B, 15B, 20B and 25B. ^{31}P MAS NMR experiments were performed on a Bruker Avance III 300 MHz (7 T) spectrometer (workgroup Prof. van Wüllen, Institute of Physics, University of Augsburg, Germany; Bruker, Billerica, MA, USA) with a resonance frequency of 121.4 MHz at MAS frequency of 10 kHz. ^{11}B-MAS NMR experiments were performed on a Varian VNMRS 500 (11 T) spectrometer (workgroup Prof. van Wüllen, Institute of Physics, University of Augsburg, Germany; Agilent Technologies, Santa Clara, CA, USA) with a resonance frequency of 160.4 MHz at MAS frequency of 30 kHz. As probes a Bruker 4 mm triple resonance probe and a Varian 1.6 mm T3 MAS probe were used. Reference substances were phosphoric acid (80%) and boric acid. The spectra were recorded with repetition times of typically 350 s for ^{31}P and 50 s for ^{11}B with typical pulse lengths of 1 µs and 1.25 µs, respectively. Used number of scans was 16 for ^{31}P and for ^{11}B the following: 1024 (glass 0.5B and 1B), 512 (glass 2.5B), 128 (glass 10B-25B). The ^{31}P and ^{11}B MAS NMR spectra were normalised to the maximum.

Plane-parallel polished glass slides were used for investigation via ***Fourier transform infrared and Raman spectroscopy.*** Grinding of the slides was done using silicon carbide (particle range 9-17 µm) and polishing was carried out using an ethanol-based 1 µm diamond suspension (DP-Suspension A, Struers GmbH, Willich, Germany). Infrared (IR) measurements were carried out using a Fourier transform vacuum IR spectrometer (FTIR; Theoretical and Physical Chemistry Institute, Athens, Greece; vertex80v, Bruker, Billerica, MA, USA) in reflectance mode with an incidence angle of ~11°, in the range of 30-7000 cm^{-1} with a resolution of 2 cm^{-1}. From these data, the spectral absorption coefficient was calculated by Kramers-Kronig transformation [52]. Raman spectra were obtained in the range from 215 to 1555 cm^{-1} with a dispersive Raman microscope (workgroup Prof. Wondraczek, OSIM, FSU Jena; inVia Raman Microscope, Renishaw, Gloucestershire, UK) using the 514 nm laser excitation line on at least two positions of the glass slide. Baseline correction of the Raman spectra was done by subtraction of a line through 5 chosen points: 218, 1320, 1550 cm^{-1} and the minima of each spectrum at ~ 550 & at ~ 800 cm^{-1} using the software OriginPro 2016G. The normalisation of the Raman spectra was performed using the band at ~945 cm^{-1}.

Additionally, from glass 45S5 and 25B Raman spectra were measured in parallel and cross polarised mode using the 514 nm laser excitation line in combination with a 2400 grid. Spectra were obtained in a range between 190 cm^{-1} and 1700 cm^{-1}. Baseline correction was carried out by subtraction of a line through 5 points at about 260, 500, 800, 1300 and 1600 cm^{-1} for the parallel-polarized spectra and at about 218, 550, 630, 1320 and 1550 cm^{-1} for the cross-polarised spectra. Subsequently, normalisation of the Raman spectra was done using the band at ~945 cm^{-1}.

The ***density*** of the glasses was measured on glass monoliths (~10 g) in a helium pycnometer (OSIM, FSU Jena; AccuPyc 1330, Micromeritics GmbH, Aachen, Germany) with an estimated error limit of ± 0.01 g/cm^3.

3.1.3. *In-vitro* Dissolution Tests on Glass Powder and Glass Discs

In-vitro dissolution and mineralisation behaviour were investigated on the one hand on fine glass powder <38 µm and on the other hand on glass discs.

For the dissolution tests on powder, glass pieces of 45S5, 1B, 5B, 10B, 15B, 20B and 25B were crushed using a stainless-steel mortar, grinding 30 min in an agate ball mill (OSIM, FSU Jena; KM1, MLW Janetzki, VEB Spezialmaschinenbau, Lutherstadt Wittenberg, Germany), and subsequently sieving using a 38 µm sieve.

Per sample container 75 mg glass powder each was immersed in 50 ml 0.062 mol l^{-1} Tris buffer solution (initial pH-value 7.4, detailed preparation in appendix) and kept at 37°C in a shaking incubator (KS4000i Control, IKA, Staufen, Germany) at an agitation rate of 60 rpm for 6h, 1, 3 or 7 days. Temperature and pH-value were measured using a pH meter (HI 8314 with pH electrode HI 1217, HANNA Instruments, Vöhringen, Germany). Afterwards, the samples were filtered (filter paper with 5-13 µm particle retention, VWR International, Vienna, Austria). Thereafter 30 ml of the filtrated solution was acidified adding 0.75 ml nitric acid (65%, Merck, Darmstadt, Germany) and elemental concentrations were analysed using inductively coupled plasma optical emission spectroscopy (ICP-OES; workgroup Prof. Mäusbacher/ workgroup Prof. Zech, Physical Geography, FSU Jena; 725-ES Varian, Agilent Technologies, Böblingen, Germany). Experiments were carried out in triplicates. Ion concentrations in the solution were normalised to the concentration of the respective ion in the untreated glass.

The residue was rinsed with acetone to stop the dissolution process and dried at room temperature. Apatite formation on the glass particles was analysed using FTIR in attenuated reflection mode (ATR-FTIR; workgroup Prof. Schacher, Institute of Organic Chemistry and Macromolecular Chemistry, FSU Jena; Frontier, Perkin Elmer, Waltham, MA, USA with ATR sample holder Specac) and XRD (workgroup Prof. Rüssel, OSIM, FSU Jena; miniFlex, Rigaku, Japan, CuKα measurements performed at room temperature). FTIR spectra were normalized to the band with the highest intensity.

For the dissolution test on glass bulk, two glass discs (~20*15*1.5 mm³) were cut from blocks of glasses 45S5, 10B, 15B, 20B and 25B. Each disc was placed in a 100 ml polypropylene container, simulated body fluid (SBF) was added and the closed container was kept for 7 days at 37°C in a shaking incubator (KS4000i Control, IKA, Staufen, Germany) at an agitation rate of 60 rpm. The disc was dried afterwards for 24 hours at room temperature while being covered between two watch glass dishes with the upper one upside down. The SBF solution SBF 10, see Table A 6, was prepared according to Müller et al. [53] and the ratio of glass disc surface to volume of the SBF was 0.4 cm^{-1} referring to Zhang et al. [54]. As a control, the pH-value of SBF without glass was measured after 7 days as well.

The surface of glass samples 45S5, 10B and 20B were investigated using scanning electron microscopy (SEM; workgroup Prof. Rüssel, OSIM, FSU Jena; Jeol JSM 6510LV, Jeol GmbH, Freising, Germany). For examination of the cross sections of glasses 45S5, 15B, 20B and 25B, one disc per glass composition was cut in half using a diamond cutter. To avoid the chipping of the edges the two halves were glued together like a sandwich. Therefore, one half of the sample was brushed with glue (M-Bond 610 Adhesive, Vishay Precision Group, Malvern, PA, USA) and the other half of the sample was placed on top. The folded samples were fixed with clamps and put in a preheated furnace at 175°C for 60 min to cure the glue. Afterwards, the samples were embedded in epoxy resin (Araldite CY212 Kit, Huntsman Advanced Materials GmbH, Basel, Switzerland) and the resin was cured for 24h at 60°C. Subsequently, a cross section was ground using silicon carbide (9 – 17 µm particle size range) and polished using an ethanol-based diamond suspension (DP-Suspension A, Struers GmbH, Willich, Germany). The cross sections were coated with carbon and investigated using scanning electron microscopy (SEM; workgroup Prof. Rüssel, OSIM, FSU Jena; Jeol JSM 7001F, Jeol GmbH, Freising, Germany), and energy dispersive X-ray analysis (EDX; workgroup Prof. Rüssel, OSIM, FSU Jena, EDX Detector Si (Li), EDAX Amatek GmbH, Berwyn, PA, USA) was applied for glasses 45S5, 20B and 25B using an acceleration voltage of 15 kV.

Glass sample 25B at 7 days in SBF was investigated by X-ray microscopy (XRM; Carl Zeiss, Oberkochen; Xradia 520 Versa, Zeiss Microscopy Customer Center Europe, Oberkochen, Germany).

3.1.4. Thermal Properties & Glass Stability Parameters

Dilatometry (workgroup Prof. Rüssel, OSIM, FSU Jena; DIL 402 PC, Netzsch, Selb, Germany; heating rate 5 K/min; glass rods 20 mm in length and 8 mm in diameter) was used to determine glass transition temperature T_g and thermal expansion coefficient α. The thermal expansion coefficient was determined by linear fitting in the range 100-400°C. The estimated error of T_g was ± 5K.

The viscosity behaviour upon heating was investigated using ***heating microscopy*** (HTM; workgroup Prof. Wondraczek, OSIM, FSU Jena; HTM instrument originally by Zeiss, Jena, Germany, alterations done by Otto Schott Institute of Materials Research). From the shape of the shadow of a cylinder, pressed from glass powder, temperatures corresponding to certain viscosities upon heating can be determined. Glass powder <125 µm was prepared by using stainless-steel mortar and a 125 µm sieve starting from glass frit. The glass powder was mixed with ethanol as a binding agent and pressed with a manual hand punch (workgroup Prof. Wondraczek, OSIM, FSU Jena; Zeiss, Jena, Germany, see Figure A1 in the appendix) into cylindrical pellets of 4 mm height and 3 mm diameter. The glass powder pellets were placed on Al_2O_3 discs and heated up in the HTM furnace with a heating rate of 5 K/min. Starting at 400°C every 5 K a picture was taken of the shadow of the glass powder pellet so that changes in shape could be investigated with varying the temperature. The accuracy of the HTM instrument was verified by measuring sodium chloride NaCl ($T_m = 801\ °C$). After HTM, the glass powder compacts were pulverised using ceramic mortar and pistil and investigated via ***XRD*** (workgroup Prof. Wondraczek, OSIM, FSU Jena; miniFlex, Rigaku, Japan, CuKα measurements performed at room temperature).

Simultaneous ***differential thermal analysis*** (SDTA; workgroup Assoc. Prof. Massera, BioMediTech Institute, Tampere University, Finland; 449 F1 Jupiter with a TGA-DSC sample carrier, Netzsch, Selb, Germany) was used to investigate glass powder <38 µm of the glass series 45S5-B with a heating rate of 10 K/min. Experiments were performed in N_2 atmosphere using platinum pans with a sample size of ~30 mg glass powder. Glass transition temperature taken as inflexion point (T_g), onset of crystallisation (T_x) and maximum of glass crystallisation (T_p) was obtained; the error of the measurements was ± 3 K.

The ***glass stability parameters***: Weinberg parameter K_W (3.3), Hrüby parameter K_H (3.4), Lu & Liu parameter K_{LL} (3.5) and Saad & Poulain parameter K_{SP} (3.6) [55] were calculated using the following equations (3.3)-(3.6).

$$K_W = \frac{(T_x - T_g)}{T_m} \qquad (3.3)$$

$$K_H = \frac{(T_x - T_g)}{(T_m - T_x)} \qquad (3.4)$$

$$K_{LL} = \frac{T_x}{(T_g + T_m)} \qquad (3.5)$$

$$K_{SP} = \frac{(T_x - T_g)(T_p - T_x)}{T_m} \qquad (3.6)$$

Characteristic temperatures for T_g, T_x, T_p and liquidus (T_m) were obtained from SDTA data for all glasses for powder <38 µm. The error of the glass stability parameters was determined using the method of partial differentiation.

3.1.5. Crystallisation Study & Impact on Dissolution

For the ***crystallisation study*** glass particles of glass 5B, 15B and 25B were prepared using a stainless-steel mortar and subsequent sieving with stainless steel sieves either to <38 µm (fine) or 500-1000 µm (coarse). For heating microscopy and solubility tests, particles were prepared using stainless-steel mortar and sieve (3150 µm) and subsequent milling in a planetary mill, Pulverisette 5 (OSIM, FSU Jena; Fritsch, Idar-Oberstein, Germany) in combination with an agate container and agate balls. Each milling of 50 g glass granules was carried out for 5 minutes at level 10 dry, followed by wet milling of the powder (addition of isopropanol) for 2*5 minutes at level 10. The particle size distribution was measured for those glass powder samples dispersed in solution using laser diffraction (workgroup Töpfer, SciTec, EAH Jena; Mastersizer 2000, Malvern Instruments, Malvern, UK).

Simultaneous differential thermal analysis (workgroup Assoc. Prof. Massera, BioMediTech Institute, Tampere University, Finland; SDTA 449 F1 Jupiter with a TGA-DSC sample carrier, Netzsch, Selb, Germany) was used to determine the glass transition temperature (T_g), the onset of crystallisation (T_x) and maximum of glass crystallisation temperatures (T_p). Thermograms were recorded at 5, 10, 15 and 20 K/min heating rates, for particle sizes <38 µm and 500-1000 µm. T_g was taken as the inflexion point of the first change in heat flow, obtained by taking the first derivate of the DSC thermogram. The working range ΔT was calculated as T_x-T_g. The investigation was performed in platinum pans with a sample size of ~30 mg in N_2 atmosphere. The precision of the measurements was ± 3 K.

Thermal treatment was performed on glass bulk cylinders with a diameter of 10 mm and a height of 5 mm, which were cut out of the glass blocks. They were placed on platinum sheets in a preheated furnace (workgroup Assoc. Prof. Massera, BioMediTech Institute, Tampere University, Finland; P330, Nabertherm, Lilienthal, Germany) either at T_x-25 K or T_x -5 K to assess the glass bulk tendency to crystallise. After heat treatment, the samples were taken out of the furnace and allowed to cool down to room temperature.

Heating microscopy (HTM) (Heating microscope; BAM Germany, section 5.6 “Glas”, Hesse Instruments, Osterode, Germany) was carried out applying a heating rate of 10 K/min with cylindrical pellets (3 mm height and diameter) pressed out of powder with 20 MPa twice for 30 s.

The activation energies linked to the glass transition E_a and the crystallisation E_c were determined by measuring T_g and T_p at heating rates 5, 10, 15 and 20 K/min and applying the ***Kissinger*** equation (3.7) [56].

$$ln\left(\frac{\beta}{T_g^2}\right) = -\frac{E_a}{R*T_g} + constant \quad (3.7)$$

In Kissinger equation β is the heating rate, T_g is the glass transition temperature measured at the four different heating rates and R is the gas constant. To calculate E_c, T_g was replaced by T_p in equation (3.7).

Friedman method [57] compared to the Kissinger method, see equation (3.8), has the advantage of not making mathematical assumptions, when calculating the activation energy for crystallisation.

$$\ln\left(\frac{d\alpha_i}{dt}\right) = -\frac{E_{c\alpha}}{R*T_i} + constant \quad (3.8)$$

Thereby $\left(\frac{d\alpha_i}{dt}\right)$ is the transformation rate at a temperature T_i. The average crystallisation energy was calculated as average from the individual $E_{C\alpha}$. Friedman method was used for the coarse particles only.

The Johnson Mehl-Avrami (JMA) exponent can be calculated using equation (3.9) proposed by ***Augis and Bennett*** [58]:

$$n = -\frac{2.5}{\Delta T_{FWHM}} * \frac{T_p^2}{\frac{E_c}{R}} \qquad (3.9)$$

where n is the JMA exponent, ΔT_{FWHM} is the full width at half maximum of the crystallisation peak, T_p is the crystallisation temperature (maximum of the exothermic peak in DSC thermogram), E_c is the activation energy of crystallisation and R is the gas constant.

The ***Ozawa*** method [59] (3.10) was applied to verify the results received from Augis-Bennett calculations for coarse particles. The area of the exothermic crystallisation peak is related to the rate of crystallisation and thereby with the dimensionality of the crystals forming in the glass. α is the fraction of glass crystallised and β is the heating rate.

$$\left[\frac{d(\ln(-\ln(1-\alpha)))}{d(\ln(\beta))}\right]_T = -\mathrm{n} \qquad (3.10)$$

Heat-treated bulk glass cylinders were cut into halves after cooling down using a low-speed diamond wheel saw (workgroup Assoc. Prof. Massera, BioMediTech Institute, Tampere University, Finland; Model 650, South Bay Technology, San Clemente, CA, USA). One-half was prepared using a polishing machine (workgroup Assoc. Prof. Massera, BioMediTech Institute, Tampere University, Finland; Knuth-Rotor 2, Struers, Copenhagen, Denmark) for investigation by light microscopy (workgroup Assoc. Prof.

Massera, BioMediTech Institute, Tampere University, Finland; LM; BH-2 Olympus, Tokyo, Japan). For glass 5B, 15B and 25B the cylinders heat-treated at 5 K below T_x for the longest duration each, the second half of the cylinder was crushed and investigated by XRD (workgroup Assoc. Prof. Massera, BioMediTech Institute, Tampere University, Finland; Empyrean Series 2, PANalytical, Almelo, Netherlands). From glass 5B additionally one heat-treated glass piece (60 min @ 660°C, T_x-25 K) was examined using 3D X-ray microscopy (XRM; Carl Zeiss, Oberkochen; Xradia 520 Versa, Zeiss Microscopy Customer Center Europe, Oberkochen, Germany) and XRD (workgroup Prof. Rüssel; miniFlex, Rigaku, Japan, CuKα measurements performed at room temperature).

To investigate the ***impact of crystallisation on the dissolution behaviour*** amorphous and crystallised glass particles were prepared for solubility tests. Glass particles were weighed (workgroup Prof. Wondraczek, OSIM, FSU Jena; AC211P, Sartorius, Göttingen, Germany), ~240 mg each were pressed into a brass mould using a hand punch. Afterwards, they were heat-treated as pellets in an annealing furnace (workgroup Prof. Wondraczek, OSIM, FSU Jena; DIL 402, Netzsch, Selb, Germany) up to T_{p1}, i.e. the temperature corresponding to the first exothermic peak, with a heating rate of 10 K/min. Thereafter the pellets were crushed using a ceramic mortar and pestle and the crystalline status of those heat-treated glass samples was verified using XRD (workgroup Prof. Rüssel, OSIM, FSU Jena; miniFlex, Rigaku, Japan, CuKα measurements performed at room temperature). For the solubility tests, the amount of 37.5 mg of glass respectively crystallised glass powder was immersed in 25 ml 0.062 mol/l Tris buffer solution (Tris) in 100 ml polypropylene containers. Samples were stored in a shaking incubator (KS4000i Control, IKA, Staufen, Germany) at 37°C at an agitation rate of 60 rpm for 1 or 3 days. Tests were carried out in triplicate. Beforehand and afterwards, the pH-value was measured using pH-Meter (HI 8314, Hanna Instruments, Vöhringen, Germany). Tris was analysed after the immersion test by inductively coupled plasma optical emission spectroscopy (ICP-OES; workgroup Prof. Mäusbacher/ workgroup Prof. Zech, Physical Geography, FSU Jena; 725-ES, Varian Agilent Technologies, Böblingen, Germany). The investigated wavelengths for the analysed elements are 249.7 nm for boron, 396.8 nm (for up to ~10 mg/l) resp.

370.6 nm (for more than~10 mg/l) for calcium, 589.0 nm for sodium, 213.6 nm for phosphorous and 251.6 nm for silicon.

The remaining powders after dissolution test were investigated using XRD (workgroup Prof. Rüssel, OSIM, FSU Jena; miniFlex, Rigaku, Japan, CuKα measurements performed at room temperature) and Fourier transform infrared spectroscopy in attenuated total reflection mode (ATR-FTIR; workgroup Prof. Schacher, Institute of Organic Chemistry and Macromolecular Chemistry, FSU Jena; Frontier, Perkin Elmer, Waltham, MA, USA). The FTIR spectra were normalised to the band with the maximum intensity in the range 525-1600 cm^{-1}.

3.2. Åbo Glasses

3.2.1. Glass Composition & Glass Preparation

The following 21 Åbo glasses, Table 4, were prepared via a melt-quench route.

Table 4: Glass composition of the Åbo glasses in mol%.

Glass name	SiO_2	Na_2O	P_2O_5	CaO	K_2O	MgO	B_2O_3
17-93	57.0	18.4	1.8	15.8	6.1	0.0	0.9
17-92	54.6	20.3	1.3	11.2	6.7	3.1	2.7
206	53.0	12.4	1.1	22.5	9.5	0.0	1.5
14-93	54.1	17.8	0.9	18.6	3.9	3.0	1.8
19-93	56.2	15.4	1.8	12.5	8.1	3.2	2.7
3-92	53.6	25.0	1.3	11.0	3.3	3.1	2.7
15-92	42.1	15.7	2.7	23.1	10.3	3.2	2.8
306	50.4	24.0	1.1	23.3	0.0	0.0	1.1
9-93	56.2	12.1	0.9	12.3	10.0	7.8	0.9
20-92	52.2	15.2	0.0	16.8	10.0	3.1	2.7
1-98	53.8	5.9	0.9	23.9	7.1	7.6	0.9
106	51.4	5.9	1.7	24.9	7.9	8.1	0.2
18-93	53.2	17.5	0.0	21.5	3.8	3.0	0.9
12-92	52.8	19.7	0.0	10.9	6.5	7.6	2.6
10-92	66.1	10.0	1.3	16.6	3.3	0.0	2.7
6-92	59.4	9.8	1.3	16.2	3.2	7.5	2.6
1606	67.4	5.1	1.8	17.0	6.9	0.0	1.8
1406	62.2	5.4	0.3	17.8	7.3	5.2	1.8
1806	64.8	17.8	0.0	16.0	0.0	0.1	1.3
1-92	55.3	14.1	0.0	20.8	0.0	7.2	2.5
15-93	58.8	8.8	0.0	21.7	5.8	3.0	1.8

Batch components SiO_2 (Carl Roth, Karlsruhe, Germany), Na_2CO_3 (Carl Roth), $NaPO_3$ (Chemiewerk Piesteritz, Lutherstadt Wittenberg, Germany), K_2CO_3 (VWR, Darmstadt, Germany), basic $MgCO_3$ (Merck, Darmstadt, Germany), $CaCO_3$ (Merck, Darmstadt, Germany), H_3BO_3 (Sigma Aldrich, Seelze, Germany) and $Ca(H_2PO_4)_2*H_2O$ (Chemische Fabrik Budenheim, Budenheim, Germany) were mixed together with a ceramic ball via shaking by hand in a polypropylene container. Melting of the glass batches was carried out in platinum crucibles (volume 250 ml) at 1320°-1573°C. Since the expected melting temperature depends on the composition, either a furnace with SiC heating elements (melting temperature up to 1350°C) or an induction furnace (melting temperature >1350°C) was used. Details can be found in Table A 7 (appendix). About 170 g of glass was melted per glass composition, quenched in a bucket filled with tap water to obtain glass frit and dried for more than 12 hours at ~140°C in drying oven (WST 3010, VEB MLW Dentalfabrik Trefffurt, Germany). Thereafter in a second step, glass blocks of ~100 g were prepared by remelting a part of the glass frit and casting into brass moulds. The blocks were annealed for at least 2 hours at an adjusted temperature of 30 K above the onset of T_g. Afterwards, the glass blocks were cooled down slowly to room temperature in the annealing furnace to remove residual stress. Pieces of the glass blocks were used for density and dilatometry measurements, as well as for Fourier transform infrared and Raman spectroscopy investigations. For all other examinations, glass frit was used to prepare powder.

The glass composition of glasses 9-93, 6-92 and 3-92 was investigated analogous like for the glass series 45S5-B via ***XRF***, see chapter 3.1.1.

3.2.2. Investigation of Glass Structure and Density

From glass 6-92, a glass disc that exhibited inhomogeneities, visible as intensive striae, a Raman line-scan was acquired orthogonally to a streak. A shadow image was taken from the glass disc 6-92 as well. The experimental setup used was a shadow apparatus at the Otto Schott Institute of Materials Research. While the extent of striae was the biggest for glass 6-92, most glasses showed no or little striae. For comparison, a shadow image of glass 1806, which showed no pronounced striae, was taken as well. To examine the influence of the striae on the Raman signal, 19 scans along a line with

333 µm apart from each other were collected. Background correction and normalisation was done in the same way as described above.

^{11}B MAS MAS ***nuclear magnetic resonance spectroscopy*** (NMR) was investigated on glass powder samples 17-93, 17-92, 9-93, 20-92, 10-92, 6-92, 1-98, 206 and 1606 and ^{31}P MAS NMR on those glasses apart from 20-92, as it does not contain phosphorus. The glass powder was prepared in the same way as for the XRD investigations. The details for ^{31}P and ^{11}B MAS NMR regarding spectrometer types, probes and reference substances are the same as described for the glass series 45S5-B in chapter 3.1.2. The spectra were recorded with repetition times of 150 s for ^{11}B and 125 s for ^{31}P with typically applied pulse lengths of 1 µs for ^{11}B and 3-4 µs for ^{31}P. The number of scans was 64-256 for ^{11}B and 32 for ^{31}P. The ^{31}P MAS NMR spectra were normalised to the maximum.

Regarding ***Fourier transform infrared and Raman spectroscopy*** the procedure was analogous to the one for the glass series 45S5-B, see chapter 3.1.2. Baseline correction of the Raman spectra was done by subtraction of a line through chosen points: 218, 1320, 1550 cm^{-1} and the minima of each spectrum at ~550 & 800 cm^{-1} using the software OriginPro 2016G. For glasses 10-92, 6-92 and 1606 this line was taken without point at ~550 cm^{-1} as these Raman spectra do not exhibit a clear local minimum at this position. Subsequently, normalisation was done using the band at ~950 cm^{-1}.

The procedure for density and XRD investigations was analogous like for glass series 45S5-B, see chapter 3.1.2.

3.2.3. Dynamic Dissolution Experiments

Dynamic dissolution experiments were carried out for glasses 17-93, 17-92, 9-93, 20-92, 10-92 and 6-92 following Fagerlund et al. [20]. Glass particles were prepared using a stainless-steel mortar and sieves (315 & 500 µm). For those glasses ion concentration profiles were measured using a dynamic flow cell, which was connected to an inductively coupled plasma optical emission spectrometer (ICP-OES; workgroup Prof. Hupa, Process Chemistry Centre, Åbo Akademi University, Åbo, Finland; Optima

5300DV, Perkin Elmer, Waltham, MA, USA) as described previously [20, 60, 61]. The ion concentration of the elements silicon, phosphorus, boron, sodium, calcium, potassium and magnesium was measured on-line every 13 s for 1000 s. The sample cell was filled with ~200 mg glass particles of size fraction 315-500 µm. A pump fed the Tris buffer solution (50 mM) upwards through the glass particles in the flow cell with a flow rate of 0.2 ml/min while keeping the temperature at 37±2°C. The initial results are given in mg/l. Those were normalized to 280 mg weighed portion of glass particles to compare with dissolution patterns by Fagerlund et al. Afterwards the results were normalized to the molar amount of the respective element in the untreated glass.

3.2.4. Thermal Properties

Regarding dilatometry the procedure to access T_g was analogous to the one used for the glass series 45S5-B, see chapter 3.1.4. For all Åbo glasses, on which no information was available in the literature by Brink et al. [48], HTM was carried out similar to their experimental setup, like done for glass series 45S5-B, see also chapter 3.1.4.

3.2.5. Mathematical Models

The ***reaction number*** [48] Anderson model modified by Brink ("modified Andersson model" (2.13), and the ***index of surface activity*** [9] of a glass (2.14) were calculated for the Åbo glasses. In both models, the glass components are given in wt%. Details regarding the validity range are found in Table A 1 and Table A 2 in the appendix.

A ***linear approach*** was used to develop formulas to calculate the bioactivity value resp. the glass transition temperature T_g from the amount of the components per individual glass, given in wt%. The composition of all glasses was fed into the program OriginPro2016G to implement a multiple regression. Afterwards, all compositions apart from the glass 17-93, 17-92, 9-93, 20-92, 10-92 resp. 6-92 were fed into the program separately to implement multiple regressions as well. The regression bioactivity value resp. to the measured T_g was investigated.

For three glasses per group 17-93, 17-92 and 206 (high bioactivity, see Table 20, 9-93, 20-92, 1-98 (medium bioactivity) and 10-92, 6-92 and 1606 (inert) (I) the ***Pearson´s coefficient of correlation*** and (II) the ***Fisher discriminant ratio*** were calculated (workgroup PD Dr. Bocklitz, Leibniz-Institut für photonische Technologien (IPHT), Jena and University of Jena). Pearson´s coefficient of correlation was determined between the nominal glass composition, Table 4 and the FTIR, Raman, ^{11}B MAS NMR or ^{31}P MAS NMR spectra. The Fisher discriminant ratio was calculated to test the separability of the two groups while group one includes the high and medium bioactive glasses (see Table 20) and group two, the inert glasses. The FTIR, Raman and MAS NMR data were used separately here like for Pearson´s coefficient of correlation.

4. Results

In this chapter, first, the experimental results of the glass series 45S5-B (4.1.) and afterwards the ones of the Åbo glasses (4.2.) are presented.

4.1. Glass Series 45S5-B

4.1.1. Glass Composition

The nominal and the via ***XRF*** analysed compositions of glasses 5B, 15B and 25B are shown in Figure 9.

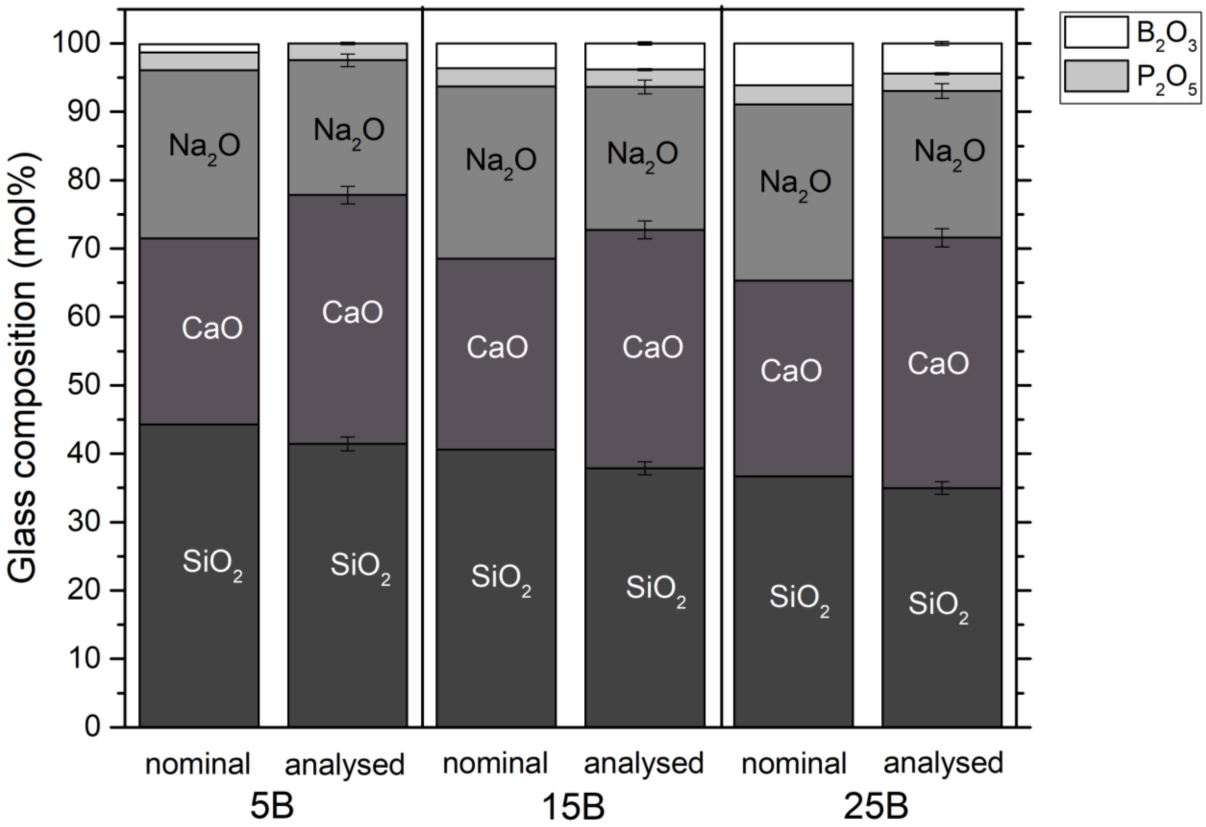

Figure 9: Nominal and via XRF analysed glass composition of glasses 5B, 15B and 25B.

For these three glasses the amount of SiO_2 and Na_2O is lower in the analysed composition than in the nominal composition, however for CaO vice versa. The amount of P_2O_5 is slightly lower in the analysed composition for glasses 15B and 25B, though in glass 5B it is the same as in the nominal one. In glass 5B no B_2O_3 could be detected via XRF. In glass 15B the amount of B_2O_3 is the same in the nominal and the analysed composition, while the amount in the analysed composition of glass 25B is lower than in the nominal one. The error bars in the analysed glass composition refer to the uncertainty of the XRF measurement. For the computation of the error, the traces like Al_2O_3 and TiO_2 were not considered. Noticeable in general is the higher amount of CaO in the analysed in comparison to the nominal composition.

4.1.2. Glass Structure & Density

The ***XRD*** results of the glass series 45S5-B are presented in Figure 10. A broad halo with its maximum at about 32° is visible for all investigated glasses, confirming their amorphous state.

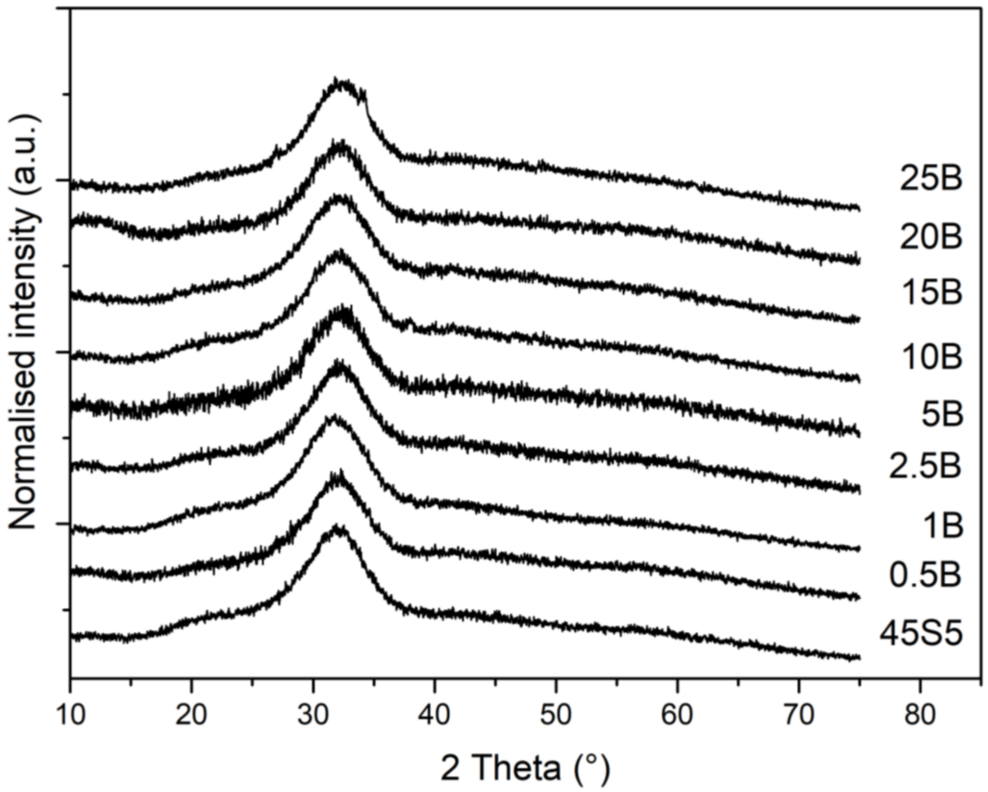

Figure 10: XRD results of glass series 45S5-B.

TEM images from the replica films obtained using ***replica technique*** on glasses 5B, 10B, 15B, 20B and 25B are shown in Figure 11. For the glasses 5B, 10B, 15B and 20B round or oval inhomogeneities are clearly visible. The scale bar in picture 25B is valid for the five small pictures (glass 5B, 10B, 15B, 20B and 25B). The enlarged replica picture from sample surface 25B enables the observation of very small inhomogeneities. Whereas for all samples structures are observed, the size of them varies.

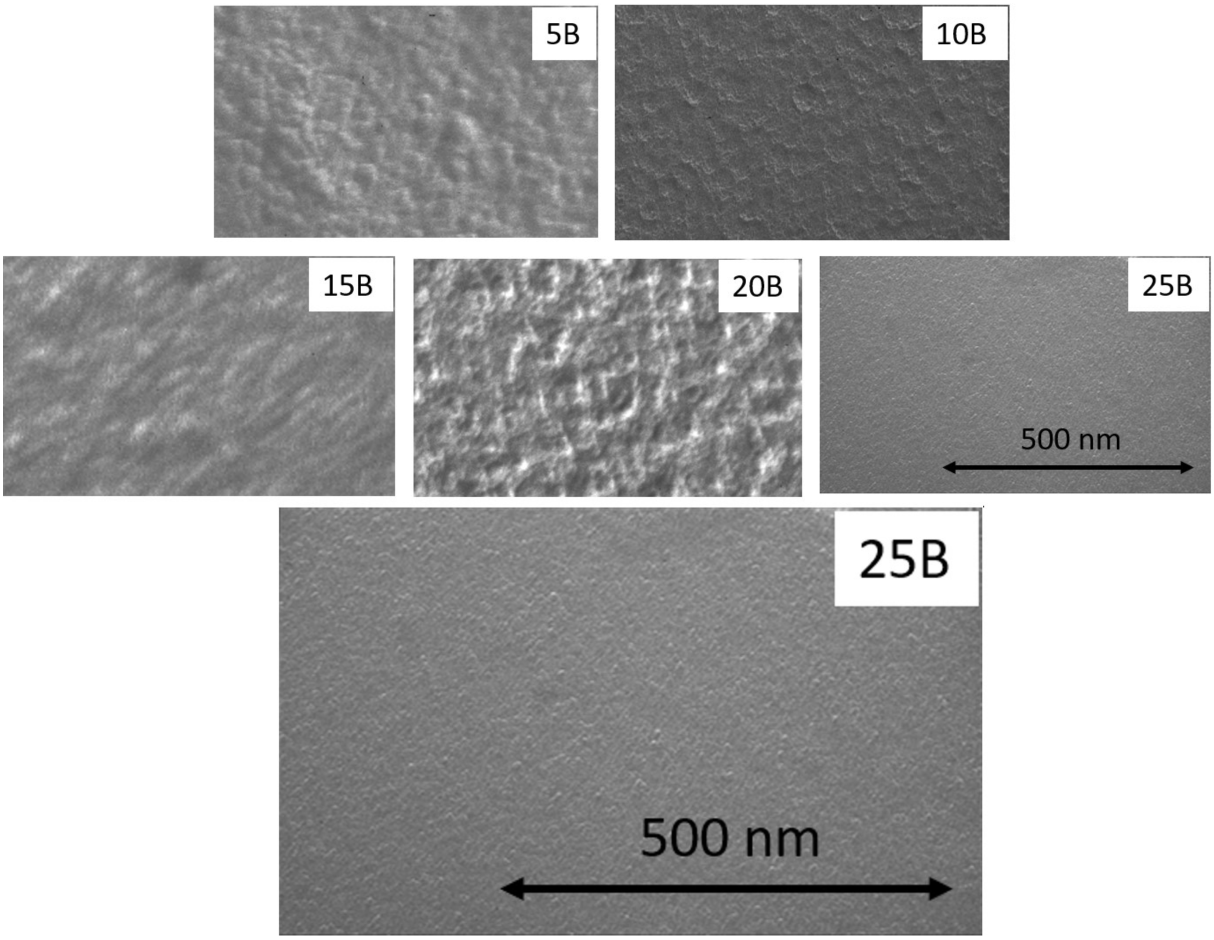

Figure 11: Replica-TEM overview: images from glasses 5B, 10B, 15B, 20B and 25B. The scale bar in picture 25B is valid for the five small pictures. Below, the Replica-TEM picture from glass 25B is presented enlarged, which enables the observation of the very small inhomogeneities.

The ***^{29}Si MAS NMR*** spectra for glass 45S5, 1B, 10B as well as for 25B are plotted in Figure 12.

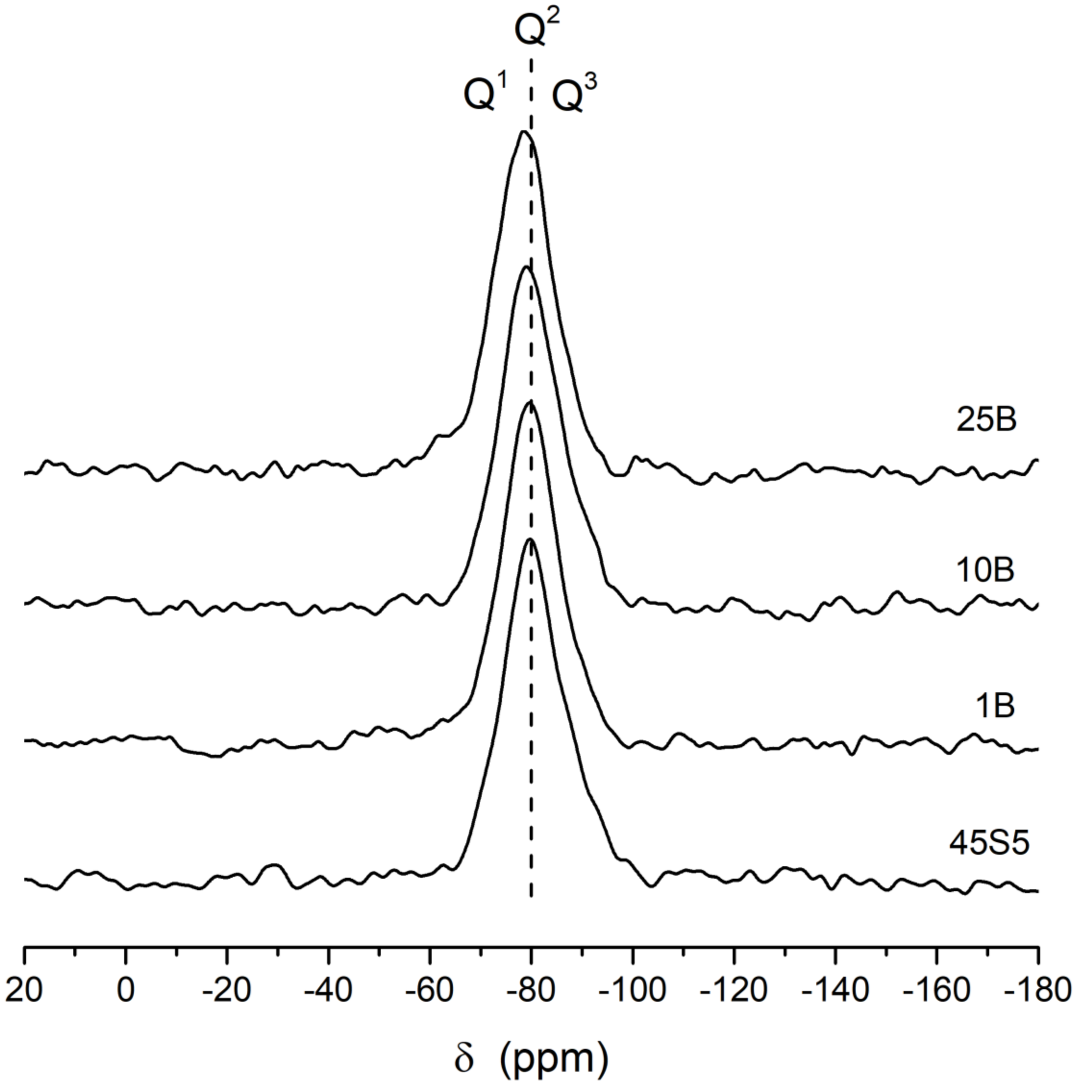

Figure 12: Si-29 MAS NMR of glasses 45S5, 1B, 10B and 25B. Band assignment acc. to Yu & Eden [43] and Mercier et al. [62].

All spectra exhibit one broad resonance band between -65 and -100 ppm, which corresponds to Q^2 groups predominantly with Q^1 and Q^3 groups in minority. Band assignment was done according to Yu & Eden [43] and Mercier et al. [62]. With increasing boron content, the maximum of the band shows a small shift to a more positive value.

Structural investigations via ***^{31}P MAS NMR,*** see Figure 13 of the examined glasses 0.5B, 1B, 2.5B, 10B, 15B, 20B as well as 25B verified the presence of orthophosphate as main phosphorous species for all glasses. Band assignment was done according to Yu & Eden [43].

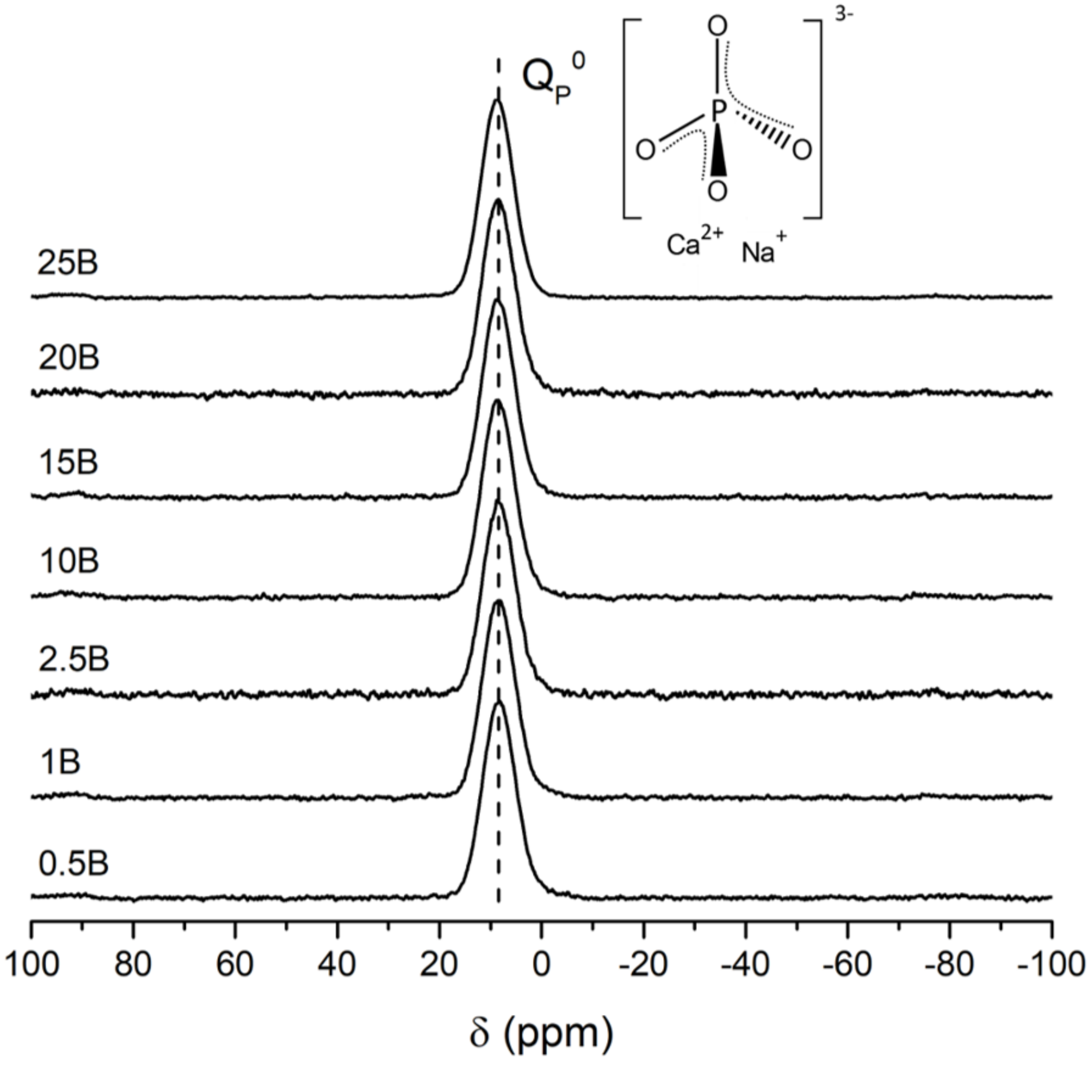

Figure 13: P-31 MAS NMR for the glasses 0.5B, 1B, 2.5B, 10B, 15B, 20B and 25B. Band assignment acc. to Yu & Eden [43].

The position of the Q_P^0 group in dependency on the B for Si substitution is plotted in Figure 14. With increasing boron content, a shift of ~0.4 ppm to higher frequencies can be identified.

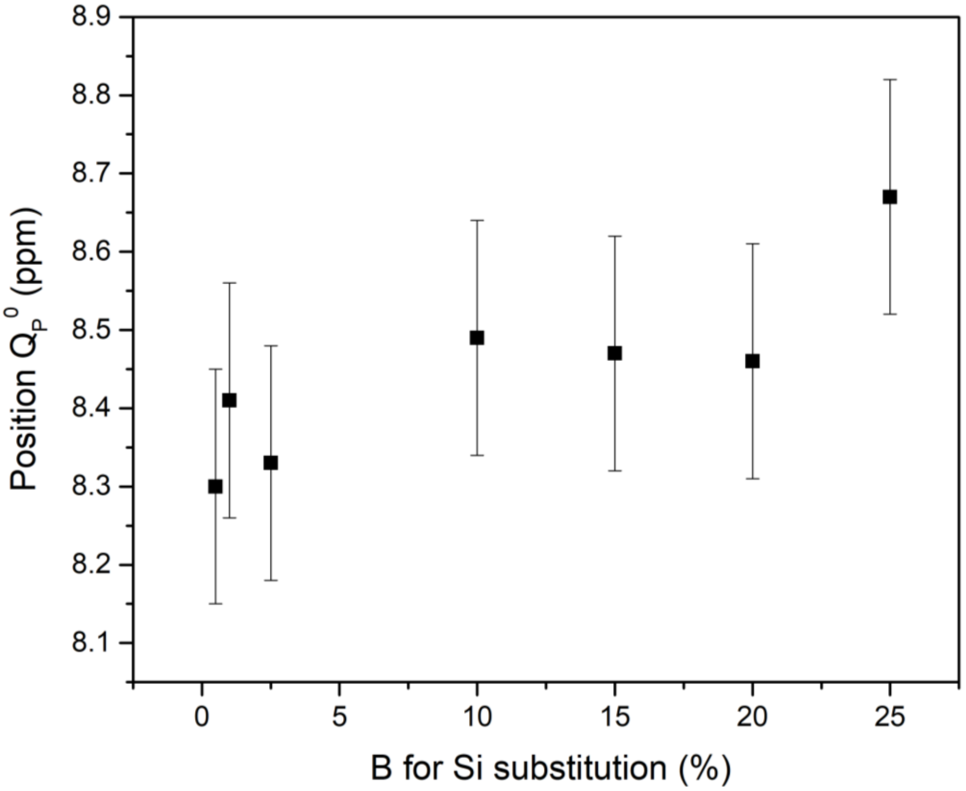

Figure 14: Position of Q_P^0 in dependency on the B for Si substitution.

The ***^{11}B MAS NMR*** spectra for glasses 0.5B, 1B, 2.5B, 10B, 15B, 20B as well as 25B are presented in Figure 15.

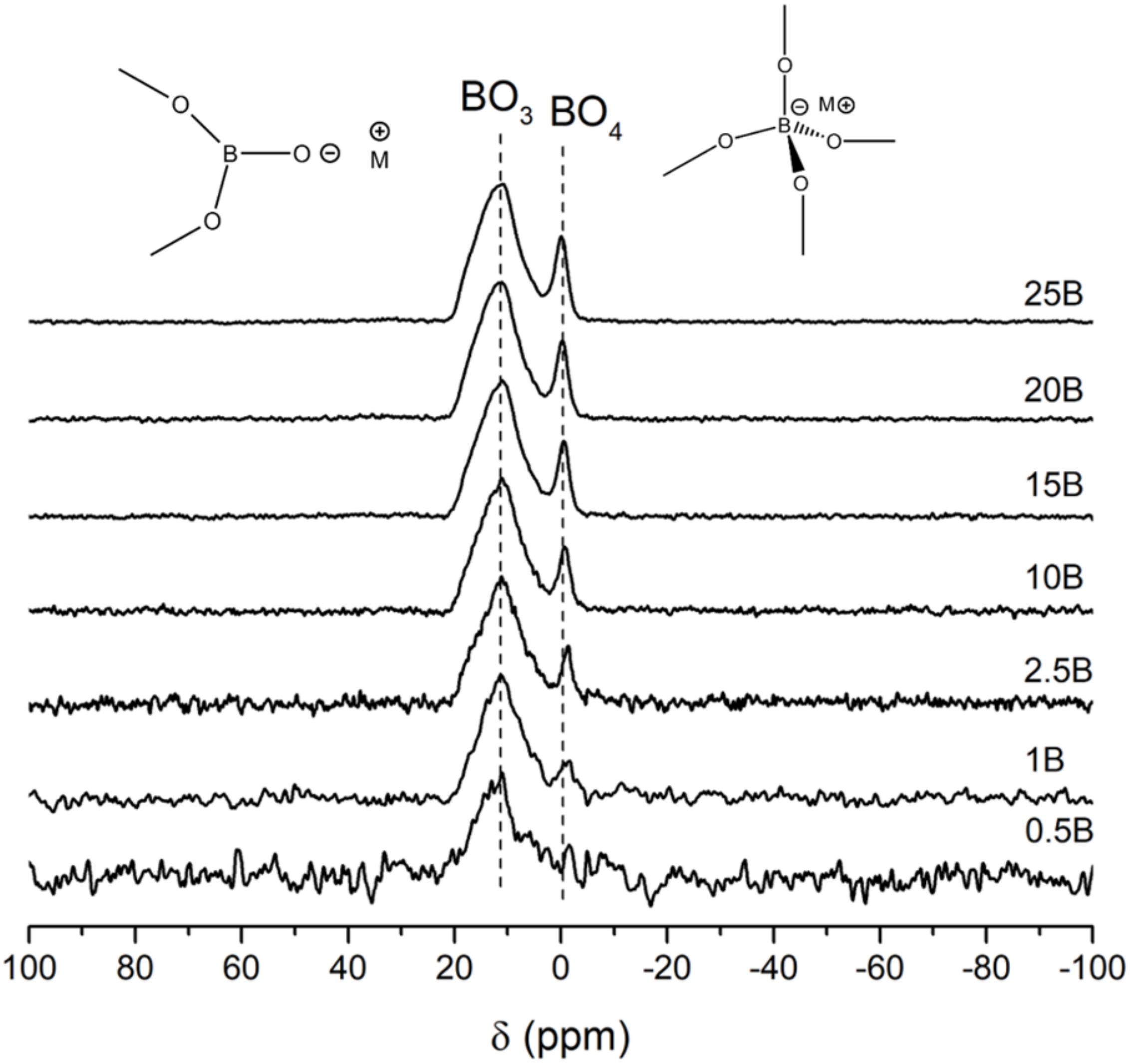

Figure 15: B-11 MAS NMR for glasses 0.5B, 1B, 2.5B, 10B, 15B, 20B and 25B. Band assignment acc. to MacKenzie [63].

BO_3 is the main B-species and BO_4 the minor species for all glasses, band assignment was done acc. to MacKenzie [63].

The relative amount of BO_3 and BO_4 units in dependency on the B for Si substitution is shown in Figure 16. The ratio of BO_3/BO_4 shows a decreasing trend within the glass series.

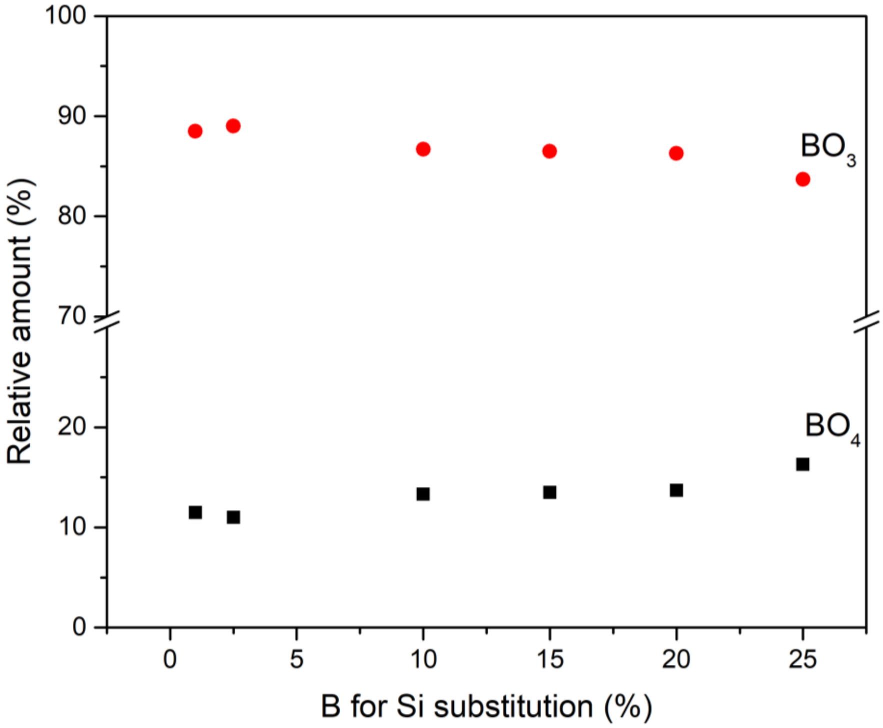

Figure 16: The relative amount of BO_3 and BO_4 units in dependency on the B for Si substitution.

Both, the position of BO_3 and of BO_4 show an increase in the chemical shift with B for Si substitution, Figure 17.

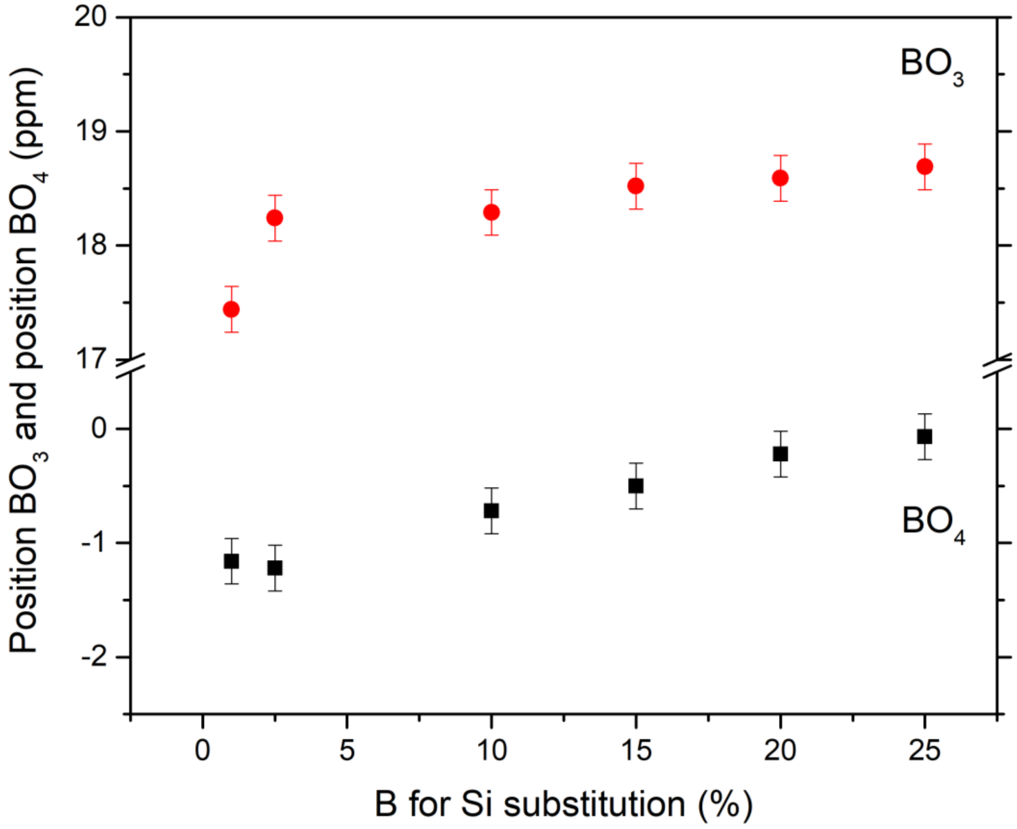

Figure 17: Position of BO_3 and BO_4 in dependence on the B for Si substitution.

The results of ***Fourier transform infrared spectroscopy*** of glass series 45S5-B are presented in Figure 18.

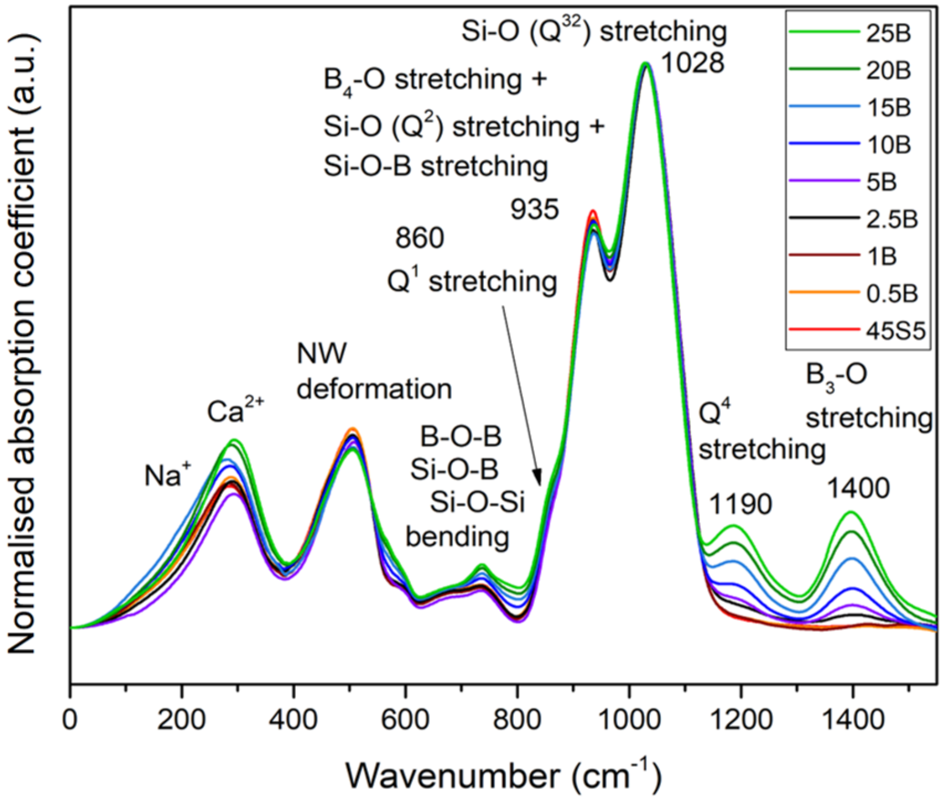

Figure 18: FTIR spectra of glass series 45S5-B. The assignment of the bands at ~200 cm^{-1} (Na$^+$), ~500 cm^{-1} (network deformation), ~670 cm^{-1} (Si-O-B bending), ~735 cm^{-1} (B-O-B deformation), ~780 cm^{-1} (Si-O-Si bending), ~860 cm^{-1} (Q^1 stretching), 935 cm^{-1} (overlapping band of Si-O-B stretching, B$_4$-O stretching and Q^2 stretching) and 1190 cm-1 (Q^4 stretching) acc. to Kamitsos et al. [64]. The assignment of the band at~280 cm^{-1} (Ca^{2+}) acc. to Kamitsos [52] and of the bands at 600-800 cm^{-1} (bending of borate segments) and 1440 cm^{-1} (B$_3$-O stretching) acc. to. Kamitsos et al.[65]. Explanations regarding the assignment of the band at 1028 cm^{-1} to stretching of Q^{32} can be found in the chapter 5.1.

The Q^3 stretching band in FTIR is expected at 1060-1100 cm^{-1} and the Q^2 stretching band at 950-985 cm^{-1} [64]. Here the band at 1028 cm^{-1} is assigned to Q^{32} stretching. Explanations regarding that can be found in the discussion, see chapter 5.1. From glass 2.5B, the intensity of the B$_3$-O stretching band at 1400 cm^{-1} [65] increases systematically within the series. Relatively to the maximum band (Q^{32} stretching, 1028 cm^{-1}), the intensity of the stretching modes of the Q^1 groups at 860 cm^{-1} [64] increases slightly within the glass series, whereas the ones of the Q^4 group at 1190 cm^{-1} [64] increases distinctly. The intensity of the bending modes of Si-O-Si at

570 cm^{-1} increases as well. At 935 cm^{-1} overlapping stretching bands of Q^2, Si-O-B and B_4-O [64] are present.

The results of the ***Raman spectroscopy*** on glass series 45S5-B are presented in Figure 19.

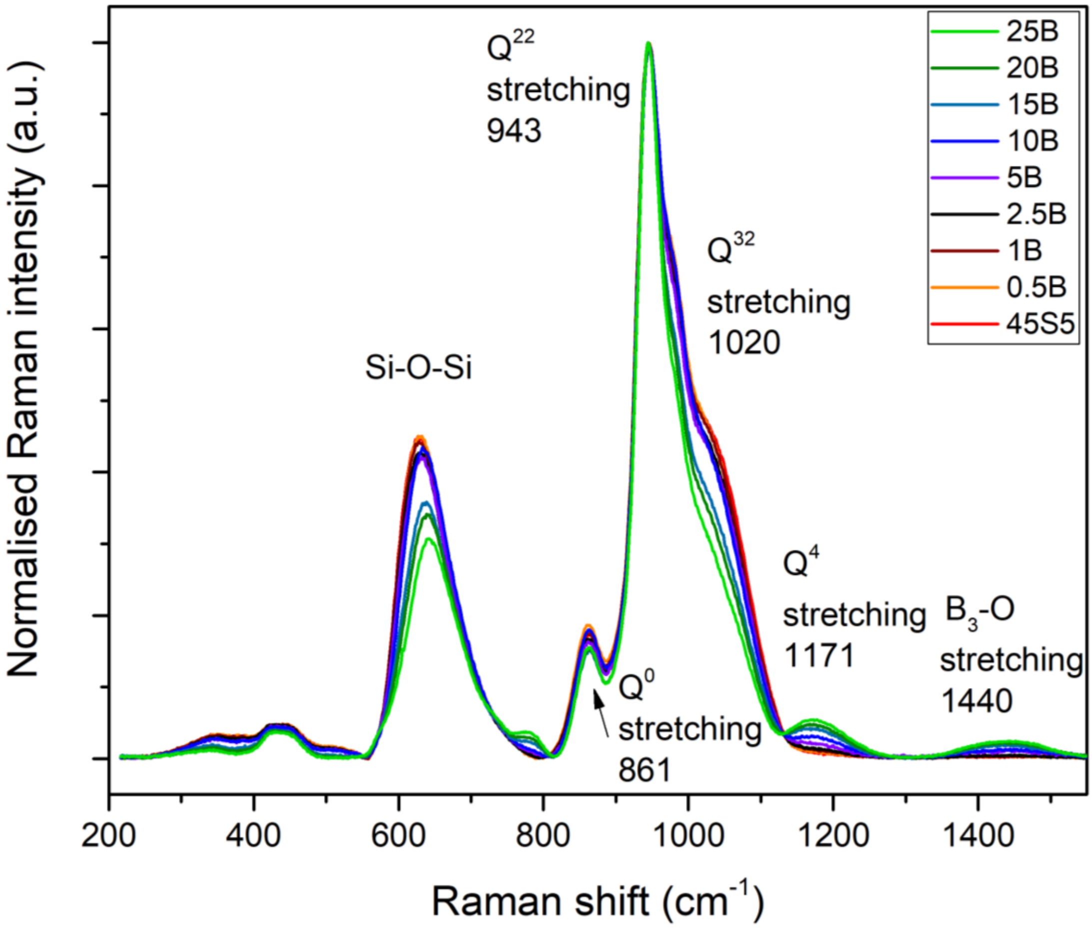

Figure 19: Raman spectra of glass series 45S5-B. Band assignment of the band at 630 cm^{-1} (Si-O-Si delocalised vibration), at 1171 cm^{-1} (Q^4 stretching) and at 1440 cm^{-1} (B_3-O stretching) acc. to Kamitsos et al. [64], at 943 cm^{-1} (Q^{22} stretching) and 1020 cm^{-1} (Q^{32} stretching) acc. to Koroleva et al. [66] and 861 cm^{-1} (Q^0 stretching) acc. to McMillan [67].

Relative to the band with the maximum intensity (943 cm^{-1}, stretching of Q^{22} groups [66]), the intensity of the band at 630 cm^{-1} (delocalised vibration of Si-O-Si bridges having bending-stretching character [64]) as well as the one at 1020 cm^{-1} (stretching of the Q^{32} groups [66]) decreases within the glass series. However, the bands at 1171 cm^{-1} (stretching of Q^4 groups [64]) and 1440 cm^{-1} (stretching of BO_3 groups [64]) intensify with the B for Si substitution. The band at ~630 cm^{-1} (for glass 45S5) shifts to a higher Raman shift within the series, to ~640 cm^{-1} for glass 25B.

For a detailed view, sections of the Raman spectra from Figure 19 are plotted in Figure 20, in A for the range 980-1080 cm^{-1} and in B for the range 1130-1550 cm^{-1}.

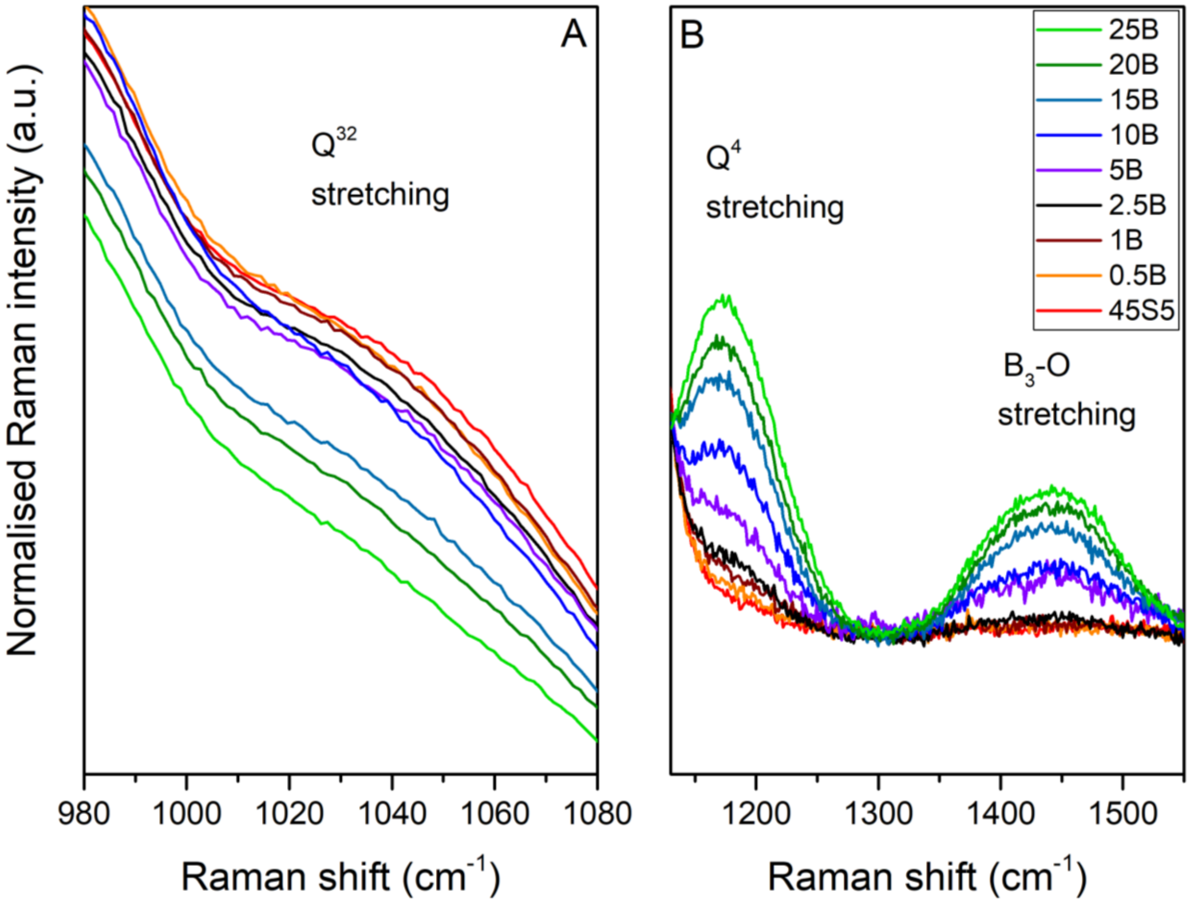

Figure 20: Sections 980-1080 cm^{-1} (A) and 1130-1550 cm^{-1} (B) from Raman spectra of the 45S5-B glass series.

The former shown Raman spectra in Figure 19 and Figure 20 are measured in non-polarised mode. From glass 45S5 and 25B additionally, a parallel-polarized spectrum (vv) and a cross-polarised spectrum (vh) have been recorded, which are presented in Figure 21.

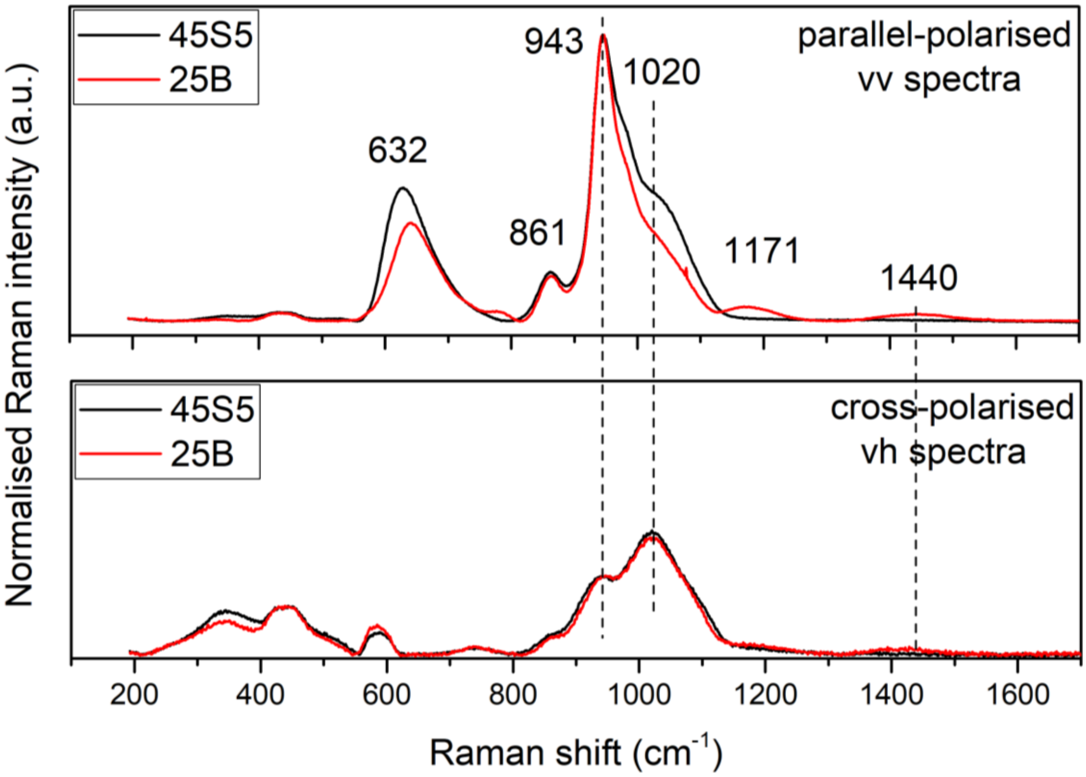

Figure 21: Raman spectra of glass 45S5 and 25B in parallel-polarised and cross- polarised mode.

Whereas in the parallel-polarised spectra, asymmetric and symmetric vibrations are visible, in the cross-polarised spectra only the asymmetric ones are [68]. Therefore, the measurement is very useful for the band assignment.

The relative intensity of the bands at 861, 943, 1171 and 1440 cm^{-1} is less pronounced in the cross-polarised mode than in the parallel-polarised one. At 1020 cm^{-1}, the position of the shoulder in the parallel-polarised spectra is the band with the highest intensity in the cross-polarised spectra. The intensity of the band at 632 cm^{-1} in the parallel-polarised spectra decreases dramatically in the cross-polarised mode.

Exemplarily for the bands at 943 cm^{-1} and at 1020 cm^{-1} the intensity in the parallel- and cross-polarised spectra, the fraction of symmetric and asymmetric vibrations and the band assignment are given in Table 5.

Table 5: Band assignment of vibrations in the parallel-polarised (vv) and cross-polarised (vh) Raman spectra of glasses 45S5 and 25B.

Position	**Intensity in the spectra**		**Fraction of**		**Band assignment**
(cm^{-1})	**vv**	**vh**	**symmetric vibrations**	**asymmetric vibrations**	
943	high	low	high	low	Q^{22} stretching
1020	medium	high	low	high	Q^{32} stretching

The band at 943 cm^{-1}, which is the maximum band in the parallel-polarised mode decreases significantly in the cross-polarised mode, suggesting a high fraction of symmetric vibrations and a low fraction of asymmetric vibrations. The band at 1020 cm^{-1} as a high amount of asymmetric vibrations, while the one at 943 cm^{-1} has a low amount of them. The stretching vibrations of a Q^{32} group have a high asymmetric fraction in contrast to the Q^{22} group, which have a high symmetric fraction. So, the assignment of the bands is in accordance with the ones made in Figure 19.

The broad low-intensity band in the parallel-polarised spectra at 1440 cm^{-1} shifts to ~1410 cm^{-1} in the cross-polarised spectra. According to Manara et al. [69] the band at 1410 cm^{-1} corresponds to BO_3-BO_4 and the one at 1480 cm^{-1} to BO_3-BO_3, which is in agreement with the results here, taking into account, that symmetric vibrations are not detectable in the cross-polarised mode. The low intensity of the bands at 861 cm^{-1} and 1170 cm^{-1} in the cross-polarised spectra suggests vibrations with a high symmetric fraction, which follows the assignment of these bands to the stretching vibration of Q^1 and of Q^4, see Figure 19.

The results of the ***density*** measurements using helium pycnometry are plotted in Figure 22.

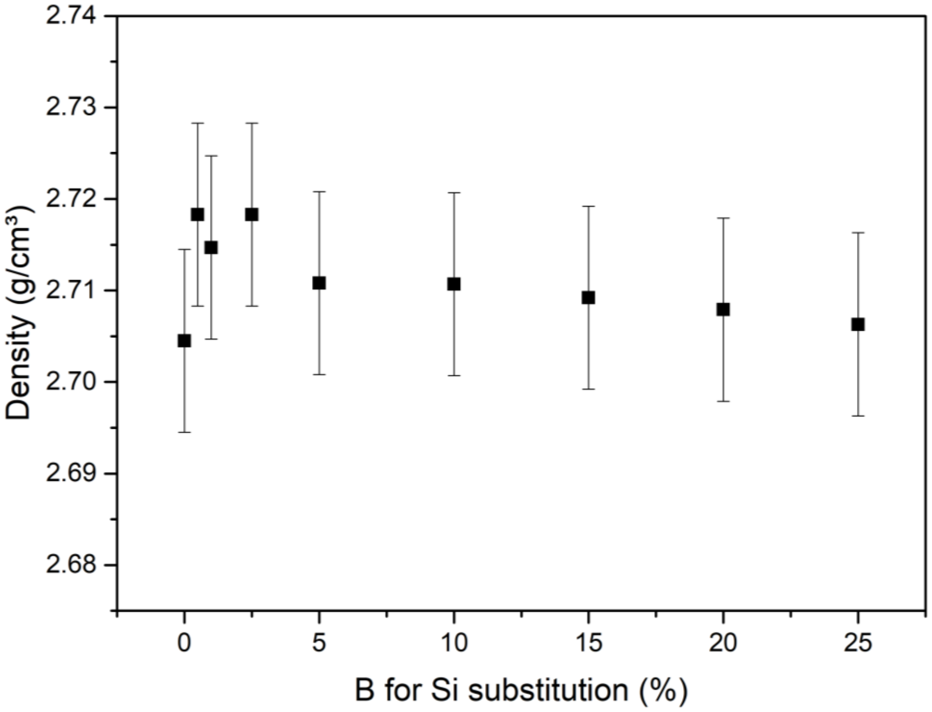

Figure 22: Density of glass series 45S5-B obtained using helium pycnometry.

For the whole glass series 45S5-B, the density is about 2.71 g/cm³, whereby the density of glass 45S5 is in agreement with data published by Tylkowsky & Brauer [70].

4.1.3. Dissolution Tests on Glass Powder and Glass Discs

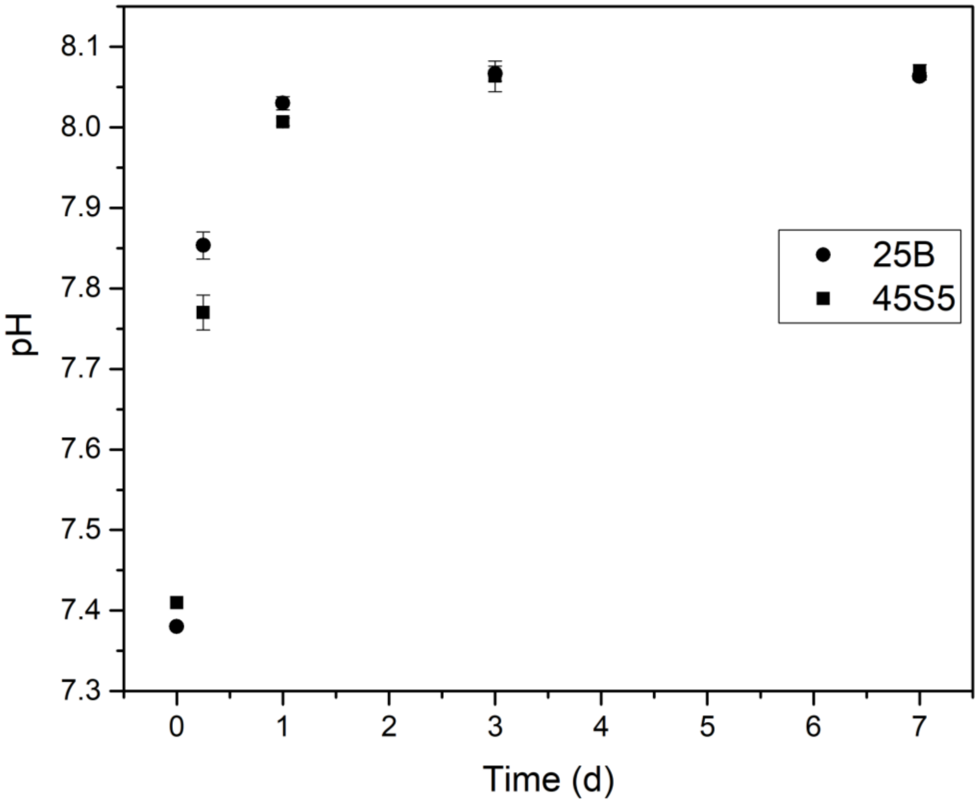

Figure 23: pH-value changes over time for the dissolution tests on glass powder 45S5 and 25B with a particle size of <38 µm.

The ***pH-value*** changes over time for dissolution tests on glass powder 45S5 and 25B, exemplarily for the whole glass series with a particle size <38 µm are shown in Figure 23. The pH-value increases distinctively for both glasses, whereby the slope during the first day is less steep for glass 45S5 in comparison to glass 25B. Within 6 h, the pH-value rose from about 7.4 to ~7.77 for glass 45S5 respectively to ~7.85 for glass 25B. Subsequently, for glass 45S5 there is an increase of about 0.24 resp. for glass 25B of about 0.18 to a pH-value of ~8. Subsequently up to 3 d, the pH-value increases slightly for both glasses to a pH-value of ~8.1, thereafter the pH-value stays constant.

The ***ions in solution*** in dependency on the time after dissolution tests on glass powder 45S5 and 25B <38 µm, exemplarily for the glass series are shown in Figure 24.

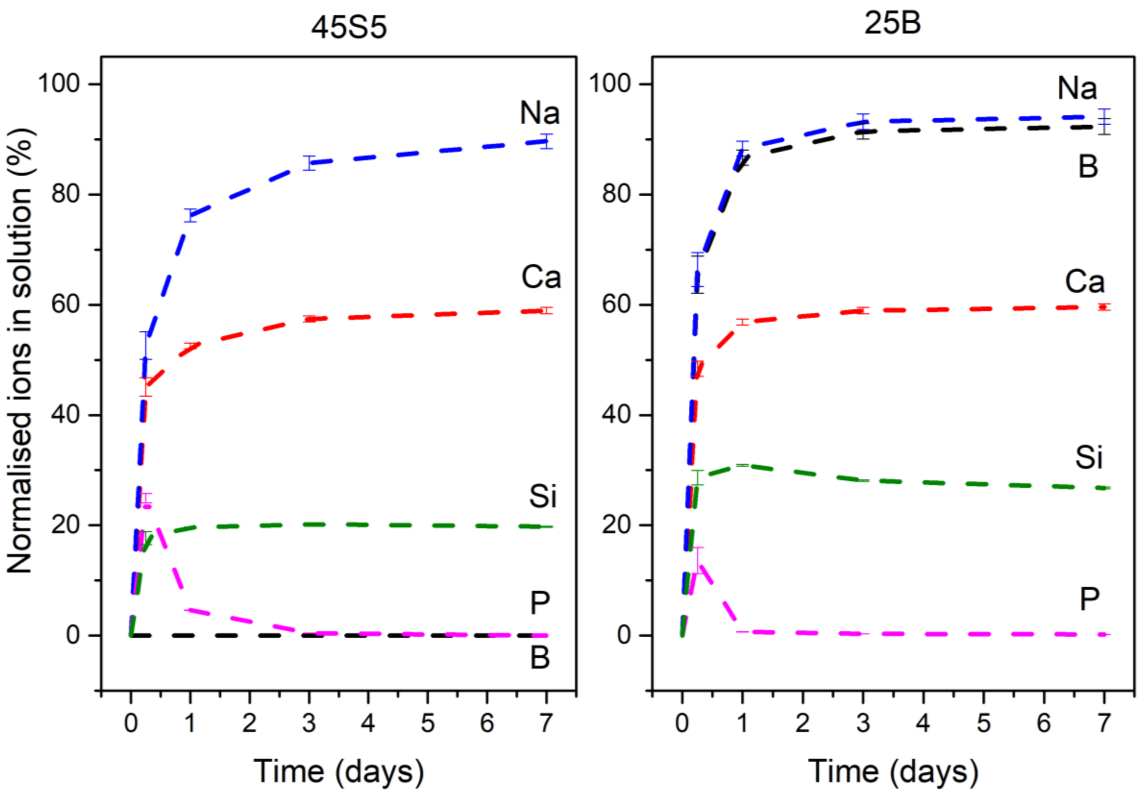

Figure 24: Ions in solution after dissolution tests on glass powder 45S5 and 25B <38µm analysed via ICP-OES.

The ions in the solution are normalised to the amount which was in the glass used for the individual test. After 6 h 52.6 ± 2.5 % sodium ions and 45.1 ± 1.7 % calcium ions for glass 45S5, respectively 66.4 ± 3.1 % sodium ions and 48.4 ± 1.4 % calcium ions for glass 25B are already present in the solution. The concentration of sodium and calcium increases further over time. After 7 days about 60 % of calcium and 90 % of sodium ions are present in the solution for glass 45S5 and 25B. Whereas for glass 45S5 no boron is detected at any point of time, for glass 25B boron is present in the solution in a similar amount like sodium. For glass 45S5 after 6 h 24.9 ± 0.9 % of phosphorus is present in the solution, whereas for glass 25B there are 13.6 ± 2.4 % at the same point of time. For 45S5 at 1 day 4.6 % of phosphorus are present in the solution, however at 3 and 7 days and at 1, 3 and 7 days for glass 25B less than 1 %.

Silicon is present in the solution for glass 45S5 in an amount of ~20% and for glass 25B in an amount of ~30 %.

The normalised amount of phosphorus in the solution at 6 h in dependency on the B for Si substitution is presented in Figure 25.

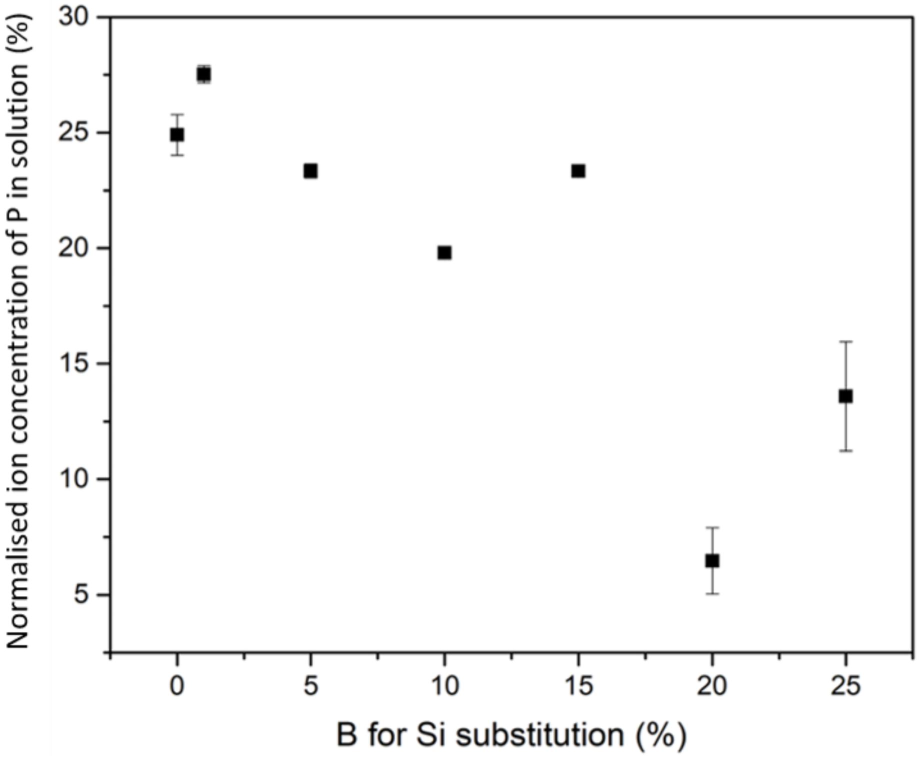

Figure 25: Normalised ion concentration of P in the solution after the dissolution test at 6 h in dependency on the B for Si substitution.

With an increasing boron content in the glass, there is a declining amount in the normalised ion concentration of the phosphorus in the solution.

FTIR spectra after 6 h and 7 d in Tris buffer solution for the glass powders with a particle size <38 µm of the glass series 45S5-B are shown in Figure 26.

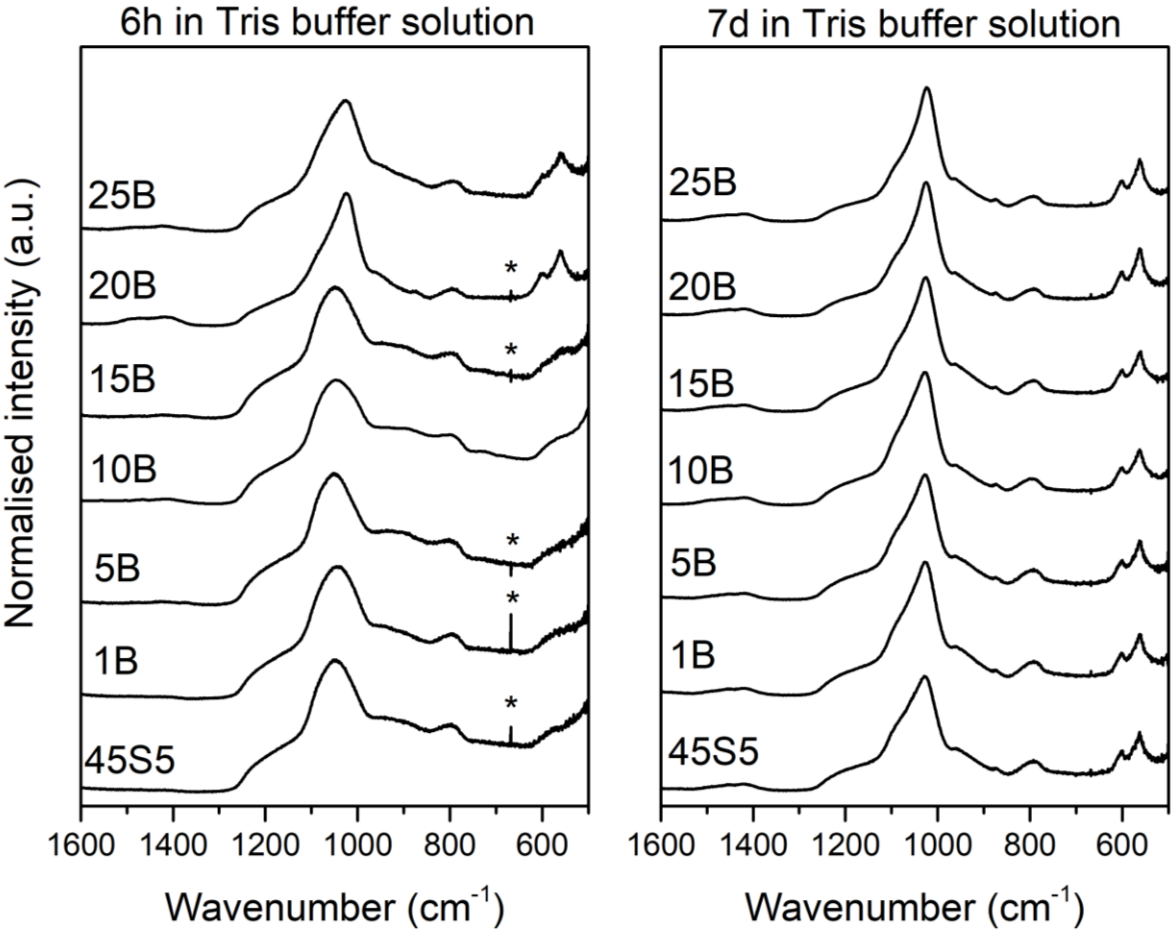

Figure 26: FTIR spectra after 6 h and 7 d in Tris buffer solution for the glass powders <38 µm of the glass series 45S5-B. The symbol "*" indicates an artefact caused by the spectrometer.

The spectra for all glasses at 7 d stay in Tris buffer solution look very similar with a double band between 560 cm^{-1} and 600 cm^{-1}, two small bands at 790 cm^{-1} and 870 cm^{-1} and a pronounced one at about 1015 cm^{-1}. The bands at 560, 600 and 1015 cm^{-1} can be assigned to forming apatite [71]. The band at 790 cm^{-1} corresponds to the formed silica-gel (ion-depleted glass) [72] and the band at 870 cm^{-1} to a C-O band [73]. The bands at 1400 cm^{-1} and higher are associated with C-O bands [73] and for the boron-containing glasses also to B_3-O bands [64].

At 6 h only the spectra for glasses 20B and 25B exhibit the double band. The spectra of glasses 45S5-15B show a broad band with its maximum at 1050 cm^{-1}, however, for 20B and 25B, there is a sharper band with its maximum at 1020 cm^{-1}. The spectra of all glasses show the small silica-gel band at 790 cm^{-1}, whereas the C-O band at 870 cm^{-1} is only present for glass 20B.

The results of the ***XRD*** measurements on the bioactive glass particles after a stay in Tris buffer solution for 6 h respectively 7 days are presented in Figure 27. In the right picture the reflections are assigned (§, hydroxyapatite, JCPDS 00-009-0432).

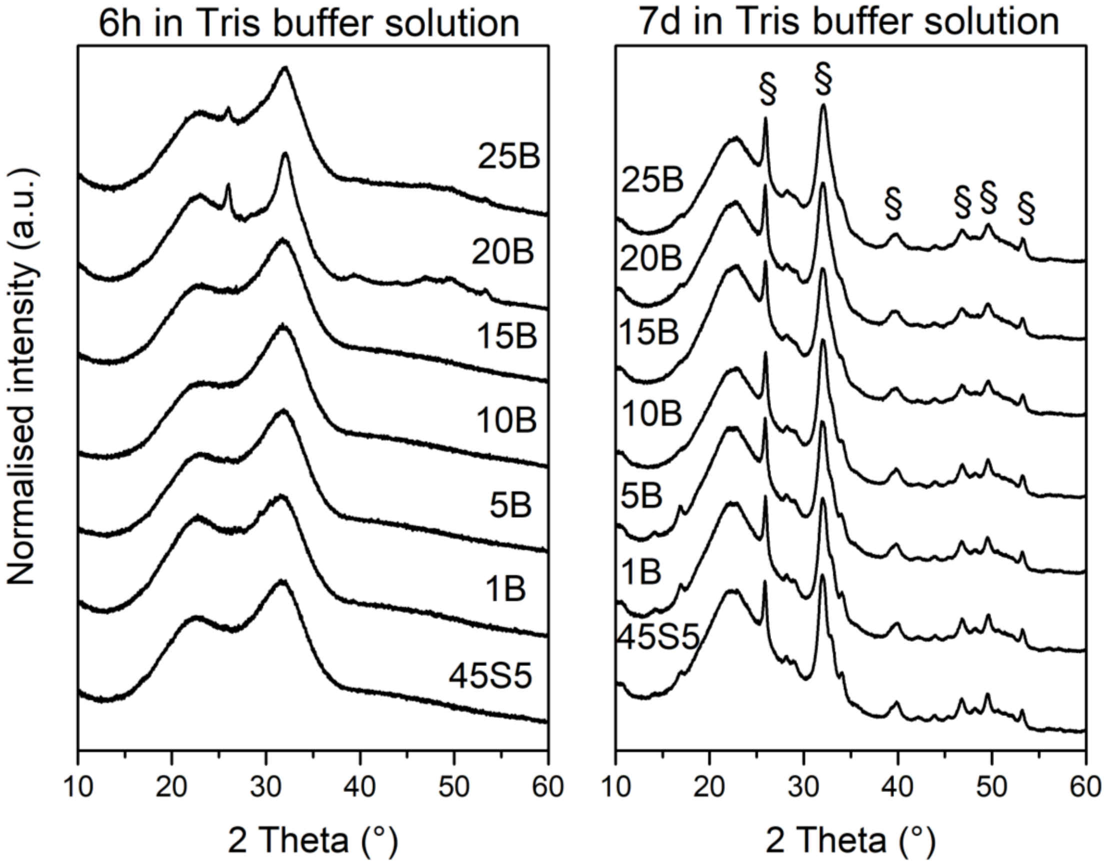

Figure 27: XRD results after 6 h and 7 d in Tris buffer solution for glass powder <38 µm on the glass series 45S5-B. In the right picture, the reflections are assigned ($, hydroxyapatite, JCPDS 00-009-0432).

At 6 h (left) apart from a broad double-signal with its maximum at 23° and 32° only glasses 20B and 25B exhibit sharper signals at about 26° and 32°. However, after 7d (right) all glasses show distinct signals at 26° and 32° and smaller ones at 17°, 40°, 47°, 50° as well as 53°. Interestingly, glasses with a low boron content exhibit sharper signals in comparison to the ones with a higher boron content.

SEM images of the surface of glass disc 45S5 after 7 d in Tris are shown in Figure 28. In picture B, one can see a “cauliflower-like” structure, circular shapes with a diameter of about 1 µm, which are coated with small needles, see also Fu et al. [74].

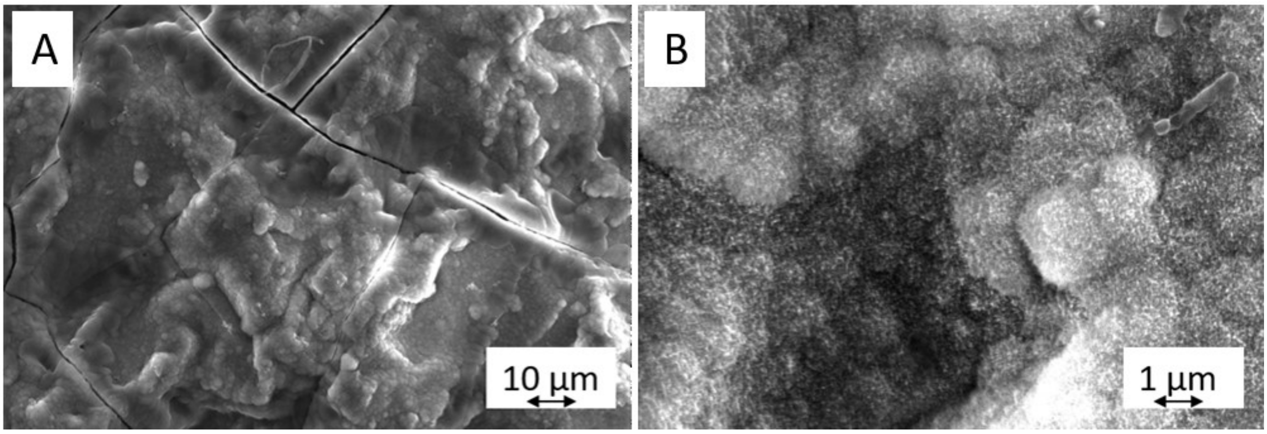

Figure 28: SEM images of glass disc 45S5 surface after 7 d in SBF. Picture A is from the master thesis of Böhme [75].

SEM images of cross sections of glasses 45S5, 15B, 20B and 25B after 7d in SBF are presented in Figure 29. Like in Figure 28 left, in all cross-sections cracks are visible, which originate from drying the samples after they have stayed in the SBF solution.

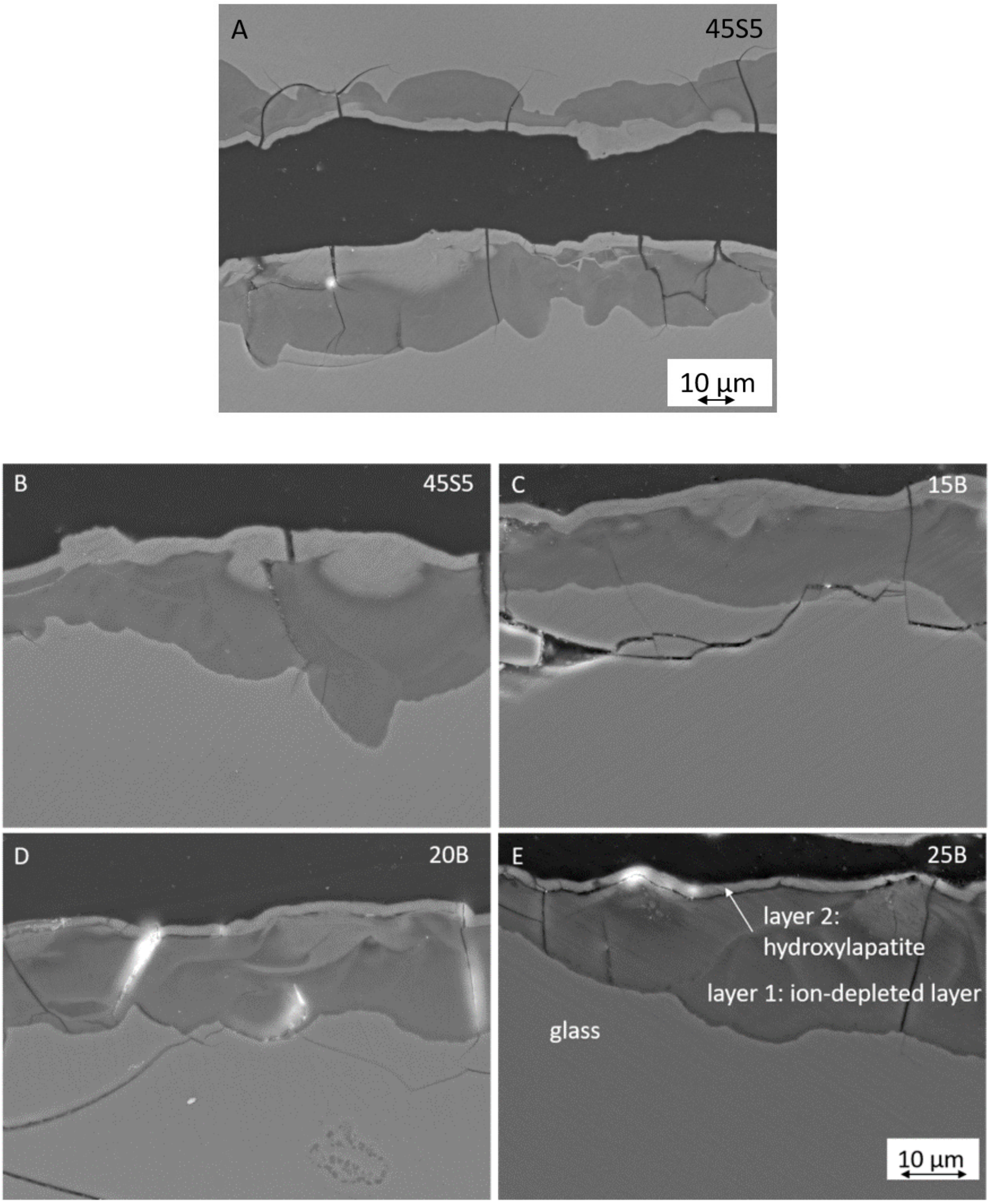

Figure 29: SEM images of cross sections of glasses 45S5, 15B, 20B and 25B after 7 d in SBF. A) shows an overview and B-E detailed sections. Pictures D and E from Böhme [75].

Picture A shows an overview, whereas picture B-E show detailed sections. In all pictures four different zones are visible. For glass 25B, in picture E they are labelled (from bottom to top): light-grey: glass, dark-grey: layer 1 and white: layer 2. The black zone is the polymer, which was used to glue the samples together. Layer 1 is the ion-depleted layer (silica-gel), and layer 2 is the formed apatite, see also chapter 2.2. The thickness of the ion-depleted and the apatite layer is non-uniform in each sample and no differences with boron content could be seen.

The results of the elemental analysis via ***EDX*** of glass discs 45S5 after 7d in SBF are presented in Table 6.

Table 6: Results of the elemental analysis via EDX of glass sample 45S5 after 7d in SBF.

45S5			
	glass (at%)		**glass (mol%)**
Si	16.3 ± 0.7	**SiO_2**	46.4 ± 2.1
Ca	9.5 ± 0.5	**CaO**	26.9 ± 1.3
Na	16.8 ± 1.2	**Na_2O**	23.8 ± 1.7
P	2 ± 0.1	**P_2O_5**	2.8 ± 0.2
	layer 1/ion-depleted layer (at%)		**layer 1/ ion-depleted layer(mol%)**
Si	29.4 ± 1.5	**SiO_2**	88.2 ± 4.6
Ca	2.5 ± 0.2	**CaO**	7.5 ± 0.6
Na	0.6 ± 0.1	**Na_2O**	0.8 ± 0.2
P	1.5 ± 0.1	**P_2O_5**	2.3 ± 0.2
Mg	0.2 ± 0.1	**MgO**	0.7 ± 0.3
Cl	0.2 ± 0.1	**Cl**	0.5 ± 0.3
	layer 2/ apatite (at%)		**layer 2/ apatite (mol%)**
Si	1.7 ± 0.2	**SiO_2**	5.0 ± 0.5
Ca	24.7 ± 1.1	**CaO**	72.0 ± 3.3
Na	0.7 ± 0.2	**Na_2O**	1.1 ± 0.3
P	12.2 ± 0.5	**P_2O_5**	17.8 ± 0.8
Mg	0.3 ± 0.1	**MgO**	0.9 ± 0.4
Cl	1.1 ± 0.2	**Cl**	3.1 ± 0.5

In the glass 45S5, the amount of silicon (16.3 ± 0.7 at%) and sodium (16.3 ± 1.2 at%) is high, whereas 9.5 ± 0.5 at% calcium and 2 ± 0.1 at% phosphorus is present. In layer 1, which is the ion-depleted layer ("silica-gel") silicon is the major component

(29.4 ± 1.5 at%). In layer 3, apatite, calcium (24.7 ± 0.1 at%) and phosphorus (12.2 ± 0.5 at%) are dominant.

The results of the elemental analysis given as ratios of Si/P, Si/Ca and Ca/P for glass discs 45S5, 20B and 25B after 7 d in SBF are shown in Table 7.

Table 7: Results of elemental analysis (EDX) given as ratios of Si/P, Si/Ca and Ca/P for glass samples 45S5, 20B and 25B after 7d in SBF.

45S5			
	glass	**layer 1 /ion-depleted layer**	**layer 2/ apatite**
Si/P	8.2 ± 0.8	19.8 ± 2.3	0.1 ± 0.0
Si/Ca	1.7 ± 0.2	11.9 ± 1.6	0.1 ± 0.0
Ca/P	4.8 ± 0.5	1.7 ± 0.2	2.0 ± 0.2
20B			
Si/P	7.2 ± 0.7	9.7 ± 1.2	0.2 ± 0.0
Si/Ca	1.4 ± 0.1	5.2 ± 0.6	0.1 ± 0.0
Ca/P	5.3 ± 0.5	1.9 ± 0.2	2.0 ± 0.2
25B			
Si/P	7.9 ± 0.7	10.8 ± 1.4	0.5 ± 0.1
Si/Ca	1.4 ± 0.1	6.3 ± 0.6	0.3 ± 0.0
Ca/P	5.7 ± 0.6	1.7 ± 0.2	1.9 ± 0.2

The Si/P ratio is about 8, the Si/Ca ratio about 1.5 and the Ca/P ratio about 5 for all glasses. In the ion-depleted layer of glass 45S5, the Si/P ratio is about 20 and the ratio of Si/Ca about 12. However, for the ion-depleted layer of the glasses 20B and 25B the Si/P ratio is about 10-11 and the Si/Ca ratio about 5-6. The Ca/P ratio is 1.7-1.9 for the ion-depleted layer of all glasses. The apatite layer exhibits a Si/P ratio as well as a Si/Ca ratio between 0.1 and 0.5 and a Ca/P ratio of about 2 for all glasses.

X-ray microscopy images of glass disc 25B after 7 d in SBF in a perspective view (A) and in a detailed view (B) are presented in Figure 30.

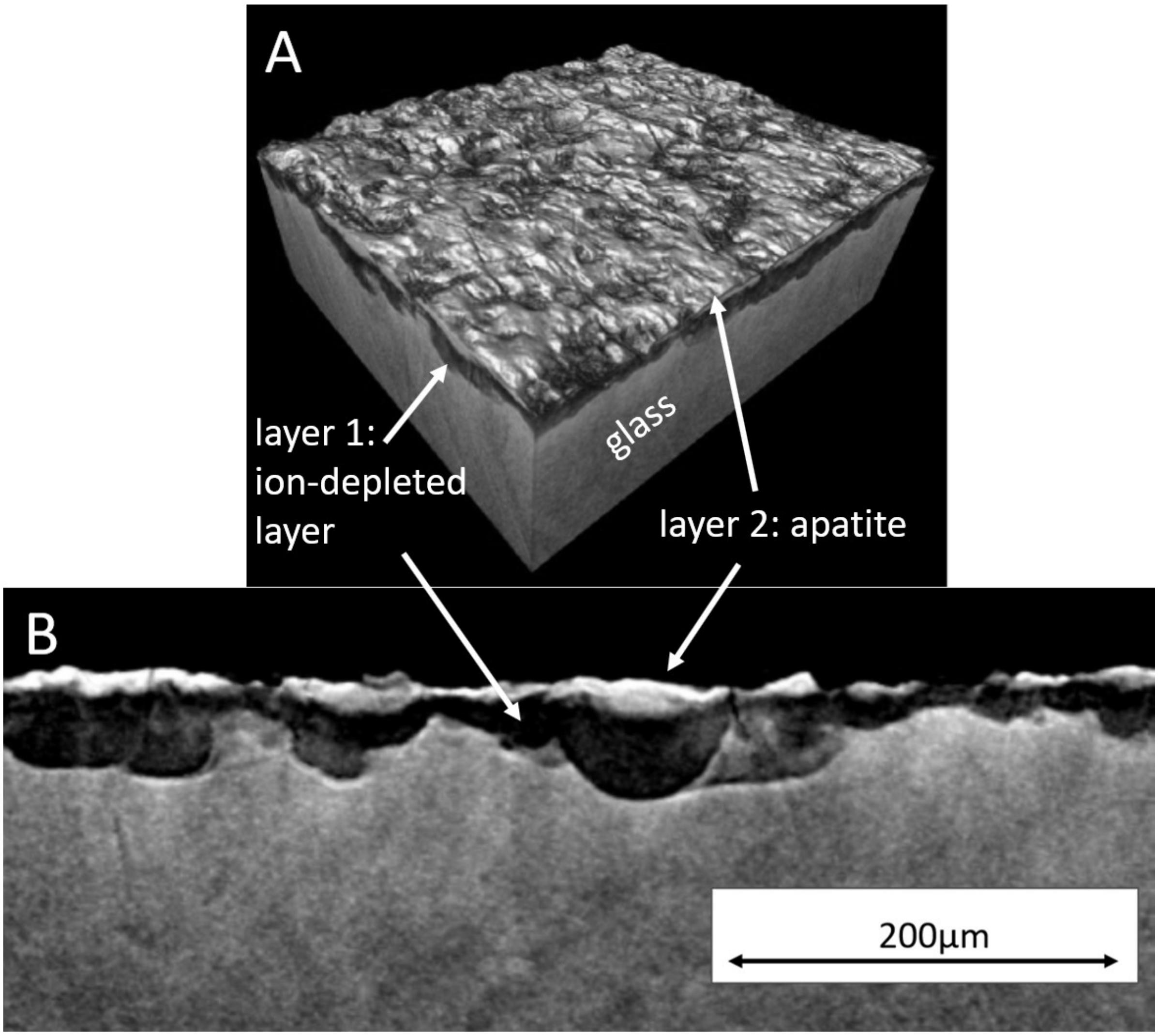

Figure 30: X-ray microscopy images of glass disc 25B after 7 d in SBF: A) in a perspective view and B) in a detailed view. Three phases are visible: glass, layer 1: ion-depleted layer and layer 2: apatite.

In the perspective as well as in the detailed view three zones are visible: grey: glass, dark grey/black: layer 1: ion-depleted layer and light grey/white: layer 2: apatite. Both layers, the ion-depleted and the apatite one, do not have a uniform depth.

4.1.4. Thermal Properties & Glass Stability Parameters

The glass transition temperatures determined by ***dilatometry*** measurements are plotted in Figure 31.

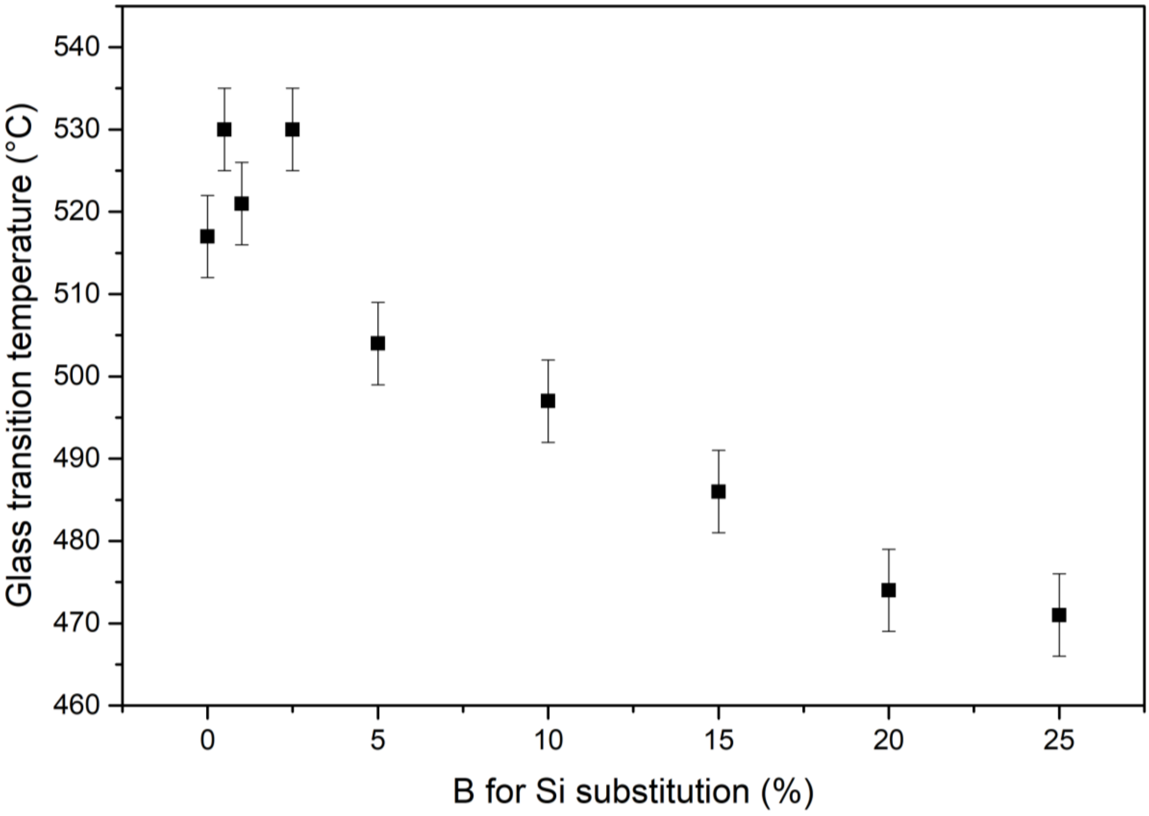

Figure 31: Glass transition temperature determined by dilatometry measurements for glass series 45S5-B.

With increasing boron content, a decrease in glass transition temperature T_g can be seen. T_g of glass 45S5 is at 517°C. Upon B for Si substitution, the T_g decreases to 471°C for glass 25B, which is 46 K lower than for glass 45S5 having a T_g of 517°C.

For the whole glass series 45S5-B, ***heating microscopy*** presented shadow images like shown for glass 45S5-5B in Figure 32 exemplarily. The glass powder compact shrinks upon heating while the cylindrical shape is maintained.

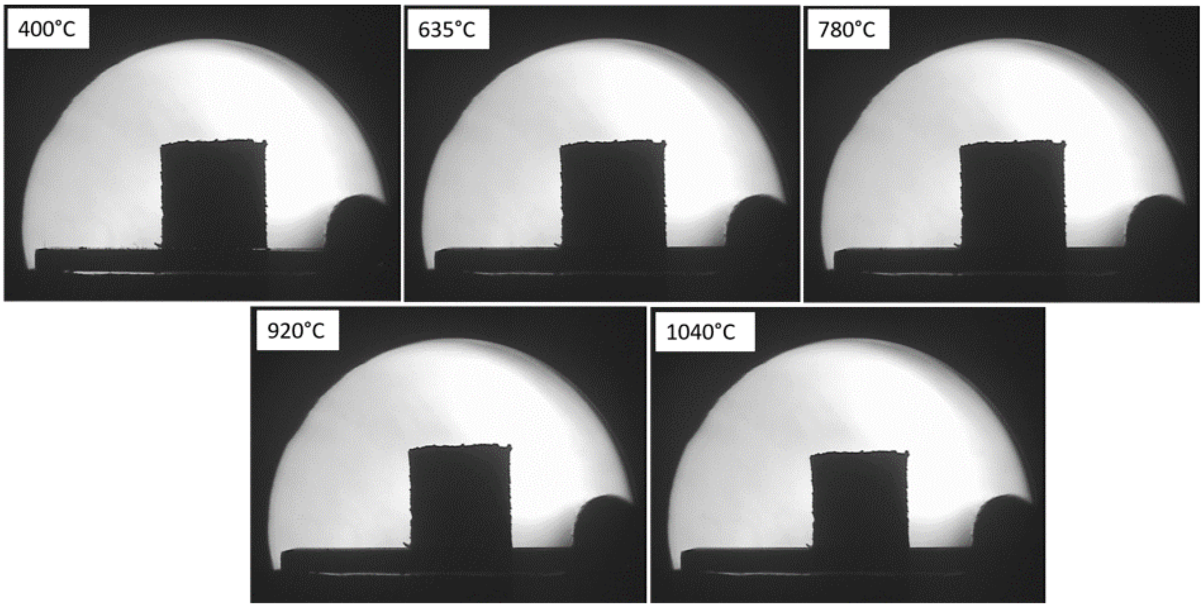

Figure 32: Shadow images of the glass powder pellet upon heating using heating microscopy, here exemplarily for glass 45S5-5B.

The powder compacts of glass series 45S5-B were powdered after the HTM measurements. The investigation via XRD verified the presence of sodium calcium silicate.

The ***differential scanning calorimetry*** thermograms of the glass series 45S5-B on powder <38 µm are presented in Figure 33.

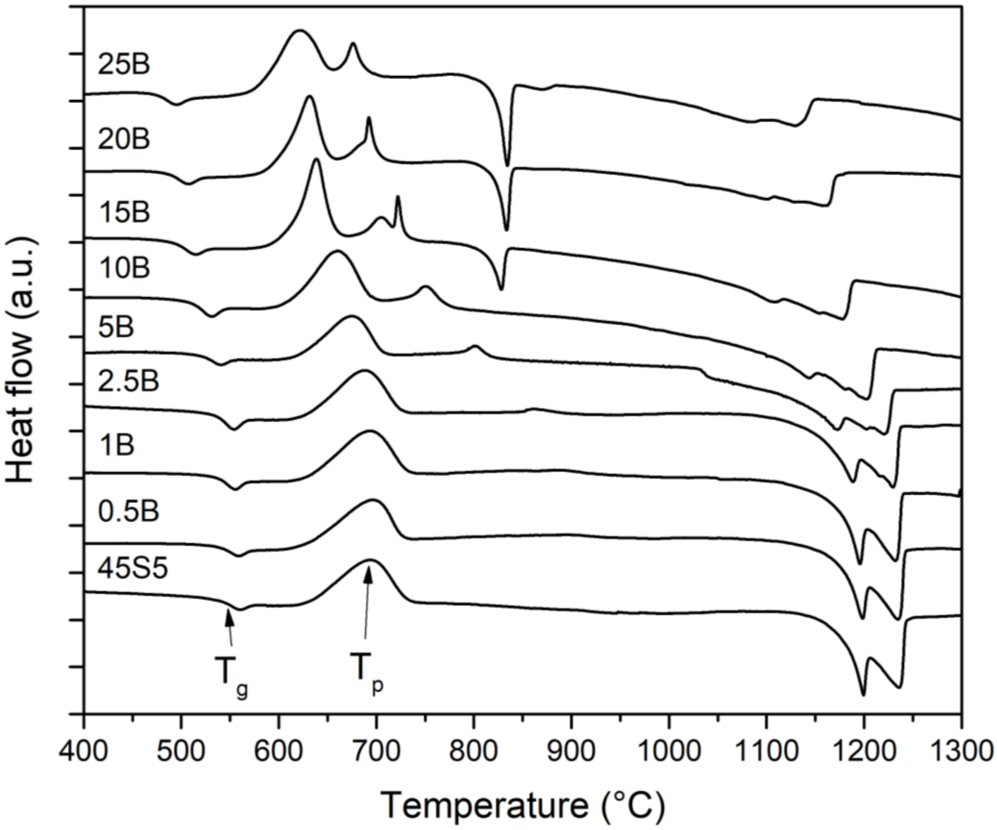

Figure 33: Differential Scanning Calorimetry of the glass series 45S5-B on powder <38 µm.

All investigated glass compositions show distinct glass transition temperatures (T_g) and crystallisation peaks. The peak maximum of the crystallisation peak (T_p) is labelled for glass 45S5, exemplarily. With increasing boron content, a decrease in glass transition temperature can be identified. Up to glass 2.5B, there is one broad exotherm crystallisation peak, whereas for the glasses 5B-25B multiple crystallisation peaks are visible. The shape of the crystallisation peaks for glasses 15B and 20B is sharper in comparison to the others. The melting of the formed crystalline phases is visible in the form of multiple partially overlapping endothermic events. With rising boron content in the glass composition, the melting of one formed crystalline phase starts at lower temperatures, for the glasses 15B, 20B and 25B already below 900°C.

The ***glass stability parameters*** (GSP) calculated for the glass series 45S5-B are plotted in Figure 34. The glass stability is the resistance of glass against devitrification upon heating [44].

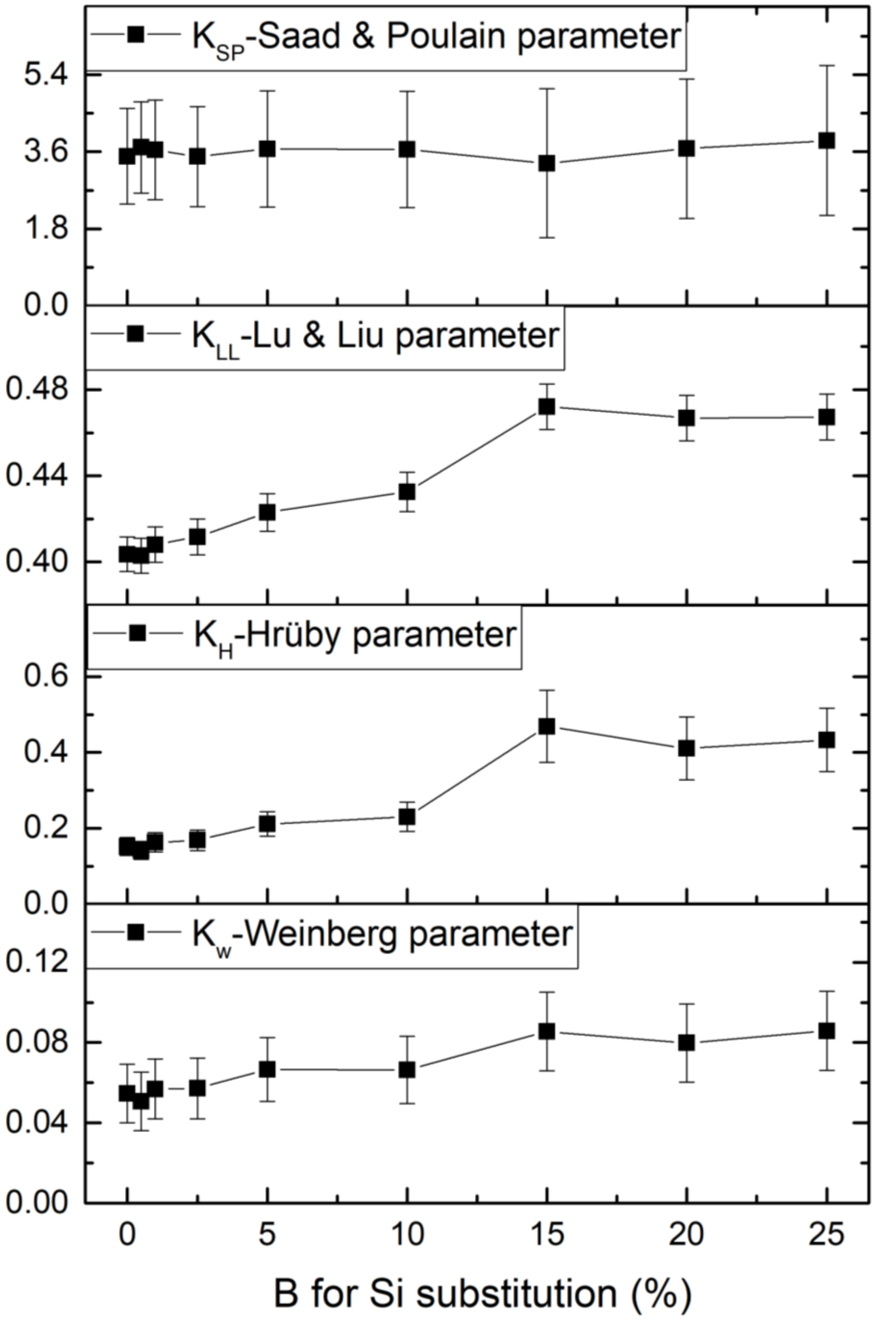

Figure 34: Glass stability parameters calculated for the glass series 45S5-B.

Glass stability is usually characterised by the difference between T_g and T_x. In the case of multiple crystallisations, only the lowest temperature peak is taken into account [21]. For the calculation of the parameters, four different formulas were used: Saad & Poulain, Lu & Liu, Hrüby and Weinberg, see 3.1.4.

Whereas for the Saad & Poulain parameter no change with boron for silicon substitution can be seen (~3.6 for all glasses), Lu & Liu, Hrüby- and Weinberg parameters show an increase. As a larger glass stability parameter reveals a decreased tendency for crystallisation according to the glass stability parameter calculation, the glasses with high boron content are less prone to crystallisation.

4.1.5. Crystallisation Mechanism & Impact on Dissolution

For the study of the ***crystallisation mechanism*** as well as its ***impact on the dissolution behaviour***, DSC, HTM and dissolution tests with glass and crystallised glass were carried out. For the crystallisation mechanism study (DSC), the glass particles were prepared using mortar and sieve to avoid cross-contamination, whereas for HTM and solubility tests milling via planetary mill was used. The particle size distribution of the glass powders 45S5, 5B, 15B, and 25B prepared by planetary milling needed to be investigated. The particle size distributions of the glasses are similar to each other, see Figure A 2. As the D50 value is around 20 µm, those glass powders are comparable with fine powder produced using mortar and sieve [76]. Therefore, both applied methods of glass preparation can be seen as equal methods to obtain a fine powder.

The heat flow in dependence on the temperature (DSC thermogram) of the glasses 45S5, 5B, 15B and 25B for powder <38 µm is presented in Figure 35.

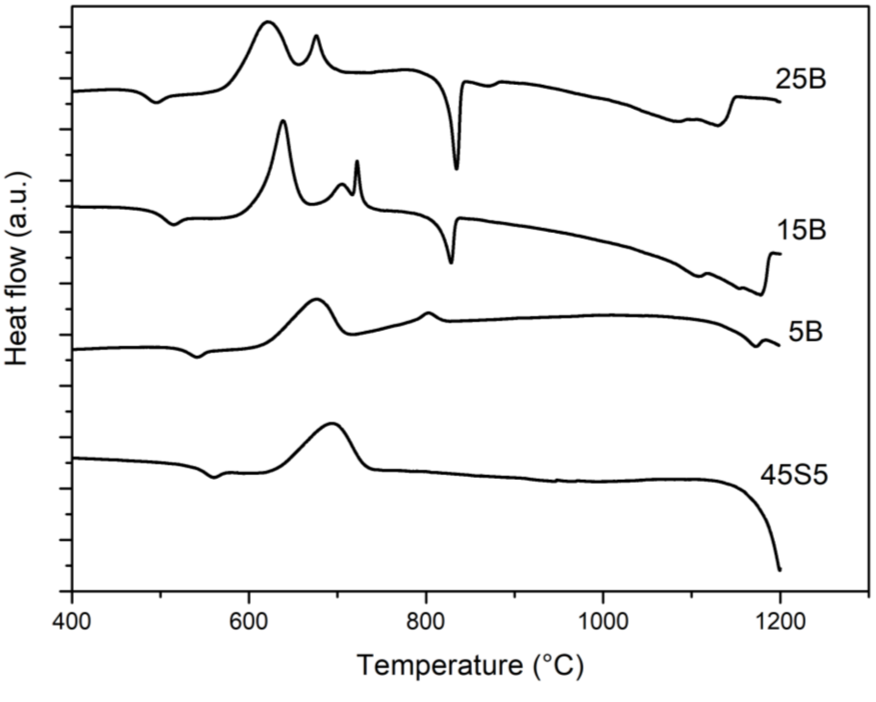

Figure 35: Heat flow in dependence on temperature (DSC thermogram) for fine glass powders <38 µm of glasses 45S5, 5B, 15B, 25B carried out with a heating rate of 10 K/min.

Whereas all glasses exhibit only one glass transition, glasses 5B, 15B and 25B show more than one crystallisation peak, as mentioned before in chapter 4.1.4. While the DSC thermogram of glass 45S5 displays one crystallisation peak, 5B shows two well-separated crystallisation peaks. The thermograms of glass 15B and 25B exhibit two to three overlapping crystallisation peaks.

The values for the glass transition temperature T_g, the onset of crystallisation T_x, the maximum of crystallisation peaks T_{p1} (T_{p2}, T_{p3}) and the working range ΔT for glasses 45S5, 5B, 15B and 25B are summarised in Table 8. With increasing boron content in the glass, T_g, T_x and T_{p1} decrease.

Table 8: Temperatures for glass transition T_g, the onset of crystallisation T_x, maximum of crystallisation peaks T_{p1}, T_{p2} and T_{p3} as well as the working range ΔT for glasses 45S5, 5B, 15B and 25B.

	10 K/min							
	45S5		**5B**		**15B**		**25B**	
µm	**<38**	**500-1000**	**<38**	**500-1000**	**<38**	**500-1000**	**<38**	**500-1000**
T_g (°C) ± 2 K	552	547	535	528	505	502	487	483
T_x (°C) ± 3 K	629	728	614	679	594	648	575	604
T_{p1} (°C) ± 3 K	694	757	676	700	639	665	622	615
T_{p2} (°C) ± 3 K			803		705	748	676	662
T_{p3} (°C) ± 3 K					722			
ΔT (K) ± 5 K	77	181	79	151	89	146	88	121

For the glasses, 45S5, 5B, 15B and 25B, T_x is higher for the coarse particles in comparison with the fine particles. The temperature of the first crystallisation peak (T_{p1}) is higher for coarse glasses 45S5, 5B and 15B in comparison to the fine glass powders. The working range ΔT for the fine glass particles increases with the boron content in the glass, whereas the one for the coarse particles decreases.

The ***DSC*** thermogram and the ***HTM*** graph for the glass 5B plotted in one diagram is presented in Figure 36A.

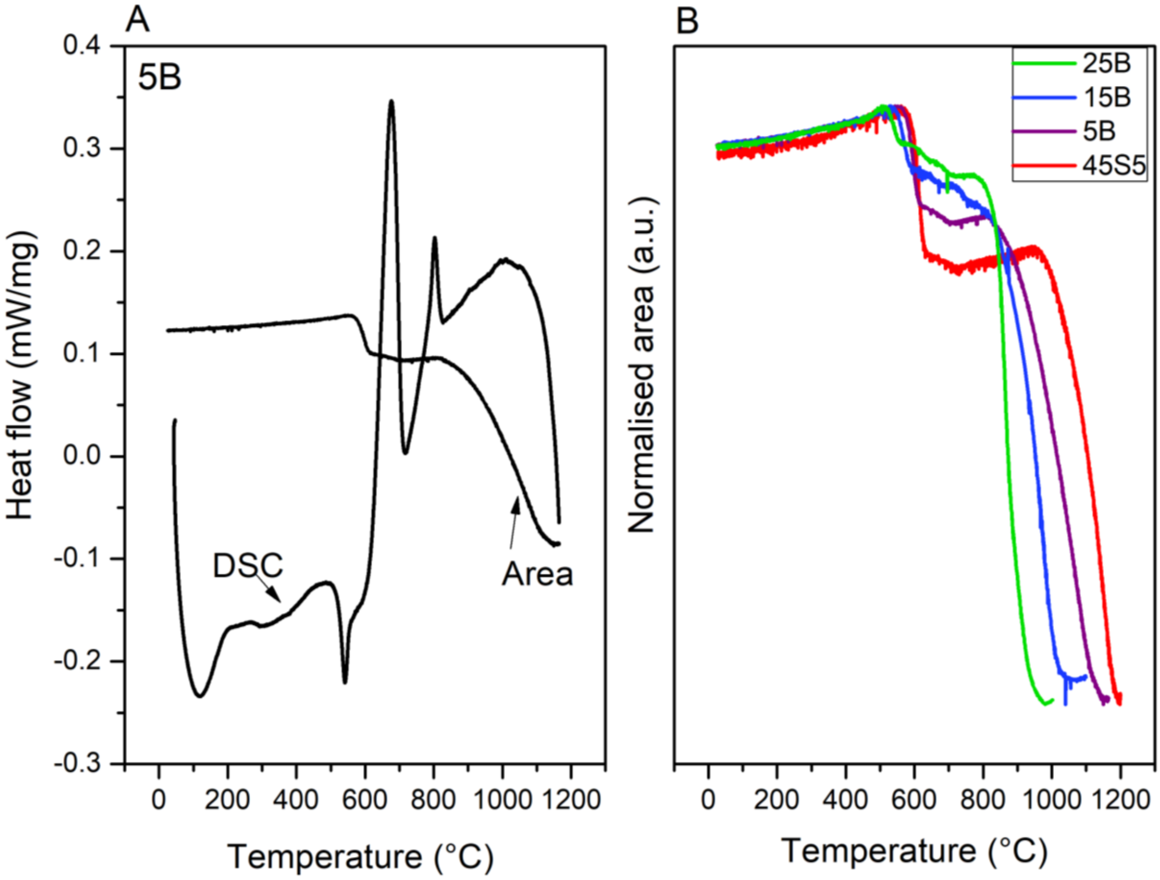

Figure 36: A) Heat flow in dependence on temperature (DSC thermogram) of fine glass powder <38 µm and HTM of fine glass powder D50~20 µm for glass 5B and B) HTM for glasses 45S5, 5B, 15B and 25B of fine glass powder D50~20 µm.

Figure 36B exhibits the HTM results for the glasses 45S5, 5B, 15B and 25B, where an earlier start of shrinkage with increasing boron content can be seen. The extent of shrinkage in the low-temperature area (~600°C) is decreasing with increasing boron content. In the high-temperature area, earlier shrinkage can be identified with increasing boron content.

The crystallisation behaviour of the glasses was examined by calculating the activation energy with two different models: ***Kissinger*** and ***Friedman***. For the coarse particles, the Friedman model was used additionally, which is advantageous as this method makes no mathematical approximations [77].

The crystallisation peaks as a function of the heating rate for fine powder (<38 µm) of glass 5B are presented in Figure 37A.

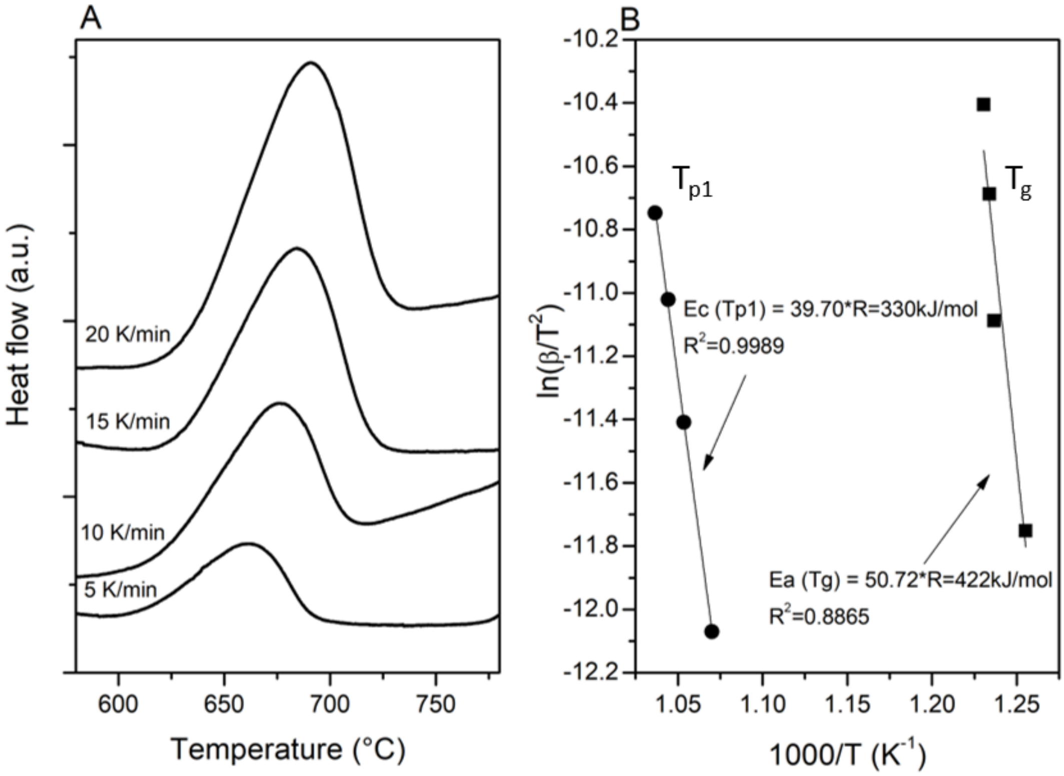

Figure 37: A) Crystallisation peaks as a function of heating rate and B) Kissinger plot using glass transition and crystallisation of fine glass powder 5B <38 µm.

The crystallisation peak shifted to higher temperatures with increasing heating rate, Figure 37. The temperature for the glass transition (T_g) and for the maximum of the first crystallisation peak (T_p) at the different heating rates (β) was evaluated. In Figure 37B ($\ln(\beta/T_g^2) = f(1000/T_g)$ as well as ($\ln(\beta/T_p^2) = f(1000/T_p)$ are shown in the Kissinger plot. The slope in the Kissinger plot is proportional to the activation energy for crystallisation respectively the activation energy for viscous flow.

The crystallised fraction α of the coarse particles of glass 5B (25B) in dependence on the temperature for the four different heating rates is presented in Figure 38 A (F).

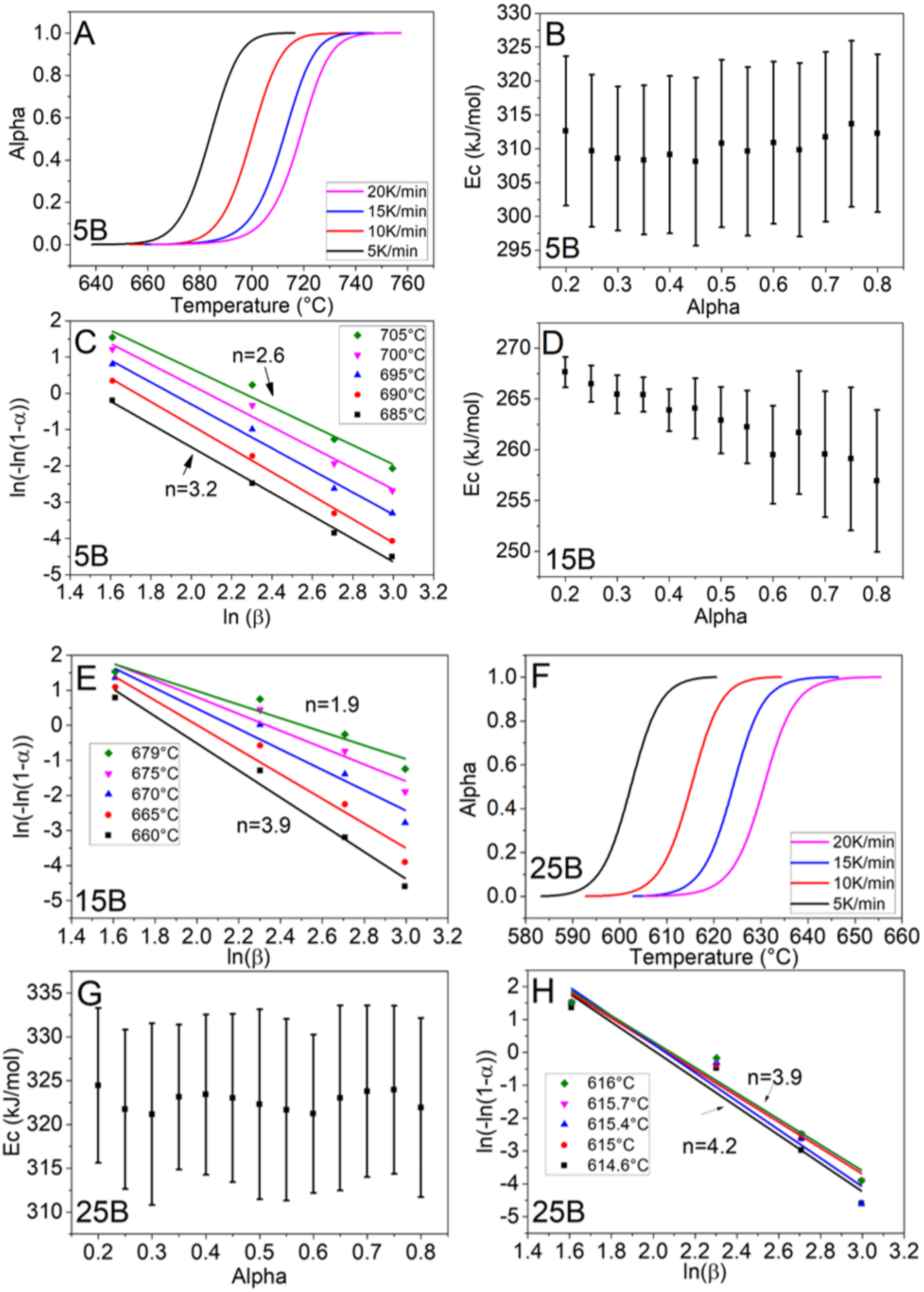

Figure 38: Fraction of glass crystallised α as a function of temperature (A, F), calculated values $E_{c\alpha}$ according to the Friedman equation as a function of α (B, D, G) and ln(-ln(1-α)) as a function of ln(β) (C, E, H) for the coarse powder of the glasses 5B, 15B and 25B.

The diagram for glass 15B can be found in the appendix. The activation energy E_c as a function of α for the glasses 5B, 15B and 25B is shown in Figure 38: B, D & G. As the activation energy is within ±10 % of the average E_c, it is regarded as constant for all glasses, although for 15B there is a decreasing trend. Constant activation energy suggests one crystallisation mechanism per investigated glass in coarse particle size. In the Ozawa method, the slope of ln(-ln(1-α) versus ln(β) is proportional to the JMA exponent, shown in Figure 38 C, E & H for the glasses 5B, 15B and 25B.

Table 9 shows the energies for viscous flow (Ea) and for the crystallisation of the first crystallisation peak calculated by using Kissinger equation for glasses 5B, 15B and 25B for fine powder <38 µm and coarse powder 500-1000 µm.

Table 9: Energies for viscous flow (E_a) and for crystallisation of the first crystallisation peak, calculated using Kissinger equation for glasses 5B, 15B and 25B for powder <38 µm (fine) and 500-1000 µm (coarse). The energy for crystallisation of the first crystallisation peak was accessed additionally for the coarse particles using Friedman calculation. The JMA exponent was calculated using Augis-Bennett calculation for fine and coarse glass powders of 5B-25B and using the Ozawa model for coarse powders additionally.

	5B		**15B**		**25B**	
	<38 µm	**500-1000 µm**	**<38 µm**	**500-1000 µm**	**<38 µm**	**500-1000 µm**
Kissinger						
E_a (kJ/mol)	422	430	498	611	616	509
±	85	9	73	146	121	17
E_c (T_{p1}) (kJ/mol)	330	288	357	245	318	308
±	6	16	5	4	15	10
Friedman						
E_c (T_{p1}) (kJ/mol)	-	310	-	263	-	323
±	-	2	-	3	-	1
Augis-Bennett using Kissinger						
n (Peak 1)	1.1	3.2	2.1	3.4	1.2	4.7
±	0.0	0.1	0.1	0.3	0.1	0.1
Ozawa						
n (Peak 1)	-	3.0	-	2.9	-	4.1
±	-	0.2	-	0.8	-	0.2

As mentioned before, the ***activation energy for crystallisation*** of the first crystallisation peak was accessed additionally for the coarse powder using the

Friedman calculation. The values reported in Table 9 correspond to the average value of the $E_{c\alpha}$ in the range of $0.2<\alpha<0.8$. There are no drastic changes in the activation energy of crystallisation comparing the results regarding the boron content and the particle sizes of the glasses.

The ***Johnson Mehl-Avrami*** exponent was calculated using the models by ***Augis-Bennett*** and ***Ozawa***. Whereas the Augis-Bennett equation utilizes the activation energy for crystallisation, the Ozawa calculation uses α (the fraction of crystallised glass) at a specific temperature as a function of the heating rate, see equation (3.10). Table 9 presents the JMA exponent calculated using the Augis-Bennett model for fine and coarse powder of 5B-25B, and JMA exponent using the Ozawa calculation for coarse powders additionally. The JMA exponent with the Augis-Bennett model was calculated using the E_c from the Friedman calculation (coarse particles) and had the same values within the accuracy of the measurements.

According to the Kissinger calculation, the activation energy for viscous flow increases with increasing boron content in the glass for the fine particles. For the fine particles, the crystallisation energies acc. to the Kissinger equation of glasses 5B, 15B and 25B are similar around 330 kJ/mol, whereas E_c acc. to Friedman for the coarse particles 5B and 15B is lower with 310 ± 2 kJ/mol and 263 ± 3 kJ/mol. E_c of 25B coarse is 323 ± 1 kJ/mol, therefore similar to the value for the fine particles of glass 25B.

The values of the JMA exponent (Augis-Benett) for the fine powders of glass 5B is 1.1 and for glass 25B 1.2. For the fine powder of glass 15B, the JMA is around 2. Increasing particle size leads to an increased JMA value: 3 for glass 5B coarse and glass 15B coarse and to above 4 for the glass 25B. The Ozawa calculation done for the coarse particles leads to the same values as the Augis-Bennett calculation for 5B and 15B and a slightly lower value for 25B.

Figure 39 A) shows a ***light microscopy*** (LM) image of bulk glass 5B after heat-treatment for 1 hour at 25 K below T_x: 650°C, whereas Figure 39 B) displays an ***X-ray microscopy*** image of the same sample in shaded surface display technique (SSD). SSD enables the display of boundaries of materials having different densities.

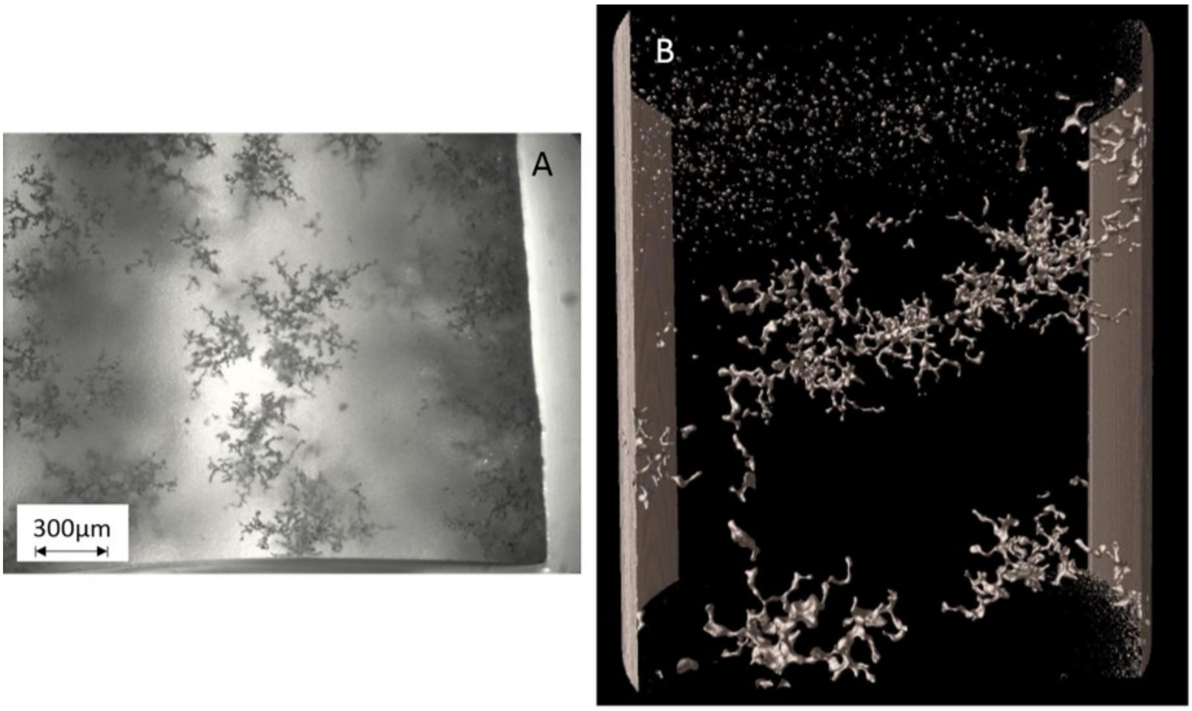

Figure 39: A) Light microscopy image and B) X-ray microscopy image in a shaded surface display technique of glass 5B bulk sample after heat-treatment for 1 hour at T_x-25 K: 650°C.

In both pictures, snow-flaky structures can be spotted. In the X-ray microscopy picture, there are smaller non-connected structures visible in the upper area, as well.

The ***X-ray diffractograms*** of powdered bulk glasses 5B, 15B and 25B after heat-treatment at 5 K below T_x are shown in Figure 40. The diffraction peaks corresponding to Sodium calcium silicate are assigned using the symbol (*).

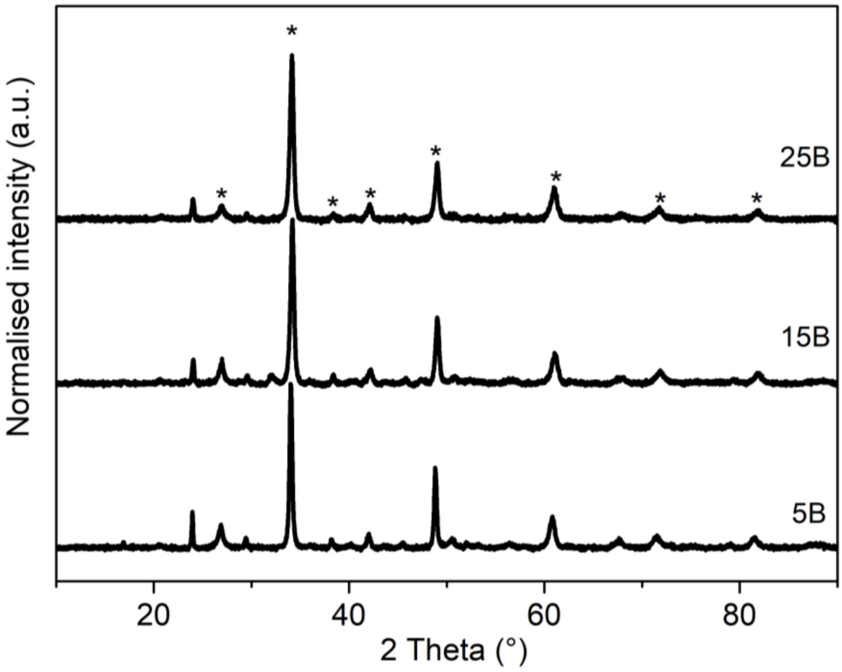

Figure 40: XRD of powdered bulk samples of glasses 5B, 15B and 25B after heat treatment 5 K below T_x with diffraction peaks of Sodium calcium silicate assigned (*) using ICDD Database (Ref. No. 04-012-6691).

The heat-treated volume samples of glasses 5B, 15B and 25B exhibit formation of Sodium calcium silicate.

In the following section, the results of the ***dissolution of amorphous versus (partly-)crystallised samples*** are presented.

The ***pH-value*** upon immersion of glasses 45S5, 5B, 15B and 25B (A) and heat-treated glasses 45S5c, 5Bc, 15Bc and 25Bc (B) is shown in Figure 41.

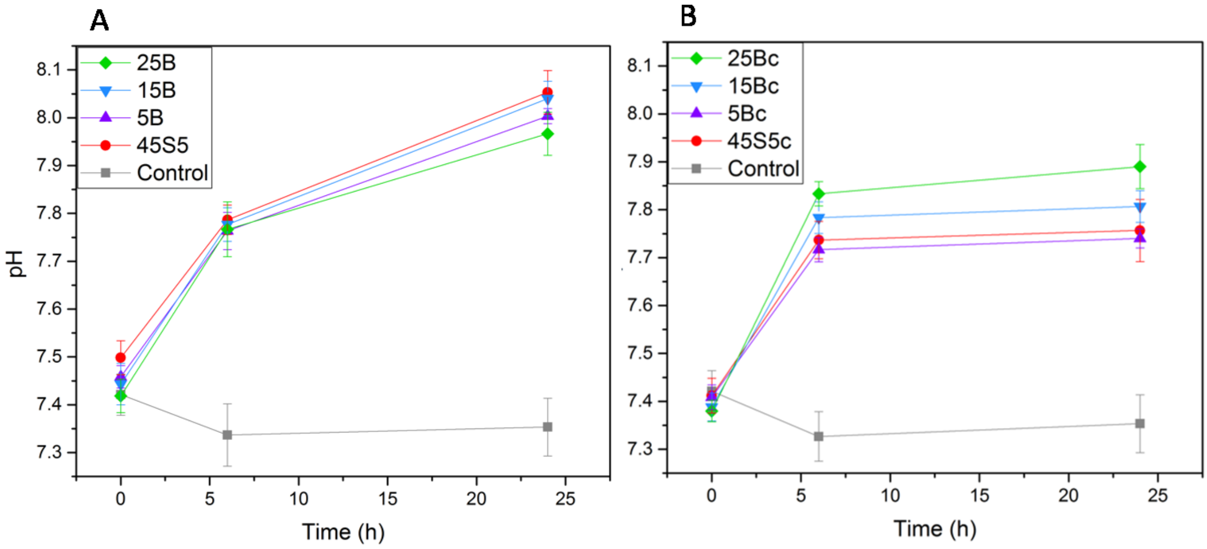

Figure 41: pH-value upon immersion of glasses 45S5, 5B, 15B and 25B (A) as well as heat-treated (partly-)crystallised glasses 45S5c, 5Bc, 15Bc and 25c (B). As reference pH-values of control samples free of glass are given. (Results are presented as mean ± SD. Lines are visual guides only.)

As reference pH-values of control samples are given. For both, glasses and (partly-)crystallised glasses, a steep increase in pH-value during the first 6 h of immersion can be seen: for the glasses up to ~7.75 and for the (partly-)crystallised glasses up to 7.7 and 7.8. For the (partly-)crystallised glasses containing relatively much boron 15Bc and 25Bc the pH-value is significantly higher than for the other ones, 45S5 and 5Bc. Afterwards, the increase in pH-value continues for the glasses up to ~8 whereas for the (partly-)crystallised glasses the pH-value stays constant.

The results from the ***ICP-OES*** analysis of the Tris buffer solution after contact with the bioactive glasses 45S5, 5B, 15B and 25B (A, C, E, G) and of the (partly-)crystallised glasses 45S5c, 5Bc, 15Bc and 25Bc (B, D, F, H) are shown in Figure 42.

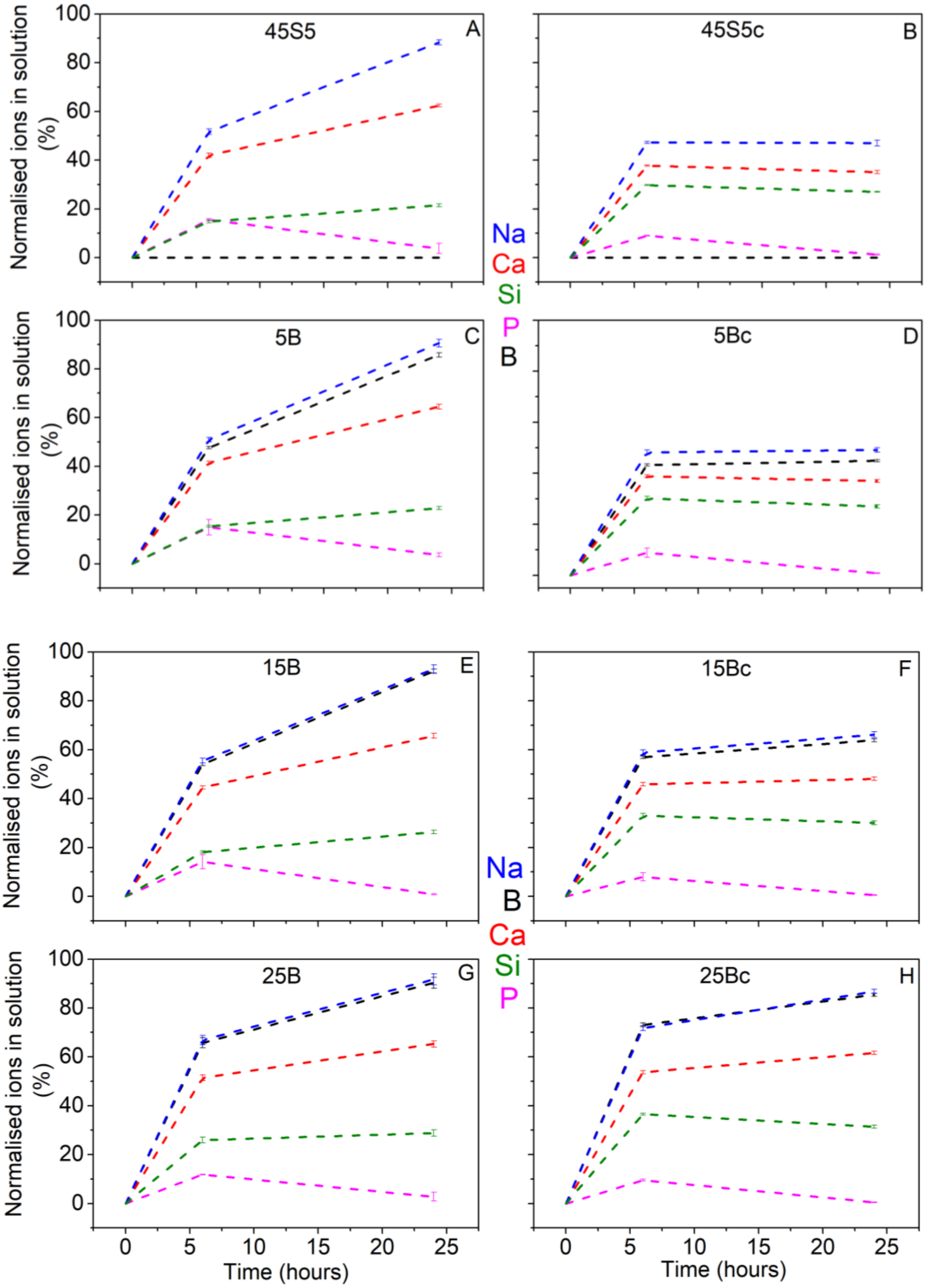

Figure 42: ICP-OES results of the Tris buffer solution for the glasses 45S5, 5B, 15B and 25B (A, C, E, G) and for the (partly-)crystallised glasses 45S5c, 5Bc, 15Bc and 25Bc (B, D, F, H).

The ion concentration in the solution is normalised to the amount, which was in the glass used for the individual test. The amount of sodium, calcium, silicon, and phosphorus present is similar for all investigated glasses. During the first 6 h of immersion, there is a steep increase regarding the ion concentration in the solution. For the glasses, the slope of the ion dissolution continues to increase between 6 h and 24 h as well, whereas for the (partly-)crystallised glasses this only occurs for 15Bc and 25Bc. For 45S5c and 5Bc, the ion concentration does not increase between 6 h and 24 h. A special role plays phosphorus: the amount, which can be found in the analysed solutions is smaller for all investigated compositions at 24 h in comparison to 6 h. Very interesting is the fact that whereas no boron was in the solution after dissolution test for samples 45S5 and 45S5c as expected; for the other glasses and 25Bc after 24 h immersion in Tris nearly 100 % of boron is present in the solution. For the other glass compositions, boron and sodium are present in the solution in a similarly high amount.

The ***FTIR*** spectra of the glasses (A, B) and of the (partly-)crystallised glasses (C, D) before (A, C) and after immersion in Tris buffer solution for 24 h (B, D) are presented in Figure 43.

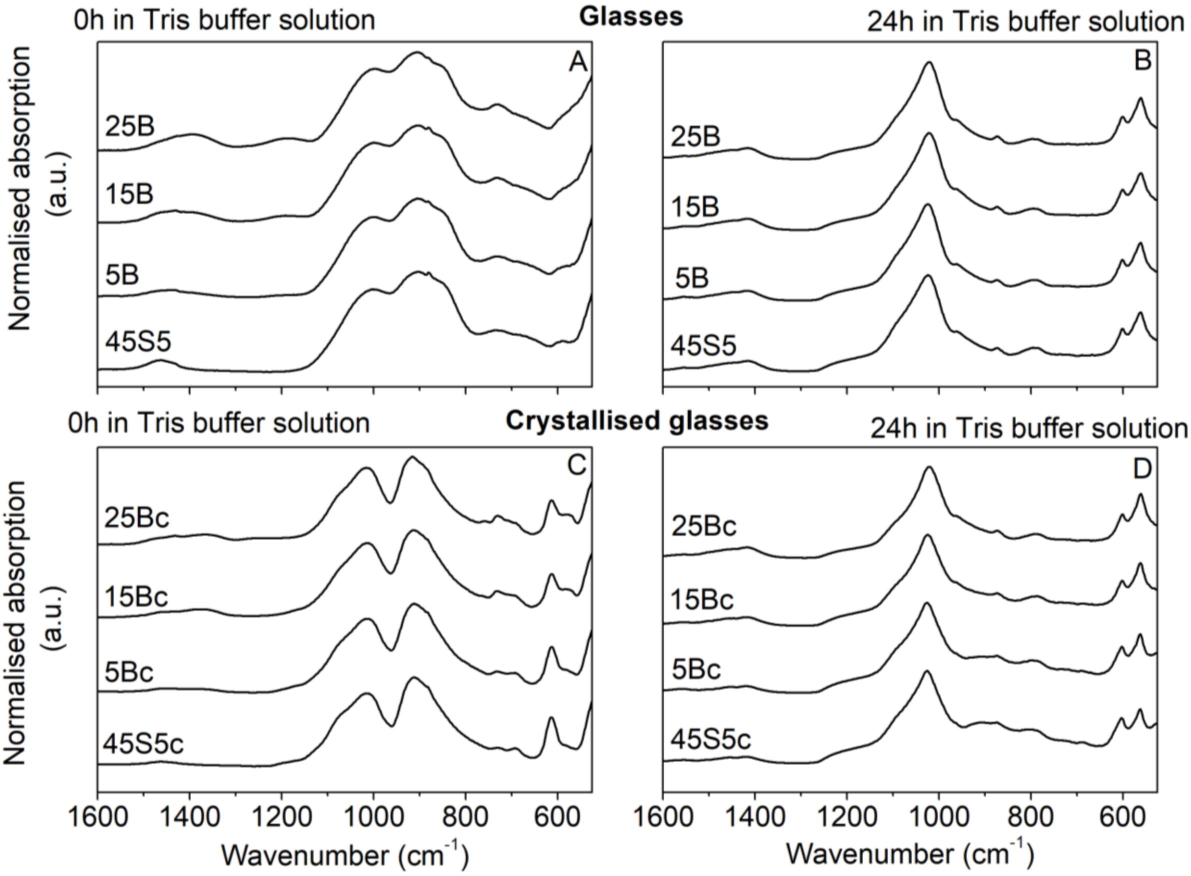

Figure 43: FTIR spectra of glasses (A, B) and (partly-)crystallised glasses (C, D) before immersion in Tris buffer solution (A, C) and after 24 h in Tris buffer solution (B, D).

FTIR spectra of the untreated glasses exhibited the typical features of bioactive silicate glasses: overlapping bands between 840 cm^{-1} and 940 cm^{-1} (non-bridging oxygen bands, NBO) as well as a bridging-oxygen (BO) band at about 1040 cm^{-1} [78]. In the spectra of the (partly-)crystallised glasses, the bands at 920 cm^{-1} and 1070 cm^{-1} can be assigned to Si-O stretching vibrations. The band at 1015 cm^{-1} can be assigned to stretching vibrations of P-O and the band at 613 cm^{-1} to bending vibration of P-O in a crystalline environment [79].

After 24 h the FTIR spectra of all investigated compositions look very similar. The NBO bands at 840 and 940 cm^{-1} disappeared, while there is a pronounced band at 1015 cm^{-1} and a double-band between 550 and 650 cm^{-1}, which is indicating the formation of apatite [71].

The apatite formation on crystallised (heat-treated) glass 45S5 was encountered before by Peitl et al. [80] The band at 790 cm^{-1} corresponds to the formed silica-gel [72] and the one at 870 cm^{-1} to C-O vibrations [73], while the ones around 1400 cm^{-1} are associated with C-O vibrations and for the boron-containing glasses to B_3-O bands [64] as well. The intensity of the C-O bands is higher for the reacted glasses than for the reacted (partly-)crystallised glasses.

The ***XRD*** patterns of the glasses (A, B) and of the (partly-)crystallised glasses (C, D) are shown in Figure 44.

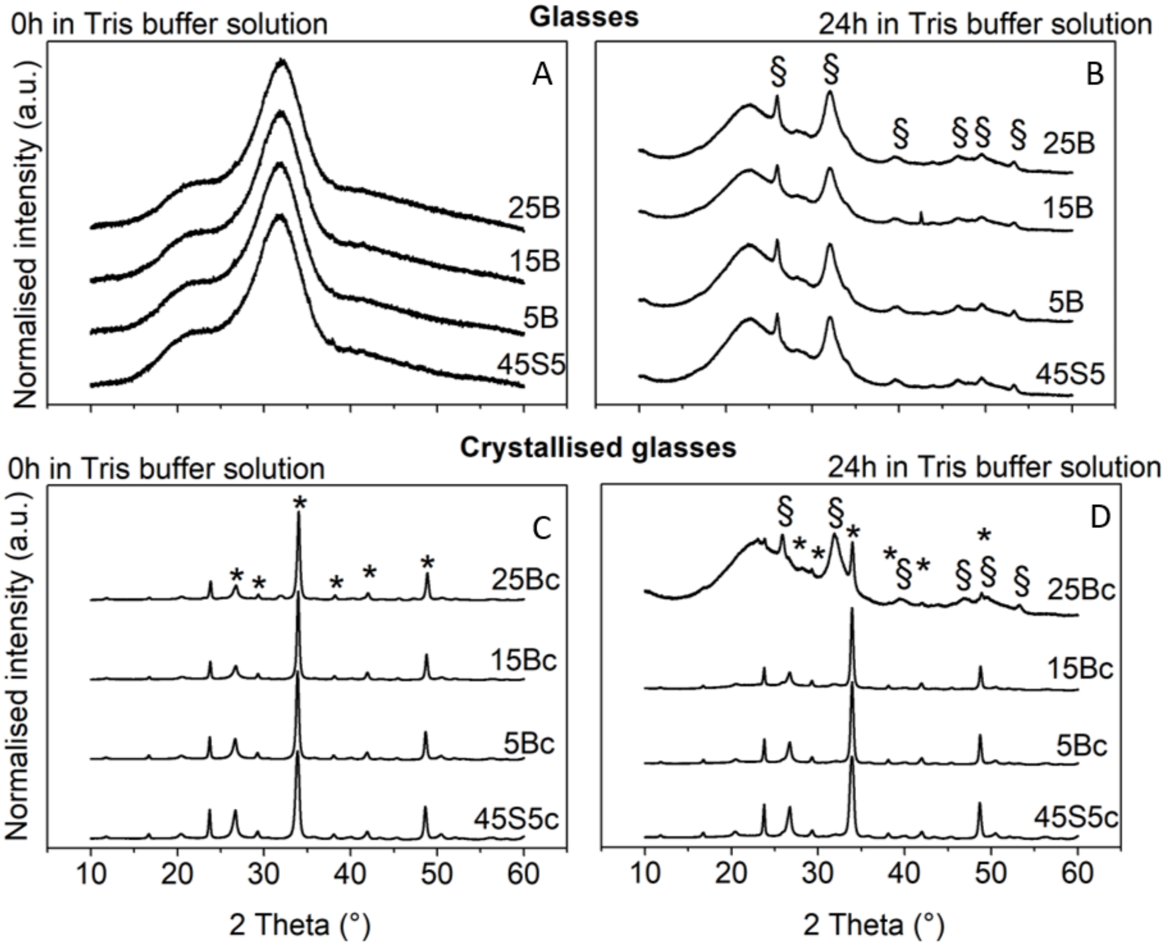

Figure 44: XRD from glasses (A, B) and heat-treated, (partly-)crystallised glasses (C, D). A and C before immersion in Tris buffer solution and B and D after 24 h in Tris buffer solution. The diffraction peaks for sodium calcium silicate (*, ICDD 04-012-6691) and hydroxyapatite (§, JCPDS 00-009-0432) are assigned.

Whereas before immersion in Tris for the glasses (A) an amorphous glass halo can be seen, after 24 h in Tris apatite was formed for all compositions. Heat treatment of the glasses led to the crystallisation of sodium calcium silicate (C). After staying in Tris for 24 h, the XRD pattern of the (partly-)crystallised glasses 45S5c, 5Bc and 15Bc look like the ones before immersion (C). However, for 25Bc after immersion, there are diffraction peaks present, assigned to hydroxyapatite in addition to the ones of sodium calcium silicate as well as an underlying amorphous halo.

4.2. Åbo Glasses

4.2.1. Definition & Glass Composition

The Åbo glasses are a combination of Brink et al. [9] and Fagerlund et al. [20] glass compositions, see Table 10.

Table 10: Nominal glass composition of the Åbo glasses in mol% with bioactivity classification: orange- high bioactivity, purple- medium bioactivity, black- inert glasses. JBS refers to the dynamic dissolution data, see chapter 4.2.3

Glass name	Brink in-vivo	Dynamic dissolution	Bioactivity	SiO_2	Na_2O	P_2O_5	CaO	K_2O	MgO	B_2O_3
17-93	bioactive	JBS group A/B	high	57	18.4	1.8	15.8	6.1	0	0.9
17-92	bioactive	JBS group A/B	high	54.6	20.3	1.3	11.2	6.7	3.1	2.7
206		Fagerlund group A	high	53	12.4	1.1	22.5	9.5	0	1.5
14-93	bioactive		high	54.1	17.8	0.9	18.6	3.9	3	1.8
19-93	bioactive		high	56.2	15.4	1.8	12.5	8.1	3.2	2.7
3-92	bioactive		high	53.6	25	1.3	11	3.3	3.1	2.7
15-92	bioactive		high	42.1	15.7	2.7	23.1	10.3	3.2	2.8
306		Fagerlund group A	high	50.4	24	1.1	23.3	0	0	1.1
9-93	layer	JBS group B	medium	56.2	12.1	0.9	12.3	10	7.8	0.9
20-92	layer	JBS group A/B	medium	52.2	15.2	0	16.8	10	3.1	2.7
1-98		Fagerlund group B	medium	53.8	5.9	0.9	23.9	7.1	7.6	0.9
106		Fagerlund group B	medium	51.4	5.9	1.7	24.9	7.9	8.1	0.2
18-93	layer		medium	53.2	17.5	0	21.5	3.8	3	0.9
12-92	layer		medium	52.8	19.7	0	10.9	6.5	7.6	2.6
10-92	inert	JBS group D	inert	66.1	10	1.3	16.6	3.3	0	2.7
6-92	inert	JBS group D	inert	59.4	9.8	1.3	16.2	3.2	7.5	2.6
1606		Fagerlund group C	inert	67.4	5.1	1.8	17	6.9	0	1.8
1406		Fagerlund group C	inert	62.2	5.4	0.3	17.8	7.3	5.2	1.8
1806		Fagerlund group C	inert	64.8	17.8	0	16	0	0.1	1.3
1-92	inert		inert	55.3	14.1	0	20.8	0	7.2	2.5
15-93	inert		inert	58.8	8.8	0	21.7	5.8	3	1.8

Whereas Brink et al. investigated the in-vivo bioactivity of glasses, Fagerlund et al. carried out dynamic dissolution experiments. So, for most of the Åbo glasses, one information is available, either the in-vivo bioactivity performance or the dynamic dissolution data. For six Brink glasses, dynamic dissolution tests were carried out additionally, see chapter 4.2.3.

Brink et al. state four groups: “bioactive”, the formation of a “silica”-rich layer, “layered structure” and “inert” to classify the in-vivo test results of their glasses. “Bioactive” stands for bonded to the bone. In the “layered structure” silica and calcium phosphate was detected and “inert” stands for no reaction. Per glass, 4 to 5 samples were tested. Whereas “inert” was a clear result, for the other group's mixtures regarding the bioactivity results occurred. For example, for glass 20-92 two tested samples present a silica-rich layer and two a layered structure. For glass 9-93, one sample show a silica-rich layer, whereas three bond to bone. Therefore, the glass samples, which show a silica-rich layer or a layered structure are assigned to the group layer here, leading to the existence of three groups: inert, layer and bioactive, see Table 10. Fagerlund et al. uses group A (fast), B (medium), C (slow) and D (inert) to categorise their dynamic dissolution test results. For the following six glasses, information regarding in-vivo performance as well as dynamic dissolution test results is available: 17-93 (bioactive & A/B), 17-92 (bioactive & A/B), 9-93 (layer & B), 20-92 (layer & A/B), 10-92 (inert & D), 6-92 (inert & D), see Table 10. A/B stands for a mixture out of pattern A and pattern B. We saw a correlation of in-vivo group “inert” with dynamic dissolution group D for both tested glasses. Dynamic dissolution group C was not involved. Whereas the group “layer” seemed to correlate with group B, a mixture pattern A/B in dynamic dissolution could be associated with “bioactive” (for the glasses 17-93 & 17-92) or with “layer” (for glass 20-92). This comparison showed that there is a correlation: high number of ions released is associated with high in-vivo bioactivity, whereas a low number of ions released is associated with low in-vivo bioactivity. To combine the results of the dynamic dissolution tests with the in-vivo investigations, the following assumptions were made: fast dissolution ***(A) ≙ (highly) bioactive (1), medium dissolution (B) ≙ silica layer or layered structure (2), slow dissolution and inert (C & D) ≙ inert (3)***. In Table 10 the affiliation to the three groups is assigned: orange-high bioactivity, purple-medium bioactivity and black-inert.

The ***average amount in mol%*** and the standard deviation for SiO_2, P_2O_5 and B_2O_3 for the different bioactivity groups are presented in Figure 45.

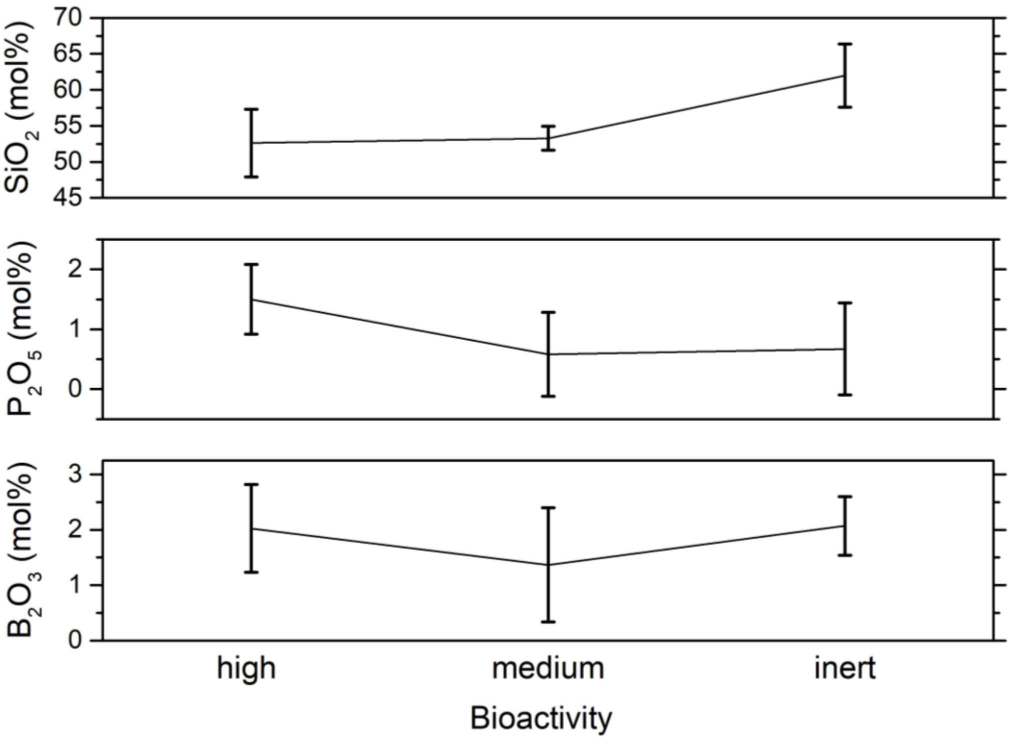

Figure 45: The amount of SiO_2, P_2O_5 and B_2O_3 presented for the different bioactivity groups: high, medium and inert. Lines are guides for the eye only.

With decreasing bioactivity, the amount of SiO_2 shows an increasing trend and the amount of P_2O_5 a decreasing one. Regarding the amount of B_2O_3, there is no difference between the groups.

The nominal and the via ***XRF*** analysed glass composition of glasses 9-93, 6-92 and 3-92 is presented in Figure 46.

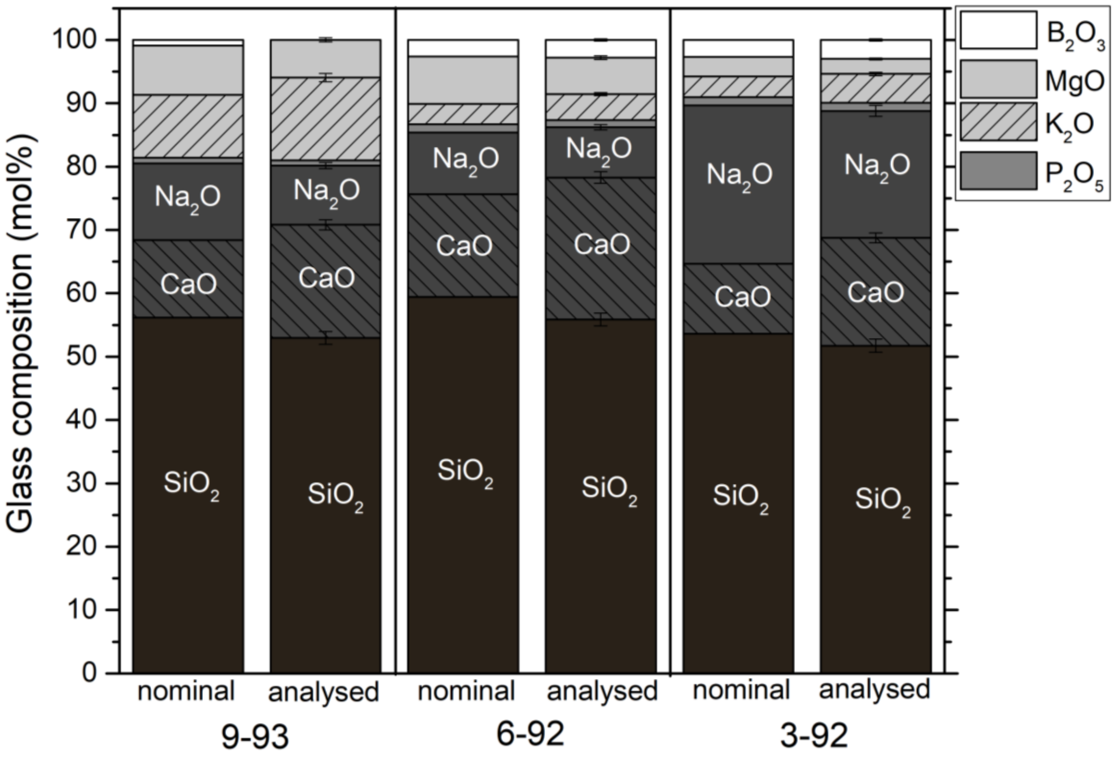

Figure 46: Nominal and via XRF analysed glass composition of glasses 9-93, 6-92 and 3-92.

As mentioned in chapter 4.1.1., each error bar in the analysed glass composition refers to the uncertainty of the XRF measurement and for the computation of the error, the traces like Al_2O_3 and TiO_2 were not considered. Whereas the amount of SiO_2, Na_2O and MgO is lower in the analysed composition in comparison to the nominal composition, the amount of CaO and K_2O is higher in the analysed one. The amount of P_2O_5 is slightly lower in the analysed composition for glasses 9-93 and 6-92, whereas for glass 3-92 it is the same as in the nominal one. For glass 9-93 no B_2O_3 could be detected via XRF, however for the other two glasses slightly more B_2O_3 was detected than expected from the nominal glass composition.

A ***shadow image*** of a glass slide with intensive striae (6-92) and of a glass slide without pronounced striae (1806) is shown in Figure 47 A & B. The Raman line scan of glass slide 6-92 is presented in Figure 53.

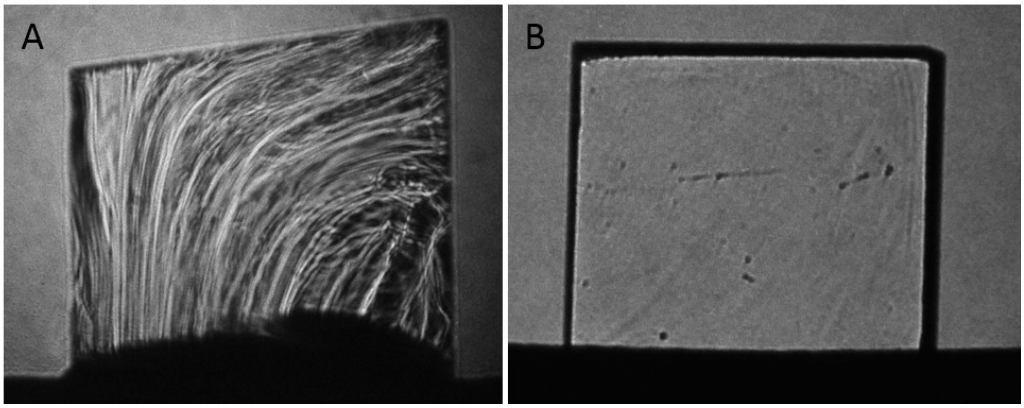

Figure 47: Shadow images of a glass slide with pronounced striae (A) 6-92 and of a glass slide without pronounced striae (B) 1806.

4.2.2. Glass Structure & Density

In the following section, the glasses of the series 45S5-B are partly included for comparison. Those glasses are ranged in the group high bioactivity.

The ***XRD*** results of the Åbo glasses are shown in Figure 48. All XRD spectra exhibit a broad halo with its maximum between 28° and 32°.

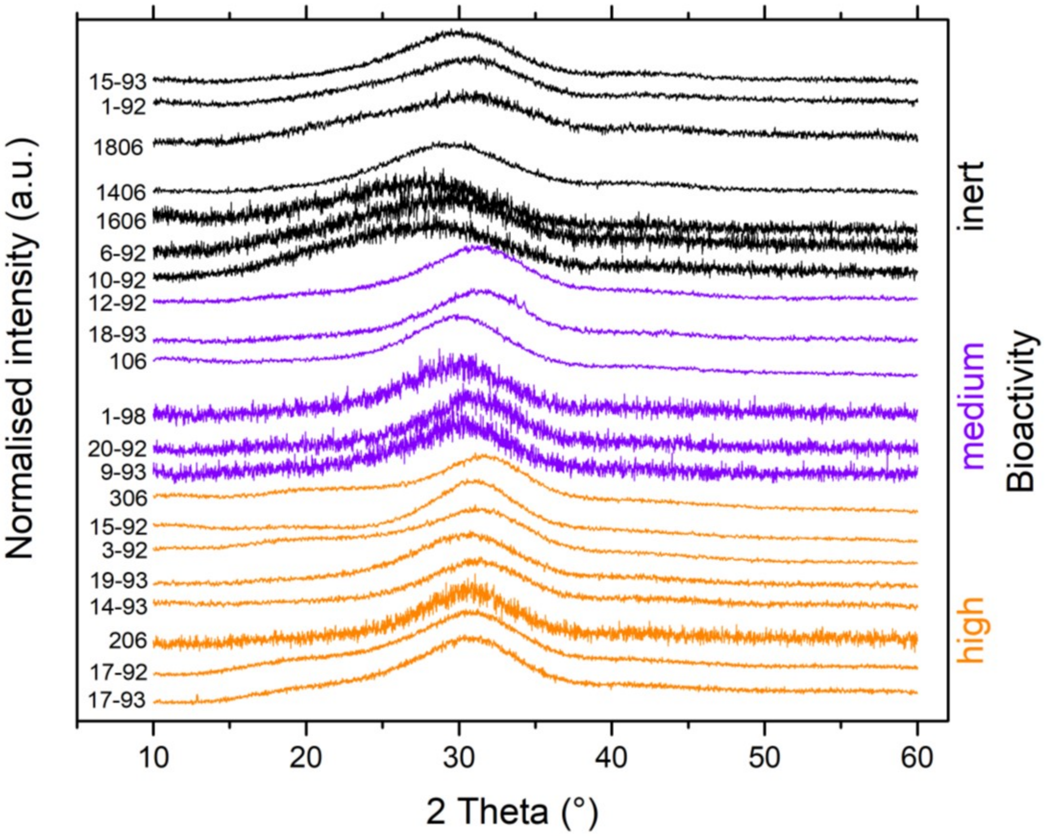

Figure 48: XRD results of the Åbo glasses.

The ^{31}***P MAS NMR*** spectra from glasses 17-93, 17-92, 206, 9-93, 1-98, 10-92, 1606 exhibit two overlapping peaks for every glass, Figure 49.

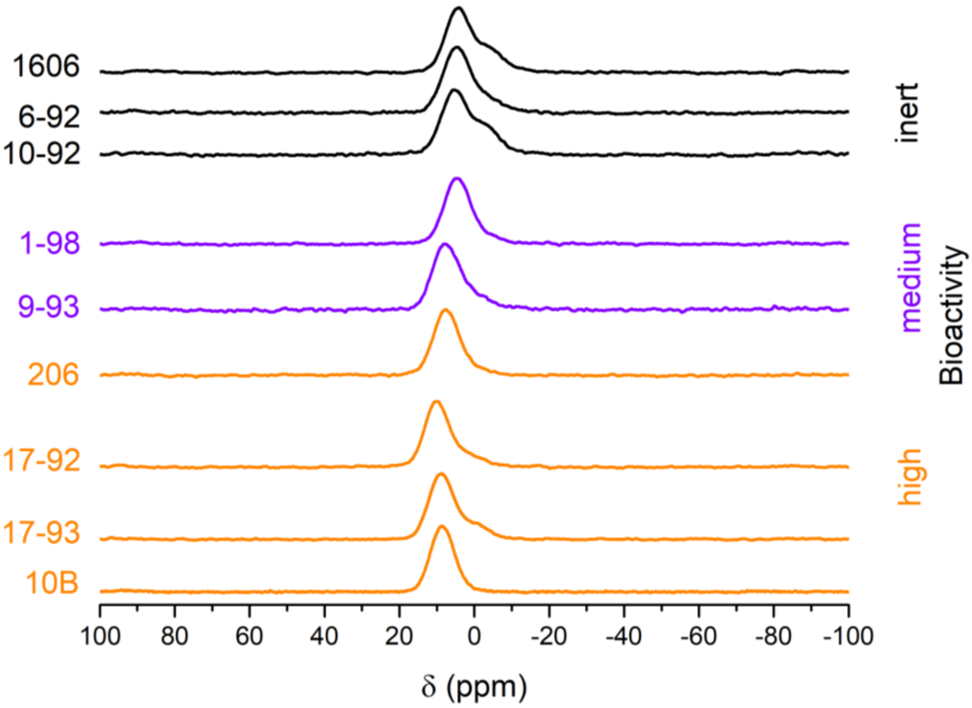

Figure 49: P-31 MAS NMR of the Åbo glasses 17-93, 17-92, 206, 9-93, 1-98, 10-92, 6-92 and 1606 and glass 10B, exemplarily from series 45S5-B.

Table 11 shows the positions as well as the relative amount of the two overlapping peaks in ^{31}P MAS NMR.

Table 11: Position and the relative amount of the two peaks from Figure 49.

Glass	Peak 1	Peak 2
	ppm/ (%)	ppm/ (%)
1606	4.68 (64)	-3.28 (36)
6-92	5.08 (68)	-1.13 (32)
10-92	5.43 (64)	-2.97 (36)
1-98	4.64 (86)	-3.23 (14)
9-93	8.23 (57)	2.67 (43)
206	7.64 (88)	0.35 (12)
17-92	10.37 (48)	6.25 (52)
17-93	8.97 (76)	0.22 (24)
10B	8.49 (~100)	-

Whereas the peak with higher intensity exhibits a more positive chemical shift, the second peak with lower intensity is positioned on the right side of the first one, towards more negative chemical shift, Figure 49. The spectrum of glass 10B is included for comparison, as well.

^{11}B MAS NMR spectra from glasses 17-93, 17-92, 206, 9-93, 1-98, 10-92, 1606 and 10B are shown in Figure 50.

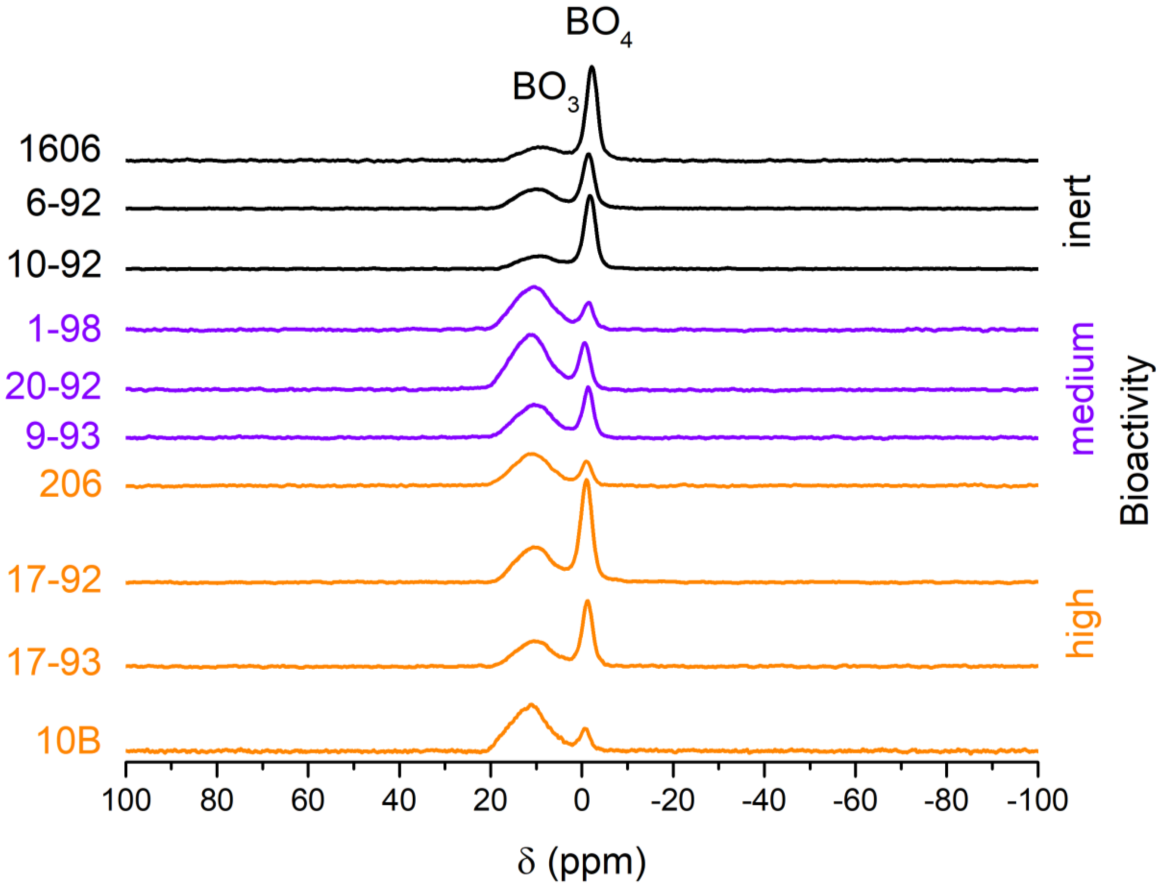

Figure 50: B-11 MAS NMR of the Åbo glasses 17-93, 17-92, 206, 9-93, 1-98, 10-92, 6-92, 1606 and glass 10B, exemplarily from series 45S5-B. Assignment acc. to MacKenzie [63].

The broad signal at about 17 ppm can be assigned to BO_3 and the sharper signal around -1/-2 ppm to BO_4 [63].

The positions, as well as the relative amount of the BO_3 and BO_4 peaks, is presented in Table 12.

Table 12: Position and the relative amount of the BO_3 and BO_4 MAS NMR peak from Figure 50.

Glass	BO_3	BO_4
	ppm/ (%)	ppm/ (%)
1606	15.82 (29)	-2.17 (71)
6-92	16.69 (50)	-1.42 (50)
10-92	16.40 (36)	-1.75 (64)
1-98	17.34 (86)	-1.35 (14)
20-92	17.92 (80)	-0.67 (20)
9-93	17.04 (72)	-1.37 (28)
206	17.33 (84)	-1.04 (16)
17-92	16.54 (50)	-0.97(50)
17-93	16.47 (56)	-1.22 (44)
10B	18.29 (86.7)	-0.72 (13.3)

Noticeably is the fact, that not one species is dominant for all glasses. The amount of BO_3 lies between 29 % and 86 % and the BO_4 content between 71 % and 14 %, depending on the investigated glass.

The ***Fourier transform infrared spectroscopy*** spectra of the Åbo glasses are presented in Figure 51: in diagram A the highly bioactive Åbo glasses together with glass 45S5-10B, in diagram B the medium bioactive glasses and in diagram C the inert glasses. Diagrams with stacked spectra for each group can be found in Figure A 4, Figure A 6 and Figure A 8 (appendix).

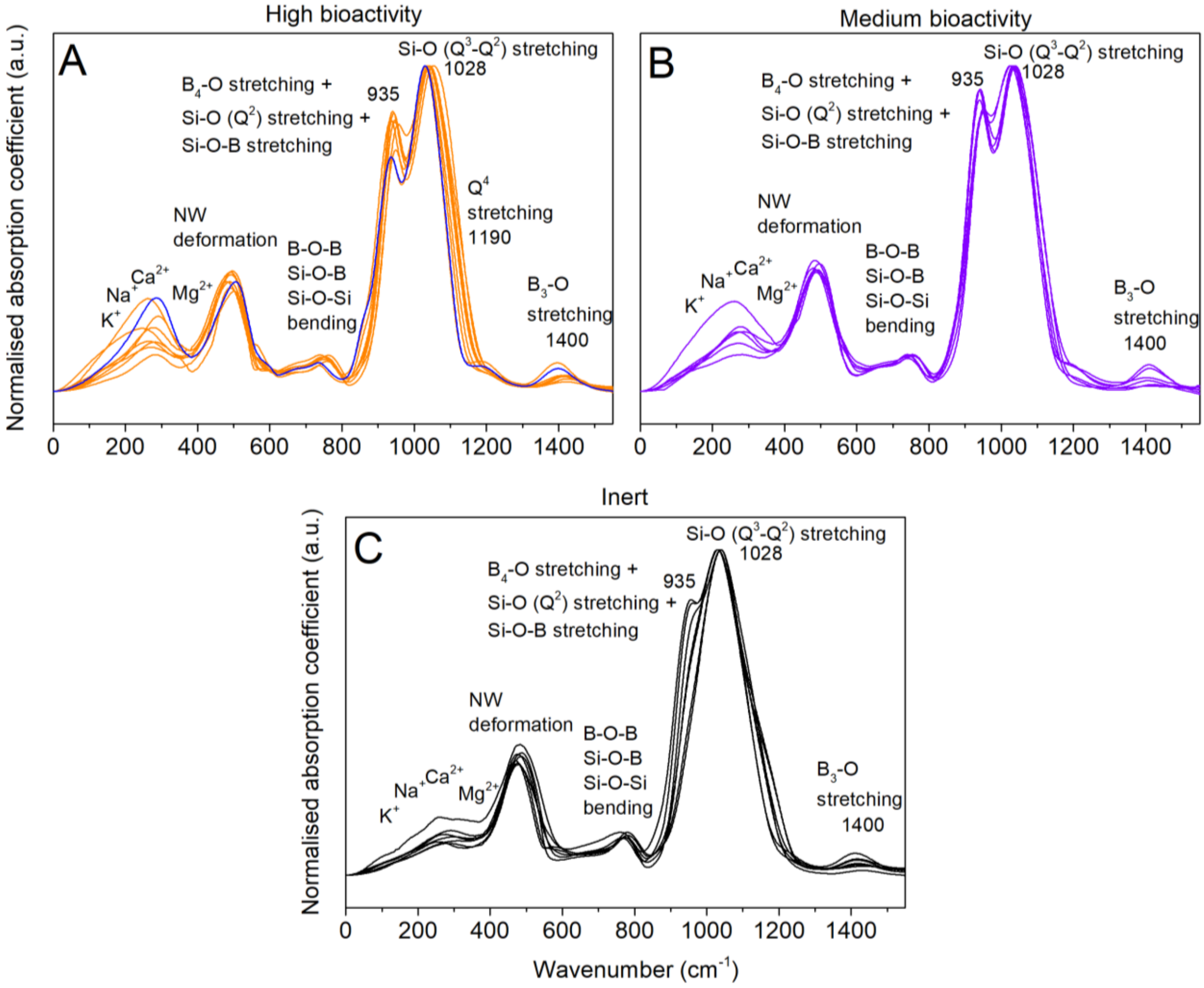

Figure 51: FTIR spectra of the Åbo glasses. In diagram A the glasses with high bioactivity and glass 45S5-10B (in blue, as representative from the glass series 45S5-B), in diagram B the glasses with medium bioactivity and in diagram C the inert glasses are presented. The assignment of the bands at ~200 cm^{-1} (Na$^+$), ~500 cm^{-1} (network deformation), ~670 cm^{-1} (Si-O-B bending), ~735 cm^{-1} (B-O-B deformation), ~780 cm^{-1} (Si-O-Si bending), 935 cm^{-1} (overlapping band of Si-O-B stretching, B_4-O stretching and Q^2 stretching) and 1190 cm^{-1} (Q^4 stretching) acc. to Kamitsos et al. [64]. The assignment of the band at ~280 cm^{-1} (Ca^{2+}) acc. to Kamitsos [52] and of the bands at 600-800 cm^{-1} (bending of borate segments) and 1440 cm^{-1} (B_3-O stretching) acc. to Kamitsos et al.[65]. Vibrations of K$^+$ are expected at about 170 cm^{-1} [81] and of Mg^{2+} at about 400 cm^{-1} [52]. Explanations regarding the assignment of the band at 1028 cm^{-1} to stretching of Q^3-Q^2 can be found in the chapter 5.1.

In the spectra of the inert glasses, the shoulder at 935 cm^{-1} is less pronounced in comparison to the high and medium bioactive glasses. At this position vibration of Si-O-B stretching, Si-O (Q^2 stretching) and B_4-O [64] stretching overlap. The intensity of the B_3-O stretching band at 1400 cm^{-1} is similar in all three groups, Figure 51.

The ***Raman*** spectra of the Åbo glasses are presented in Figure 52. Normalisation was done using the Q^2 stretching band at about 955 cm^{-1} [67]. Stacked spectra for the different groups are presented in Figure A 5, Figure A 7 and Figure A 9, (appendix).

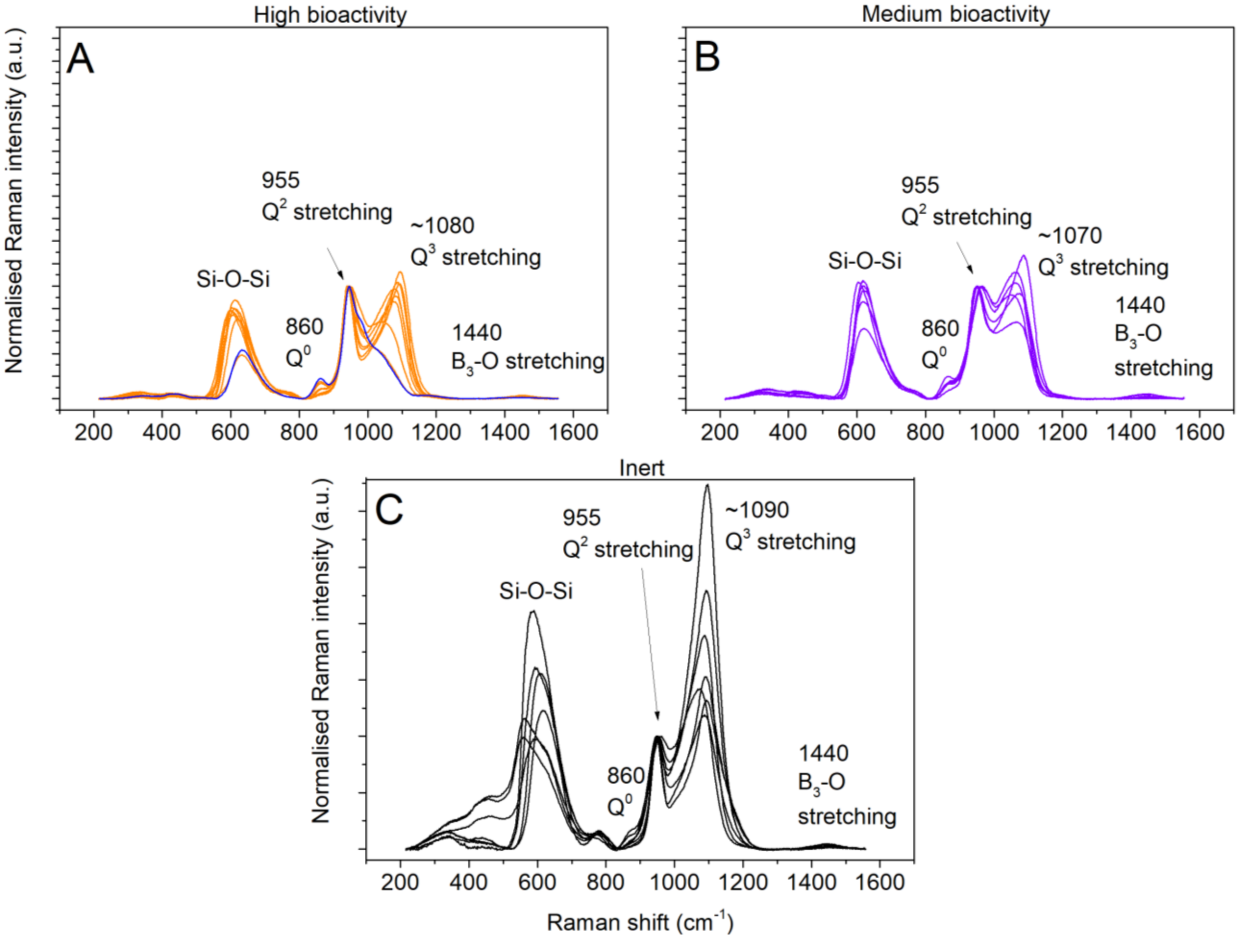

Figure 52: Raman spectra of the Åbo glasses. In diagram A the glasses with high bioactivity plus glass 45S5-10B (in blue, as representative of the glass series 45S5-B), in diagram B the glasses with medium bioactivity and in diagram C the inert glasses are shown. Band assignment of the Si-O-Si band at ~600 cm-1, the Q^0 stretching band at 860 cm^{-1} according to Kamitsos et al. [64]. The band at 955 cm^{-1} is assigned to Q^2 stretching and the band at~1080 cm^{-1} is assigned to Q^3 stretching acc. to McMillan [67] and Kamitsos et al. [64]. The band at 1440 cm^{-1} is assigned to B_3-O stretching acc. to Kamitsos et al [64] and Angeli et al. [82].

Diagram A shows the Raman spectra of the highly bioactive Åbo glasses together with 45S5-10B, while in diagram B the spectra of the medium bioactive glasses and in diagram C the inert glasses are presented. The high and medium bioactive glasses exhibit similar Raman spectra. However, for all inert glasses, the intensity of the bands at 600 cm^{-1} (delocalised vibration of Si-O-Si) [64] and 1090 cm^{-1} (Q^3 stretching) [64, 67] are remarkably higher in comparison to the other groups.

A ***Raman line scan*** spectrum from glass 6-92, which exhibited intensive striae, is presented in Figure 53. Normalisation was done using the band at about 955 cm^{-1} (Q^2 stretching) as well. Along the line scan, the height of the band at ~1090 cm^{-1} (Q^3 stretching) varies relative to the Q^2 stretching band. The ratio of the Q^2 to the Q^3 band is between 50 and 62 %.

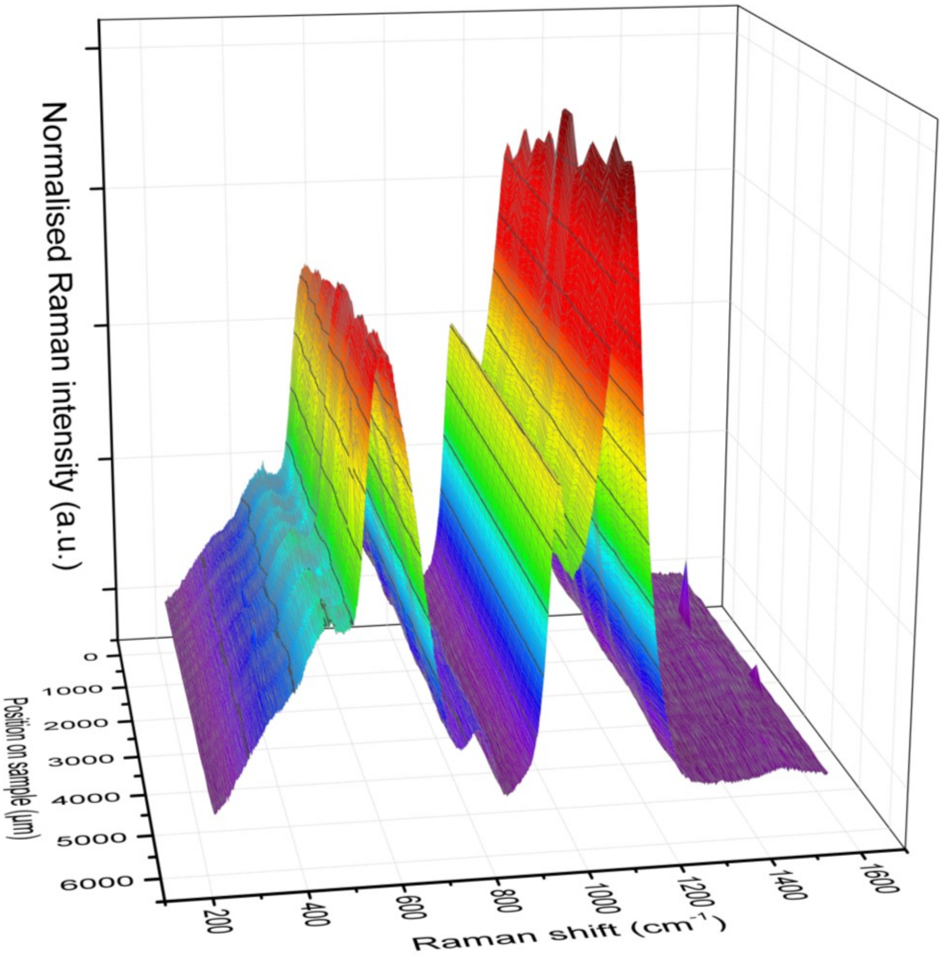

Figure 53: Raman line-scan of glass 6-92 normalised to the band at ~950 cm^{-1}.

The ***density*** of the Åbo glasses and of the glass series 45S5-B, assorted regarding bioactivity, is presented in Figure 54. The names of all Åbo glasses are assigned in the Figure, whereas for glass series 45S5-B, of glass 45S5 and 25B only. The other glasses of series 45S5-B are between 45S5 and 25B, see also Figure 22.

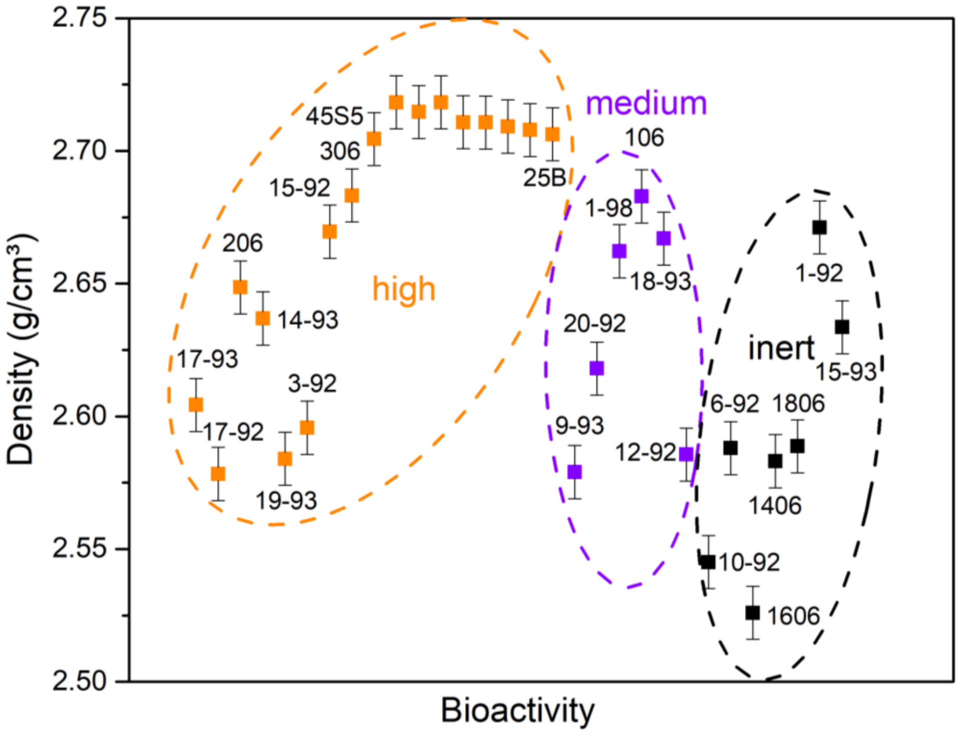

Figure 54: Density of the Åbo glasses and of the glass series 45S5-B. For the Åbo glasses, the glass names are assigned, for the glass series 45S5-B, 45S5 and 25B only. The other glasses of series 45S5-B are between 45S5 and 25B, see also Figure 22.

The density of the Åbo glasses is between 2.53 and 2.72 g/cm³, Figure 54 while no significant difference between the bioactivity groups can be seen. Overall, there is a slight trend to higher density values in the bioactive glasses, and to lower density values in the inert glasses.

4.2.3. Dynamic Dissolution Experiments

The initial dissolution of the glasses 17-93, 17-92, 9-93, 20-92, 10-92 and 6-92 was investigated via dynamic dissolution experiments. The dissolution patterns were assigned according to Fagerlund et. al [20] by using absolute ion concentrations, see Table 13. A detailed explanation regarding the group assignment can be found in chapter 4.2.1.

Table 13: Patterns of initial dissolution (A, B, C or D) acc. to Fagerlund et al. [20] of glasses 17-93, 17-92, 9-93, 20-92, 10-92 and 6-92 investigated via dynamic dissolution experiments.

Glass	Dissolution pattern acc. to Fagerlund et al. [20]
17-93	A/B
17-92	A/B
9-93	B
20-92	A/B
10-92	D
6-92	D

The results of the dynamic dissolution experiments on glasses 17-93, 17-92, 9-93, 20-92, 10-92 and 6-92 are plotted as normalised ion concentrations in Figure 55.

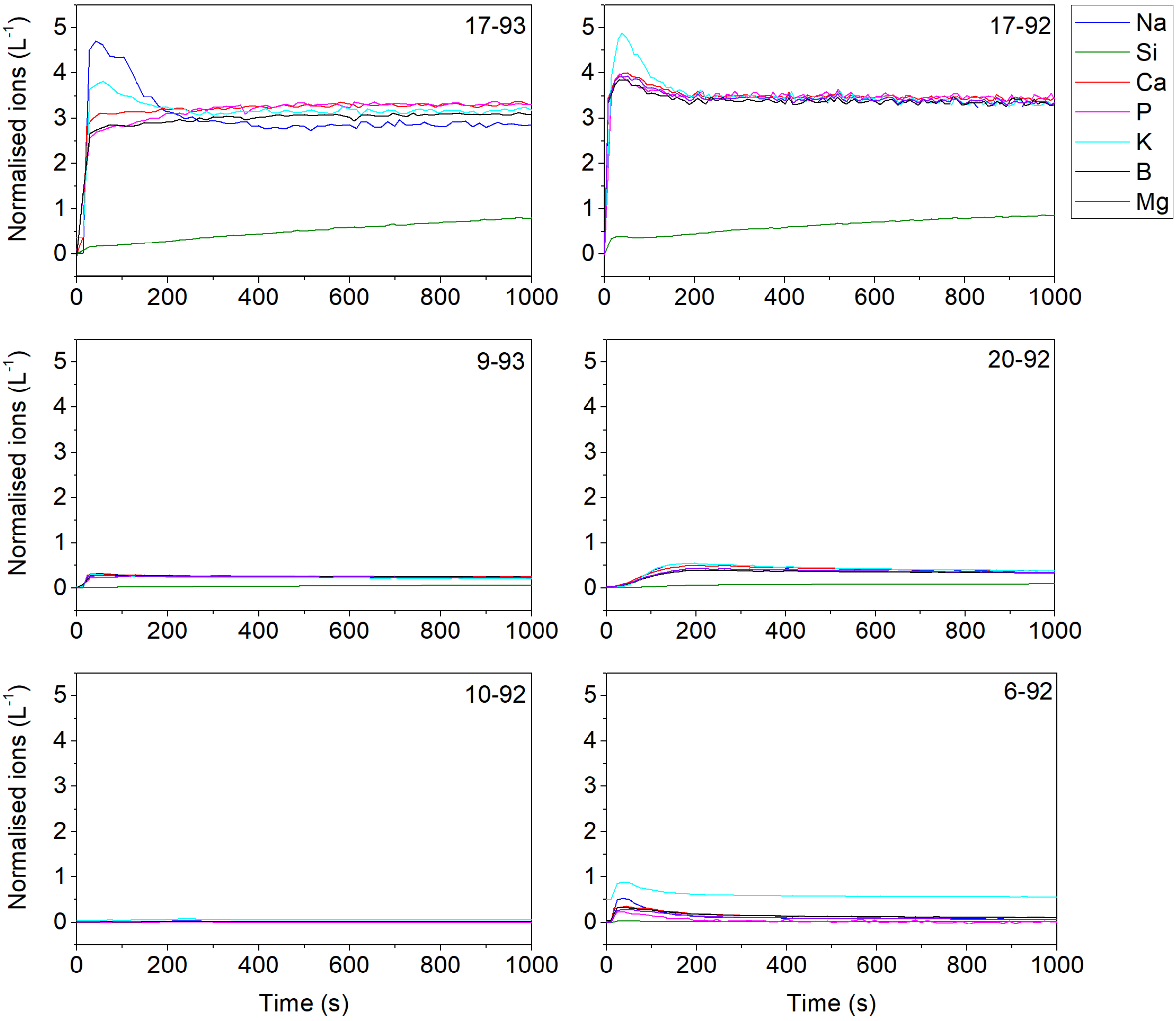

Figure 55: Results from dynamic dissolution experiments on glasses 17-93, 17-92, 9-93, 20-92, 10-92 and 6-92 immersed in Tris buffer solution showing the normalised concentration of ions in solution versus time.

For glass 17-92 the sodium concentration was partially higher than the detection limit [20] and is therefore not available. The ion concentration of glass 17-93 is in the same range as the one of glass 17-92: apart from silicon, all elements are present around 2-5 L^{-1}. The other four glasses show an ion concentration below 1 L^{-1} for all elements.

The normalised concentration of potassium versus time for all six investigated glasses is presented in Figure 56.

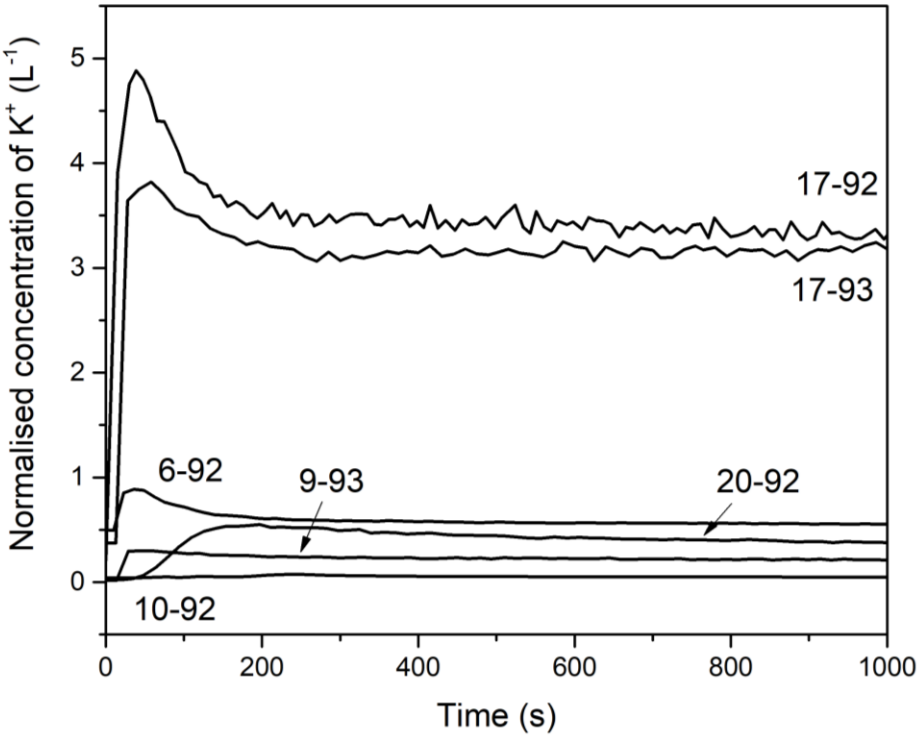

Figure 56: Normalised ion concentration of potassium (K$^+$) versus time plotted for the glasses 17-93, 17-92, 9-93, 20-92, 10-92 and 6-92.

For the other ions, the detailed results are presented in Figure A 10 (Si), Figure A 11 (Ca), Figure A 12 (P), Figure A 13 (B) and Figure A 14 (Mg).

4.2.4. Thermal Properties

The ***glass transition temperatures (T_g)*** obtained via ***Dilatometry*** measurements for the Åbo glasses and the glass series 45S5-B ordered by bioactivity are presented in Figure 57. For the highly bioactive glasses, the T_g is between 439 and 530°C. However, the ones of the inert glasses are significantly higher, between 556 and 607°C. Four of the medium bioactive glasses exhibit a T_g in the range of the highly bioactive ones, whereas two glasses exhibit a T_g in the range of the inert glasses. The group of the medium bioactive glasses lies in the range between 453 and 584°C and is situated between the other two groups.

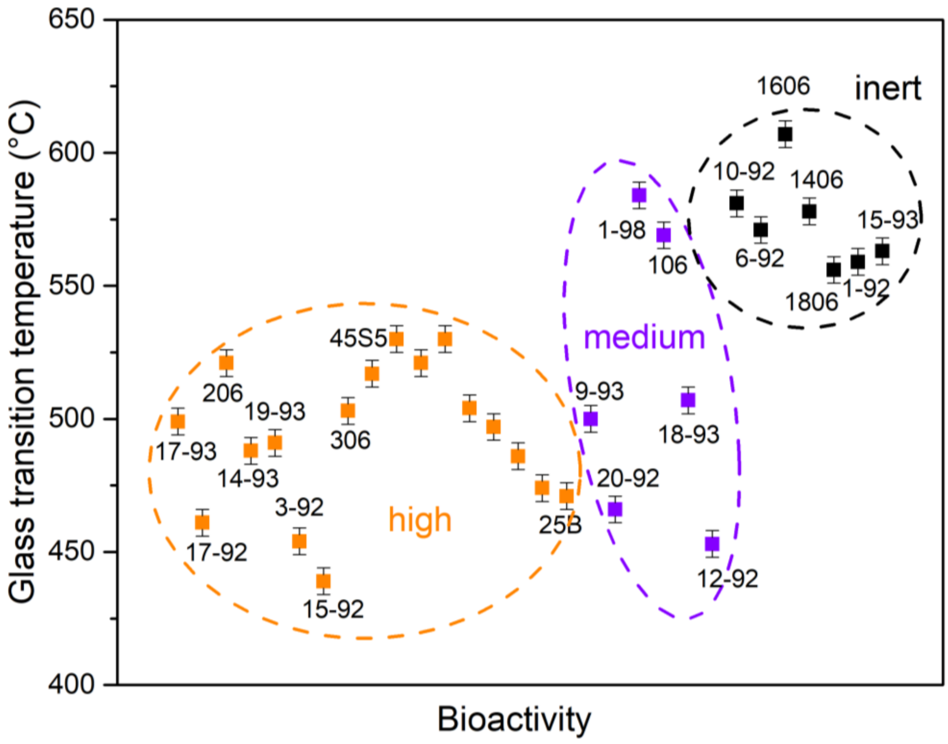

Figure 57: Glass transition temperature for the Åbo glasses and glass series 45S5-B.

The ***thermal expansion coefficient*** (α) for the Åbo glasses and for the glass series 45S5-B according to their bioactivity is presented in Figure 58.

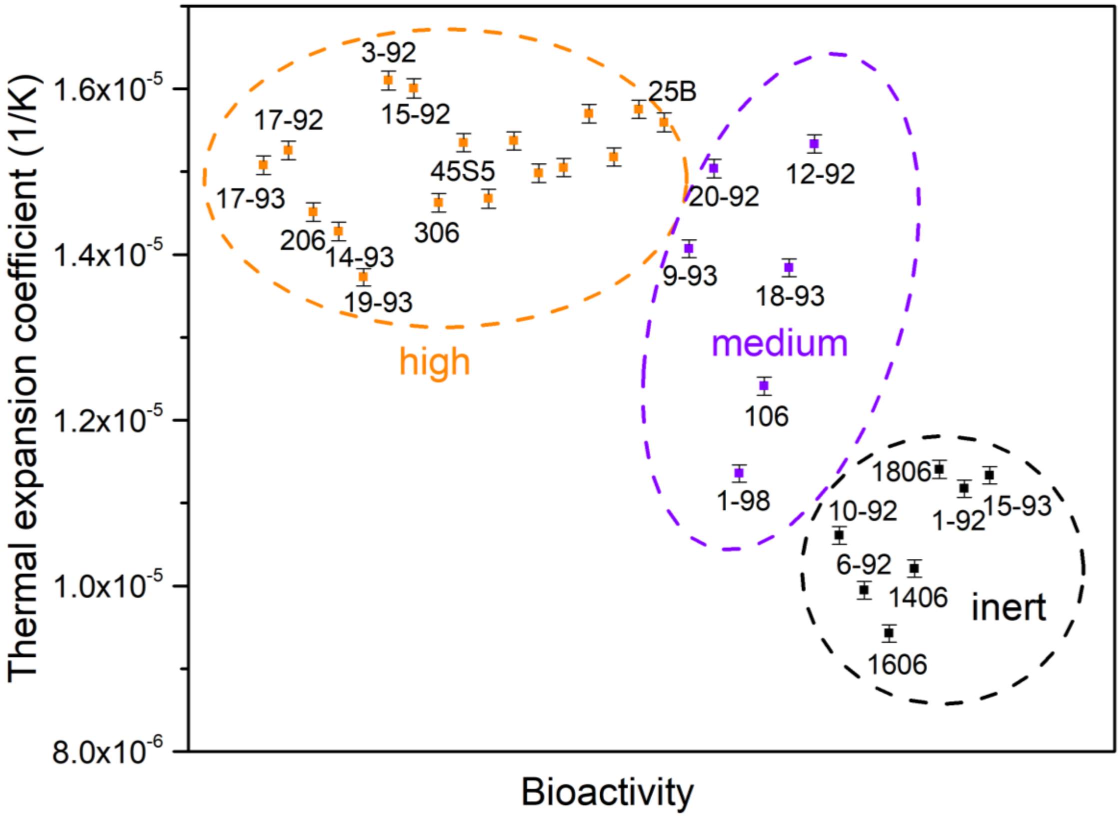

Figure 58: Thermal expansion coefficient (1/K) for the Åbo glasses and the 45S5-B series.

The glasses with high bioactivity exhibit an average α of about 1.5*10^{-5} 1/K, while α of the glasses of the inert glasses is significantly lower, on average about 1.0*10^{-5} 1/K. The α range of the medium bioactive glasses is located in between.

The shadow images upon heating obtained using ***heating microscopy*** are shown exemplarily for glass 6-92 in Figure 59. This method is useful to investigate the viscosity (η) behaviour of glass upon heating.

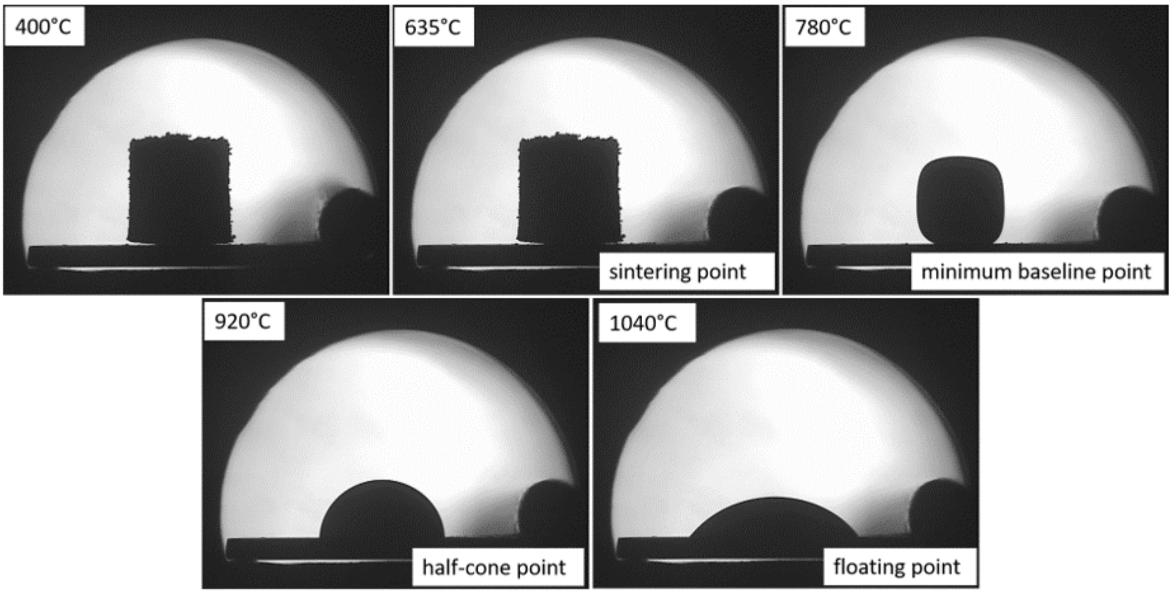

Figure 59: Shadow images upon heating of the glass powder pellet using heating microscopy, here exemplarily for glass 6-92.

Assigned characteristic points are the sintering point (SP), the minimum baseline point (MBP), the half-cone point (HCP) as well as the floating point (FP), see Table 14.

Table 14: Determined temperatures of the characteristic points upon heating for several Åbo glasses.

Glass name	Sintering point (°C)	Minimum baseline point (°C)	Half-cone point (°C)	Floating point (°C) @ γ = 45°	
206	575	-	990	γ > 45°	
306					devitrified
1-98	650	805	1020	1055	
106	650	810	1070	1110	
1606	665	860	1040	γ > 45°	
1406	640	810	1055	γ > 45°	
1806	615	800	-	1015	

At the SP the glass powder compact starts to densify and at the MBL the contact with the surface (the baseline) is minimal. At the HCP the sample has the shape of a hemisphere and at the FP the sample has floated out. The complete data set of the temperatures of the characteristic points for all measured glasses in comparison with the values determined by Brink [48] is presented in Table 15.

Table 15: Overview of the determined temperatures for the characteristic shapes upon heating for several Åbo glasses. The ones taken from literature [48] are denoted by "_Brink".

Glass name	Sintering point (°C)	Minimum baseline Point (°C)	Half-cone point (°C)	Floating point (°C) @ 45°	
17-93	555	-	955	995	
17-93_Brink	535	745	910	970	
17-92	500	-	890	900	
17-92_Brink	525	790	930	955	
206	575	-	990	γ > 45°	
14-93	560	-	1010	1020	
14-93_Brink	555	890	950	985	devitrified
19-93	540	700	860	915	
19-93_Brink	550	720	865	965	
3-92	510	-	-	930	
3-92_Brink	525	875	920	930	devitrified
15-92					devitrified
15-92_Brink	530	955	995	1010	devitrified
306					devitrified
9-93	540	700	860	920	
9-93_Brink	560	715	880	990	
20-92	515	-	960	970	
20-92_Brink	535	875	975	1010	devitrified
1-98	650	805	1020	1055	
106	650	810	1070	1110	
18-93					devitrified
18-93_Brink	570	1040	1120	1125	
12-92	490	-	910	925	
12-92_Brink	520	875	950	995	
10-92	650	820	935	1075	
10-92_Brink	595	825	955	1060	
6-92	635	780	920	1040	
6-92_Brink	595	785	870	1005	
1606	665	860	1040	γ > 45°	
1406	640	810	1055	γ > 45°	
15-93_Brink	625	775	1070	1095	
1-92_Brink	605	760	1065	1085	
1806	615	800	-	1015	

Whereas the HTM investigations were carried out at a constant heating rate of 5 K/min, Brink used a heating rate up to 12 K/min. The particle size was the same: <125 µm. Whereas a slower heating rate would lead to a shift of the characteristic points to lower temperatures, a faster heating rate would lead to a shift of the characteristic points to higher temperatures. Taking the error regarding the reproducibility of the temperatures into account, ± 15-30 K [48] and the different heating rates, the results can be seen as equal.

4.2.5. Mathematical Models

The results of the application of the ***modified Andersson model*** [48] on the glasses, subdivided into Brink glasses and Fagerlund glasses are shown in Table 16. More details regarding the models can be found in chapter 3.2.5. In yellow the agreement of the bioactivity with the reaction number is highlighted.

Table 16: Results of the application of the modified Andersson model on the Brink and Fagerlund glasses. Highlighted in yellow: agreement of the bioactivity with the reaction number.

Glass name	Bioactivity	Reaction number (modified Andersson model)
Brink glasses		
17-93	high	6.91 ± 0.42
17-92	high	5.40 ± 0.42
14-93	high	6.21 ± 0.42
19-93	high	4.79 ± 0.42
3-92	high	5.40 ± 0.42
15-92	high	4.31 ± 0.42
9-93	medium	7.08 ± 0.42
20-92	medium	5.78 ± 0.42
18-93	medium	6.93 ± 0.42
12-92	medium	5.65 ± 0.42
10-92	inert	0.55 ± 0.42
6-92	inert	2.09 ± 0.42
15-93	inert	4.68 ± 0.42
1-92	inert	2.79 ± 0.42
Fagerlund glasses		
206	high	7.05 ± 0.42
306	high	6.99 ± 0.42
1-98	medium	not in the validity range of the model
106	medium	not in the validity range of the model
1406	inert	3.69 ± 0.42
1606	inert	2.25 ± 0.42
1806	inert	3.01 ± 0.42

For the modified Anderson model, there is an agreement between the bioactivity value and the calculated reaction number for about 36 % of the relevant Åbo glasses. As two glasses (1-98 and 106) are not in the validity range of the model, see Table A 1 in the appendix, they have not been considered.

The ***Index of surface activity*** of a glass (ISA) [9] calculated for the Brink and Fagerlund glasses is plotted in Table 17. In yellow the agreement of the result of the calculation with the bioactivity is highlighted.

Table 17: Results of the application of the ISA model on the Brink and Fagerlund glasses. Highlighted in yellow: agreement of the bioactivity with the ISA number.

Glass name	Bioactivity	ISA
Brink glasses		
17-93	high	3.58 ± 0.44
17-92	high	3.57 ± 0.44
14-93	high	3.53 ± 0.44
19-93	high	4.33 ± 0.44
3-92	high	3.57 ± 0.44
15-92	high	3.77 ± 0.44
9-93	medium	3.21 ± 0.44
20-92	medium	2.63 ± 0.44
18-93	medium	2.76 ± 0.44
12-92	medium	2.42 ± 0.44
10-92	inert	1.44 ± 0.44
6-92	inert	1.29 ± 0.44
15-93	inert	1.23 ± 0.44
1-92	inert	0.38 ± 0.44
Fagerlund glasses		
206	high	3.72 ± 0.44
306	high	not in the validity range of the model
1-98	medium	not in the validity range of the model
106	medium	not in the validity range of the model
1406	inert	0.92 ± 0.44
1606	inert	0.84 ± 0.44
1806	inert	1.32 ± 0.44

For the ISA model, the agreement between the bioactivity and the calculated index of surface activity is about 89 % for the relevant Åbo glasses. As three glasses (306, 1-98 and 106) are not in the validity range of the model, see Table A 2 in the appendix, they have not been considered.

The results of the ***linear mathematical models*** are shown in Table 18. In the first column of Table 18, the glass names and the defined bioactivity value for the model generation (1: bioactive, 2: medium and 3: inert) are plotted. In the second (third…) column the regression bioactivity values (rBA) for the linear mathematical model, which was developed using all glasses apart from 17-93 (17-92…) are given. Finally, in the last column, the rBA from the model, which was developed by using all glasses is shown. The standard deviation, as well as the R² value (coefficient of determination), is plotted for each model in the table below as well. The agreement of the regression value with the bioactivity value is highlighted in yellow.

Table 18: Regression bioactivity value (rBA) accessed with seven linear mathematical models. The standard deviation and the R² value (coefficient of determination), is plotted for each model in the table below additionally. Highlighted in yellow: agreement of the regression value with the bioactivity value.

Glass name (BA value)	***Model without glass… leads to a regression bioactivity value (rBA) of…***						***Model all glasses***
Brink glasses	***17-93***	***17-92***	***9-93***	***20-92***	***10-92***	***6-92***	
17-93 (1)		1.00	0.81	1.38	3.00	0.84	1.02
17-92 (1)	1.19		1.00	1.38	3.50	1.09	1.27
14-93 (1)	1.64	1.63	1.69	2.00	3.50	1.53	1.69
19-93 (1)	1.42	1.50	1.25	1.50	4.50	1.34	1.52
3-92 (1)	1.00	1.13	0.75	1.13	3.50	0.88	1.06
15-92 (1)	0.34	0.44	0.31	0.63	3.75	0.28	0.45
9-93 (2)	1.66	1.75		2.00	3.50	1.56	1.72
20-92 (2)	1.75	1.81	1.63		4.50	1.72	1.83
18-93 (2)	1.77	1.81	1.75	2.13	3.50	1.69	1.81
12-92 (2)	1.77	1.94	1.56	2.00	4.00	1.66	1.83
10-92 (3)	2.88	2.94	2.75	3.25		2.72	2.95
6-92 (3)	2.84	2.94	2.56	3.25	5.50		2.92
15-93 (3)	2.84	2.81	2.75	3.13	5.00	2.75	2.91
1-92 (3)	3.00	3.06	2.94	3.13	5.50	2.84	3.08
Fagerlund glasses							
206 (1)	1.38	1.44	1.25	1.75	3.50	1.34	1.45
306 (1)	0.95	1.00	0.81	1.50	2.50	0.84	0.98
1-98 (2)	2.42	2.50	2.25	2.88	4.50	2.31	2.47
106 (2)	1.80	1.81	1.44	2.00	3.50	1.69	1.88
1406 (3)	3.13	3.13	2.94	3.38	5.00	2.97	3.19
1606 (3)	2.72	2.69	2.50	3.25	4.00	2.63	2.80
1806 (3)	2.59	2.69	2.44	3.25	4.00	2.53	2.66
standard deviation	0.41	0.40	0.39	0.40	0.39	0.40	0.39
R²	0.86	0.87	0.88	0.87	0.87	0.86	0.87

The regression glass transition temperature values (rT_g) calculated with seven different linear mathematical models are shown in Table 19. In the first column the glass name is given, whereas in the second column the measured T_g can be found. The standard deviation and the R² value (coefficient of determination) is plotted for each model in the table below as well. The agreement of the model value with the Tg value is highlighted in yellow.

Table 19: Regression glass transition temperature values (rTg) accessed with seven linear mathematical models. The standard deviation and the R² value (coefficient of determination) is plotted for each model in the table below as well. Highlighted in yellow: agreement of the model value with the Tg value.

Glass name		***Model without glass… leads to a regression value for T_g (rT_g) of…***						***Model all glasses***
Brink glasses	***T_g***	***17-93***	***17-92***	***9-93***	***20-92***	***10-92***	***6-92***	
17-93	499		504	494	501	496	506	504
17-92	461	456		456	456	448	464	452
14-93	488	504	500	500	505	480	509	500
19-93	491	484	488	486	487	464	490	480
3-92	454	446	440	440	446	432	452	444
15-92	439	448	452	448	450	416	455	454
9-93	500	500	504		503	464	508	500
20-92	466	462	460	466		448	468	464
18-93	507	512	512	510	512	496	517	508
12-92	453	450	448	450	450	432	457	444
10-92	581	580	580	574	586		592	580
6-92	571	564	560	560	570	560		564
15-93	563	566	564	560	565	512	569	564
1-92	559	552	556	550	556	512	561	556
Fagerlund glasses								
206	521	508	504	502	508	480	514	512
306	503	492	484	490	494	480	500	496
1-98	584	568	564	566	573	544	578	572
106	569	568	568	564	570	528	573	568
1406	578	578	572	576	581	544	586	584
1606	607	600	604	592	603	592	608	596
1806	556	558	556	552	560	544	567	556
standard deviation		9	9	9	9	8	9	9
R²		0.98	0.98	0.98	0.98	0.98	0.98	0.98

Apart from the above-shown model results, ***Pearson´s coefficient of correlation*** with composition and ***Fisher discriminant ratio*** has been determined for nine selected Åbo glasses additionally, see Table 20.

Table 20: Pearson´s coefficient of correlation regarding composition and Fisher discriminant ratio were calculated for these nine selected Åbo glasses.

Glass name	Bioactivity
17-93	high
17-92	high
206	high
9-93	medium
20-92	medium
1-98	medium
10-92	inert
6-92	inert
1606	inert

The results of ***Pearson´s coefficient of correlation*** regarding composition on nine selected Åbo glasses are plotted in Figure 60 (FTIR), Figure 61 (Raman), Figure 62 (P^{31} MAS NMR) and Figure 63 (B^{11} MAS NMR). Pearson´s coefficient of correlation can be a value between 1 and -1. A pure positive (negative) correlation between the concentration of a component and a band/peak in the spectra is marked in red (blue) with value 1 (-1). Strong positive correlations between the FTIR or Raman band and the respective concentration of the component according to Pearson´s coefficient are summarised in Table 21 respectively Table 22. Regarding the NMR spectra, positive and negative correlations between the NMR peak and the concentration of the components are shown analogous in Table 23 and Table 24.

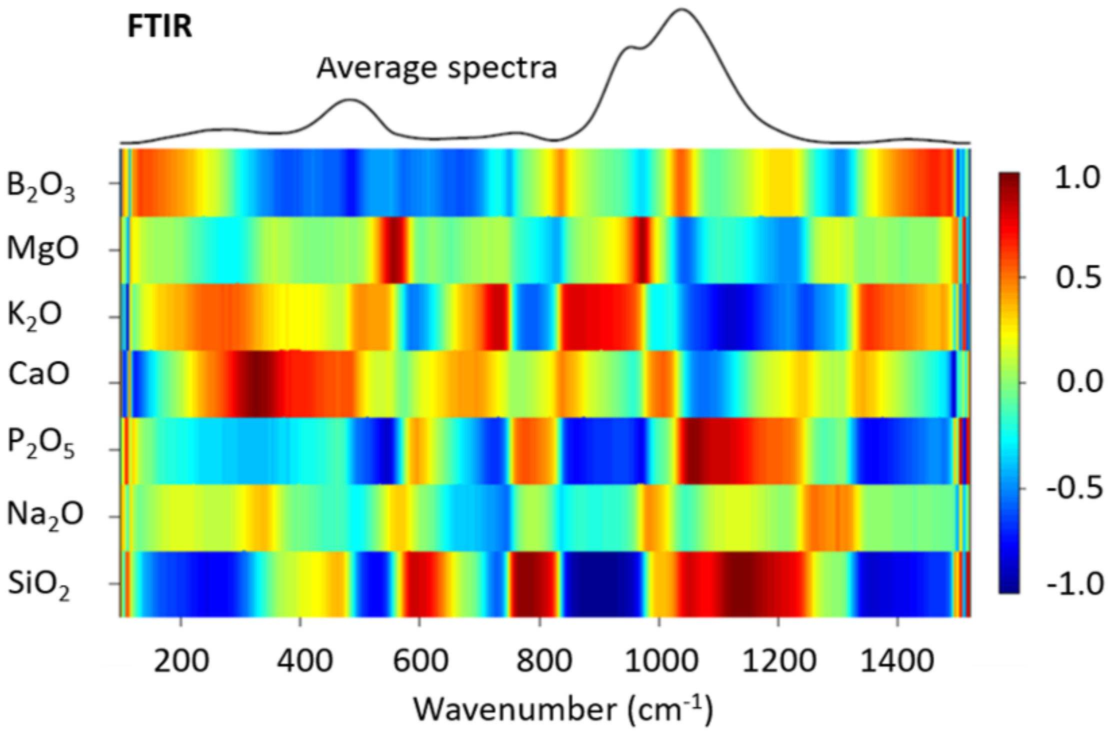

Figure 60: Pearson´s coefficient of correlation of the glass composition with the FTIR spectra from nine selected Åbo glasses.

Table 21: FTIR band positions, which show a strong positive correlation (>0.7) with the respective component according to Pearson´s coefficient.

Component	**FTIR band position (~, cm^{-1})**
MgO	530-570 & 930-980
K_2O	720-750 & 830-920
CaO	270-370
P_2O_5	1030-1100
SiO_2	560-630, 750-820 & 1030-1250

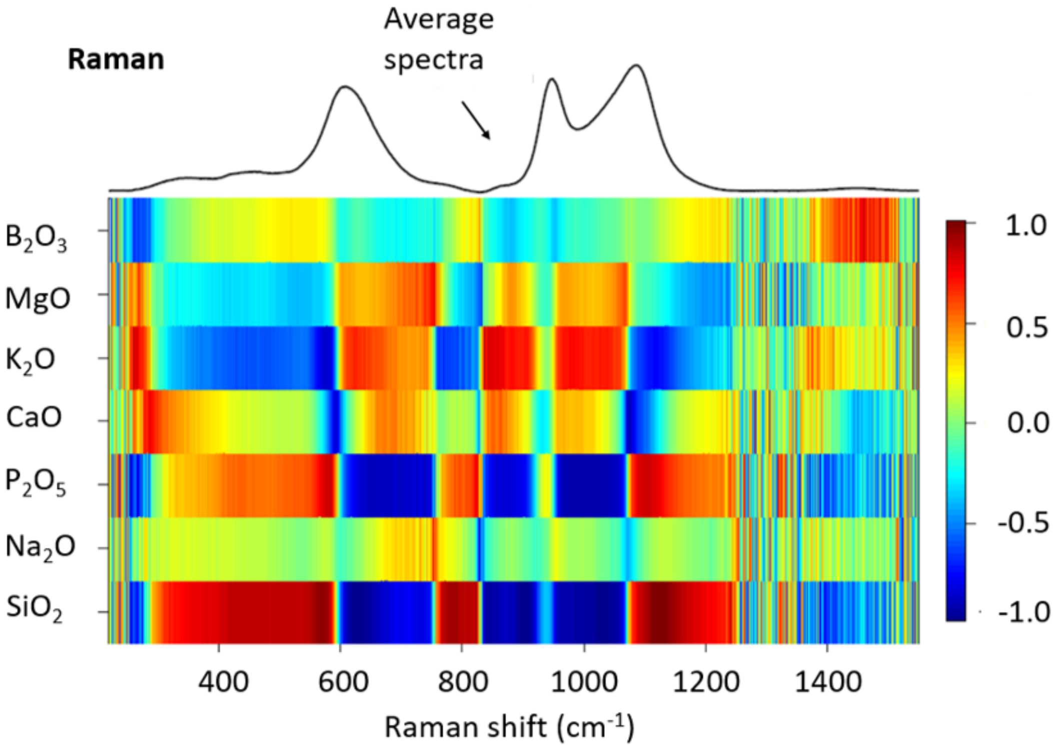

Figure 61: Pearson´s coefficient of correlation of the glass composition with the Raman spectra from nine selected Åbo glasses.

Table 22: Raman band positions, which show a strong positive correlation (>0.7) with the respective component according to Pearson´s coefficient.

Component	**Raman band position (~, cm^{-1})**
K_2O	850-870
P_2O_5	570-590 & 1080-1120
SiO_2	400-590, 760-830 & 1100-1200

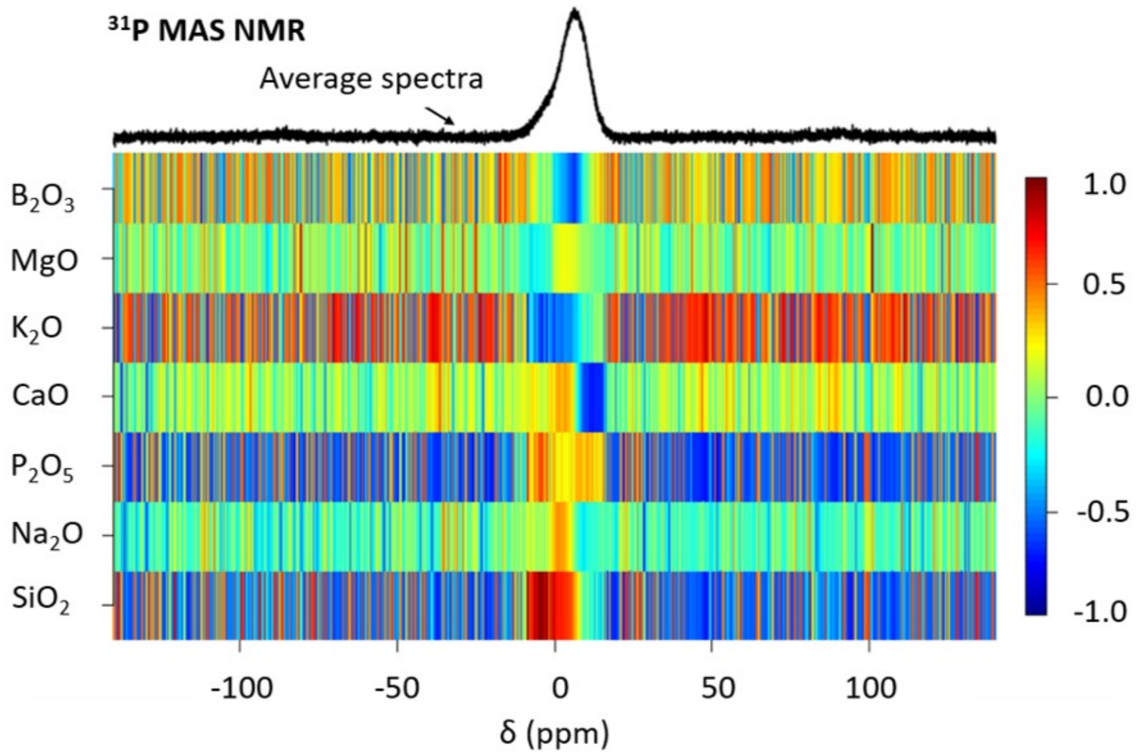

Figure 62: Pearson´s coefficient of correlation of the glass composition with the P-31 MAS NMR spectra from nine selected Åbo glasses.

Table 23: P-31 MAS NMR peak positions, which show a strong positive correlation (>0.7) respectively a strong negative correlation (<-0.5) with the respective component according to Pearson´s coefficient.

Component	NMR peak position (~, ppm)	Correlation
SiO_2	0 to -8	positive
B_2O_3	8	negative
K_2O	0 to -4	negative
CaO	8 to 20	negative

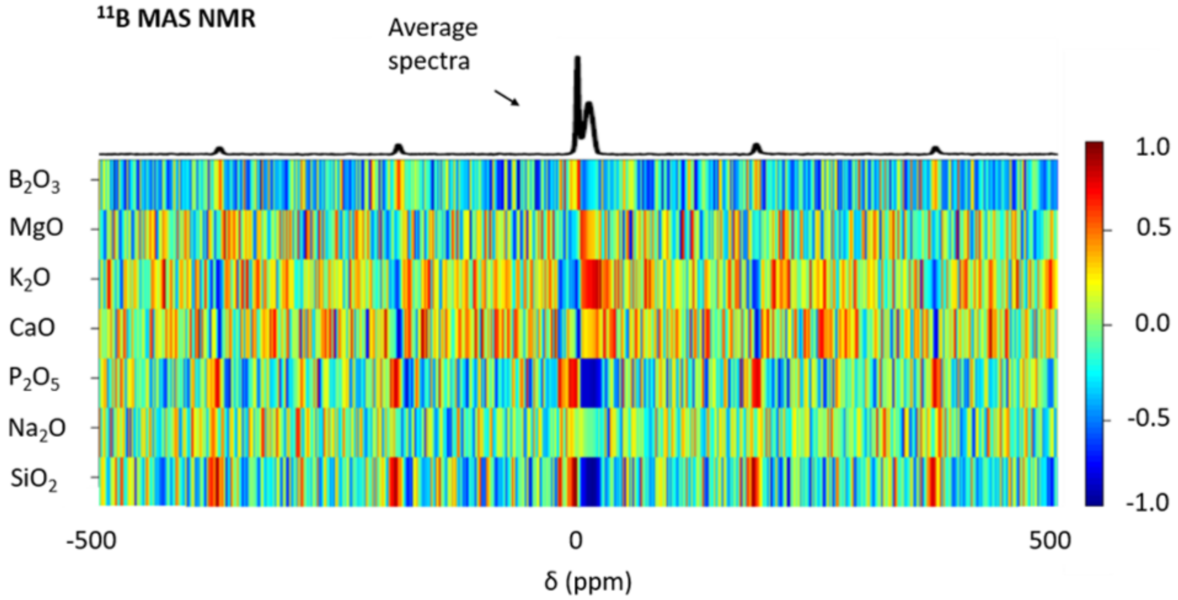

Figure 63: Pearson´s coefficient of correlation of the glass composition and the B-11 MAS NMR spectra from nine selected Åbo glasses.

Table 24: B-11 MAS NMR peak positions, which show a strong positive correlation (>0.7) respectively a strong negative correlation (<-0.5) with the respective component according to Pearson´s coefficient.

Component	NMR peak position (~, ppm)	Correlation
SiO_2	-2	positive
SiO_2	5 to 20	negative
P_2O_5	-2	positive
P_2O_5	5 to 20	negative
K_2O	5 to 20	positive

The results of the ***Fisher discriminant ratio*** on nine selected Åbo glasses, see Table 20 regarding the separability of the groups (one: high and medium bioactivity; two: inert) are shown in false-colour images in Figure 64 (FTIR), Figure 65 (Raman), Figure 66 (P^{31} MAS NMR) and Figure 67 (B^{11} MAS NMR). A fisher discriminant ratio of zero, marked in dark blue in the diagrams indicates no difference between the groups concerning the measured value. For the Raman and FTIR spectra, clear wavelength areas with a Fisher discriminant ratio different from zero can be seen clearly, while in the NMR spectra the result is not that obvious. In the FTIR spectra the Fisher discriminant ratio is ~16 at ~800 cm^{-1}, ~11 at ~920 cm^{-1} and ~17 at 1150 cm^{-1}.

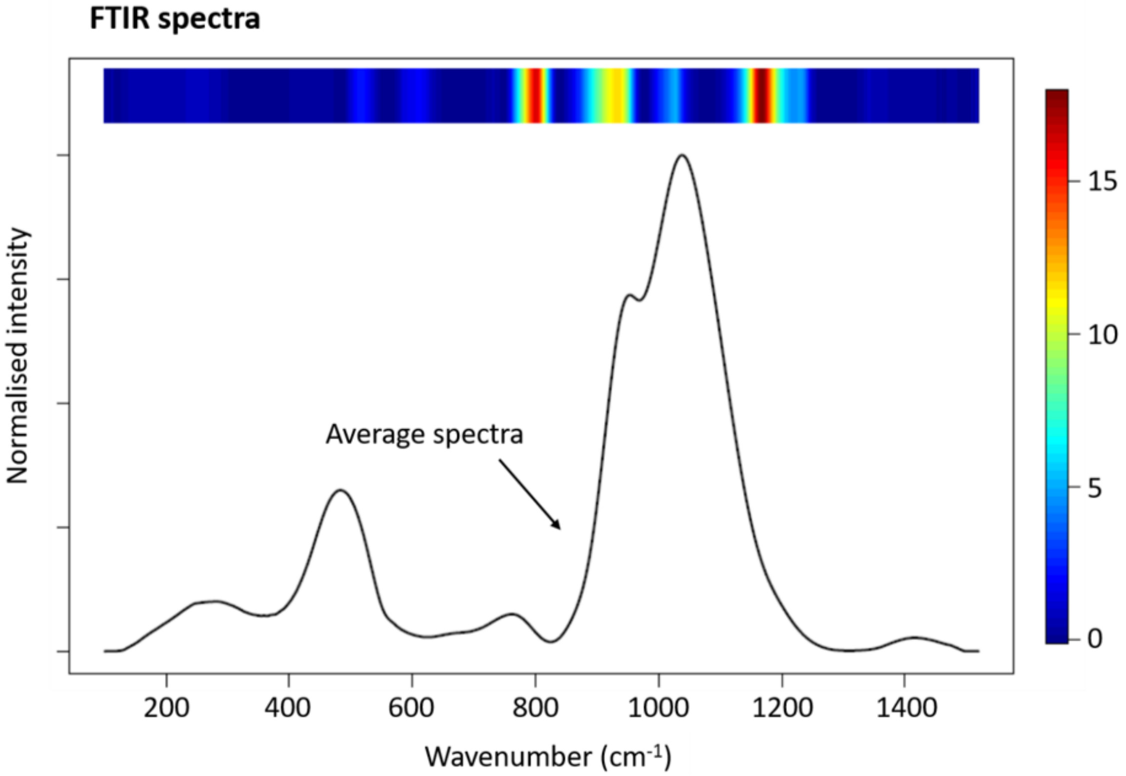

Figure 64: Fisher discriminant ratio depicted in a false-colour image of FTIR data of nine selected Åbo glasses.

In the Raman spectra the Fisher discriminant ratio is between ~13 and 35 at a Raman shift of ~800 cm^{-1}, between 13-20 at ~920 cm^{-1} and ~13 at ~350-500 cm^{-1}.

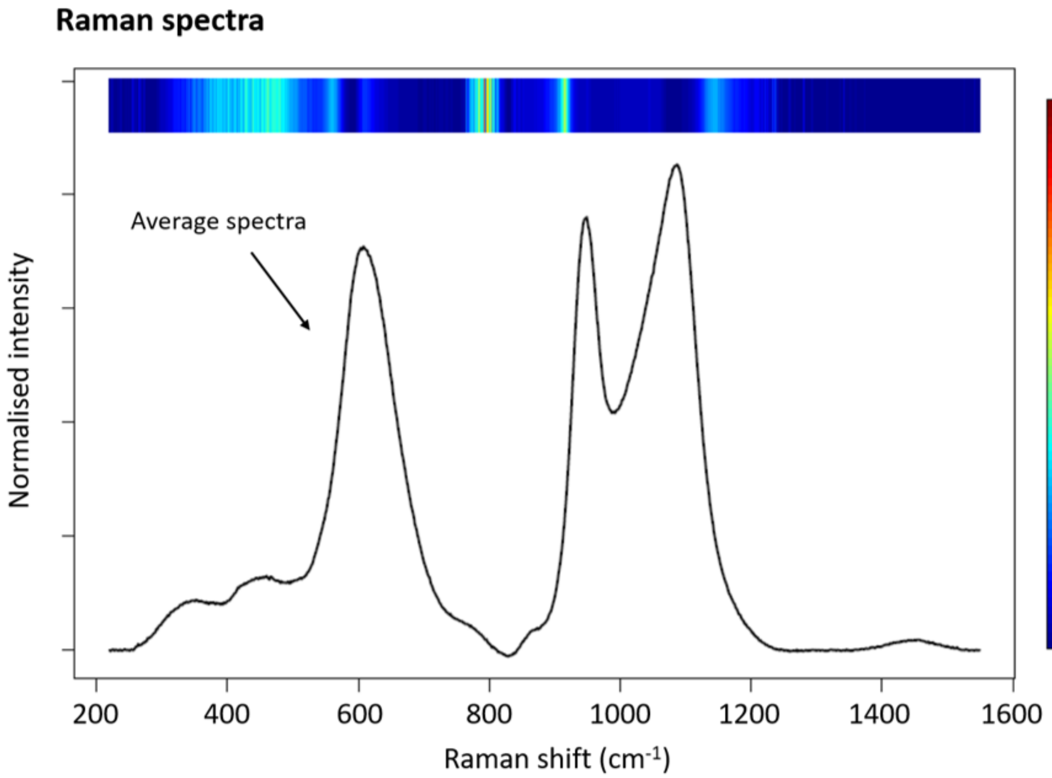

Figure 65: Fisher discriminant ratio depicted in a false-colour image of Raman data of nine selected Åbo glasses.

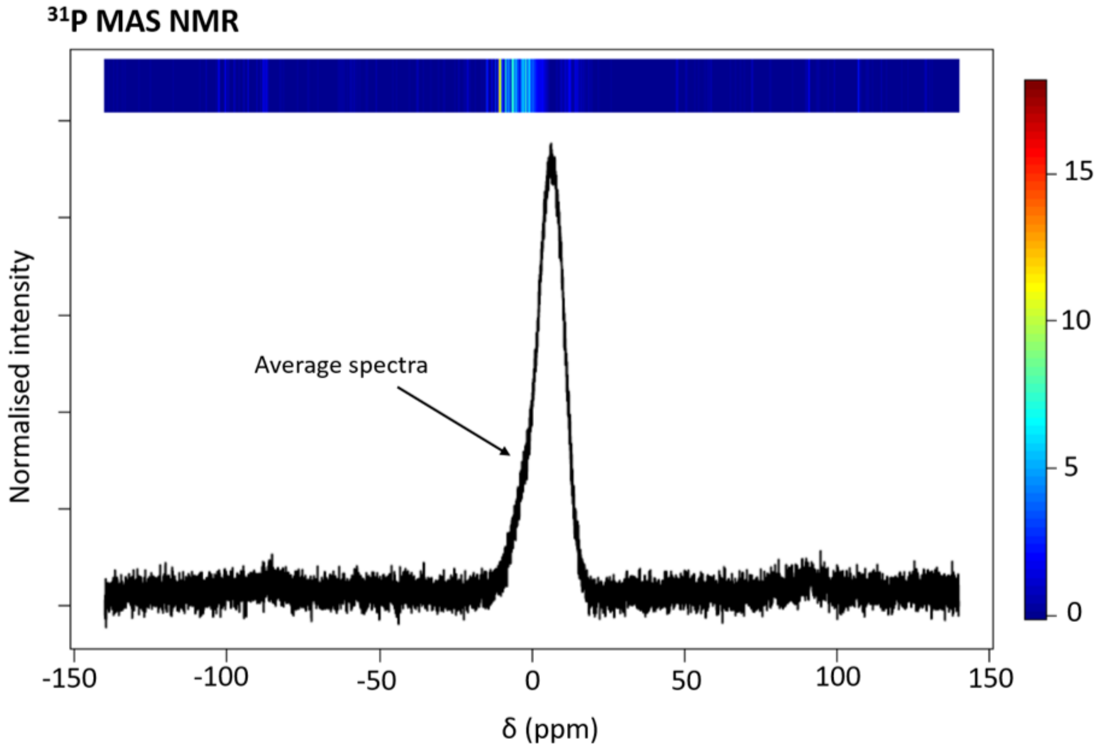

Figure 66: Fisher discriminant ratio of P-31 MAS NMR data of nine selected Åbo glasses.

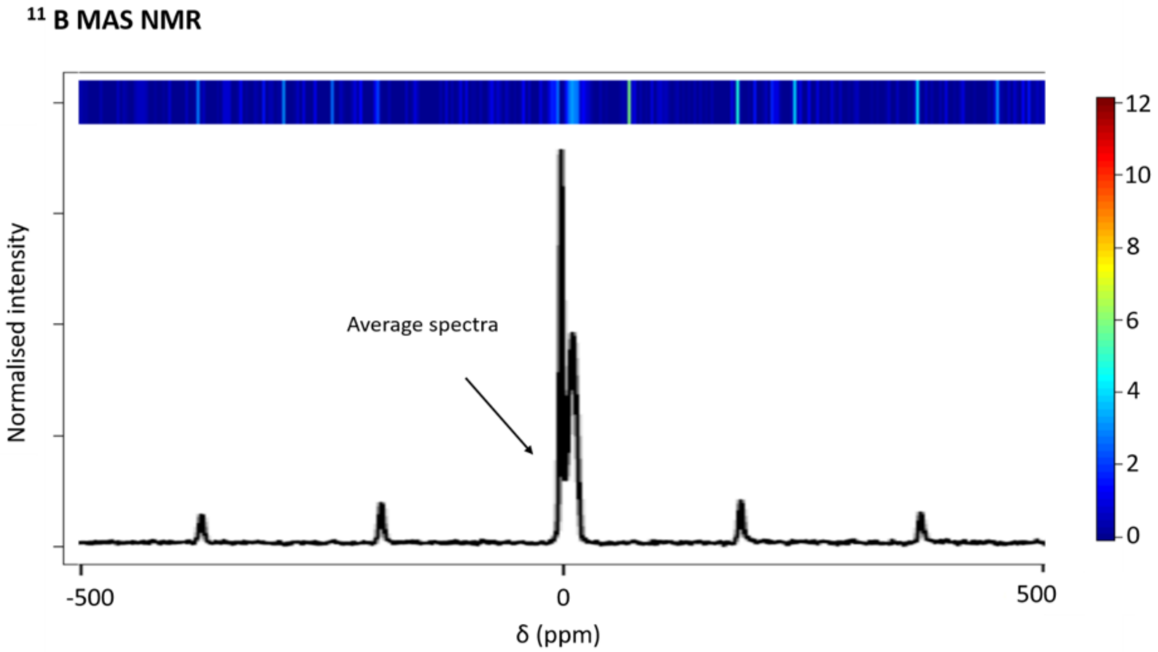

Figure 67: Fisher discriminant ratio of B-11 MAS NMR data of nine selected Åbo glasses.

5. Discussion

The purpose of this thesis was to gain an enhanced understanding of how boron influences the glass structure, the solubility and the crystallisation behaviour in bioactive glasses. The knowledge of the structure-property relationship is very important, as the development of future implants made of bioactive glass requires the fine-tuning of solubility, bioactivity and crystallisation tendency.

The first part of the discussion is about the glass series 45S5-B. Starting from the Bioglass® 45S5, boron was systematically substituted for silicon up to 25 %. The structure of the Bioglass® 45S5 is well known. Phosphorus is present in the form of orthophosphate, charge balanced mainly by sodium and calcium ions [32], while the remaining components form the silicate glass structure. Systematic investigations are advantageous to gain knowledge about the influence of one certain glass component, here boron, on the glass structure, the properties and potential applications of the glass.

The second part of the discussion is dealing with the Åbo glasses. FTIR and Raman spectroscopy were used to investigate the structure of 21 Åbo glass compositions. The potential correlation between the published *in-vivo* data of the performance in rabbit tibia [9], the dynamic dissolution test results [20] and the structure of the glasses will be discussed. The density, the glass transition temperature as well as the thermal expansion coefficient of all glasses were investigated and will be discussed, as well. ^{31}P and ^{11}B MAS NMR were investigated in nine selected glasses. Different mathematical models were used on the Åbo glasses to gain a deeper understanding of the structure-property relationship.

5.1. Glass Series 45S5-B

In the glass series 45S5-B boron was systematically substituted for silicon up to 25% starting from the well-known Bioglass® 45S5. The ratio between (B+Si) and the sum of the other components was kept constant for the whole series.

Beginning with the composition and the structure of the glass series 45S5-B the following properties will be discussed: (1) density, (2) solubility behaviour & (apatite formation), (3) thermal properties, (4) crystallisation behaviour and (5) the impact of crystallisation on the solubility. An overview of the investigations on the glasses of the series is shown in Figure 68.

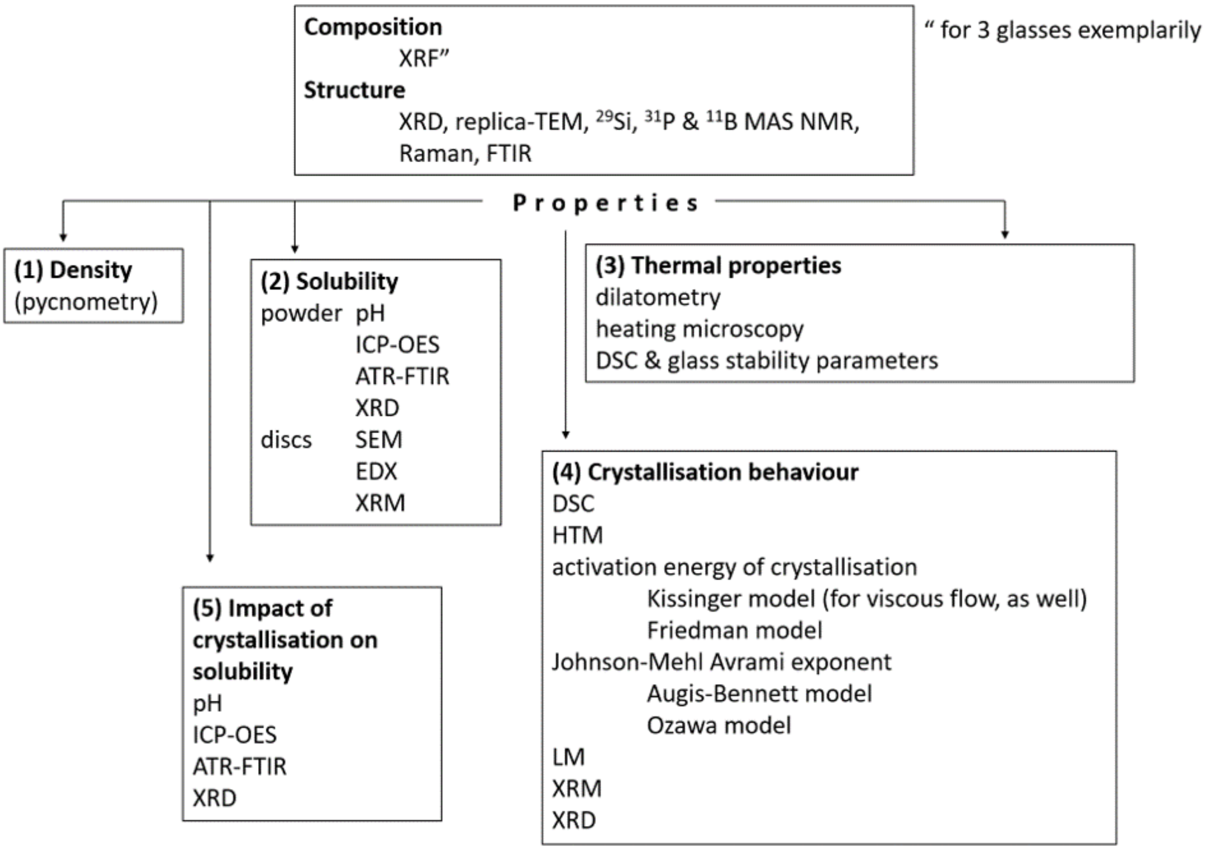

Figure 68: Overview of the investigations on glass series 45S5-B.

The investigation of the glass ***composition*** is very important. There are different wet-chemical analytical methods as well as direct instrumental analysis methods for solid samples to investigate the composition of glass. However, the component boron in the glasses makes the investigation of the composition difficult. Decompositions of glasses are used to transfer the non-soluble glass matrix to soluble salts. An acidic decomposition with hydrofluoric and mineral acids of the boron containing glasses would lead to the formation of volatile components like BF_3 which would, therefore, e.g. inhibit the quantification of boron.

Inductively coupled mass spectrometry with a laser ablation system (LA-ICP-MS) is a micro-analytical investigation method which can be applied on solid samples [83]. As the optimum range of the method is between 10^{-6} and 0.01 wt% [84], it is not suitable to analyse the glass composition of the glasses dealt with here. Although there have been advances in EDX analysis [85], the analysis of a glass containing small amounts of boron remains an issue. One option to investigate a glass composition including boron is XRF [86].

To spot-check the glass compositions, XRF investigations were carried out on three glasses. As mentioned in chapter 4.1.1, a larger amount of CaO in the analysed composition in comparison to the nominal one was found in the investigated glasses. Differences between the nominal and the analysed glass composition can have various reasons. On the one hand, there are effects which occur before the melting of the glass: e.g. (I) impurities of the used chemicals, (II) absorbed water on the chemicals and (III) losses during glass batch preparation. Potentially, one chemical tends to attach more to the material in contact during glass batch preparation than another one, e.g. to the polypropylene container or to the ceramic ball used for mixing the components. On the other hand, during glass melting at elevated temperatures some components of the glass are volatile during melting. Losses due to volatilisation are especially prominent for components having a high vapour pressure at elevated temperatures, like alkali oxides, boron and phosphorus [21]. There is probably no large change of the absolute amount of CaO during melting, but the relative amount is higher in the analysed composition because of volatilisation losses of the other components, especially of Na_2O.

Glass is an amorphous solid material. In contrast to crystalline materials, glass has no long-range order, see chapter 2.1. Structure investigations of glasses deal with the short-range order, the basic building units of the material. The following section is about the ***structure*** of the glass series 45S5-B. XRD diffractograms of crystalline materials show sharp reflections caused by diffraction of beams at the lattice planes [87]. Definite interatomic distances in the material lead to sharp reflections. In contrast to crystalline materials in an amorphous material like glass, there are no well-defined interatomic distances. The absence of sharp reflections and the presence of the typical glass halo in the XRD diffractogram verifies the amorphous state of the produced glasses, see Figure 10. The amorphous state is an important requirement for the investigations of the bioactive glasses. As a crystallised glass exhibits a different structure in comparison to an amorphous glass, a difference in properties is expected. The replica films, investigated using TEM, presented round or oval inhomogeneities in a different size for all examined glasses (5B, 10B, 15B, 20B and 25B). Upon preparation of the samples for replica technique, the glass surface is etched, see chapter 3.1.2 [51]. So, if phases with different chemical solubilities are present, the dissolution of the more soluble phase leads to the formation of a topography upon etching. This topography is reproduced on the replica film, which becomes apparent using a TEM. Therefore, the visible structures on the replica film indicate phase separation of the investigated glass. However, it is known that borosilicate glasses tend to phase-separate [21] and often the formed microphases differ in chemical resistance [51]. In the Vycor process a nearly pure SiO_2 glass is obtained by melting a glass in the compositional area: 55-75 wt% SiO_2, 20-35 wt%B_2O_3 and 5-10 wt% Na_2O (I). A subsequent heat-treatment leads to phase separation (II). Afterwards the soluble sodium borate phase is extracted (III) [51]. Finally, (IV) the less soluble, porous SiO_2-rich phase is sintered to obtain a dense, nearly pure SiO_2 glass. In the ternary system SiO_2-B_2O_3-Na_2O a large immiscibility region is present [51]. In areas with small amounts of SiO_2, SiO_2-rich droplets are in a sodium-borate rich phase, whereas in regions with large amounts of SiO_2, the situation is vice versa. In glass series 45S5-B the presence of a phase-separated glass having a sodium-borate rich phase and a silica-rich phase can be assumed. As SiO_2 is the main component for all glasses, the formation of sodium-borate rich droplets in a silica-rich matrix is likely. An investigation of the phase-separated areas would enable a deeper understanding of the structure. However, the size of the droplet phases is too small to investigate their composition by EDX as in this technique the analysed volume is at least 1 µm in diameter [88]. Auger analysis would potentially be an option for the glass analysis [89] as Auger element maps can provide a spatial resolution of less than 10 nm [88]. Depending on the size of the phase-separated areas and the detection range of the applied measurements, average information from the glass phases might be obtained. In contrast to 45S5, a phase-separated glass containing boron is expected to exhibit Si-O-B bonds. NMR studies by Möncke et al. [90] verify the presence of Si-O-B bonds in their investigated borosilicate glass systems. Interestingly the degree of Si-O-B connectivity is larger comparing quenched glass to annealed glass.

In the following section, the results of the MAS NMR spectroscopy investigations will be discussed. It is important to mention that an average information from the phases present, is recorded. However, first the technique will be explained. Nuclear magnetic resonance spectroscopy (NMR) is a method which probes the local environment of a nucleus and which is based on the investigation of energy differences between nuclear spin states in nuclides using magnetic fields [91]. Whereas these spin states exhibit the same energy without a magnetic field, in a magnetic field they are split into different energy levels, which is called Zeeman effect. This splitting increases with the strength of the magnetic field applied. Due to the magnetic effects caused by electron motion in the local chemical environment of the investigated nucleus, there are small energy-level deviations. The motion of electrons in the bonds of the investigated nucleus generates a magnetic field which interacts with the applied magnetic field. For convenience, measured chemical shifts are reported relatively to the shielding of a reference standard. The peak positions indicate geometric parameters, e.g. the coordination numbers. The peak intensity is directly related to the amount of the respective species [91]. So, the quantitative determination of the short-range order is possible. The magic angle spinning technique (MAS) was first described by Andrew et al. in 1958 [92] enabling useful NMR measurements on solids. There are anisotropic nuclear interactions, which are subject to the molecular orientation [93]. In a liquid, due to the molecular movement, these nuclear interactions are averaged. The rotation of the solid sample during MAS substitutes the insufficient molecular movement.

Advances in the NMR technique in the 1970s led to a large increase in peak resolution [91].

For glass 45S5 theoretically, 2.11 bridging oxygen atoms are present per silicon atom [4], see chapter 2.2. So, for 45S5 a large amount of Q^2 groups is expected, which is in accordance with the presented ^{29}Si MAS NMR results. As shown in Figure 12, Q^2 groups are the predominant groups with Q^1 and Q^3 groups in minority for all investigated glasses. With increasing boron content in the glass, a trend towards a less negative chemical shift is visible. This small decrease in shielding (~1.2 ppm) can be caused by partial substitution of ^{29}Si-O-Si by ^{29}Si-O-$B^{(IV)}$ bonds [43]. Furthermore, potentially a larger amount of Q^1 groups could be present because of the increasing amount of network modifier present in relation to the amount of silicon. However, the distribution of the atoms in the two assumed phases silicate-rich and borate-rich is not known. For all investigated glasses orthophosphate is the main phosphorus species. The position of the Q_P^0 group in dependency on the B for Si substitution is plotted in Figure 14. With B for Si substitution, a shift of ~0.4 ppm to higher frequencies can be identified, which can be caused by a de-shielding effect of sodium relative to calcium [43]. In the investigated 45S5-B glasses besides orthophosphate as main phosphate species, a small amount of pyrophosphate is present: 5.6% in 45S5, 4% in 1B, 3.2% in 10B and 1.6% in 25B [94]. The de-shielding shift in combination with the decrease of the amount of pyrophosphate suggests a favoured association of orthophosphate species with Ca^{2+} ions [95]. Ren et al. found in their molecular dynamics simulations of the B_2O_3/SiO_2 substitution in the bioactive glass system Na_2O-CaO-SrO-P_2O_5-SiO_2, Ca^{2+} ions to prefer to “gather around PO_4 groups” [96]. However contrarily, studies by Brauer et al. [32], Elgayar et al. [97] and Lockyer et al. [30] show an equal distribution of the network modifier ions calcium and sodium around orthophosphate in bioactive glasses. As mentioned before, in glass 45S5, SiO_2 is the major network former as phosphorus is mainly present as orthophosphate, see chapter 2.2, which was also verified by the ^{31}P MAS NMR results. Because of the tetrahedral formation [98], SiO_2 can form a 3D-network. The vitreous B_2O_3 network can be 3-fold or 4-fold coordinated leading to a 2D or a 3D network. The ^{11}B MAS NMR measurements verified trigonal BO_3 as main species and tetragonal BO_4 as minor B-species for the whole series. In all glasses the amount of BO_3 was between 80% and 90%, whereas the amount of

BO_4 was between 10% and 20%, see Figure 16. An overview of the relative and the absolute amount of BO_3 and BO_4 units of the 45S5-B glasses is shown in Table 25. For example, for glass 25B, 25% of silicon is substituted by boron atoms. As 80% of the 25% substituted boron were present in the form of BO_3, there were 20.9% in BO_3 and only 4.1% in BO_4.

Table 25: Relative and absolute amount of BO_3 and BO_4 for the glasses of series 45S5-B.

Glass name	B for Si substitution (%)	Relative amount BO_3 (%)	Absolute amount BO_3 (%)	Relative amount BO_4 (%)	Absolute amount BO_4 (%)
45S5-1B (1B)	1	88.5	0.9	11.5	0.1
45S5-2.5B (2.5B)	2.5	89	2.2	11	0.3
45S5-10B (10B)	10	86.7	8.7	13.3	1.3
45S5-15B (15B)	15	86.5	13.0	13.5	2.0
45S5-20B (20B)	20	86.3	17.3	13.7	2.7
45S5-25B (25B)	25	83.7	20.9	16.3	4.1

Because of the substitution of mainly trigonal BO_3 for 100% tetragonal SiO_4, the average polymerisation of the network decreases with B for Si substitution in comparison to glass 45S5. With increasing boron content in the glass, the relative amount of BO_4 shows an increasing trend. Yu and Edén [43] carried out an extensive NMR study on glasses in the Na_2O-CaO-B_2O_3-SiO_2-P_2O_5 system. In their study they replaced SiO_2 by B_2O_3 while keeping the amount of Na_2O and CaO constant. For increasing B_2O_3 content, their ^{11}B MAS NMR results show continuous conversion from BO_3 to BO_4, which agrees with the NMR results presented here. The position of both BO_3 and BO_4 showed a de-shielded shift with rising boron content, as presented in Figure 17. Yu and Edén found a de-shielding shift for BO_4 with rising boron content as well, which can be attributed to the reduction of the number of Si-neighbours in the $B^{(IV)}$-O-Si species. The de-shielding shift of the BO_3 signal with increasing boron content in the glass can be caused by the potential formation of more $B^{(III)}$-O-$B^{(IV)}$ groups. Yu and Edén propose “strong preferences” for the formation of $B^{(III)}$-O-$B^{(III)}$ and $B^{(IV)}$-O-Si bonds. Small domains of BO_3 groups in boroxol rings and a network built by SiO_4 and BO_4 units are proposed by Yu and Edén [43], which agrees with the verified phase separation found here. Borosilicate glasses are known to phase-separate into a borate-rich and a silicate-rich phase [21]. Commercially used borosilicate glasses are known for their chemical stability, their low thermal expansion coefficient as well as their good light transmittance. The low thermal expansion coefficient is leading to a high thermal shock resistance. Together with the outstanding chemical stability one important application of borosilicate glass is as laboratory glassware material. However, traditional borosilicate glasses are used in manifold applications. Corning´s famous borosilicate glass Pyrex® was introduced as early as in 1915 [99]. The molar composition of Pyrex® is $4.0Na_2O-1.4Al_2O_3-11.6B_2O_3-83.0SiO_2$ [99]. MAS NMR investigations of the structure of Pyrex® by Tricot [99] show a network based on Q^4 groups including Al^4 as well as B^4 units while separate networks are formed by B^3 groups. While Q^4 groups are SiO_4 tetrahedra with four bridging oxygen atoms, Al^4 and B^4 units are AlO_4 respectively BO_4 tetrahedra with four bridging oxygen atoms. B^3 groups are planar BO_3 units with three bridging oxygen atoms. 2-dimensional MAS NMR investigations led to the identification of B^4 units connected to four silicon atoms and B^4 units connected to three silicon atoms and one B^3 unit. Furthermore, B^3 units forming rings and B^3 units not forming rings were identified. B^3 ring units were connected to the silicate network through a B^4 unit, whereas non-ring B^3 units were directly connected to the silicate network. Sodium ions are located completely at Al^{3+} and B^{3+} positions leading to the “absence of non-bridging oxygen atoms in the Pyrex® network” [99]. Two-dimensional MAS NMR experiments on annealed low alkali borosilicate glasses by Möncke et al. revealed that BO_4 tetrahedra prefer connections with borate entities rather than with silicate units in the glass network [100]. Feller et al. [101] tried to estimate the structure of borosilicate glasses from the composition. In their “proportional sharing” model the assumption is that modifier oxide is shared proportionally between the borate and silicate network. However, this model cannot be applied on the bioactive borosilicate glasses as the composition is in a different range. The traditional borosilicate glasses exhibit a very low amount of network modifiers in comparison to the bioactive glasses investigated in this thesis.

FTIR – and Raman spectroscopy are two important spectroscopic methods, which have been applied to investigate the bioactive borosilicate glasses in this thesis. Before the results will be discussed, these two methods will be introduced briefly. Vibrational spectroscopy, like FTIR- and Raman spectroscopy is a powerful technique to analyse the glass structure [68]. As glasses, in contrast to crystalline materials, do not exhibit a long-range order, the benefit of vibrational spectroscopy is large for the investigation of the glass structure [52]. FTIR and Raman spectroscopy base on the interaction of electromagnetic radiation with the material, but there are different physical principles behind the two methods. Employing FTIR spectroscopy, energy is transferred from the IR photon to the molecule by absorption [102], leading to molecular vibrations. This energy transfer is only possible if the molecular vibration causes an alteration in the dipole moment of the molecule. So, vibrations are visible, in which the electric dipole moment changes [103]. According to this selection rule, asymmetric vibrations are visible (IR active), while symmetric ones are not. Infrared reflectance spectroscopy of bulk glass samples in combination with Fourier-transform spectrometers and software for the analysis is a valuable technique as one glass sample is used for data acquisition over a broad frequency range, including the mid- (4000-400 cm^{-1}) [102] and the far infrared (400-10 cm^{-1}) [102] spectral ranges [52]. A quantitative analysis of the glass structure is possible. The Raman effect was theoretically predicted by A. Smekal in 1923 and demonstrated by C.V. Raman in 1928 [104]. The Raman effect is an inelastic light scattering process [68]. The monochromatic light used for excitation changes its frequency upon interaction with the investigated sample. Photons of the laser light are reemitted very fast after irradiation, whereas the frequency of the laser light is either shifted up (anti-Stokes effect) or shifted down (Stokes effect). As the intensity of the Stokes bands is more intense in comparison to the anti-Stokes ones, they are used for the analysis. The differences of the Raman frequencies from the excitation frequency are characteristic for vibrations of certain molecular groups. In Raman spectroscopy, a vibration is detectable if its polarisability changes [68, 105], which is the case for symmetric vibrations. If the polarisability of the vibration does not change, which would be the case for a purely asymmetric vibration, it would not be detectable. The polarisability is a measure of the deformability of the electron cloud around an atom or molecule. So, in Raman spectra, there are intensive bands for non-polar groups, which are easy to polarise and less intensive bands for highly polar bonds as they are difficult to polarise. As the discovered phase-separated areas, see Figure 11 were small in comparison to the investigated area in FTIR- and Raman spectroscopy, average information from the phases was recorded. Having a detailed look on the band at 900-

1100 cm^{-1} in the FTIR spectra, there are four instead of just two positions: a Q^2 group connected to another Q^2 group (Q^{22}); Q^2 connected to a Q^3 (Q^{23}), and respectively Q^{32} as well as Q^{33} [64]. So, the band at 1028 cm^{-1} was assigned to Q^{32} as the location is close to the range assigned to Q^3: 1060-1100 cm^{-1}. With increasing boron content, a slight increase of Q^1 band intensity and a distinct one of Q^4 band intensity was present. In the Raman spectra, the intensity of the Q^4 stretching band increased as well. Furthermore, the intensity of the Q^{32} band decreased. In the Raman spectra, the band with the maximum intensity was assigned to Q^2 stretching mode, which agrees with the presence of Q^2 as dominating unit as verified by the ^{29}Si MAS NMR investigations. The band at ~630 cm^{-1} (for glass 45S5) shifted to a higher Raman shift within the series (to ~640 cm^{-1} for glass 25B), indicating an increase of Q^2 groups present [64]. Kamitsos et al. [64] suggest the formation of Q^2, Q^1 and Q^4 units at the expense of Q^3 species upon introduction of boron in their FTIR (& Raman) study of trivalent ions in sodium trisilicate glass. The increase in the intensity of the Q^4 and the Q^1 stretching units implies a similar disproportionation reaction taking place, although evaluation is more complicated due to the relatively small amount of boron in the investigated glass system. Kamitsos et al. investigated the glass system Na_2O-xB_2O_3-$(3-2x)SiO_2$ with x up to 1, which leads to more pronounced changes in band intensities. From glass 2.5B, the intensity of the B_3-O FTIR stretching band (1400 cm^{-1}) increased systematically within the series, which corresponds to the increase of the B-O-B deformation band at 735 cm^{-1} [64]. In the Raman spectra, the band at 1440 cm^{-1} corresponding to the stretching of the BO_3 groups intensified with the B for Si substitution as well. Even though in FTIR- and Raman spectroscopy an increase of Q^4 with B for Si substitution was verified, this effect could not be seen in NMR spectroscopy. An excellent option for further structural clarification, especially because the Si signals in the one-dimensional MAS NMR are overlapping profoundly, would be two-dimensional NMR spectroscopy. The investigation of the glasses e.g. by ^{11}B/^{29}Si 2D NMR like carried out by Möncke et al. [100] would provide 2D maps and thereby information about the connectivity between the silicate and the borate species. While FTIR and Raman spectroscopy showed an increase in the BO_3 stretching intensity within the series, according to the NMR results the ratio of B_3/B_4 is increasing. The absolute amount of B_3 increased as more boron is in the glass system. So, in the two vibrational spectroscopy methods, more B_3 units are visible. However, the absolute amount of B_4 increased slightly within the series, see Figure 16.

The influence of B for Si substitution on density within the glass series is difficult to predict. The density of a material is defined by the mass of the material divided by its volume. In general, there are different influencing variables on the density of glass. (I) The molar mass, (II) the ionic radius and (III) the bond length of the present atoms or ions. The smaller molar mass of boron (M_B = 10.811 g/mol) in comparison to silicon (M_{Si} = 28.0855 g/mol) is likely to have a decreasing impact on the density, whereas the smaller atomic radius of boron (90 pm) versus silicon (118 pm) may have an increasing influence. Furthermore, the bond length of Si-O and of B-O in the glass network as well as the coordination of the network formers have an effect on the density. Ren et al. carried out molecular dynamics simulations on bioactive glasses of the system Na_2O-CaO-SrO-P_2O_5-SiO_2 [96]. They found the length of the Si-O bond to be 1.6 Å, and the length of the bond B_4-O and B_3-O being shorter with 1.5 Å resp. 1.4 Å. The arrangement in trigonal or tetragonal coordination requires a different volume. However, here, the various effects compensate each other, leading to a constant density for the whole glass series.

In the following remarks the investigation of the structure of the 45S5-B glasses will be summarised.

- The boron-containing glasses showed droplet in matrix phase separation
- According to ^{31}P MAS NMR investigations, orthophosphate was the main phosphorus specification for the whole series.
- ^{29}Si MAS NMR showed Q^2 as the main silicon species for the glasses.
- ^{11}B MAS NMR verified BO_3 as the major boron species (>80 %), FTIR- & Raman spectroscopy results showed an increasing intensity of BO_3 stretching vibrations within the series.

The increasing substitution of boron in the glass 45S5 led to an overall ***decreased network polymerisation***.

Dissolution tests are carried out to investigate the ***solubility behaviour*** and the ***apatite formation*** on bioactive glasses, see chapter 2.2. For the dissolution tests on glass powder, a Tris buffer solution was used, which is advantageous to study the performance of the bioactive glass while blanking out potential interactions with other ions. The dissolution process of bioactive glass in contact with aqueous media is described in chapter 2.2. In contrast to Tris buffer solution, SBF solution contains many ions, see Table A 6, which potentially participate in the dissolution tests. For example, the investigation of the effect of chloride ions on bioactive glass apatite mineralization [72] would not have been possible using SBF solution. Thereby one Tris buffer solution was buffered using hydrochloric acid and the other one using acetic acid. The formed mineralization products were investigated using SEM and EDX among other methods. Furthermore, using a Tris buffer solution offers relatively tough test conditions. The phosphorus species necessary for the mineralization, here orthophosphate, need to originate from the glass as it is not provided by the solution.

For two reasons it is important to know the time-dependent course of the pH-value. The dissolution process causes a change of the pH-value. Furthermore, the formation of apatite occurs preferentially in an alkaline milieu [38]. When bioactive glasses dissolve, as described in chapter 2.2, ion exchange takes place. Network modifier ions are leached out of the glass and protons (H^+) from the water bond to the non-bridging oxygen ions. This exchange causes an increase in the pH-value due to an excess of OH^- ions in the solution. That behaviour is shown for the first and the last glass of the series 45S5-B exemplarily: glass 45S5 and 25B. For both glasses, a pronounced increase in pH-value was observed. In accordance with previous investigations [71], during the first 24 h, the pH-value increased significantly, whereas the increase afterwards was levelled off. A strong increase in pH-value is ascribed to an exchange reaction which proceeds at a high rate. In contrast, a less pronounced increase shows that the exchange reaction takes place in a less intense manner. First, the exchange reaction occurs in the layer which is close to the surface. With longer exposure in the solution, the speed of the exchange slows down because the particle layer close to the surface is already exchanged to a high degree.

The ICP-OES measurements provided the ion concentration in Tris buffer solution. The normalised ion concentration in a solution after dissolution test of glass 45S5 and glass 25B is presented in Figure 24. At 24 h for both glasses, the concentration of the network modifier ions in solution corresponds to more than 70 % of sodium and more than 50 % of calcium of the bioactive glass. Afterwards, the change of the ion concentration is less pronounced, which agrees with previous investigations [26, 71]. At the beginning of the exchange reaction, the whole surface of the particle is available. After a time span, the ion exchange from the layer closest to the surface is completed. As the ion exchange of deeper layers takes more time, the steep increase in ion concentration followed by a less pronounced one found here, was expected. Noticeable is the fact that calcium is present in a reduced amount in comparison to sodium. On the one hand, the single-charged sodium can be leached out of the glass more easily than calcium, which is double-charged and therefore stronger bound in the glass network. On the other hand, if apatite is formed, the released calcium ions are incorporated into it. Hence, the ion concentration of calcium in the solution is lower than it would have been without the formation of apatite. For glass 45S5 about 5 % of phosphorus is detected in the solution at one day, whereas at 6 hours 25 % is present. After three days no phosphorus could be detected anymore. For glass 25B the course is similar, having the maximum at 6 hours with a concentration of 14 % and no phosphorus present in the solution after 1 day already. The decreasing phosphate concentration suggests the formation of apatite. First, phosphate is released due to the dissolution of the glass. Afterwards, it is partially precipitated from the solution in case of apatite formation as it is incorporated together with the calcium ions in the material. The apatite can be detected using XRD and FTIR investigations. The presence of phosphorus plays a special role regarding the apatite precipitation. As mentioned in chapter 2.2, the chemical formula of hydroxyapatite is $Ca_5(PO_4)_3OH$. So, the molar ratio of calcium to phosphorus necessary to form a stoichiometric form is 5:3. According to the composition of glass 45S5 (25B), Table 3, the amount of CaO is with 26.9 (28.6) mol% significantly higher than the amount of P_2O_5 with 2.6 (2.8) mol%. We can clearly see that calcium is present in excess and that the phosphorus concentration is the limiting factor for the formation of hydroxyapatite.

For glass 25B, the time-dependent course of boron concentration in solution is similar to the one of sodium, showing a fast release to a great extent (~90 % at 3 days). Boron and sodium are released in a similar amount, which supports the assumption of having a sodium-borate rich phase in a silicate-rich matrix. Trigonal BO_3 groups which are present in the majority of the boron-containing glasses are easily attacked by water, which leads to a hydrolysis of the borate network [98]. The normalised calcium ion concentration in the solution for glasses 45S5 and 25B is similar for all points in time. However, apatite is formed faster for glass 25B in comparison to glass 45S5. As calcium is present in excess, the influence is probably not visible.

At 1 day the amount of phosphorus present in the solution of 45S5 was 4.6 % and below 1 % for glass 25B. This behaviour suggests an earlier apatite formation for glass 25B, as the phosphate is incorporated into the material, as mentioned above. The concentration of phosphorus is presented for the whole glass series 45S5-B at 6 hours in Figure 25. Whereas for the glasses with a B for Si substitution between 0 and 5 %, the concentration of P is above 20 %, for glass 20B and 25B the concentration of P is below 15 %. This decreasing trend with substitution supports the suggestion of an earlier formation of apatite. Orthophosphate is the main modification of phosphorus for the whole glass series. In comparison to larger units, orthophosphate units can be leached out of the bioactive glass relatively easily, promoting apatite formation.

Sodium ions are present in higher concentration in the solution of glass 25B than of glass 45S5. As shown in chapter 4.1.2 and discussed earlier, the structure of glass 25B is less polymerised in comparison to the structure of glass 45S5. The lower network polymerisation leads to increased solubility of the glasses with B for Si substitution. So far, we considered the average of the silicate and the borate part of the glass structure. Considering only the silicate part, both vibrational spectroscopy methods show more Q^4 vibrations for an increasing amount of boron in the glass. However, the 1D MAS NMR results do not support the presence of an increased amount of Q^4 units. The network former atom silicon can be detected in the solution as well: after 3 days ~20 % for glass 45S5 and ~30 % for glass 25B. Silicon is released from glass 25B faster and in greater extent in comparison to glass 45S5. The structure of glass 45S5 is highly fragmented. As discussed earlier the main components are Q^2 units. So, short Si-network units can be leached into the solution during the dissolution test. A decreased amount of silicon being leached from the glass 25B in comparison to glass 45S5 could be caused by an increased network connectivity of the silicate part of the glass, see the FTIR- and Raman results. However, the solubility of the silicate part of the glass network in water is limited [106] and strongly dependent on the pH value [107].

Besides the pH value and the ICP-OES measurements, XRD, FTIR and SEM measurements give evidence on the ion release of the bioactive glasses. In the XRD diffractogram, see Figure 27 the formation of the ion-depleted (silica gel) layer can be identified. The underlying halo shifts from about 31°2θ at 6 hours to 23°2θ at 7 days.

The formation of apatite was investigated via FTIR spectroscopy and XRD measurements. After 7 days in a Tris buffer solution, the FTIR spectra for all glasses look very similar, see Figure 26. The double band at 560/600 cm^{-1} can be assigned to bending vibrations and the pronounced band at 1015 cm^{-1} to stretching vibrations of P-O. The double band at 560/600 cm^{-1} is characteristic for a calcium orthophosphate [108]. Since the most stable type in the pH-value area above 5 is hydroxyapatite [38], its presence can be assumed, suggesting the formation of a hydroxyapatite surface layer [109] on the bioactive glass. During the formation of apatite besides amorphous CaP, octacalcium phosphate ($Ca_8(HPO_4)_2(PO_4)_4*5H_2O$) [72] is a precursor [110]. According to the study by Brown et al. [110] the octacalcium phosphate is quickly hydrolysed into apatite. During this process, the formation of a “transition product” containing octacalcium phosphate domains as well as apatite domains is possible [110]. The band at 870 cm^{-1} can be assigned to carbonate [73], suggesting carbonate substitutions in the formed apatite. All spectra at 7 d and at 6 h show the band at 790 cm^{-1}, which can be assigned to vibrations of Si-O-Si in the ion-depleted glass (silica gel), originating from the dissolution process of the bioactive glass [72]. At 6 hours, the spectra of glasses 20B and 25B exhibit the typical features of forming hydroxyapatite mentioned, whereas for glass 25B they are less pronounced than for 20B. The broad band at about 1050 cm^{-1}, which is visible in the spectra of all glasses apart from 20B, can be assigned to vibrations of bridging oxygen atoms in Si-O-Si [72]. In glass 25B, there is a mixture of P-O and Si-O-Si bands present. The FTIR spectra of untreated glasses 45S5 and 25B (0 h stay in Tris buffer solution) are presented in Figure 43. Overlapping bands at 840, 940 and 1040 cm^{-1} are visible, which are typical features of bioactive silicate glasses: non-bridging oxygen bands (840 & 940 cm^{-1}) and a bridging oxygen band (1040 cm^{-1}) [78]. In the spectra at 6 hours the intensity of the bands at 840 and 940 cm^{-1} is less pronounced in comparison to the spectra at 0 hours, see Figure 26. Caused by the dissolution process including the reaction of the negatively charged non-bridging-oxygen atoms with the H^+ from the aqueous solution, see chapter 2.2, the non-bridging oxygen atoms bands disappear. The X-ray diffractograms of the reacted bioactive glasses after 6h and 7d in the Tris buffer solution are presented in Figure 27. After 7 days all glasses exhibit pronounced signals at 26 and 32 as well as smaller ones at 17, 40, 47, 50 and 53 °2θ, which are assigned to hydroxyapatite (JCPDS 00-009-0432). The apatite reflections are broad, which is typical for bioactive glasses and indicates apatite formation of poor crystallinity [26]. The XRD reflections are broadened due to substitutions [111] in the lattice leading to a non-stoichiometric apatite and potentially because of nanometre size crystals [87] as well. Interestingly, glasses with a low boron content exhibit sharper signals in comparison to the ones with a higher boron content. The potential incorporation of boron into the lattice of apatite is a possible reason for that. BO_3 groups can be introduced at PO_4 positions [38, 112]. Apart from the apatite signals, there is a broad underlying halo with its maximum at about 23°2θ. At 6 hours only, glasses 20B and 25B exhibit sharper signals at about 26 and 32°2θ, whereas all other glasses show a broad double signal with its maximum at 23 and 31°2θ. As mentioned earlier in the chapter, dealing with the ion release, the maximum of the underlying halo shifts due to the formation of the ion-depleted layer (silica-gel) from about 31°2θ at 6 hours to 23°2θ at 7 days. FTIR and XRD results suggest the starting formation of hydroxyapatite in form of a surface layer earlier for the glasses 20B and 25B, which agrees with the low phosphate concentrations in the Tris buffer solution after the dissolution tests. The question “Is it possible to control the ion release via the boron content of the glass?” which was asked in the introduction, can be answered with “Yes”. Since the less polymerised network of the boron-containing glasses leads to increased solubility, an earlier apatite formation was expected.

Using ***glass discs*** over fine glass powder makes it possible to prepare cross-sections after the immersion tests. That approach has the advantage to see the different layers that were formed using SEM and it allows EDX measurements on those different layers. Performing EDX using area measurements is advantageous in the investigation of bioactive glass, as for EDX point measurements, the high mobility of ions like sodium caused by energy intake from the electron beam can affect the EDX results and show lower than actual sodium concentrations. The disadvantage of using discs in the immersion tests is the small surface area. Contrarily to the tests with powder, the surface area of a disc is relatively small which limits the release of phosphorus from the glass. For fine powder used for the dissolution tests on powder in Tris buffer solution, the surface area is large, leading to a fast release of phosphate ions. So, bioactive glass discs were treated in SBF solution for 7 d. SBF solution was used instead of Tris buffer solution here, to make sure enough phosphorus is present. As discussed earlier, phosphorus is the limiting factor for the apatite formation. In the SBF solution 1 mmol/l phosphorus in the form of HPO_4^{2-} is present, which is similar to the concentration in the human blood plasma [53]. Test conditions using SBF instead of Tris buffer solution resemble the real environment in the human body, as there are various ions present as well. Because of the dissolution of bioactive glass in aqueous solution, the ions in the outer layer of the glass are leached leading to the formation of the silica-gel layer, see chapter 2.2. As the local ion concentration is high at the surface of the bioactive glass, it acts as a nucleation site leading to the formation of apatite as an outer layer on the bioactive glass. SEM pictures of the disc surface of glass 45S5 after 7 d in SBF are shown in Figure 28. In the right picture, the typical cauliflower-like structure of the formed apatite crystals is visible, see also Fu et al. [74]. Due to drying the samples after a stay in SBF solution, cracks occur, which are visible in Figure 28 and Figure 29. Cross sections of the reacted glass discs are presented in Figure 29. Picture A shows an overview of glass 45S5, while B, C, D and E show sections of glasses 45S5, 15B, 20B and 25B. All SEM pictures exhibit four different zones. The black zone is the polymer used to embed the samples, whereas layer one and two are the leached glass and the formed apatite. The lowest layer as labelled in the figure is the bioactive glass. The thickness of the leached glass layer varies widely within every sample across the edge. No differences could be observed comparing glasses with different B for Si substitution. The thickness of the apatite layer varies within one sample, which is visible in the overview picture of glass 45S5. A more complete dissolution and apatite formation of the bioactive glass with increasing boron content has been investigated by Huang et al. [113]. In their study, they started from glass 45S5 and replaced one third or two third SiO_2 by B_2O_3. So, one atom silicon was replaced by two atoms boron. In comparison with our glass composition, their boron content is at least three times higher leading to a different starting situation. In our glass powder results, a difference in apatite formation is visible at an early point of time (6 hours), but not after 7 days. So potentially, there might be a difference in apatite formation on the glass discs at earlier points of time as well. The EDX analysis of sample 45S5 after 7 days in SBF solution is presented in Table 6. The analysed composition of the glass corresponds to the theoretical glass composition, Table 3. Here in the base glass, the amount of silicon (16.3 ± 0.7 at%) and sodium (16.3 ± 1.2 at%) is high, whereas 9.5 ± 0.5 at% calcium and 2 ± 0.1 at% phosphorus is present. The leached glass layer exhibits 88.2 ± 4.6 mol% SiO_2, which meets the expectation of a high amount of SiO_2 being present, as well as earlier investigations [72]. The apatite layer exhibits a high amount of calcium (24.7 ± 0.1 at%) and phosphorus (12.2 ± 0.5 at%). The results of the elemental analysis of the three layers of glasses 45S5, 20B and 25B after 7 days in SBF are presented in Table 7. Ratios of Si/P, Si/Ca as well as Ca/P are given to compare the results. For glass 45S5 the ratios based on EDX results agree with the nominal value, see Table 26.

Table 26: The ratio of Si/P, Si/Ca and Ca/P for the glasses 45S5, 20B and 25B based on EDX results compared with the ones based on the nominal composition, called nominal value here.

45S5	**EDX**	**nominal value**
Si/P	8.2 ± 0.8	8.9
Si/Ca	1.7 ± 0.2	1.7
Ca/P	4.8 ± 0.5	5.2
20B		
Si/P	7.2 ± 0.7	7.2
Si/Ca	1.4 ± 0.1	1.4
Ca/P	5.3 ± 0.5	5.2
25B		
Si/P	7.9 ± 0.7	6.6
Si/Ca	1.4 ± 0.1	1.3
Ca/P	5.7 ± 0.6	5.1

Because of the B for Si substitution, the Si/P and the Si/Ca ratios are expected to be smaller for glass 20B (7.2 & 1.4) and 25B (6.6 & 1.3) in comparison to glass 45S5 (8.9 & 1.7). For glasses 20B and 25B the values determined by EDX measurements agree with the nominal ones, apart from the Si/P ratio for glass 25B. Here the ratio calculated from EDX measurements is higher than the nominal ratio. However, the composition analysis using XRF measurements showed no abnormalities for this glass. For all apatite layers, the Ca/P ratio is about 2, see Table 7, which is close to the Ca/P ratio of 1.67 in stochiometric hydroxyapatite [114]. For the hydroxyapatite structure $Ca_5(PO_4)_3OH$ various substitutions are known. In A-type substitutions the OH^- is substituted, whereas in B-type substitutions the PO_4^{3-}. Ca^{2+}, for example, can be replaced by Mg^{2+} or Sr^{2+}, PO_4^{3-} by CO_3^{2-} (B-type substitution) and OH^- by Cl^-, CO_3^{2-} or F^- (A-type substitution) [38, 73]. Some of these substitutions can influence the Ca/P ratio. One option for an elevated Ca/P ratio is the partial incorporation of carbonate groups at phosphate positions. The ATR-FTIR spectra (Figure 26) of the glass powder after the dissolution tests show carbonate substitution in the formed apatite as well. The Tris buffer solution used for dissolution tests on powder does initially not contain carbonate. So, one option is the incorporation of carbonate, originating from dissolved CO_2 from the air above the Tris buffer solution in the reaction beaker. The SBF solution used for the dissolution tests on discs comprises 10 mmol/l HCO_3^-. According to Müller et al. [53] HCO_3^- can be incorporated, leading to the formation of a hydroxycarbonate apatite. The chemical composition of the inorganic part of the human blood plasma is similar to that of SBF solution. Presumably, a crystalline phase close to the biological apatite in human bones which contains a CO_3^{2-} substitution up to 8 wt% [53] precipitates. The ratios of Si/P and Si/Ca in the apatite layers are between 0.1 and 0.5, as expected. One reason for the presence of Si in the apatite layer could be the substitution of SiO_4^{4-} at PO_4^{3-} positions [73]. The silica-gel layer of all glasses exhibits high Si/P (10-20) and Si/Ca ratios (5-12), which was expected as SiO_2 is the main component in this layer. Two XRM pictures of glass disc 25B after 7 days in SBF solution, are presented in Figure 30, whereas A) shows a perspective view and B) a detailed one. Like in the SEM pictures, three phases are detectable: the base glass, layer one and layer two. Layer one corresponds to the layer of the leached glass and layer two to the formed apatite. The XRM pictures show nicely, that the thickness of the apatite and of the silica-rich layers are not uniform, which agrees with the SEM investigations of the cross-sections. Molecular dynamics simulations by Tilocca et al. [35] suggest that the bioactive glass surface is not homogeneous and that there are preferred absorption sites for water molecules. This means that the ion exchange does probably not occur on the entire bioactive glass surface at the same rate, leading to different layer thicknesses. Depending on how fast ions are exchanged in the glass, the ion concentration in the solution varies. In general, the precipitation of apatite requires a local supersaturation of calcium, phosphate and hydroxyl ions in the solution. In the XRM pictures, Figure 30, the apatite layer seems to be thick at positions where the depth of the silica-layer is thick as well. That would suggest that a deep ion-exchanged layer provides a large local ion concentration, thereby enhancing local apatite precipitation. However, for the cross-sections investigated using SEM the thickness of the apatite layer does not seem to correlate with the one of the silica-rich layer. The SEM sample preparation included breaking the sample, glueing, embedding and polishing. During this procedure, it is possible that a part of the brittle apatite layer may break off, especially at areas of larger thickness. The morphology of the surface might have an influence on the apatite formation as well. During sample preparation, the discs were only cut, but not polished. Therefore, the surface of the discs exhibits a certain roughness. The areas, which are more exposed to the solution, e.g. top of a hill, can be ion-exchanged from multiple sides at the same time. An area in a valley cannot, but a higher local ion concentration can be expected here. In the XRM picture, it looks like the hills show apatite formation in contrast to the valleys. In SBF solution the ion concentration is much higher than in Tris buffer solution. So, the situation in Tris and SBF is different. Kirste et al. [72] investigated the apatite formation on glass powder in different Tris buffer solutions. They found areas covered with apatite preferentially in gaps and corners between the glass particles. The assumption made here was, that the protected areas lead to higher ion concentrations of calcium and phosphate in solution, which enable the local apatite precipitation. Surface imperfections like small scratches might act as nuclei for the crystallisation of the forming apatite, which could lead to inhomogeneous growth of the apatite along the sample and subsequently to this appearance as well.

The ability to form apatite on the surface is a very important property of an implant material. The apatite formation on the surface supports the osteointegration of the implant. Originally the term osteointegration was used to describe the biological fixation of a titanium dental implant [115]. Nowadays the term is used to define the direct-structural and functional connection between living bone and the surface of a dental or orthopedic implant.

For clinical applications, an earlier apatite formation in the human body potentially is of great advantage. A good performance at early instants of time is beneficial for the incorporation of the implant. A big problem is the infection with bacteria during implantation [116]. Chouirfa et al. [117] reviewed surface modifications and coatings of titanium implants to reduce the bacterial adherence. Chemical methods for surface modifications are more expensive and often require several steps in comparison to physical methods. The topic of implant surface modifications is a research area with a potentially growing interest among others because the reduction of antibiotics is desired. Nowadays, after implantation, patients are often treated with antibiotics to reduce the risk of an infection at the implant site. Presently, in orthopaedic surgery, the infection risk is 2-5 % [117]. To achieve high success rates for dental implantation the use of antibiotics is required to prevent postoperative infections, see the review by Surapaneni et al. [118]. Anyway, reimplantation because of infections and the resistance of bacteria to antibiotics are common clinical problems [116, 119, 120]. Another advantageous influence of the boron-containing glasses might be the pronounced ion release, see Figure 24, and the steep initial pH rise, see Figure 23. The alkaline environment and a continuous release of ions show antimicrobial effects [121]. If the body cells are supported by the implant with early hydroxyapatite formation, the bond to the human tissue (bone) is favoured.

In the following chapter the ***thermal and the crystallisation behaviour*** of the glasses of series 45S5-B will be discussed.

The glass transition temperature T_g of the glass series 45S5-B was investigated using dilatometry, see Figure 31 and DSC analysis, see Figure 33. With increasing boron content in the glass, the dilatometry measurements show a decrease in T_g of about 50 K. In the DSC measurements the clear decrease in T_g is visible as well. Whereas the decrease of T_g is clearly visible in the dilatometry results when considering the entire series, no decrease is apparent for the glasses 45S5, 0.5B, 1B and 2.5B. For the glasses 0.5B, 1B and 2.5B the changes in T_g are smaller than the error of the measurement. For those glasses, only a relatively small amount of B_2O_3, see Table 3 in chapter 3.1.1, was introduced. Potentially, the composition of these glasses is influenced by losses during glass processing leading to small variations in T_g. The decreasing T_g, taking into account the whole series, agrees with studies by Ren et al. [96], who investigated the B for Si substitution on a glass system with a higher SiO_2 content. Whereas the SiO_2 content in their study was up to 56.5 mol%, for the series 45S5-B it is between 36.7 mol% and 46.1 mol%. The shift of the glass transition to lower temperatures with B for Si substitution was expected because of the decrease of polymerisation in the glass series 45S5-B, which was discussed earlier. According to our structural investigation, see chapter 4.1.2, most of the boron is present in form of BO_3 units, while BO_4 is the minor species. The three-fold coordinated boron species BO_3 is expected to enable an increased mobility in the glass network. For glass 45S5 one broad crystallisation peak and two melting peaks were observed. From glass 5B and further, another crystallisation peak appeared at higher temperatures, while the first one is shifting to lower temperatures. Glasses 15B and 20B even exhibit three crystallisation peaks. Regarding the melting, for glasses 45S5 to 10B, multiple peaks are visible at about 1200°C, while the melting in general starts at lower temperatures with increasing boron content. The glasses 15B, 20B and 25B exhibit an additional melting peak at about 850°C. As mentioned before, with increasing B for Si substitution, the network polymerisation of the glass series 45S5-B decreases. Upon increasing the temperature, the less connected structure causes an elevated mobility of atoms present. So, the B for Si substitution leads to earlier glass transition, glass crystallisation as well as glass melting. The multiple crystallisation peaks, as well as the additional melting peak at ~ 900°C for the glasses with a high boron content, provides evidence of the formation of additional crystal phases. Interestingly, only one glass transition per glass is visible, although the presence of a major silicate-rich phase and a minor sodium-borate rich phase is likely. Probably only the T_g of the major silicate-rich phase is visible, see Figure 33. The thermal effect of the glass transition of the minor phase is possibly not strong enough to cause a signal in the dilatometry and DSC analysis. The position of this potential second T_g is difficult to predict, as the distribution of the ions in the assumed two phases is not known.

The glass stability is the resistance of glass against devitrification during heating [44]. ***Glass stability parameters*** (GSP), calculated from the DSC data, are presented in Figure 34. For multiple crystallisations, the lowest temperature peak was considered to calculate GSP. For the calculation of the parameters, four different equations were used: Saad & Poulain K_{SP}, Lu & Liu K_{LL},, Hrüby K_H and Weinberg K_W, see chapter 3.1.4. As shown in Figure 34, the K_{SP} parameter is ~3.6 for all glasses of the 45S5-B series. However, as for the K_{LL}, the K_H and the K_W parameter a small increase within the glass series can be seen, therefore a slightly increased stability towards crystallisation is assumed. Nascimento et al. studied the glass stability of eight different glass-forming systems. The glass stability parameters they obtained, are in the following range: K_{SP} ~3-28, K_{LL} ~0.40-0.52, K_H ~0 -1.4 and K_W ~0.01-0.24, see Table 27.

Table 27: Comparison of the glass stability parameter range of series 45S5-B with results by Nascimento et al. [44] who investigated eight different glass systems.

Glass stability parameter	GSP range of eight different glass-forming systems by Nascimento et al. [44]	GSP results of glass series 45S5-B
K_{SP}	~3-28	~3.6
K_{LL}	~0.40-0.52	~0.40-0.47
K_H	~0-1.4	~0.15-0.5
K_W	~0.01-0.24	~0.05-0.09

The question "How is the influence of the boron substitution on the crystallisation tendency" asked in the Introduction & Motivation can be answered here. In comparison to the study by Nascimento et al., the values for glass system 45S5-B are in the same range, but in general in the lower area of that GSP range. So, although there is a small increase with B for Si substitution in comparison to the eight different glass-forming systems tested by Nascimento et al., the glass stability of the series 45S5-B is low. The low glass stability of the glass series 45S5-B agrees with the well-known high tendency towards crystallisation for bioactive glasses [12] which makes the glass processing at high temperatures complex. The reason for the high tendency towards crystallisation of the bioactive glass can be ascribed to the low polymerisation of the glass structure. The low polymerisation enables a high degree of movement and rearrangement of the building units in the bioactive glass at relatively low temperatures.

The following chapter outlines the ***crystallisation*** of glasses in general. On the one hand there is the intended fabrication of glass ceramics, which requires the controlled crystallisation of a glass [122]. After the fabrication and the quality control of the glass, nucleation and crystal growth are necessary subsequent processing steps to obtain a glass ceramic. It is desired to have a high nucleation rate and a low crystal growth during the nucleation. In the subsequent processing step, crystals grow on many nuclei. So, for the well-controlled production of glass ceramics, a small overlap of the nucleation range and the crystal growth range is beneficial. Glass ceramics contain at least one functional crystalline phase and a glass phase, whereby the crystallised volume can vary in a broad range, from ppm to almost 100% [123]. From the glass system Li_2O-Al_2O_3-SiO_2 (LAS), β-eucryptite, β-quartz, spodumene or keatite can be crystallised [124]. This glass ceramic system is of large economic importance as it is in mass production, mainly by Corning Glass and SCHOTT AG [124]. Commercial low-expansion glass ceramics are usually composed of many oxides each having a specific function [125]. Caused by the low thermal expansion, glass ceramics enable the usage in applications, which rely on a very low thermal expansion, like substrates of large telescope mirrors as well as the famous kitchen Ceran® cooktop. The thermal expansion of the crystallised phases in glass ceramics can vary in a wide range [126]. The production of materials having zero thermal expansion is possible as well [127]. On the other hand, there is the unintended crystallisation of a glass, like the crystallisation of a bioactive glass during heat-treatment. Commercially available bioactive glasses, like Bioglass® (glass 45S5) and Bonalive® (glass S53P4) exhibit a high tendency towards crystallisation [128], which unfortunately limits their hot-forming workability. Sintering of bioactive glass particles, which is one option to form 3D shapes, is usually inhibited by crystallisation [46]. Upon heat treatment of glass 45S5, separation in a silicate-rich and a phosphate-rich phase takes place [129], being a preliminary stage before crystallisation [26]. The heating microscopy experiments on glass series 45S5-B resulted in crystalline sodium calcium silicate powder compacts, which agrees with the DSC results and the generally low GSP values.

In the following chapter the ***crystallisation behaviour*** of glasses 45S5, 5B, 15B and 25B involving the results of the activation energy for viscous flow, the activation energy for crystallisation and crystallisation dimensionality will be discussed. All investigated glasses showed distinct crystallisation peaks (T_{ps}). As discussed in the chapter of the structure of the glass series 45S5-B, with B for Si substitution the structure is less polymerised. Upon temperature increase, the less connected structure leads to an elevated mobility of the atoms in the glass and thus to a shift of the onset of crystallisation to lower temperatures with B for Si substitution. The crystallisation for the boron containing glasses at lower temperatures in comparison to glass 45S5 can be ascribed to that. For the coarse particles, the working range shows a pronounced decrease with B for Si substitution. However, the working range for all coarse glass powders is above 100 K, which should allow shaping of 3D structures via viscous flow [12]. If viscous flow takes place before the crystallisation, hot-forming would be possible. However, a high activation energy for viscous flow and a large fragility of a glass, can lead to crystallisation although the working range is large [12], which was shown for the bioactive glass S53P4, Bonalive® [46, 130].

Moreover, the working range values for the fine particles show a slight increase with B for Si substitution, which agrees with the increase in their glass stability parameter. The nature in the crystallisation mechanism of the fine powder in comparison to the coarse powder will be explained later.

Lefebvre et al. investigated Bioglass® 45S5 upon heating using a heating rate of 5 K/min [129]. They found phase separation in a silicate-rich phase and a phosphate-rich phase to occur at 580°C. In their study the major phase sodium calcium silicate $Na_2CaSi_2O_6$ crystallised at 610-700°C, whereas a secondary phase named silico-rhenanite $Na_2Ca_4(PO_4)_2SiO_4$ crystallised at 800°C. The major phase sodium calcium silicate evolves from the silicate-rich phase and the silico-rhenanite phase from the phosphate-rich phase. So potentially, in our study, 45S5 forms two phases upon heating, whereas both crystallisation peaks heavily overlap. To gain a deeper insight into the crystallisation behaviour, investigations with a scanning electron microscopy during crystallisation using an in-situ heating stage could be used.

Introducing boron into the glass system leads to more separated crystallisation peaks of the different forming phases, see Figure 35. Replica pictures verified phase separation, as discussed earlier, whereas the formation of a borate-rich and a silicate-rich phase is assumed. Subsequently, upon heating, the formation of a silicate-rich crystal phase and a borate-rich crystal phase is expected.

With increasing boron content in the glass, an earlier start of shrinkage is presented in the high temperature microscopy for the fine particles, Figure 36. Although the working range for the fine particles increases slightly, Table 8, HTM clearly shows a decreased shrinkage with increasing boron content. Therefore, the ***sintering ability*** of the glasses with boron is decreased in comparison to glass 45S5. The sintering in the area ~600°C nicely corresponds to the crystallisation in the DSC thermogram, Figure 36A. The sintering in the low-temperature area is stopped by the starting crystallisation of the glass. The further decrease of area in the HTM graph at the first crystallisation peak can be explained with the formation of sodium calcium silicate, which is assumed to be the main crystalline phase forming and has a higher density in comparison to the bioactive glass. Whereas the density of the bioactive glasses is about 2.7 g/cm^3, the density of the forming sodium calcium silicate is expected to be higher due to increased order in the structure. This assumption is supported by the density of synthetic crystalline sodium calcium silicate, which is with 2.82 g/cm^3 [131] larger than the density of the bioactive glasses investigated here. Because of the crystallisation of a crystalline phase from an amorphous glass, no stochiometric formation of sodium calcium silicate can be expected. However, the density of the forming crystal is assumed to be larger than the density of the glass. In the high-temperature area, the boron-containing glasses shrink at lower temperatures in comparison to glass 45S5, see Figure 36.

Bretcanu et al. [132] investigated the sintering and crystallisation of 45S5 Bioglass® powder. They detected the formation of two crystalline phases. The main crystal phase is assumed to be a sodium calcium silicate phase and the minor phase a phosphate phase [132]. They found these crystalline phases to start melting between 1150 and 1180°C, which agrees with the investigation here, see DSC results Figure 33. As discussed earlier, in the boron containing glasses the presence of a borate-rich phase and a silicate rich phase is assumed. So, the formation of more than one crystalline phase is likely, which is supported by the DSC results here, too. The starting melting of the expected borate-rich phase could be an explanation for the shrinkage in the temperature range at ~800°C. In comparison to the crystalline sodium calcium silicate phase and the crystalline phosphate phase forming in bioactive silicate glass, the crystalline borate-rich phase is expected to melt at lower temperatures. The composition of the assumed borate-rich phase in the glass is not known. In the crystalline samples of the whole glass series 45S5-B, powdered after HTM investigation, see Figure 32, no phase besides sodium calcium silicate was detected. Potentially the amount of the second forming phase is small and their crystallinity poor, which impedes its detection. The melting point of the crystalline borate phase sodium tetraborate is at 741°C [133], whereas there is a melting peak at ~830°C in the DSC for glasses 15B and 25B. In our study, a crystalline borate-rich phase enriched with Si-species could be present. This potential phase could have a higher melting temperature in comparison to a borate phase, which does not contain Si-species.

The ***activation energy for viscous flow*** was calculated using the Kissinger equation, see Table 28.

Table 28: Activation energy of viscous flow accessed using the Kissinger and Moynihan model.

	5B		15B		25B	
	<38 µm	**500-1000 µm**	**<38 µm**	**500-1000 µm**	**<38 µm**	**500-1000 µm**
Kissinger						
Ea (kJ/mol)	422	430	498	611	616	509
±	85	9	73	146	121	17
Moynihan						
Ea (kJ/mol)	435	444	511	624	628	522
±	85	9	73	146	121	17

According to Blaine & Kissinger, the Kissinger method is fast and reliable in use and “one of the most popular approaches for determining kinetic parameters by thermal analysis” [56]. However, the Kissinger model has been developed for chemical reactions [134]. So, to verify the Kissinger model calculations, the Moynihan model [135] was applied additionally, see results in Table 28. In both models, the activation energies are calculated from T_g, depending on the heating rate and the calculations result in the same individual activation energies. The activation energy for viscous flow for glass 45S5 was investigated by Massera et al. [46].The values found there were 745 ± 30 kJ/mol for fine glass powder (<45µm) and 757± 30 kJ/mol for coarse glass powder (300-500 µm). The activation energies for viscous flow of the boron containing glasses have large error ranges, see Table 28. So, no clear trend with boron content is visible. In comparison with the activation energies for crystallisation, the activation energies for viscous flow are high. A high activation energy of viscous flow together with rapid crystallisation kinetics can inhibit hot-forming even if the working range is >100 K [12]. Although the working range shows an increasing trend with B for Si substitution for fine particles, the working range is below 100 K. So, regarding the processability of the glass powders, 5B is expected to perform better in comparison to 15B and 25B.

The crystallisation behaviour of the glasses was examined by calculating the ***activation energy of crystallisation*** with two different models: Kissinger and Friedman. As expected, with the increased heating rate, the crystallisation peak shifted to higher temperatures due to thermal lag [46], see Figure 37. The Kissinger equation is known to have limitations regarding the description of crystallisation processes. One of its assumption is that there is only one mechanism and so kinetics parameters are the same during the reaction although this is seldom the case [56]. The activation energy determined at the peak of the reaction might not be the same in comparison to early or late stages of the same reaction. So, the Kissinger equation is only valid in case of needle-like surface crystallisation [12]. The coarse particles in this study show no simple needle-like surface crystallisation. The Friedman model was additionally used for the coarse particles, as this method makes no mathematical approximations [77]. There are no drastic changes in the activation energy of crystallisation comparing glasses with different boron content and particle sizes, Table 9. The activation energy of crystallisation for glass 45S5 calculated by Massera et al. [46] is for fine powder with 338 ± 30 k J/mol equal to the values calculated for particles of glass 5B and for coarse powder with 230 ± 30 kJ/mol similar to them. The results of the Friedman calculation, Figure 38, propose that for the coarse particles there is one crystallisation mechanism per glass because the values for the crystallisation energy Ec in dependency on α (fraction of glass crystallised) are within ±10 %.

Jean et al. [136] and Moğulkoc et al. [137] studied the activation energy for crystallisation in traditional borosilicate glasses, see Table 29.

Table 29: Overview of the investigated glass shape, activation energy of crystallisation and forming crystals for Pyrex® from Jean et al. [136], BOROFLOAT® 33 from Moğulkoc et al. [137], for a boron containing glass series starting from glass S53P4* by Fabert et al. [12] as well as glass series 45S5-B.

Glass type	Pyrex®	BOROFLOAT® 33	S53P4 series*	Series 45S5-B
Shape	pressed powder	bulk	particles	powder
Activation energy of crystallisation	70-80 kJ/mol	185 ± 10 kJ/mol	308 ± 30 to 248 ± 30 kJ/mol	245 ± 4 to 323 ± 1 kJ/mol
Proposed mechanism	diffusion of Na^+ ions	diffusion of boron	complex crystallisation	complex crystallisation
Type of crystal	cristobalite	cristobalite	various crystal phases depending on the substitution	sodium calcium silicate

Jean et al. [136] investigated the devitrification of the borosilicate glass Pyrex®. According to their study cristobalite is formed. Jean et al. determined an activation energy of 70-80 kJ/mol, which suggests the diffusion of Na^+ ions as the rate-limiting step during the crystallisation. Moğulkoc et al. [137] investigated the crystallisation behaviour of bulk samples of borosilicate glass BOROFLOAT®. The activation energy for crystal growth is estimated to be 185 ± 10 kJ/mol, which is assigned to the diffusion of boron during the crystallisation of cristobalite. For the crystal growth of cristobalite, boron "needs to be pushed out of the amorphous silica framework" [137]. Fabert et al. [12] investigated the crystallisation and sintering behaviour of a boron containing glass series starting from glass S53P4. In their glass design B_2O_3 is substituted by SiO_2 up to 100% and particles are used. Depending on the substitution different crystal phases are formed, while the activation energy of crystallisation is in the same range like for the glass series 45S5-B.

According to Clupper and Hench, during the crystallisation of 45S5 the breaking of Si-O and P-O bonds is unlikely due to the high strength of these bonds: 443 kJ/mol respectively 464 kJ/mol [138]. Ca-O and Na-O bonds are more likely to break during crystallisation as their bond strength are with 111 kJ/mol and 84 kJ/mol [138] lower than the activation energy for crystallisation [139]. The activation energy for crystallisation for the 45S5-B glasses was higher in general than for Pyrex® and BOROFLOAT®, between 245 ± 4 kJ/mol and 323 ± 1 kJ/mol depending on the glass and on the applied model. It is assumed that the crystallisation mechanisms occurring in these borosilicate glasses cannot be transferred easily to the bioactive borosilicate glass because of the different structure of the glasses. The structure of BOROFLOAT® is assumed to be very similar to the one of Pyrex®, which was discussed earlier in this chapter and both exhibit a large amount of Q^4 units. In contrast to that, the bioactive glasses exhibit a large amount of Q^2 units and a large amount of network modifier atoms. In the end, the bioactive glasses of glass series 45S5-B crystallise mainly to sodium calcium silicate while Pyrex® and BOROFLOAT® crystallise to cristobalite. However, maybe there is a parallelism: the diffusion of the boron, like suggested by Moğulkoc et al., could play a role in the glass series 45S5-B as well. Earlier in the discussion it was assumed to have phase-separated glasses. In the major silicate-rich phase, an amount of boron could diffuse upon crystallisation of the calcium sodium silicate here as well. The interaction of the network modifier ions sodium and calcium, which interferes with the potential diffusion of the boron, could be the reason for the higher activation energy of crystallisation in comparison to the glass BOROFLOAT®. Within the glass series, the ratio of boron to the network modifier atoms sodium and calcium increases. So, the influence of the network modifier atoms on the potential boron diffusion would be lower with B for Si substitution. However, the distribution of the atoms in the assumed two phases, major silica-rich phase and a minor borate-rich phase see earlier in this chapter, is not known. For both crystallisation studies on bioactive glasses a complex crystallisation is assumed.

It is important to mention that for all investigated glasses in both particle sizes, the activation energy for viscous flow is higher than the activation energy for crystallisation, see Table 9, which is confirming the strong tendency of these bioactive glasses to crystallise during thermal treatment [139]. The strong tendency towards crystallisation is not desired and, as mentioned earlier, impedes the processing of the bioactive glasses at elevated temperatures.

The ***crystallisation dimensionality*** was investigated, as it can provide information whether crystallisation is initiated at the surface or in the bulk of the glass. If crystallisation is surface initiated, sintering is likely to be partially or fully inhibited. For bulk crystallisation, it would be possible that the remaining glassy phase goes through viscous flow enabling the sintering of particles. As mentioned in chapter 2.4, the JMA exponents can be assigned to different crystal growth behaviours: 1 surface crystallisation, 2 volume crystallisation in 1D, 3 volume crystallisation in 2D, 4 interface correlated volume crystallisation in 3D, >4 complex crystallisation in 3D [46, 47], see Table 30.

Table 30: JMA exponents assigned to different crystal growth behaviour acc. to Massera, Fagerlund et.al. [46] and Massera, Mayran et al. [47].

JMA exponent	crystal growth behaviour
1	surface crystallisation
2	volume crystallisation in 1D
3	volume crystallisation in 2D
4	Interface correlated volume crystallisation in 3D
>4	complex crystallisation in 3D

The Ozawa plots, in Figure 38 show the JMA exponent in dependence on the temperature during the crystallisation for the coarse glass particles. For glass 5B the values between 685°C and 705°C are between 3.2 and 2.6. For glass 15B the JMA exponent lies between 3.9 (660°C) and 1.9 (679°C), which is not in accordance with the Friedman statement of the presence of one crystallisation mechanism. So, according to JMA results during the heating process, there is a change from a more to a less complex crystallisation type e.g. from a spherical to a needle-type shape. In total, the shape of the formed crystals could look like sea urchins. For glass 25B the temperature-versus-alpha plot for the four heating rates is broad, which leads to a very narrow temperature range for the Ozawa plot. Here the JMA exponent changes slightly from 4.2 (614.6°C) to 3.9 (616°C). The fine powders of glass 5B and 25B have JMA exponents (Augis-Bennett) of 1.1 and 1.2, which suggest surface crystallisation. Earlier studies investigating the behaviour of glass 45S5 in particle sizes of <5 µm and <32 µm by Baino and Fiume [132] as well as of glass 45S5 in particle size <45 µm by Massera et. al [46] showed surface crystallisation as well.

If the validity of the JMA model would be assumed, the following conclusions could be made. A bulk crystallisation in 1D or a mixture of bulk and surface crystallisation could be suggested by the JMA value around 2 for fine glass powder 15B. For all glasses, the JMA value changed with particle size, which suggests changes in crystal dimensionality for the fine in comparison to the coarse glasses. According to the results, in all coarse glasses, no simple nucleation and growth processes are present, but more complex crystallisation processes. A change in the JMA exponent from ~1 for the fine powder to ~3 for coarse powder like shown here for glass 5B was presented for glass 45S5 by Massera et al. [46]. The surface crystallisation in the fine glass powders is not a property of the glass but induced by a large surface to volume ratio. The smaller the particle size, the larger is the surface area of the glass powder and therefore the number of nucleation sites for potential surface crystallisation [140]. Bioactive glasses, crystallising in the volume, would provide the potential for the sintering of 3D scaffolds, which would be very interesting. To verify the calculations and to gain deeper insight into the shape of the formed crystals, advanced SEM investigations should be carried out. Electron backscatter diffraction would be a suitable technique as it enables to detect crystal orientations in microstructures [141-143]. The glasses of series 45S5-B exhibit phase separation like discussed earlier. So, regarding the crystallisation of the glasses, not a simple nucleation and crystal growth process of one phase can be assumed. There often is more than one crystal phase forming and the crystallisation peaks are partially overlapping. Therefore, the application of the JMA model probably is inadequate, as suggested for glass 45S5 in crystallisation studies by Massera et al. [46] as well as by Baino and Fiume [139]. The application of a proposed model by Malek et al. could be used to proof the validity of the JMA model for the glasses [46].

The volume samples of glasses 5B, 15B and 25B, which were heat-treated at 5 K below T_x, exhibit the formation of sodium calcium silicate and the microscopy pictures from glass 5B show snow-flaky structures in the volume of the glass. According to XRD investigations, those structures are aggregates of a material having a density considerably lower in comparison to the crystalline matrix. As it follows, pore formation or a remaining amorphous phase are the two possibilities. ***Pore formation*** upon crystallisation has been seen earlier [144]. Because the density of the forming crystal phase is larger than the density of the glass, there is a decrease in volume required for the material upon heating. Due to stress relief, the formation of pores is energetically preferred [145]. Furthermore, SEM pictures of Massera et al. show similar structures for heat-treated glass 45S5 [46]. So, probably the formation of partly connected and single pores occurs upon heating.

The relevance of pores in an implant in the potential application will be discussed here. On the one hand, pores in implants can be of great advantage as they allow the infiltration of body tissue thereby promoting the structural and functional connection between the living bone and the surface of the implant, called osteointegration. However, to enable this infiltration the diameter and the connectivity of the pores play an important role. Blood vessels like capillaries need a certain diameter and connected pores to penetrate the implant. On the basis of cell size, migration requirements and transport, the required minimum pore size is ~100 µm, but >300 µm is recommended for the formation of capillaries [146]. On the other hand, pores lead to a decrease of strength of the material, which needs to be considered especially in load bearing applications. The mechanical strength is lowered in comparison to a material without pores. The pores visible in the XRM are not connected and the size of the pores is not homogeneous. So, there is no benefit expected from these pores in the potential real application, whereas the controlled formation of pores is of great importance.

As mentioned earlier, fine glass powder crystallises easily at the surface caused by the large surface to volume ratio. In contrast to that, the crystallisation study on the coarse particles provides information about the behaviour of the (bulk) material. Upon B for Si substitution the working range for the coarse particles decreased, which can be assigned to the less polymerised network of the glass. The JMA model results partially suggest real volume crystallisation. However, as proposed earlier, the JMA model is highly likely to be invalid for the glass series 45S5-B, as caused by the phase separation, no simple nucleation and growth process is present. As discussed for the structure of the glass series 45S5, the existence of droplet-in-matrix phase separation is assumed. So, a surface-initiated crystallisation at the phase boundaries of the phase separated structures is more likely, than a real volume crystallisation. A complex surface crystallisation of sodium calcium silicate at the boundary of the phase separated sodium-borate rich droplets can be proposed. The pore formation in the bulk material could be caused by the shrinkage of the glass material upon crystallisation afterwards as discussed earlier or simultaneously. So maybe with the JMA approach used here, a combination of the complex surface crystallisation and the pore formation (for glass 5B) is investigated. As pores are assumed to form at positions with high stress, their formation within the crystallisation area is likely. However, the snow-flake shape of the pores of sample 5B cannot be explained so far. In the study by Massera, Fagerlund et al. [46], the activation energy for crystallisation for glass 45S5 is similar to the one of the boron containing glasses found in this study. Furthermore, the structures in the SEM pictures in their study seem to be pores as well. Lefebvre et al. found phase separation upon heating in glass 45S5 in a silicate-rich phase and a phosphate-rich phase [129], as mentioned earlier in this chapter. Potentially the process including phase separation, crystallisation and pore formation is similar in glass 45S5 like for the glasses of series 5B. Bulk samples of the glasses 15B and 25B did not show pores after heat treatment. So, for these compositions a process including phase separation and crystallisation is assumed.

As mentioned before, bioactive glass particles and granules can be prepared relatively easily, whereas complex shapes requiring forming of the bioactive glass at elevated temperatures are difficult to obtain. However, the systematic investigation of the influence the ***crystallisation*** has ***on the solubility*** is valuable in respect of the future development of implants. The following section focuses on the impact of crystallisation on solubility. Here, the dissolution behaviour of the (partly-)crystallised samples in comparison to the amorphous samples will be discussed. The results of the pH-value measurements nicely agree with the ICP-OES results. In general, for the amorphous glass powders, the pH-value increases to relatively high values ~8, and a high number of ions can be found in solution after the dissolution test. So, the exchange reaction of hydrogen ions (from the Tris buffer solution) and the network modifier ions sodium and calcium (from the glass) proceeds to a large extent. For the (partly-)crystallised samples, the increase in pH-value is less pronounced at the timepoint 24 h, whereas the increase during the first 6 hours is in the same range as for the amorphous glasses. For the ICP-OES results no increase of ions in the solution is present between 6 h and 24 h for (partly-)crystallised glasses 45S5c, 5Bc and 15Bc, which agrees nicely with the steady pH-value in this range. Only for 25Bc the ion concentration for Na, Ca and P is very similar for the (partly-)crystallised and amorphous glass. As sodium and boron are found in the solution in a similar amount for all experiments, the assumption made earlier of having a silicate-rich phase and a sodium-borate rich phase, is supported here.

As described in chapter 3.1.5, the heat treatment of the glasses to achieve (partly-)crystalline glasses was carried out up to the maximum of the first crystallisation peak. For the glasses 5B, 15B and 25B smaller second and third (for 15B) crystallisation peaks at higher temperatures are present. So potentially, the major sodium calcium silicate phase crystallises earlier while the minor sodium-borate rich phase is still amorphous. The sodium calcium silicate phase is the major crystalline phase as verified by the XRD results. As discussed for the solubility behaviour of the glass series 45S5-B, the borate-rich phase is easily attacked by water leading to a fast release of ions in a high amount. So, the potentially fast dissolution of the sodium-borate rich phase can be assumed here which is supported by the pH and ICP-OES results. Probably this more soluble phase dissolves fast and thereby completely during the first 6 h for 45S5c, 5Bc and 15Bc leading to the constant value between 6 h and 24 h. For the (partly-)crystallised glass 25Bc the situation is a bit different. Here a slight increase in the normalised ion concentration between 6 h and 24 h is visible. As discussed before, the ion exchange reaction in glasses with a high boron content can proceed faster than in the more connected glass 45S5. Possibly there is a larger ion release depth with B for Si substitution in the (partly-)crystallised material. When the more soluble borate-rich phase is dissolved, the remaining crystallised phase is less soluble in comparison to amorphous glasses. The presence of this crystallised phase in a large amount markedly slows down the leaching in the (partly-)crystallised glasses 45S5c and 5Bc. The amount of P present in the solution after 6 h is in general higher for all the (partly-)crystallised samples than at 24 h. So, this decrease in the amount of P present in the solution indicates the formation of a P-containing precipitate. For all (partly-)crystallised glasses in comparison to the amorphous glasses, a higher amount of Si can be found in the solution. During the first 6 h, the release is relatively high, whereas afterwards no further release occurs. It can be assumed that potentially Si surrounding the sodium-borate rich areas is released simultaneously. Furthermore, the release of small amounts of Si potentially present in the sodium-borate phase is possible. As mentioned before the solubility of Si-species in water is limited [106] and strongly dependent on the pH value [107].

The characteristic double-band between 550 and 650 cm^{-1} together with a pronounced band at 1015 cm^{-1} in the FTIR indicate the presence of ***apatite*** for all the amorphous and (partly-)crystalline glasses after a 24 h stay in Tris, see 4.1.5. The pronounced band at ~613 cm^{-1} which is assigned to bending vibration of P-O in a crystalline environment agrees with the expected higher degree of order in the (partly-)crystalline samples. The intensity of the C-O bands (at ~870 cm^{-1}) is less pronounced for the (partly-)crystallised samples after the dissolution test than for the amorphous samples, suggesting incorporation of carbonate in the apatite lattice to a larger extent for the glasses. The XRD results show amorphous glasses before stay in Tris and apatite formation after 24 h in Tris, see chapter 4.1.5. For the (partly-)crystalline samples, the XRD reflexes can be assigned to sodium calcium silicate, which is assumed to be the main phase present before staying in Tris and after a stay in Tris for 45S5c, 5Bc and 15Bc as well. Interestingly, no second phase can be assigned to the XRD reflexes although having two phases would agree with the presence of a phase-separated glass which was heat-treated. Potentially an underlying remaining amorphous phase is not visible in XRD because the crystalline phase is the dominating one. (Partly-)crystallised glass 25Bc shows a special formation. As explained earlier, see 4.1.5, there are reflexes assigned to sodium calcium silicate, to apatite as well as an underlying amorphous halo. As traditionally the apatite is forming on the surface of the bioactive glass, see Figure 29 and Figure 30, the apatite formation can be considered as a type of surface crystallisation. The penetration depth of the used methods: ATR-FTIR and XRD are different, which is assumed to explain the different results regarding apatite formation on the (partly-)crystallised glasses during a stay in Tris. Whereas the FTIR shows apatite formation for all the samples, XRD results verify the presence of sodium calcium silicate for 45S5c, 5Bc and 15Bc and a mixture of phases present for 25Bc. The penetration depth of ATR-FTIR from the surface of the material is ~0.5-3 µm [147], whereas XRD measurements probe a larger volume of the specimen, which is up to 10 µm in depth [88]. So, potentially for the XRD measurements, the signal from the sodium calcium silicate is more intensive than the minor signal from the apatite on the surface. It can be assumed that on all (partly-)crystallised samples a thin layer of apatite is present which is detectable by FTIR. The thickness of the apatite layer on glass 25Bc is assumed to be thicker in comparison to the others, as XRD verifies the presence of apatite here as well. However, the reflexes for sodium calcium silicate are broad. So, the crystallinity is not pronounced, which agrees with the sensitivity of the (partly-)crystalline glasses towards an aqueous solution (Tris). The broad underlying halo of sample 25Bc after a stay in Tris has its maximum at the same position as the glass samples after staying in Tris, see also Figure 44. So, a formed silica-gel layer with apatite and calcium silicate crystalline phases is assumed here. The forming apatite for sample 25Bc, as verified by FTIR and XRD, nicely agrees with the high ion concentration detected via ICP-OES in the Tris buffer solution. As stated before, after the dissolution of the more soluble borate-rich phase, the remaining crystallised phase is more stable in comparison to the amorphous glasses. For glass 25B the borate-rich phase is expected to be present in a relatively large amount as the B for Si substitution is with 25 % comparatively high. It would be advantageous to investigate such a sample by EDX to gain insight into the formation of the phases present. Potentially the core is sodium calcium silicate, as this is the “material” the dissolution process has started from. A silica-rich layer around that core and the very outer layer of apatite would be a possible assembly. Peitl et al. [80], who crystallised 45S5 using thermal treatments to 8-100 % found apatite formation as well. In contrast to the study here, they used the immersion medium SBF solution. So, the ions necessary for apatite formation can be provided by the solution. In SBF even glass compositions without phosphorus have shown apatite formation [148]. Peitl et al. found the apatite formation to be faster for the samples crystallised up to 36 % in comparison to the ones with a higher amount of crystallised areas. After 40 h in SBF solution, their FTIR spectra showed apatite formation for all samples. The bioactivity of heat-treated glass 45S5 has been shown to decrease because of crystallisation processes [149]. During (partly-)crystallisation, on the one hand, the amount of crystal phase increases, and the amount of the amorphous phases decreases, which influences the bioactivity. On the other hand, the network connectivity of the remaining amorphous phase increases because of the formation of a crystalline phase [150]. However, the discovery of the apatite formation on the (partly-)crystallised glass 25Bc is very interesting, as it shows that a potential implant which crystallised (partially) e.g. upon hot-forming would still be able to form apatite on the surface.

5.2. Åbo glasses

In the Åbo glasses, five to seven components are present in different amounts, see chapter 3.2.1. Random glass compositions were chosen deliberately to test a broad composition range in combination with a relatively small number of glasses [10].

The Åbo glasses contain the following components: SiO_2, P_2O_5, B_2O_3, Na_2O, CaO, K_2O and MgO. First the role of these different components will be covered briefly. The Stanworth classification [21] of oxides (the anion is always oxygen) classifies the oxides according to the fractional ionic character of the cation-anion bond. Cations, which form bonds with oxygen with a fractional ionic character of ~50 %, usually act as network formers. The majority of the Åbo glasses contain the three network formers SiO_2, P_2O_5 and B_2O_3, leading to a complex system. In general, SiO_2 dominates the material, as it is the main component for all the glasses. Furthermore, Na_2O, CaO, K_2O and MgO are present. Whereas Na_2O, CaO and K_2O are known to act as network modifiers, MgO acts as an intermediate. Modifiers are cations, which have very low electronegativities. Accordingly, they form highly ionic bonds. Network modifiers are not able to act as network formers and they serve ions to modify the glass network. Intermediates cannot form a glass by itself but they can partially replace cations from the network former [21]. Blochberger et al. [151] investigated the ion release on Bioglass® 45S5, where calcium was replaced by magnesium up to 100%. The results suggested magnesium to act predominantly as a typical network modifier. Structure and property investigations on the glass system (mol-%) $49.5SiO_2$-$1.1P_2O_5$-$(23.0(1-x))CaO$-$xMgO$-$26.4Na_2O$ with $0 \leq x \leq 1$ by Watts et al. [152] have shown ~86% of the magnesium to act as a network modifier, while ~14% enter the silicate network. Magnesium plays an important role in bone development because it stimulates osteoblast proliferation and angiogenesis [153, 154]. This shows that magnesium is an interesting component in bioactive glasses. The influence of magnesium on the thermal properties of bioactive glass S53P4 was investigated by Massera et al. [153]. They found an increased working range in combination with a decreased tendency towards crystallisation. Tainio, who investigated the substitution of magnesium for calcium in the system $47.1SiO_2$-$6.7B_2O_3$-$22.7Na_2O$-$21.8CaO$-$1.7P_2O_5$ in mol-%, found the working range to increase from 30 to 50 K with a substitution of 5 to 10 mol% [76] and suggested magnesium to contribute to a stronger glass network.

The structure and properties of bioactive glasses are influenced by the field strength of the cations present. Glasses which are rich in high field-strength cations (e.g. Ca^{2+}, Mg^{2+}) degrade less than glasses which are rich in low field-strength cations (e.g. Na^{+}; K^{+}) [95].

The structure of the Åbo glasses is difficult to predict, making its investigation necessary. Besides, the amount and assembly of different network former units, the distribution of non-bridging oxygen atoms would be interesting to know.

An overview of the investigations carried out on the Åbo glasses is shown in Figure 69.

Composition
XRF"
Structure
XRD, ^{31}P & ^{11}B MAS NMR*, Raman, FTIR

" for 3 glasses exemplarily
* for 9 glasses only

Properties
density (pycnometry)
solubility
dynamic dissolution* (ICP-OES)
thermal properties
dilatometry
heating microscopy

Mathematical models
modified Anderson model (reaction number)
index of surface activity
linear approach regarding Tg & BA
Pearson´s coefficient of correlation
Fisher discriminant ratio

Figure 69: Overview of the investigations carried out on the Åbo glasses.

In general, the XRF investigations, which were carried out to investigate the glass ***composition***, showed similar results like for the glass series 45S5-B. As mentioned in chapter 5.1, there are various reasons for differences between the nominal and the analysed glass composition. For the Åbo glasses, differences in the amount of CaO and K_2O are noticeable, see XRF results, Figure 46. For both components, the amount was in general higher in the analysed composition than in the nominal one. It is known that the rate of alkali losses due to volatilisation decreases in the order Li - Na - K - Rb - Cs [21]. So, one would expect a lower loss of potassium in comparison to sodium, which agrees with the XRF results. It is assumed that there is no large change in the absolute amount of CaO and K_2O upon the melting of the glasses. The relative amount of the two components is higher in the analysed composition, probably due to volatilisation losses of the other components.

Exemplarily for the Åbo glasses, the structure property relationship on one glass, 1-98 will be discussed in the following chapter. From the applicational point of view, a bioactive glass should possess a medium to high solubility and apatite forming ability in the human body. Furthermore, a low crystallisation tendency is desired to enable the processing at elevated temperatures. The investigation of the structure of glass 1-98 showed a similar intensity of the Q^2 and Q^3 stretching bands in Raman spectroscopy and a relatively pronounced band of the Q^3-Q^2 stretching band in the FTIR measurements. So, for a bioactive glass, the network is relatively strongly polymerised. Most B-species are present as BO_3 (86%) and the majority (86%) of P-species is present as orthophosphate. As discussed earlier, these two factors are known to enforce the solubility of the glass. In comparison to other P-species, orthophosphate can easily be leached out of the glass. BO_3 units in the glass structure promote the solubility as the connectivity of the glass is decreased with these planar groups in comparison to 3D structure elements. The large amount of calcium in the glass composition of 1-98 is assumed to strengthen the glass network. Zhang et al. characterised bioactive glasses in vitro [54]. They combined dissolution tests in SBF with SEM investigations on glass discs and correlated the results. Thereby, the thickness of the forming layers on the bioactive glass, here named silica-rich and CaP layer, was investigated. Like for the SEM investigations on glass discs of series 45S5-B after a stay in SBF solution, cross-sections were prepared. Whereas the investigation of glass 45S5 presented a CaP layer thickness of 2.82 µm after 72 h in SBF solution, the CaP layer thickness of glass 1-98 at the same point of time was 0.56 µm. Whereas the surface of glass 45S5 was totally covered, the one of 1-98 was partly covered. The thickness of the silica-rich layer shows a nice correlation to the pH of the SBF solution. As expected, a large change in pH correlates with a thick silica-rich gel layer and a low pH change with a thin silica-rich layer. For glass 1-98 the pH increase was not pronounced and matches the defined in vitro reactivity “medium”. According to the dynamic dissolution investigations by Fagerlund et al.[20], glass 1-98 was assigned to group B, medium bioactivity here, which agrees nicely with the investigations by Zhang et al. [54]. The crystallisation kinetics of glass 1-98 were examined by Fagerlund et al.

[155]. Coarse glass powder, having a size of 300-500 µm, was used in their investigation. On the glass, surface crystallisation starting at around 800°C was found, whereas the primarily crystalline phase wollastonite, $CaSiO_9$ is formed. According to Arstila et al. [156] glasses like 1-98, which are in the wollastonite primary field, can be hot-formed at well controlled time-temperature conditions. That is a remarkable difference in comparison to the glass series 45S5-B, which mainly crystallises to the phase sodium calcium silicate. Arstila et al. stated, 45S5 is not “suitable to products which require heat-treatments” [156] caused by its low glass stability. However, glass 1-98 crystallises during fibre drawing, as well. Fibre drawing is typically done from melt and the drawing of fibres of bioactive glass is of interest, as potentially bioactive wound dressings could help in the recovery of wounds.

With 1-98, a glass is present, which exhibits some of the important characteristics: solubility, bioactivity and processability. The overall assumed connectivity of the network matches the dissolution behaviour “medium”.

Following up, the ***structure*** and the density of all the investigated Åbo glasses will be discussed. For the individual Åbo glasses the maximum of the glass halo in the XRD diffractograms is at different positions. This can be ascribed to a diverse distribution of interatomic distances of the atoms in the different glasses. The structure of the Åbo glasses is formed by the interaction of up to seven components, leading to a complex situation. However, XRD verified the amorphous nature for all Åbo glasses.

The Raman measurements show similar results for the high and medium bioactive Åbo glasses, see Figure 52. Whereas for the inert glasses, the band corresponding to the stretching of Q^3 groups is very strong in comparison to the Q^2 stretching band. The band at ~630 cm^{-1}, corresponding to delocalised vibrations of Si-O-Si [64] exhibits a pronounced intensity for the inert glasses, as well. Some of the Åbo glasses exhibited striae. To verify the influence of a stria on the recorded spectra, exemplarily for glass 6-92, a Raman line scan was performed. Striae are two dimensional [21], local discontinuities in the glass composition and visible because of alterations in the refractive index [157]. Among other reasons, they can be caused by an inhomogeneous melt or by a non-uniform density caused by volatilisation during melting and casting. The glass 6-92 exhibited the most intensive striae, see Figure 47. However, the ratio of the Q^2 to the Q^3 band along the striae was between 50 and 62%. So, there are small variations visible in the Raman spectra along the striae. However, concluding from the measurement on glass 6-92, the qualitative information from one glass compared to another glass is not influenced by striae in one glass. For the Raman measurements at least at two different positions on the glass slide spectra was recorded, see chapter 3. Like for the Raman spectra, for the high and medium bioactive glasses, the shape of the FTIR spectra looks similar. The spectra of the inert glasses in contrast to other bioactivity groups exhibit a less intense peak at 935 cm^{-1}. At this position stretching of B_4-O, Q^2 and Si-O-B overlap. For the inert glasses, this peak appears in the shape of a shoulder of the 1028 cm^{-1} main peak. According to the nominal composition of the glasses, the average amount of B_2O_3 is the same for the three groups, while the amount of SiO_2 is tendentially higher in the inert glasses, see Figure 45. The band intensity of the B_3-O stretching (1400 cm^{-1}) is similar in all three groups, Figure 51. So, a lower amount of Q^2 groups in the inert glasses in contrast to the bioactive glasses can be assumed.

Both methods, FTIR and Raman spectroscopy suggest a more connected network for the inert glasses than for the high and medium bioactive glasses, which was expected. For the different bioactivity groups, the concentration of the network formers, see 4.2.1 is plotted in Figure 45. The inert glasses are the ones with a higher SiO_2 concentration in comparison to the other groups. The structure of a glass system having three network formers is rather complex. However, as the amount of B_2O_3 and P_2O_5 is relatively low, in general, a larger amount of SiO_2 leads to a more connected structure and a decreased bioactivity, see chapter 2.2. For the B_2O_3 content, no difference is visible for the bioactivity groups. Glasses with a high amount of P_2O_5 exhibit high bioactivity. As mentioned in chapter 2.2, a glass is called bioactive, when living bone can bond to it [48]. As components of the thereby forming apatite are calcium and phosphorus, the correlation of a high content of P_2O_5 with elevated bioactivity was expected, as well. According to Mathew et al. [95], the phosphate content and the silicate network connectivity are the primary bioactivity-controlling parameters, which agrees with the results shown here. As the investigated Åbo glasses are composed of seven components including three network formers in random non-systematic proportions, a straight-forward study of their structure could not be expected. The Raman and FTIR spectroscopy results suggest a more connected network for the inert glasses in comparison to the glasses of other bioactivity groups.

Whereas the Raman and FTIR measurements were accomplished for all Åbo glasses, the ^{11}B and ^{29}P MAS NMR investigations were carried out on nine selected glasses only. The ^{11}B MAS NMR results show the presence of BO_3 and BO_4 groups for all Åbo glasses, see Table 31.

Table 31: Composition of the Åbo glasses 1606, 6-92, 10-92, 1-98, 20-92, 9-93, 206, 17-92, 17-93 together with 10B in mol%, the BO_3 resp. BO_4 amount according to B-11 MAS NMR results as well as the amount of peak 1 and peak 2 according to P-31 MAS NMR results.

								^{11}B MAS NMR		^{31}P MAS NMR	
Glass name	**SiO_2**	**Na_2O**	**P_2O_5**	**CaO**	**K_2O**	**MgO**	**B_2O_3**	**BO_3 (%)**	**BO_4 (%)**	**Peak 1 (%)**	**Peak 2 (%)**
1606	67.4	5.1	1.8	17	6.9	0	1.8	29	71	64	36
6-92	59.4	9.8	1.3	16.2	3.2	7.5	2.6	50	50	68	32
10-92	66.1	10	1.3	16.6	3.3	0	2.7	36	64	64	36
1-98	53.8	5.9	0.9	23.9	7.1	7.6	0.9	86	14	86	14
20-92	52.2	15.2	0	16.8	10	3.1	2.7	80	20	-	-
9-93	56.2	12.1	0.9	12.3	10	7.8	0.9	72	28	57	43
206	53	12.4	1.1	22.5	9.5	0	1.5	84	16	88	12
17-92	54.6	20.3	1.3	11.2	6.7	3.1	2.7	50	50	48	52
17-93	57	18.4	1.8	15.8	6.1	0	0.9	56	44	76	24
10B	42.5	24.9	2.7	27.5	0	0	2.4	86.7	13.3	100	-

For the glasses of series 45S5-B in general, the amount of BO_3 groups was above 80% and the amount of BO_4 below 20%. In an NMR study of Pyrex® by Howes et al. [158] a distribution of about 75% BO_3 units and of about 25% BO_4 units is verified. So, the ratio of BO_3 to BO_4 units in the glass series 45S5 and the Pyrex® glass are similar to each other, having BO_3 units in majority and BO_4 units in minority. For the Åbo glasses the situation is different. In the following four out of nine Åbo glasses, the amount of BO_3 units is high and the one of BO_4 is low, similar to Pyrex and 45S5-B: 1-98, 20-92, 9-93 and 206. But, the amount of B_2O_3 in these four glasses is different: 1-98: 0.9 mol%; 20-92: 2.7 mol%; 9-93: 0.9 mol% and 206: 1.5 mol%.

Glass 10B, which does contain 2.4 mol% B_2O_3, has 86.7% BO_3 and 13.3% BO_4 units. For glass 20-92 the amount of B_2O_3 (2.7 mol%) and the distribution of BO_3 and BO_4 (80 and 20 mol%) is similar to the one of glass 10B (2.4 mol%/86.7%/13.3%). However, for other glasses with a relatively large amount of B_2O_3, the distribution of BO_3 and BO_4 is completely different. In glass 1606, which contains 1.8 mol% B_2O_3, the majority of boron is present in the form of BO_4 units (71%), whereas BO_3 units are in minority (29%) here. So, for the Åbo glasses no obvious correlation between the amount of the two B-species and the concentration of the glass components can be found.

The ^{31}P MAS NMR results show two peaks for the investigated glasses. For the presence of two peaks, there are at least two possible reasons: first, the existence of orthophosphate groups (Q_P^0) next to pyrophosphate groups (Q_P^1) [43] and second, the presence of the same phosphate type, in this case, orthophosphate coordinated with different network modifier cations for charge balance [159]. Regarding the amount of peak 1 and peak 2, no apparent correlation with the concentration of the components can be found, as well.

For the Åbo glasses the amount of P_2O_5, lying between 0 and 1.8 mol% and B_2O_3, lying between 0.9 and 2.7 mol% is comparably low. So, no large impact of these components on the properties of the glass can be expected. In contrast to that, the amount of SiO_2, see Figure 45 shows a correlation with bioactivity: a large amount of SiO_2 correlates with low bioactivity and a low amount of SiO_2 correlates with high bioactivity. This behaviour can be explained by the overall expected network connectivity of a glass. As we do have three network formers, the network connectivity cannot be calculated easily like it is common to do for less complex glass compositions, like 45S5, see chapter 2.2.

In the systematical approach glass 45S5-B series, the substitution of B for Si up to 25% led to a less polymerized glass network because the majority of the B-units were present in the form of BO_3, whereas BO_4 groups were in minority. The presence of orthophosphate over other P-species leads to a fast release and thereby to a high bioactivity. For the Åbo glasses P-species peak 1 is the dominating one (for 8 out of 9 glasses), but a clear correlation between the bioactivity and the amount of P-species 1 and 2 cannot be found.

However, the distribution of the B- and the P-species for the glasses 10-92 and 1-98 is interesting. For glass 10-92, 36 % BO_3 and 36 % of peak 2 (^{31}P MAS NMR) as well as 64 % BO_4 and 64 % peak 1 (^{31}P MAS NMR) is present. For glass 1-98 contrarily, there is an amount of 86 % BO_3 as well as 86 % peak 1 (^{31}P MAS NMR), whereas 14 % BO_4 and 14% peak 2 (^{31}P MAS NMR) is present. The application of two-dimensional NMR would help here to see if there is a correlation between the respective B- and P-units or if it is a coincidence that the same amounts are present.

As further dependencies are difficult to identify, Pearson´s coefficient of correlation and Fisher discriminant ratio were calculated. While Pearson´s coefficient of correlation is a measure of the correlation between two random variables, the Fisher discriminant ratio is a measure for the separability of samples between two groups, see chapter 2.5. Pearson´s coefficient of correlation and the Fisher discriminant ratio were calculated for 9 of 21 Åbo glasses. For Pearson´s coefficient of correlation, strongly positive correlations ($r > 0.7$) were summarized in Tables, see 4.2.5. Comparing them with the FTIR spectra, Figure 51, the assignment visibly agrees with Ca^{2+}, Si-O-Si bending as well as for stretching of Q^3 and Q^4 (1030-1250 cm^{-1}), whereas in the Raman spectra there is an agreement in the region of ~Q^3 stretching. For the ^{11}B and ^{31}P MAS NMR results, no obvious correlation with the composition is visible. However, the results suggest a positive Pearson correlation of peak 1 at the ^{31}P NMR peak position 0 to -8 ppm with SiO_2. Some negative Pearson correlations are visible, as well. Regarding ^{31}P NMR the band at 0 to -4 ppm shows a negative correlation with K_2O and the one at 8-20 ppm shows a negative correlation with CaO. So, an increase in CaO is correlated with a decrease in intensity of peak 1 and an increase in K_2O to a decrease in intensity of peak 2. As discussed earlier, there are at least two options for the peak assignment: peak 1 being orthophosphate and peak 2 pyrophosphate or both orthophosphate with different network modifier cations around for charge balance. Pearson´s coefficient shows a positive correlation in ^{11}B MAS NMR for BO_4 groups with the components SiO_2 and P_2O_5 and BO_3 groups with the component K_2O. A negative correlation of Pearson´s coefficient is visible for BO_3 groups with SiO_2 and P_2O_5. However, two-dimensional (2D) NMR spectroscopy would be an excellent tool for further investigations to gain a deeper understanding of the structure of the individual Åbo glasses including the connectivity of tetrahedral borate, trigonal borate, phosphorus groups and the silicate network. Interestingly, Möncke et al. [100] found differences in 2D NMR results of annealed, in comparison to quenched borosilicate glasses.

The Fisher discriminant ratio showed differences between high and medium bioactive glasses in comparison to inert glasses at some wavelength/Raman shift areas in the investigated FTIR and Raman spectra. For the area at about 800 cm^{-1} in both spectra, as well as at about 1150 cm^{-1} in the FTIR spectra, there is an agreement with the Pearson correlation for SiO_2, see Figure 60 and Figure 61. So, possibly bioactive glasses can be distinguished from inert glasses by the content of SiO_2, as suggested by Figure 45 for the whole Åbo glasses and also by Brink et al. [9].

The significance of Pearson´s coefficient of correlation and Fisher test for the Åbo glasses is limited, as only nine glasses were involved in this approach. Therefore, it is recommended to investigate the influence of boron in bioactive glasses thoroughly in a systematical approach first. An excellent tool for the further investigation of the Åbo glasses would be 1D ^{29}Si MAS NMR and especially 2D MAS NMR of the network former atoms to gain deeper knowledge about the glass structure.

As discussed in chapter 5.1, there are different influences on the density of a glass network, e.g. the molar mass, the atomic radius and the bond length of the atoms or ions present. Elements, which have a higher molar mass will lead to a comparably high density, whereas lighter elements will lead to a relatively low density. Elements with a larger ionic radius will stretch the glass network, leading to a decreased density. Smaller ions will lead to a more compact network and thereby to an increased density. Besides that, the coordination and the bond length between the network former atoms has an influence on the density. As mentioned earlier, the maximum of the glass halo in the XRD diffractogram, Figure 48 is at different positions for the Åbo glasses, which gives evidence for the different interatomic distances and the distribution thereof. Bioactive glasses in comparison to inert glasses exhibit a less-connected structure [26] and a comparably high amount of network modifier atoms. The density of the Åbo glasses shows no significant difference between the bioactivity groups. There is a trend towards higher density values for the bioactive glasses. This might be ascribed to the number of heavy elements present in the glass. Whereas inert glasses tendentially contain more SiO_2, see Figure 45, the context is vice versa for bioactive glasses.

In the following chapter the ***solubility behaviour*** and the bioactivity of the Abo glasses will be discussed. Dynamic dissolution tests were carried out on six glasses 17-93, 17-

92, 9-93, 20-92, 10-92 and 6-92. As from these glasses, in-vivo data was published by Brink et al. [9], a direct comparison of the in-vitro dissolution behaviour and the performance in living tissue is possible. This approach was used to classify the Åbo glasses in different bioactivity groups, see 4.2.1. Fagerlund et al. [20] allocated the dissolution pattern of the absolute ion concentrations in mg/l to the initial dissolution profiles A, B, C and D.

The dynamic dissolution study is advantageous to quantitatively analyse the initial dissolution of the glasses. So, this setup provides an impression of the situation around an implant at early points of time after implantation. As Tris buffer solution was used here, the potential interaction with ions from surrounding media e.g. SBF solution is excluded. Whereas in static dissolution tests, time points need to be chosen for the analysis of the ion concentration by ICP-OES, in the dynamic setup there is a continuous measurement. However, a disadvantage of the dynamic dissolution method is the fact that glass particles cannot be taken during the measurement to be analysed e.g. by FTIR or XRD. The initial ion release from the glass is expected to be a function of its surface area. So, the procedure of sample preparation described in 3.2.3 could be improved by measuring the surface area of the used glass particles prior to testing.

The normalised dynamic dissolution test results show differences between the investigated glasses, see the overview for all ions for all glasses in Figure 55. A detailed view on the K^+ release is shown additionally, as it is a component of all tested glasses and it was detected for the whole time period for all glasses, see Figure 56. For the bioactive glasses 17-93 and 17-92, a larger percentage of K^+ ions is released in comparison to the other glasses. Comparing bioactive and inert glasses, the structure is different. Whereas inert glasses have a more connected structure, bioactive glasses are less connected. However, for the Åbo glasses the situation is more complex, as the three network formers present can form joint or separate networks. As glasses 17-93 and 17-92 are in the group “highly bioactive”, a pronounced ion release caused by a relatively less connected structure was expected. However, glass 17-93 is especially interesting, as it contains a relatively large amount of SiO_2 (57 mol%) for a bioactive glass.

Tendentially, for glasses containing a large amount of SiO_2, a more connected structure and therefore a less pronounced ion release is expected. For glass 17-93 in the dynamic dissolution tests a significant amount of Si was found in solution. As SiO_2 is acting purely as network former and therefore is part of the glass network, the release is especially interesting. As shown for the 45S5-B glasses, Si can be found in solution after dissolution tests. Short chains of connected SiO_2 units can be released. According to Tilocca [36] the "open matrix" of a bioactive glass is more sensitive towards hydrolysis than the structure of an inert glass. The number of covalent Si-O bonds, which need to be broken to release $-O-(Si-O)_n-$ units, is lower for a bioactive glass than for an inert glass, having a cross-linked structure containing Q_3 and Q_4 units [36]. For a glass like 17-93 a more connected network with a low amount of these short and thus mobile chains is expected. So, potentially hydrolysis of the glass network is occurring here.

Depending on the pH of the solution and the connectivity of the glass network, glass is attacked in a different extent. Furthermore, it must be taken into account that the solubility of SiO_2 modifications is relatively low [106] and depending on the pH value. In general, in acidic (and neutral) solutions the mechanism "ion exchange" leads to the leaching of network modifier ions from the glass structure. In pH neutral environment, bioactive glasses in contrast to inert glasses release ions from deeper layers. The dynamic dissolution results by Fagerlund et al. [20] nicely shows a small initial dissolution peak in the release of network modifier ions e.g. sodium for float glass (inert glass) at a pH value of 7.3. In contrast to that, in bioactive glasses ions are leached at a relatively constant high level, see Figure 55. This behaviour can be ascribed to the structural difference regarding the connectivity of the glass network.

In alkaline media the "hydrolytic attack" leads to a dissolution of the glass network [160]. Because in this mechanism the OH^- ions from the alkaline solution react with the glass network, it degrades [161]. So, comparing the situation in alkaline solutions with the one in acidic or neutral solutions, a higher amount of Si can be found in the alkaline solution. So, in the case of glass 17-93, potentially the ion exchange could locally cause a high pH value which could enable the hydrolysis of parts of the glass network.

The prediction of the structure and the properties of a glass from its composition would be ideal to save a lot of work and time, which is usually needed to make and characterise the glass. However, the development of suitable models is challenging. Here, reaction number (RN) and index of surface activity (ISA) calculations were used, see chapter 2.5. The calculation of the RN is based on Andersson et al. [8], who developed a phenomenological model to estimate the bioactivity of a glass composition in the system SiO_2-Na_2O-CaO-P_2O_5-Al_2O_3-B_2O_3. Brink et al. modified the model of Andersson ("modified Andersson model") to include the components K_2O and MgO. The ISA model was developed by Brink et al. [9] to calculate the relative *in-vivo* bioactivity. By calculating the RN and the ISA, the transferability of the two models from the Brink glasses to the Fagerlund glasses was tested, as well. There is an agreement of the RN (modified Anderson model) with the bioactivity value for 36% of the glasses, as shown in chapter 4.2.5. By contrast, the ISA model leads with 89% to a larger agreement of bioactivity with the index of surface activity value. The transferability of the model was possible for 4 of 7 Fagerlund glasses, here. Comparing the two equations, the one for ISA (2.14) is more advanced in comparison to the one for RN (2.13), see chapter 2.5. Obviously, the ISA model is advantageous over the modified Andersson model (RN). The modified Andersson model assumes K_2O acting like Na_2O and MgO like CaO. The charge of the potassium ion and the sodium ion is 1+ and of the magnesium and the calcium ion 2+. But, there are differences between the ions in the network, e.g. the ion radius and the cation-oxygen distance [106]. So, it is suggested here, that K_2O and MgO do not behave like Na_2O and CaO.

The strong interfacial bond a bioactive glass can form with bone is shown in a SEM picture by Brink et al. [9] in chapter 2.2. Whereas the bioactive glass forms a tight bond to the bone, between the inert glass and the bone remains a gap. The advantage of mathematical models is especially obvious when animal testing needs to be done as potentially the number of sacrificed individuals could be reduced due to advanced preselection.

To test the impact the substitution of one glass has on a developed mathematical model, linear regression models were compared. The defined bioactivity values for the model generation were: 1 for bioactive, 2 for medium and 3 for inert. The regression bioactivity values (rBA) are shown and the agreement of the rBA with the bioactivity value is highlighted in yellow in Table 18. There are large differences in the agreement of the model value and the real BA value. Whereas the conformity is 0 % for the model without glass 10-92, it is between 65 % and 80 % for the other models. Glass 10-92 appears to be essential to get a useful model. To show the comparison of the models, exemplarily for glass 19-93 the rBA is shown in Figure 70.

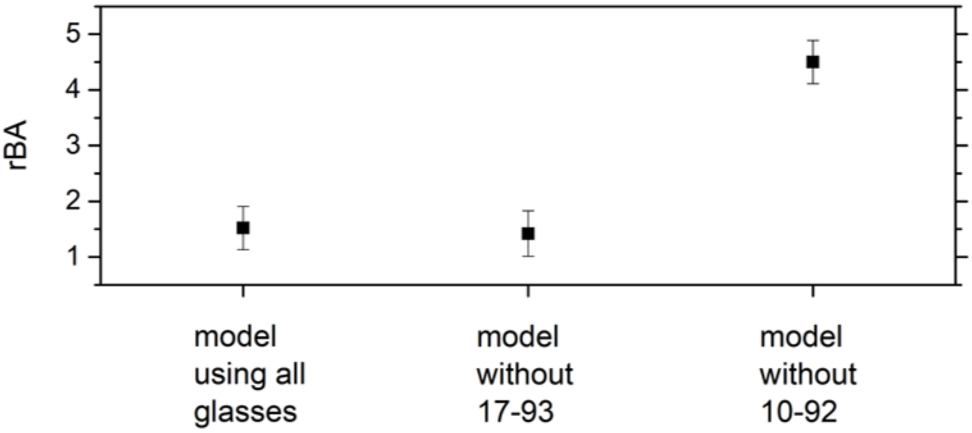

Figure 70: The regression bioactivity values for glass 19-93 accessed via different models: left: a model using all glasses, middle: a model without glass 17-93 and right: a model without glass 10-92.

In the diagram the rBA calculated with different models is presented: left: a model using all glasses (I), middle: a model without glass 17-93 (II) and right: a model without glass 10-92 (III). The rBA for glass 19-93 obtained with the model I (1.52 ± 0.39) and model II (1.42 ± 0.41) is close to the bioactivity value (1). However, the model without glass 10-92 (III) with a bioactivity value of 4.5 ± 0.39 leads to a large deviation from the bioactivity value 1. This large deviation shows that this simple approach is not suitable to predict the bioactivity from the glass composition reliably. However, overall this simple linear approach has had a relatively good outcome.

In this chapter the ***thermal characterisation*** of the Abo glasses will be discussed. The behaviour of a bioactive glass upon temperature increase is very important. Ideally a bioactive glass does not crystallise easily to enable the forming of a specific shape at elevated temperatures. However, the glass series 45S5-B crystallises relatively easily.

The glass transition temperature refers to the temperature of the transformation between the undercooled liquid and the solid state of glass, see chapter 2.1. The inert glasses exhibit a significantly higher T_g in comparison to the highly bioactive glasses, Figure 57, which follows the expectations. The inert glasses exhibit a larger amount of SiO_2 in comparison to the other bioactivity groups as shown in Figure 45 as discussed earlier. The glass transition temperature is related to the connectivity of the glass network [162]. FTIR and Raman results show that the network of the inert glasses is more connected in comparison to the one of bioactive glasses. A glass with a more cross-linked network is supposed to feature T_g at higher temperatures, as more energy is necessary to enable the mobility necessary for glass transition. Four of the medium bioactive glasses show a T_g in the range of the highly bioactive ones, whereas two glasses exhibit a T_g in the range of the inert glasses. So, the glass transition temperature of the medium bioactive glasses lies in between the other groups, which was expected as well.

The results of the thermal expansion coefficient, Figure 58 are in accordance with the results of T_g. The range of thermal expansion of the inert glasses (average $\sim 1.0*10^{-5}$ 1/K) is significantly lower than the one of the highly bioactive ones (average $\sim 1.5*10^{-5}$ 1/K), while the medium bioactive ones are in between. In silicate glasses, the network connectivity largely controls the thermal expansion [21]. A glass with higher network connectivity is more rigid, which leads to a less pronounced expansion upon increasing temperature. Conversely, a glass with lower network connectivity is less rigid, which causes a more pronounced expansion upon increasing temperature.

The glass transition is detected at higher temperatures and the thermal expansion is lower for the inert glasses. These results were expected, as they are associated with the relatively high amount of SiO_2 leading to a more connected structure in the inert glasses, see Figure 45.

Analogous to the approach regarding the BA value, linear models were developed, and their performance was compared. The regression values for T_g (rT_g) are shown in Table 19, chapter 4.2.5. The agreement of the rT_g value with the recorded glass transition value (T_g) is highlighted in yellow in Table 19. Like for the BA approach, there are large differences in the agreement of the model value and the T_g value. The agreement in the model without glass 10-92 is 10 %, whereas for the other models it is between 60 % and 80 %. To show the comparison of the models, exemplarily for glass 19-93 the rT_g is shown in Figure 71.

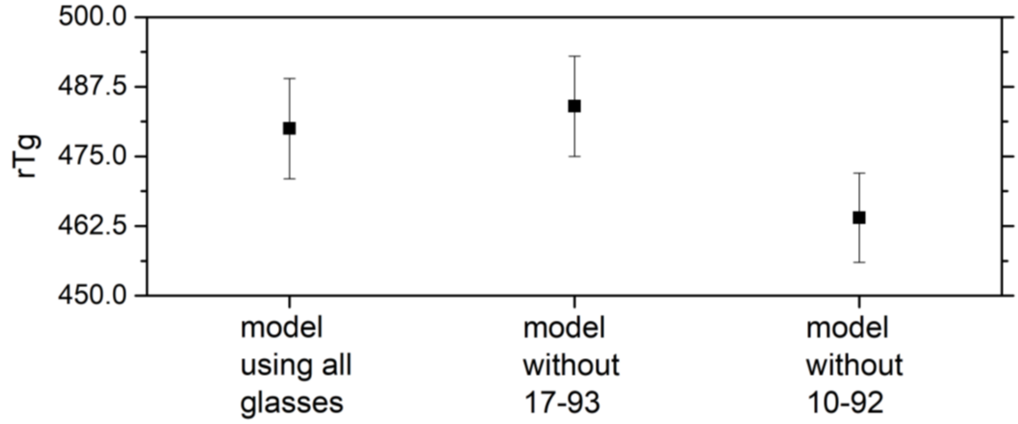

Figure 71: The regression Tg values for glass 19-93 accessed via different models: left: a model using all glasses, middle: a model without glass 17-93 and right: a model without glass 10-92.

For the regression T_g value, the model using all glasses (480 ± 9°C) provides a value close to T_g (491°C) and the model without 17-93 (484 ± 9°C) an equal value. However, the model without glass 10-92 exhibits a large deviation from the T_g of 491°C with T_g (464 ± 8°C). Like for the bioactivity value approach, this large deviation shows that this simple approach is not suitable to predict the glass transition temperature from the glass composition reliably. Apparently, like in the linear models for the BA values, glass 10-92 is indispensable to develop a suitable model. If one glass out of 21 has this great impact on the performance of the model, a linear approach is questionable. However, this simple approach nicely shows the pros and cons of a mathematical approach. While saving time and work because the glass properties are calculated by a model in theory, the outcome might not be reliable. The use of this kind of mathematical models can give a hint and be used to show a trend to decide deliberately about further investigations. Potential reasons for the large impact of glass 10-92 on the model performance could be the position within the tested glasses. Glass 10-92 exhibits a comparable high T_g and a large amount of SiO_2.

Heating microscopy (HTM) investigations are valuable to determine the temperature-viscosity behaviour. Besides the dissolution behaviour, the hot-working properties are very important to develop glass compositions for specific clinical applications [163]. In HTM a certain shape of the sample is related to a specific viscosity [48] upon heating, see Table 32. The characteristic points are the sintering point (SP), the minimum baseline point (MBL), the half cone point (HCP) and the floating point (FP).

Table 32: Characteristic points upon heating of a glass powder compact sample using heating microscopy with related viscosity value, as well as the viscosity of the working range [48].

Characteristic point	log 10 (η/dPas)
SP	10.0 ± 0.3
MBL	6.1 ± 0.2
HCP	4.55 ± 0.1
FP	4.2 ± 0.1
working range	~3 - 7

The temperature interval at which glass forming can be realised is the working range, whereby the viscosity is about 10^3 - 10^7 dPa*s [48]. If a glass has a short working range, the viscosity changes fast during temperature change. In contrast to that, a long working range offers more options regarding glass forming because of the slowly changing viscosity. According to Brink et al. a large working range is a requirement for the medical use of bioactive glasses in the form of sintered or blown products. In contrast to the glass series 45S5-B, for the majority of the Åbo glasses, all characteristic points could be recorded. The tendency towards crystallisation is lower for a glass with a high amount of SiO_2 because it exhibits a more cross-linked structure. Furthermore, in bioactive glasses containing less SiO_2 and much Na_2O as well as CaO, K_2O and MgO have shown to increase the stability against crystallisation [9]. It needs to be considered that HTM is not able to detect partly crystallisation of the glasses during heating. For the correct interpretation of the HTM results, DSC data or XRD during heating of these glasses would be very interesting. In a next step, it would be beneficial to investigate the hot-forming ability of the glasses which show a low crystallisation tendency.

6. Summary & Outlook

The increasing life expectancy of human individuals causes a growing demand for implants to maintain the quality of life for the aged people. Bioglass® has gene activating properties inducing bone tissue repair and regeneration and it is the first material which was able to bond to human bone [2]. Up to today, bioactive glasses are used commercially as granules or powder to support bone tissue regeneration in bone defects [7]. Complex structures, which require forming at elevated temperatures, are difficult to obtain because bioactive glasses show a high tendency to crystallisation. Besides that, the complete dissolution in the human body is desired, whereas bioactive glass Bonalive® has shown to dissolve not completely even after 14 years in the human body [12]. The element boron plays a role in the metabolism of healthy bones [13-15]. In cell tests borosilicate glasses show to support cell growth, adhesion and differentiation [16] and in-vivo enhanced bone formation [17]. Furthermore, an increasing amount of boron in the glass leads to a faster and more complete dissolution process which enables an earlier formation of the inorganic substance of bones, hydroxyapatite [18, 19].

In this thesis the influence of boron on structure, solubility and crystallisation behaviour in bioactive glasses has been investigated. The glass series 45S5-B was designed by substituting boron for silicon up to 25% starting from Bioglass® 45S5. The structural investigations have shown that the silicon species are connected by two oxygen atoms (Q^2 groups) to neighbouring silicon atoms in majority, forming a chain-like structure. Furthermore, for the whole series boron was present in trigonal configuration most of the time (>80%). Orthophosphate was the main phosphorus modification for the whole series, which can be leached out of the glass easily, supporting the precipitation of apatite. The increasing substitution of boron for silicon led to an overall decreased network polymerisation. The dissolution test results of the series 45S5-B revealed that it is possible to control the solubility behaviour by the boron content of the glass. A larger boron content in the glass led to an earlier apatite formation. With boron for silicon substitution for the fine glass powders investigated, a slight decrease in crystallisation tendency was found, although the crystallisation tendency of glass series 45S5-B in comparison to other glass systems is high in general. For the fine glass powders predominantly surface crystallisation is assumed, while for the coarse powders a complex crystallisation linked to phase separation is proposed. Interestingly glass 25B was able to form apatite even after partly crystallisation caused by heat-treatment.

The investigation of the structure of the Åbo glasses has shown a more connected network for the inert glasses than for the high and medium bioactive glasses. As expected, the glass transition was detected at higher temperatures and the thermal expansion was lower for the inert glasses. The reduced crystallisation tendency of the majority of the Åbo glasses, probably caused by the presence of K_2O and MgO in the glass composition [10], is a substantial benefit.

In further systematic studies the influence of potassium and magnesium in the glass system 45S5-B could be investigated to obtain a glass composition which would allow hot-forming due to reduced crystallisation tendency. The production of 3D scaffolds, cell tests and in-vivo studies in living organisms would be interesting next steps on the suitable glass composition afterwards.

7. References

1. Ylänen, H.O., *Bioactive Glasses*. 2011, Duxford: Woodhead Publishing
2. Hench, L.L., *The story of Bioglass®.* Journal of Materials Science-Materials in Medicine, 2006. **17**(11): p. 967-978.
3. Hench, L.L. and J.M. Polak, *Third-generation biomedical materials.* Science, 2002. **295**(5557): p. 1014-+.
4. Jones, J. and A.G. Clare, *Bio-Glasses* 2012, West Sussex: Wiley.
5. Nicholson, J.W. and J.A. Connor, *The Chemistry of Medical and Dental Materials*. 2002, Cambridge, UK Royal Society of Chemistry
6. Wilson, J. and S. Low, *Bioactive ceramics for periodontal treatment: comparative studies in the Patus monkey.* Journal of Applied Biomaterials, 1992. **3(2):123-9.**
7. Boccaccini, A.R., D.S. Brauer, and L. Hupa, *Bioactive Glasses*. 2017, Cambridge, UK Royal Society of Chemistry
8. Andersson, O.H., et al., *Invivo Behavior of Glasses in the SiO2-Na2O-CaO-P2O5-Al2O3-B2O3 System.* Journal of Materials Science-Materials in Medicine, 1990. **1**(4): p. 219-227.
9. Brink, M., et al., *Compositional dependence of bioactivity of glasses in the system Na2O-K2O-MgO-CaO-B2O3-P2O5-SiO2.* Journal of Biomedical Materials Research, 1997. **37**(1): p. 114-21.
10. Hupa, L. and K.H. Karlsson, *Tailoring of Bioactive Glasses*, in *Bioactive Glasses*, A.R. Boccaccini, D.S. Brauer, and L. Hupa, Editors. 2017, The Royal Society of Chemistry: Cambridge.
11. Bonalive. www.bonalive.com. [Website] [cited 2018 10 October].
12. Fabert, M., et al., *Crystallization and sintering of borosilicate bioactive glasses for application in tissue engineering.* Journal of Materials Chemistry B, 2017. **5**(23): p. 4514-4525.
13. Nielsen, F.H., *Studies on the relationship between boron and magnesium which possibly affects the formation and maintenance of bones.* Magnesium and trace elements, 1990. **v.9** (no. 2): p. pp. 61-69.
14. Beattie, J.H. and H.S. Peace, *The Influence of a Low-Boron Diet and Boron Supplementation on Bone, Major Mineral and Sex Steroid-Metabolism in Postmenopausal Women.* British Journal of Nutrition, 1993. **69**(3): p. 871-884.
15. Newnham, R.E., *Essentiality of boron for healthy bones and joints.* Environ Health Perspect, 1994. **102 Suppl 7**: p. 83-5.
16. Fu, Q.A., et al., *Silicate, borosilicate, and borate bioactive glass scaffolds with controllable degradation rate for bone tissue engineering applications. II. In vitro and in vivo biological evaluation.* Journal of Biomedical Materials Research Part A, 2010. **95a**(1): p. 172-179.
17. Gorustovich, A.A., et al., *Biological performance of boron-modified bioactive glass particles implanted in rat tibia bone marrow.* Biomedical Materials, 2006. **1**(3): p. 100-5.
18. Huang, W., et al., *Kinetics and mechanisms of the conversion of silicate (45S5), borate, and borosilicate glasses to hydroxyapatite in dilute phosphate solutions.* Journal of Materials Science: Materials in Medicine 2006. **17**(7): p. 583-96.
19. Yao, A.H., et al., *In vitro bioactive characteristics of borate-based glasses with controllable degradation behavior.* Journal of the American Ceramic Society, 2007. **90**(1): p. 303-306.
20. Fagerlund, S., L. Hupa, and M. Hupa, *Dissolution patterns of biocompatible glasses in 2-amino-2-hydroxymethyl-propane-1,3-diol (Tris) buffer.* Acta Biomaterialia, 2013. **9**(2): p. 5400-5410.
21. Shelby, J.E., *Introduction to Glass Science and Technology*. 2005, Cambridge: Royal Society of Chemistry.
22. Zachariasen, W.H., *The atomic arrangement in glass. .* Journal of the American Chemical Society, 1932. **54**(10): p. 3841-3851.

23. Seyler, R.J., *Assignment of the Glass Transition* 1994, Philadelphia, PA, USA: American Society for testing and materials
24. Rao, K.J., *Structural chemistry of glasses*. Vol. 1. 2002, Amsterdam: Elsevier.
25. Ratner, H., *Biomaterials Science*. 2013, Amsterdam: Elsevier.
26. Brauer, D.S., *Bioactive glasses-structure and properties.* Angewandte Chemie International Edition in English 2015. **54**(14): p. 4160-81.
27. Williams, D.F., *The Williams Dictionary of Biomaterials* 1999, Liverpool: Liverpool University Press.
28. Lohmeyer, S., *Werkstoff Glas III*. 2001, Renningen: Expert Verlag
29. Tilocca, A., A.N. Cormack, and N.H. de Leeuw, *The structure of bioactive silicate glasses: New insight from molecular dynamics simulations.* Chemistry of Materials, 2007. **19**(1): p. 95-103.
30. Lockyer, M.W.G., D. Holland, and R. Dupree, *Nmr Investigation of the Structure of Some Bioactive and Related Glasses.* Journal of Non-Crystalline Solids, 1995. **188**(3): p. 207-219.
31. O'Donnell, M.D., et al., *Effect of P2O5 content in two series of soda lime phosphosilicate glasses on structure and properties - Part I: NMR.* Journal of Non-Crystalline Solids, 2008. **354**(30): p. 3554-3560.
32. Brauer, D.S., et al., *Structure of fluoride-containing bioactive glasses.* Journal of Materials Chemistry, 2009. **19**(31): p. 5629-5636.
33. Eden, M., *The split network analysis for exploring composition-structure correlations in multi-component glasses: I. Rationalizing bioactivity-composition trends of bioglasses.* Journal of Non-Crystalline Solids, 2011. **357**(6-7): p. 1595-1602.
34. Jones, J.R., *Review of bioactive glass: From Hench to hybrids.* Acta Biomaterialia, 2013. **9**(1): p. 4457-4486.
35. Tilocca, A. and A.N. Cormack, *Exploring the surface of bioactive glasses: Water adsorption and reactivity.* Journal of Physical Chemistry C, 2008. **112**(31): p. 11936-11945.
36. Tilocca, A., *Molecular Dynamics Simulations of Bioactive Glass Structure and In vitro Reactivity* in *Bioactive Glasses*, A.R. Boccaccini, D.S. Brauer, and L. Hupa, Editors. 2017, The Royal Society of Chemistry: Cambridge.
37. Tilocca, A., *Atomic-scale models of early-stage alkali depletion and SiO2-rich gel formation in bioactive glasses.* Physical Chemistry Chemical Physics, 2015. **17**(4): p. 2696-2702.
38. Elliott, J.C., *Structure and Chemistry of the Apatites and Other Calcium Orthophosphates.* 1994, Amsterdam: Elsevier.
39. Gentleman, E., et al., *The effects of strontium-substituted bioactive glasses on osteoblasts and osteoclasts in vitro.* Biomaterials, 2010. **31**(14): p. 3949-3956.
40. Rahaman, M.N., et al., *Review - bioactive glass implants for potential application in structural bone repair.* Biomedical Glasses, 2017. **3**: p. 56-66.
41. Rahaman, M.N., et al., *Bioactive glass in tissue engineering.* Acta Biomaterialia, 2011. **7**(6): p. 2355-2373.
42. Balasubramanian, P., et al., *Angiogenic potential of boron-containing bioactive glasses: in vitro study.* Journal of Materials Science, 2016. **52**(15): p. 8785-8792.
43. Yu, Y. and M. Eden, *Structure-composition relationships of bioactive borophosphosilicate glasses probed by multinuclear B-11, Si-29, and P-31 solid state NMR.* Rsc Advances, 2016. **6**(103): p. 101288-101303.
44. Nascimento, M.L.F., et al., *Can glass stability parameters infer glass forming ability?* Journal of Non-Crystalline Solids, 2005. **351**(40-42): p. 3296-3308.
45. Massera, J., *Nucleation and growth behavior of tellurite-based glasses suitable for mid-infrared applications*, in *Materials Science and Engineering*. 2009, Clemson University: Clemson
46. Massera, J., et al., *Crystallization Mechanism of the Bioactive Glasses, 45S5 and S53P4.* Journal of the American Ceramic Society, 2012. **95**(2): p. 607-613.

47. Massera, J., et al., *Crystallization behavior of phosphate glasses and its impact on the glasses' bioactivity.* Journal of Materials Science, 2015. **50**(8): p. 3091-3102.

48. Brink, M., *The influence of alkali and alkaline earths on the working range for bioactive glasses.* Journal of Biomedical Materials Research, 1997. **36**(1): p. 109-17.

49. Sharma, A.K., *Text Book Of Correlations And Regression*. 2005, New Dehli: Discovery Publishing House.

50. Candan, K.S. and M.L.Sapino, *Data management for multimedia retrieval* 2010, Cambridge: Cambridge University Press

51. Vogel, W., *Glass Chemistry*. 1994, Berlin: Springer-Verlag.

52. Kamitsos, E.I., *Infrared spectroscopy of glasses*, in *Modern glass characterization* M. Affatigato, Editor. 2015, John Wiley & Sons Inc. : Hoboken, New Jersey. p. 32-73.

53. Muller, L. and F.A. Muller, *Preparation of SBF with different HCO3- content and its influence on the composition of biomimetic apatites.* Acta Biomater, 2006. **2**(2): p. 181-9.

54. Zhang, D., et al., *In vitro characterization of bioactive glasses.* Bioceramics, Vol 17, 2005. **284-286**: p. 481-484.

55. Nascimento, M.L.F., et al., *Can glass stability parameters infer glass forming ability?* Journal of Non-Crystalline Solids, 2005. **351**(40): p. 3296-3308.

56. Blaine, R.L. and H.E. Kissinger, *Homer Kissinger and the Kissinger equation.* Thermochimica Acta, 2012. **540**: p. 1-6.

57. Friedman, H.L., *Kinetics of thermal degradation of charforming pstics from thermogravimetry. Application to a phenolic plastic. .* Journal of Polymer Science, 1963. **6C**: p. 183-195.

58. Augis, J.A. and J.E. Bennett, *Calculation of Avrami Parameters for Heterogeneous Solid-State Reactions Using a Modification of Kissinger Method.* Journal of Thermal Analysis, 1978. **13**(2): p. 283-292.

59. Ozawa, T., *Kinetics of Non-Isothermal Crystallization.* Polymer, 1971. **12**(3): p. 150-158.

60. Fagerlund, S., et al., *On determining chemical durability of glasses.* Glass Technology-European Journal of Glass Science and Technology Part A, 2010. **51**(6): p. 235-240.

61. Fagerlund, S., et al., *Dissolution Kinetics of a Bioactive Glass by Continuous Measurement.* Journal of the American Ceramic Society, 2012. **95**(10): p. 3130-3137.

62. Mercier, C., et al., *Influence of P2O5 content on the structure of SiO2-Na2O-CaO-P2O5 bioglasses by 29Si and 31P MAS-NMR.* Journal of Non-Crystalline Solids 2011. **357**: p. 3901–3909.

63. MacKenzie, K.J.D., *Multinuclear Solid-State NMR of Inorganic Materials* 2002, Amsterdam: Pergamon

64. Kamitsos, E.I., et al., *Vibrational Study of the Role of Trivalent Ions in Sodium Trisilicate Glass.* Journal of Non-Crystalline Solids, 1994. **171**(1): p. 31-45.

65. Kamitsos, E.I., et al., *Infrared Reflectance Spectra of Lithium Borate Glasses.* Journal of Non-Crystalline Solids, 1990. **126**(1-2): p. 52-67.

66. Koroleva, O.N., et al., *Structure of Na2O-SiO2 melt as a function of composition: In situ Raman spectroscopic study.* Journal of Non-Crystalline Solids, 2013. **375**: p. 62-68.

67. McMillan, P., *Structural Studies of Silicate-Glasses and Melts - Applications and Limitations of Raman-Spectroscopy.* American Mineralogist, 1984. **69**(7-8): p. 622-644.

68. Almeida, R.M. and L.F. Santos, *Raman spectroscopy of glasses*, in *Modern Glass Characterization*, M. Affatigato, Editor. 2015, John Wiley & Sons, Inc.: Hoboken, New Jersey. p. 74-106.

69. Manara, D., A. Grandjean, and D.R. Neuville, *Advances in understanding the structure of borosilicate glasses: A Raman spectroscopy study.* American Mineralogist, 2009. **94**(5-6): p. 777-784.

70. Tylkowski, M. and D.S. Brauer, *Mixed alkali effects in Bioglass® 45S5.* Journal of Non-Crystalline Solids, 2013. **376**: p. 175-181.
71. Bingel, L., et al., *Influence of dissolution medium pH on ion release and apatite formation of Bioglass® 45S5.* Materials Letters, 2015. **143**: p. 279-282.
72. Kirste, G., et al., *Effect of chloride ions in Tris buffer solution on bioactive glass apatite mineralization.* International Journal of Applied Glass Science, 2017. **8**(4): p. 438-449.
73. LeGeros, R.Z., et al., *Two types of carbonate substitution in the apatite structure.* Experientia, 1969. **25**(1): p. 5-7.
74. Fu, Q., et al., *Mechanical and in vitro performance of 13–93 bioactive glass scaffolds prepared by a polymer foam replication technique.* Acta Biomaterialia, 2008. **4**(6): p. 1854-1864.
75. Böhme, L., *Bioaktive Borosilicatgläser*. 2016, Friedrich Schiller University Jena.
76. Tainio, J., *Impact of magnesium and strontium on dissolution and sintering of bioactive borosilicate glasses*. 2016, TUT Tampere
77. Starink, M.J., *The determination of activation energy from linear heating rate experiments: a comparison of the accuracy of isoconversion methods.* Thermochimica Acta, 2003. **404**(1-2): p. 163-176.
78. Serra, J., et al., *Influence of the non-bridging oxygen groups on the bioactivity of silicate glasses.* Journal of Materials Science-Materials in Medicine, 2002. **13**(12): p. 1221-1225.
79. Aguiar, H., et al., *Orthophosphate nanostructures in SiO2-P2O5-CaO-Na2O-MgO bioactive glasses.* Journal of Non-Crystalline Solids, 2008. **354**(34): p. 4075-4080.
80. Peitl, O., G.P. LaTorre, and L.L. Hench, *Effect of crystallization on apatite-layer formation of bioactive glass 45S5.* Journal of Biomedical Materials Research, 1996. **30**(4): p. 509-514.
81. Stavrou, E., et al., *Vibrational study of thermally ion-exchanged sodium aluminoborosilicate glasses.* Journal of Non-Crystalline Solids, 2014. **401**: p. 232-236.
82. Angeli, F., et al., *Effect of temperature and thermal history on borosilicate glass structure.* Physical Review B, 2012. **85**(5).
83. Strubel, C., *Inductively Coupled Mass Spectrometry with Laser Ablation System* in *Analysis of the Composition and Structure of Glass and Glass Ceramics* H.K. Bach, Dieter, Editor. 1999, Springer Berlin.
84. Meckel, L.e.a., *The Chemical Analysis of Glasses, Glass Ceramics, and Related Materials*, in *Analysis of the composition and structure of glass and glass ceramics*, H.K. Bach, Dieter, Editor. 1999, Springer: Berlin.
85. Berlin, J., *Analysis of Boron with Energy Dispersive X-ray Spectrometry.* Imaging&Microscopy 2011. **13**.
86. Meckel, L., H. Müller, and B. Valentin, *Qualitative and quantitative Analysis of Major Components* in *Analysis of the Glass Composition and Structure of Glass and Glass Ceramics*, H.K. Bach, Dieter, Editor. 1999, Springer: Berlin.
87. Suryanarayana, C. and M.G. Norton, *X-ray Diffraction A Practical Approach*. 1998, New York and London: Plenum Press.
88. Flewitt, P.E.J. and R.K. Wild, *Physical Methods for Materials Characterisation*. Third Edition ed. 2017, Boca Raton: CRC Press.
89. Pantano, C.G., D.B. Dove, and G.Y. Onoda, *Glass surface analysis by Auger Electron Spectroscopy.* Journal of Non-Crystalline Solids, 1975. **19**: p. 41-53.
90. Moncke, D., et al., *Influence of melting and annealing conditions on the structure of borosilicate glasses.* Physics and Chemistry of Glasses, 2003. **44**(2): p. 113-116.
91. Kroeker, S., *Nuclear magnetic resonance spectroscopy of glasses*, in *Modern Glass Characterization*, M. Affatigato, Editor. 2015, John Wiley & Sons, Inc.: Hoboken, New Jersey.
92. Andrew, E.R., A. Bradbury, and R.G. Eades, *Nuclear Magnetic Resonance Spectra from a Crystal rotated at High Speed.* Nature, 1958. **182**: p. 1659.

93. Hennel, J.W. and J. Klinowski, *Magic-Angle Spinning: a Historical Perspective*, in *New Techniques in Solid-State NMR*, J. Klinowski, Editor. 2005, Springer Berlin Heidelberg: Berlin, Heidelberg.

94. Avila Salazar, D.A., et al. *Characterization of structural changes induced by borate incorporation into bioactive phospho-silicate glasses*. in *The 9th International Conference on Borate Glasses, Crystals and Melts and the 2nd International Conference on Phosphate Materials* 2017. Oxford University, St Annes College.

95. Mathew, R., B. Stevensson, and M. Eden, *Na/Ca Intermixing around Silicate and Phosphate Groups in Bioactive Phosphosilicate Glasses Revealed by Heteronuclear Solid-State NMR and Molecular Dynamics Simulations.* Journal of Physical Chemistry B, 2015. **119**(17): p. 5701-5715.

96. Ren, M.G., et al., *B2O3/SiO2 substitution effect on structure and properties of Na2O-CaO-SrO-P2O5-SiO2 bioactive glasses from molecular dynamics simulations.* Physical Chemistry Chemical Physics, 2018. **20**(20): p. 14090-14104.

97. Elgayar, I., et al., *Structural analysis of bioactive glasses.* Journal of Non-Crystalline Solids, 2005. **351**(2): p. 173-183.

98. Brauer, D.S. and D. Möncke, *Introduction to the structure of silicate, phosphate and borate glasses*, in *Bioactive Glasses* A.R. Boccaccini, D.S. Brauer, and L. Hupa, Editors. 2017, Royal Society of Chemistry: Cambridge

99. Tricot, G., *The structure of Pyrexs (R) glass investigated by correlation NMR spectroscopy.* Physical Chemistry Chemical Physics, 2016. **18**(38): p. 26764-26770.

100. Moncke, D., et al., *On the connectivity of borate tetrahedra in borate and borosilicate glasses.* Physics and Chemistry of Glasses-European Journal of Glass Science and Technology Part B, 2015. **56**(5): p. 203-211.

101. Steve Feller, T.M., Maranda Franke, Suarav Bista, Anthony O'Donovan-Zavada,, et al., *Structure and properties of barium and calcium borosilicate glasses.* 2012.

102. Larkin, P.J., *Infrared and Raman spectroscopy: principles and spectral interpretation*. 2011, Waltham: Elsevier.

103. Stuart, B.H., *Infrared Spectroscopy*. 2004, West Sussex: John Wiley and Sons Ltd.

104. Raman, C.V. and K.S. Krishnan, *A New Type of Secondary Radiation.* Nature, 1928. **121**: p. 501.

105. Amer, M.S., *Raman Spectroscopy, Fullerenes and Nanotechnology*. 2010, Cambridge: RSC Publishing.

106. Scholze, H., *Glass*. 1991, New York: Springer.

107. Tournié, A., P. Ricciardi, and P. Colomban, *Glass corrosion mechanisms: A multiscale analysis.* Solid State Ionics, 2008. **179**(38): p. 2142-2154.

108. Filgueiras, M.R., G. LaTorre, and L.L. Hench, *Solution effects on the surface reactions of three bioactive glass compositions.* Journal of Biomedical Materials Research, 1993. **27**(12): p. 1485-93.

109. Jones, J.R., P. Sepulveda, and L.L. Hench, *Dose-dependent behavior of bioactive glass dissolution.* Journal of Biomedical Materials Research, 2001. **58**(6): p. 720-726.

110. Brown, W.E., N. Eidelman, and B. Tomazic, *Octacalcium Phosphate as a Precursor in Biomineral Formation.* Advances in Dental Research, 1987. **1**(2): p. 306-313.

111. Brauer, D.S., et al., *Fluoride-containing bioactive glasses: Effect of glass design and structure on degradation, pH and apatite formation in simulated body fluid.* Acta Biomaterialia, 2010. **6**(8): p. 3275-3282.

112. Baykal, A., et al., *Discussion on the structure of boron containing apatite.* Euro Ceramics 2004. **264-268**: p. 2017-2021.

113. Huang, W.H., et al., *Mechanisms for converting bioactive silicate, borate, and borosilicate glasses to hydroxyapatite in dilute phosphate solution.* Physics and Chemistry of Glasses-European Journal of Glass Science and Technology Part B, 2006. **47**(6): p. 647-658.

114. Bohner, M., *Calcium orthophosphates in medicine: from ceramics to calcium phosphate cements.* Injury-International Journal of the Care of the Injured, 2000. **31**: p. S37-S47.

115. Legeros, R.Z. and R.G. Craig, *Strategies to Affect Bone Remodeling - Osteointegration.* Journal of Bone and Mineral Research, 1993. **8**: p. S583-S596.

116. Spriano, S., et al., *A critical review of multifunctional titanium surfaces: New frontiers for improving osseointegration and host response, avoiding bacteria contamination.* Acta Biomaterialia, 2018. **79**: p. 1-22.

117. Chouirfa, H., et al., *Review of titanium surface modification techniques and coatings for antibacterial applications.* Acta Biomaterialia, 2019. **83**: p. 37-54.

118. Surapaneni, H., et al., *Antibiotics in dental implants: A review of literature.* Journal of pharmacy & bioallied sciences, 2016. **8**(Suppl 1): p. S28-S31.

119. van de Belt, H., et al., *Infection of orthopedic implants and the use of antibiotic-loaded bone cements. A review.* Acta Orthopaedica Scandinavica, 2001. **72**(6): p. 557-71.

120. Campoccia, D., L. Montanaro, and C.R. Arciola, *The significance of infection related to orthopedic devices and issues of antibiotic resistance.* Biomaterials, 2006. **27**(11): p. 2331-2339.

121. Gubler, M., et al., *Do bioactive glasses convey a disinfecting mechanism beyond a mere increase in pH?* International Endodontic Journal, 2008. **41**(8): p. 670-678.

122. McMillan, P.W., *The crystallisation of glasses.* Journal of Non-Crystalline Solids, 1982. **52**(1): p. 67-76.

123. Deubener, J., et al., *Updated definition of glass-ceramics.* Journal of Non-Crystalline Solids, 2018. **501**: p. 3-10.

124. Vladislavova, L., *Nucleation agents in the glass system BaO/SrO/ZnO/SiO2*. 2018, FSU Jena Jena.

125. Guedes, M., A.C. Ferro, and J.M.F. Ferreira, *Nucleation and crystal growth in commercial LAS compositions.* Journal of the European Ceramic Society, 2001. **21**(9): p. 1187-1194.

126. Sternitzke, M. and G. Muller, *Crystal-Structure and Thermal-Expansion of Quartz-Type Aluminosilicates.* Journal of Materials Science, 1991. **26**(11): p. 3051-3056.

127. Tauch, D., *Low thermal expansion glass-ceramics in the system BaO - Al2O3 -B2O3 -crystallisation and properties-*. 2005, FSU Jena Jena.

128. Ohja, N., *Borosilicate glass with enhanced hot forming properties and conversion to hydroxyapatite*. 2016, TUT Tampere.

129. Lefebvre, L., et al., *Structural transformations of bioactive glass 45S5 with thermal treatments.* Acta Materialia, 2007. **55**(10): p. 3305-3313.

130. Fagerlund, S., et al., *Phase composition and in vitro bioactivity of porous implants made of bioactive glass S53P4.* Acta Biomaterialia, 2012. **8**(6): p. 2331-2339.

131. Ohsato, Maki, and Takeuchi, *Structure of Na2CaSi2O6.* Acta Crystallographica, 1985. **C41**(Part 11): p. 1575 - 1577.

132. Bretcanu, O., et al., *Sintering and crystallisation of 45S5 Bioglass® powder.* Journal of the European Ceramic Society, 2009. **29**(16): p. 3299-3306.

133. Bertin, E.P., *Principles and Practice of X-Ray Spectrometric Analysis*. 1975, New York: Plenum Press.

134. Kissinger, H.E., *Reaction Kinetics in Differential Thermal Analysis.* Analytical Chemistry, 1957. **29**(11): p. 1702-1706.

135. Strbac, G.R., et al., *Glass transition kinetics and fragility index of chalcogenides from Ag-As-S-Se system.* Journal of Thermal Analysis and Calorimetry, 2018. **134**(1): p. 297-306.

136. Jean, J.H. and Y.C. Fang, *Devitrification kinetics and mechanism of Pyrex borosilicate glass.* Journal of Materials Research, 2001. **16**(6): p. 1752-1758.
137. Mogulkoc, B., et al., *Surface Devitrification and the Growth of Cristobalite in Borofloat (R) (Borosilicate 8330) Glass.* Journal of the American Ceramic Society, 2010. **93**(9): p. 2713-2719.
138. Clupper, D.C. and L.L. Hench, *Crystallization kinetics of tape cast bioactive glass 45S5.* Journal of Non-Crystalline Solids, 2003. **318**(1): p. 43-48.
139. Baino, F. and E. Fiume, *Quantifying the effect of particle size on the crystallization of 45S5 bioactive glass.* Materials Letters, 2018. **224**: p. 54-58.
140. Marotta, A., et al., *Activation-Energy for the Crystallization of Glass from Ddta Curves.* Journal of Materials Science, 1982. **17**(1): p. 105-108.
141. Wisniewski, W., *Crystal orientations in glass-ceramics determined using electron backscatter diffraction (EBSD)*. 2011, FSU Jena
142. Kracker, M., et al., *Surface crystallization of low thermal expansion Ba0.5Sr0.5Zn2Si2O7 from an 8 BaO center dot 8SrO center dot 34ZnO center dot 50 SiO2 glass.* Rsc Advances, 2017. **7**(71): p. 44834-44842.
143. Vladislavova, L., et al., *Crystallisation of Ba1-xSrxZn2Si2O7 from BaO/SrO/ZnO/SiO2 glass with different ZrO2 and TiO2 concentrations.* Solid State Sciences, 2018. **78**: p. 107-115.
144. Fokin, V.M., et al., *Stress induced pore formation and phase selection in a crystallizing stretched glass.* Journal of Non-Crystalline Solids, 2010. **356**(33-34): p. 1679-1688.
145. Karamanov, A., et al., *Pore formation in glass-ceramics: Influence of the stress energy distribution.* Journal of Non-Crystalline Solids, 2010. **356**(2): p. 117-119.
146. Karageorgiou, V. and D. Kaplan, *Porosity of 3D biomaterial scaffolds and osteogenesis.* Biomaterials, 2005. **26**(27): p. 5474-5491.
147. Bruker, C. *Application Note 79: Attenuated Total Reflection (ATR) – a versatile tool for FT-IR spectroscopy*. 2011 [cited 2019 08.02.].
148. Peitl, O., E. Dutra Zanotto, and L.L. Hench, *Highly bioactive P2O5–Na2O–CaO–SiO2 glass-ceramics.* Journal of Non-Crystalline Solids, 2001. **292**(1): p. 115-126.
149. Chevalier, J. and L. Gremillard, *Ceramics for medical applications: A picture for the next 20 years.* Journal of the European Ceramic Society, 2009. **29**(7): p. 1245-1255.
150. Magallanes-Perdomo, M., et al., *Bioactivity modulation of Bioglass® powder by thermal treatment.* Journal of the European Ceramic Society, 2012. **32**(11): p. 2765-2775.
151. Blochberger, M., L. Hupa, and S. Brauer Delia, *Influence of zinc and magnesium substitution on ion release from Bioglass 45S5 at physiological and acidic pH.* Biomedical glasses, 2015. **1**: p. 93–107.
152. Watts, S.J., et al., *Influence of magnesia on the structure and properties of bioactive glasses.* Journal of Non-Crystalline Solids, 2010. **356**(9-10): p. 517-524.
153. Massera, J., L. Hupa, and M. Hupa, *Influence of the partial substitution of CaO with MgO on the thermal properties and in vitro reactivity of the bioactive glass S53P4.* Journal of Non-Crystalline Solids, 2012. **358**(18): p. 2701-2707.
154. Ma, J., et al., *In vitro degradability and bioactivity of mesoporous CaO-MgO-P2O5-SiO2 glasses synthesized by sol–gel method.* Journal of Sol-Gel Science and Technology, 2010. **54**(1): p. 69-76.
155. Fagerlund, S., et al., *T-T-T behaviour of bioactive glasses 1-98 and 13-93.* Journal of the European Ceramic Society, 2012. **32**(11): p. 2731-2738.
156. Arstila, H., et al., *Influence of heat treatment on crystallization of bioactive glasses.* Journal of Non-Crystalline Solids, 2008. **354**(2-9): p. 722-728.
157. Lentes, F.-T. and N. Neuroth, *Optical Quality* in *The Properties of Optical Glass*, H. Bach and N. Neuroth, Editors. 1998, Springer-Verlag Heidelberg.

158. Howes, A.P., et al., *Boron environments in Pyrex (R) glass-a high resolution, Double-Rotation NMR and thermodynamic modelling study.* Physical Chemistry Chemical Physics, 2011. **13**(25): p. 11919-11928.
159. Brow, R.K., et al., *Cation Effects on P-31 Mas Nmr Chemical-Shifts of Metaphosphate Glasses.* Journal of the American Ceramic Society, 1991. **74**(6): p. 1287-1290.
160. Molchanov, V.S. and N.E. Prikhidko, *Corrosion of silicate glasses by alkaline solutions.* Bulletin of the Academy of Sciences of the USSR, Division of chemical science, 1957. **6**(10): p. 1179-1184.
161. Scholze, H., *Chemical Durability of Glasses.* Journal of Non-Crystalline Solids, 1982. **52**(1-3): p. 91-103.
162. Micoulaut, M., *Glass Transition Temperature Variation as a Probe for Network Connectivity*, in *Phase Transitions and Self-Organization in Electronic and Molecular Networks*, M.F. Thorpe and J.C. Phillips, Editors. 2001, Springer US: Boston, MA.
163. Fagerlund, S., *Understanding the in vitro dissolution rate of glasses with respect to future clinical applications*. 2012, Åbo Akademi University Turku.

8. Register of Illustrations

9. Register of Tables

10. Appendix

The appendix provides supplemental information for the individual chapters.

2.5. Mathematical Models

The validity range of the reaction numbers (RN) of the modified Andersson model are plotted in Table A 1.

Table A 1: Validity range of the modified Andersson model [48].

Component	(wt%)
$Na_2O + K_2O$	15-30
$CaO + MgO$	10-25
P_2O_5	0-8
B_2O_3	0-3
Al_2O_3	0-3
SiO_2	38-65.5

The validity range of the Index of surface activity model is plotted in Table A 2.

Table A 2: Validity range of the Index of surface activity (ISA) model [9].

Component	(wt%)
Na_2O	0-25
K_2O	0-15
MgO	0-5
CaO	10-20
B_2O_3	0-3
P_2O_5	0-6
SiO_2	39-70

3.1.1. Glass Composition & Glass Preparation (Glass series 45S5-B)

Table A 3: Glass calculation of series 45S5-B, Step I: decide about the distribution of Si & B

Glass	SiO_2 (mol%)	P_2O_5 (mol%)	CaO (mol%)	Na_2O (mol%)	B_2O_3 (mol%)	Si/(Si+B) (%)	B/(Si+B) (%)
45S5	46.13	2.60	26.91	24.35	0.00	100	0
45S5-0.5B	45.90	not decided yet			0.12	99.5	0.5
45S5-1B	45.67	not decided yet			0.23	99	1
45S5-2.5B	44.98	not decided yet			0.58	97.5	2.5
45S5-5B	43.83	not decided yet			1.15	95	5
45S5-10B	41.52	not decided yet			2.31	90	10
45S5-15B	39.21	not decided yet			3.46	85	15
45S5-20B	36.91	not decided yet			4.61	80	20
45S5-25B	34.60	not decided yet			5.77	75	25

Table A 4: Glass calculation of series 45S5-B, Step II: keep the amount of the other components constant. The sum of the components is not 100%, yet. So, a factor needs to be applied to proceed.

Glass	SiO_2 (mol%)	P_2O_5 (mol%)	CaO (mol%)	Na_2O (mol%)	B_2O_3 (mol%)	Si/(Si+B) (%)	B/(Si+B) (%)	Sum (mol%)	Factor
45S5	46.13	2.60	26.91	24.35	0.00	100	0	100.00	1.000
45S5-0.5B	45.90	2.60	26.91	24.35	0.12	99.5	0.5	99.88	1.001
45S5-1B	45.67	2.60	26.91	24.35	0.23	99	1	99.77	1.002
45S5-2.5B	44.98	2.60	26.91	24.35	0.58	97.5	2.5	99.42	1.006
45S5-5B	43.83	2.60	26.91	24.35	1.15	95	5	98.85	1.012
45S5-10B	41.52	2.60	26.91	24.35	2.31	90	10	97.69	1.024
45S5-15B	39.21	2.60	26.91	24.35	3.46	85	15	96.54	1.036
45S5-20B	36.91	2.60	26.91	24.35	4.61	80	20	95.39	1.048
45S5-25B	34.60	2.60	26.91	24.35	5.77	75	25	94.23	1.061

Table A 5: Glass calculation of series 45S5-B, Step III: Normalisation of the composition to 100%.

Glass	SiO_2 (mol%)	P_2O_5 (mol%)	CaO (mol%)	Na_2O (mol%)	B_2O_3 (mol%)	Si/(Si+B) (%)	B/(Si+B) (%)	Sum (mol%)
45S5	46.13	2.60	26.91	24.35	0.00	100.0	0.0	100
45S5-0.5B	45.95	2.61	26.94	24.38	0.12	99.5	0.5	100
45S5-1B	45.78	2.61	26.97	24.41	0.23	99.0	1.0	100
45S5-2.5B	45.24	2.62	27.07	24.49	0.58	97.5	2.5	100
45S5-5B	44.34	2.63	27.23	24.63	1.17	95.0	5.0	100
45S5-10B	42.50	2.67	27.55	24.93	2.36	90.0	10.0	100
45S5-15B	40.62	2.70	27.88	25.22	3.58	85.0	15.0	100
45S5-20B	38.69	2.73	28.21	25.53	4.84	80.0	20.0	100
45S5-25B	36.72	2.76	28.56	25.84	6.12	75.0	25.0	100

3.1.3. In-vitro Dissolution Tests on Glass Powder and Glass Discs (Glass series 45S5-B)

Preparation of 0.062 mol l^{-1} Tris buffer solution

- add about 1600 ml deionized water into a 2 l PE beaker
- add 15.090 g tris(hydroxymethyl)aminomethane (TRIS; Carl Roth, Karlsruhe, Germany) slowly while stirring using a magnetic mixer (C-MAG HS7, IKA, Staufen, Germany)
- when dissolved add 44.2 ml 1 M hydrochloric acid (HCl; Carl Roth, Karlsruhe, Germany)
- heat up to 37°C in shaking incubator (KS4000i Control, IKA, Staufen, Germany) at an agitation rate of 60 rpm overnight
- use a water bath (TW20, Julabo, Seelbach, Germany) to keep the temperature of the solution at ~ 37°C
- adjust pH-value to 7.4 with 1M HCl
- fill to 2000 ml with deionized water (2 l volumetric flask)
- store in PE beaker at 37°C in shaking incubator

Table A 6: Theoretical total ion concentrations in SBF 10 according to Müller at al [53].

mmol/l	SBF 10
Na^+	142.0
K^+	5.0
Ca^{2+}	2.5
Mg^{2+}	1.0
Cl^-	126.0
HCO_3^-	10.0
SO_4^{2-}	1.0
HPO_4^{2-}	1.0

3.1.4. Heating Microscopy in Thermal Properties (Glass series 45S5-B)

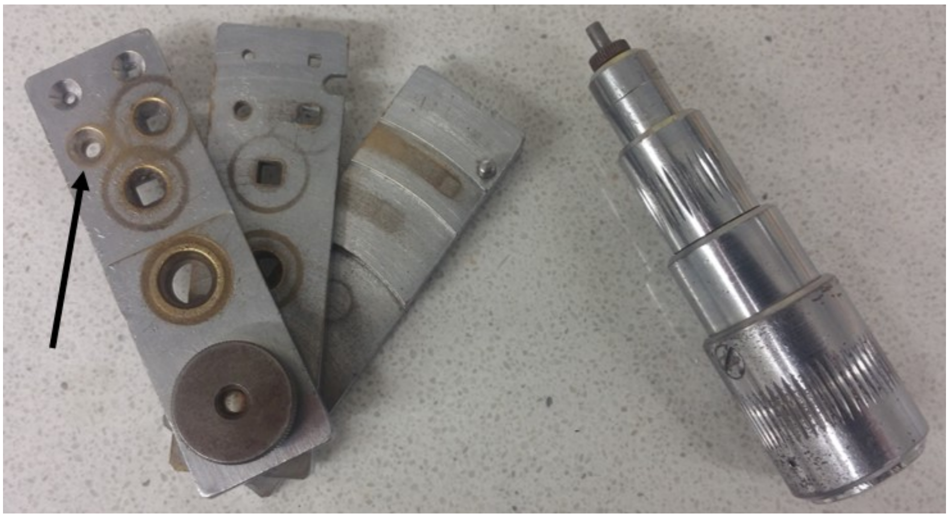

Figure A 1: Picture of hand press used to prepare pellets for heating microscopy. The black arrow shows which hole was used.

3.2.1. Glass Composition & Glass Preparation (Åbo Glasses)

Table A 7 shows which furnace was used for the processing of the individual glass of the Åbo glass series; either the furnace with SiC heating elements, whose maximum working temperature is at 1350°C or the induction furnace, which is used to melt glasses, which require higher process temperatures. The maximum process temperature given in the table is the temperature at which the refinement of the glass was carried out. Melting and casting of the glasses usually took place at lower temperatures (~-30-50 K).

Table A 7: Details regarding glass processing of the Åbo glasses.

Glass	Furnace	Maximum process temperature
17-93	SiC	1350°C
17-92	SiC	1350°C
206	SiC	1340°C
14-93	SiC	1350°C
19-93	SiC	1350°C
3-92	SiC	1320°C
15-92	SiC	1320°C
306	SiC	1350°C
9-93	SiC	1350°C
20-92	SiC	1300°C
1-98	SiC	1350°C
106	SiC	1350°C
18-93	SiC	1350°C
12-92	SiC	1350°C
10-92	Induction	1573°C
6-92	SiC	1350°C
1606	Induction	1485°C
1406	Induction	1553°C
15-93	Induction	1397°C
1-92	Induction	1408°C
1806	Induction	1490°C

4.1.5. Crystallisation Study (Glass Series 45S5-B)

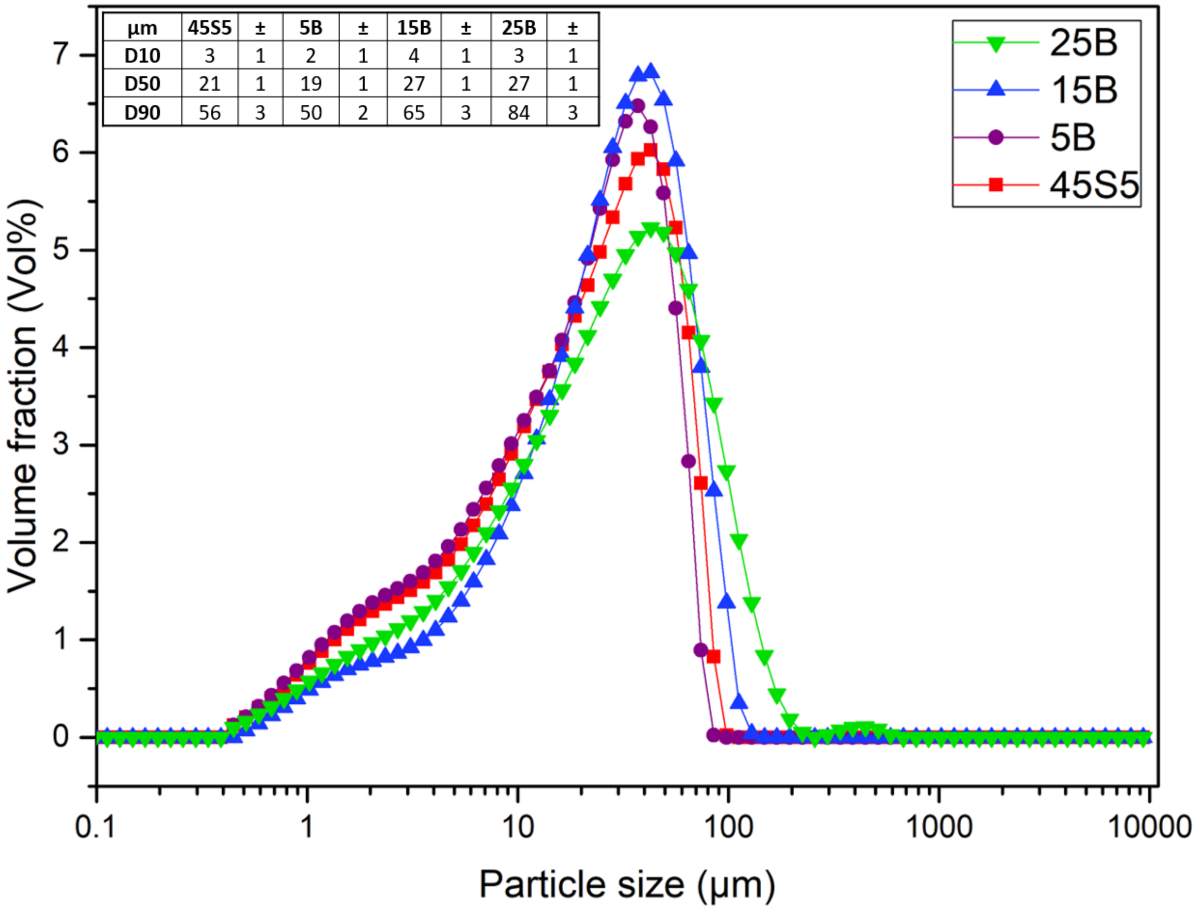

µm	45S5	±	5B	±	15B	±	25B	±
D10	3	1	2	1	4	1	3	1
D50	21	1	19	1	27	1	27	1
D90	56	3	50	2	65	3	84	3

Figure A 2: Volume fraction in percent in dependence of particle size for glasses 45S5, 5B, 15B and 25B.

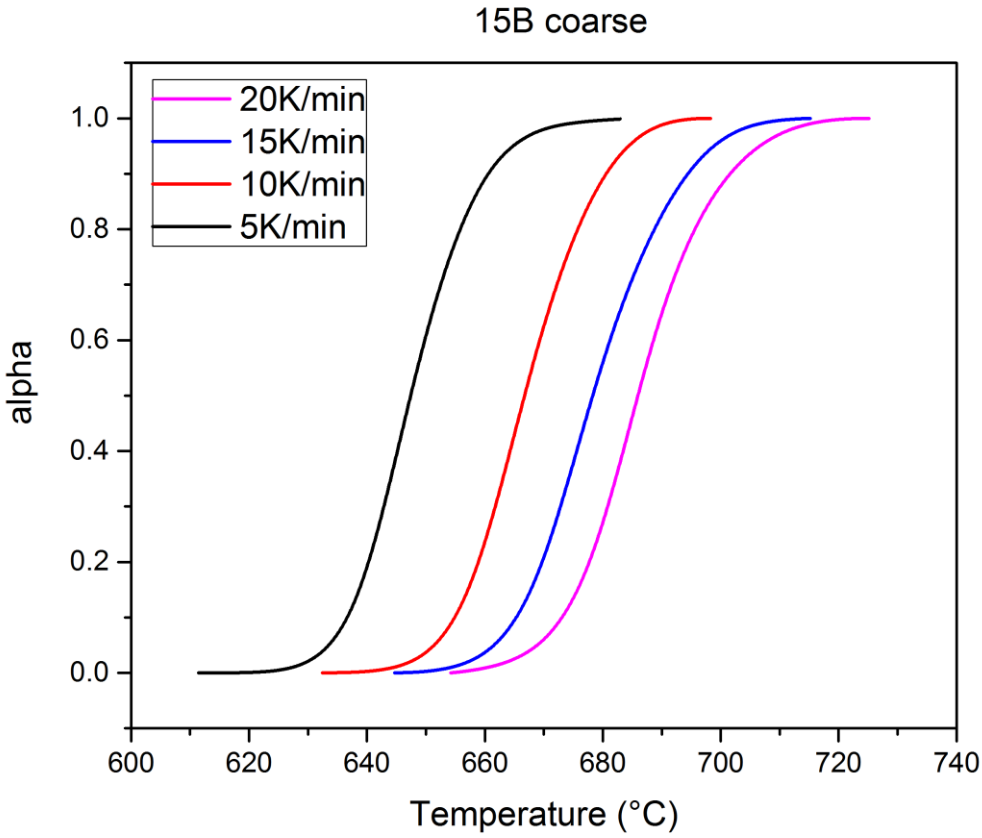

Figure A 3: Fraction of glass crystallised α as a function of temperature for glass 15B coarse.

4.2.2. Glass Structure & Density (Åbo Glasses)

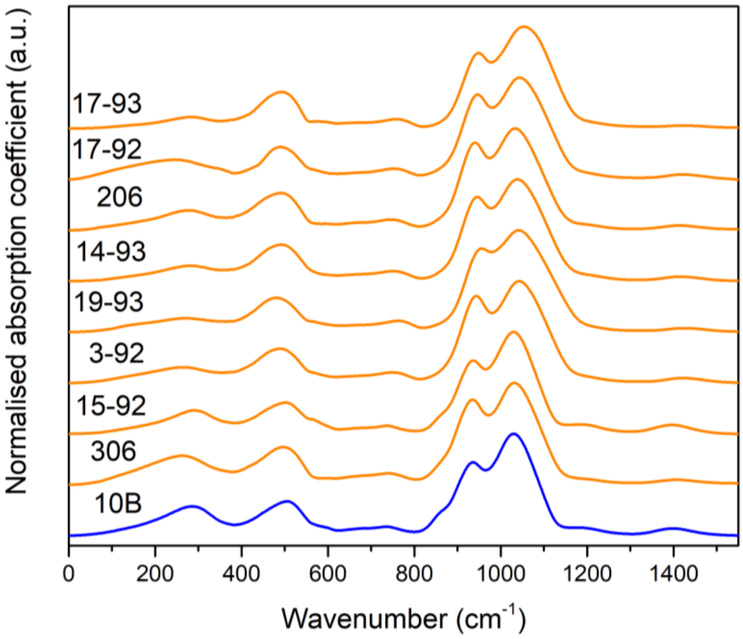

Figure A 4: FTIR spectra of the highly bioactive Åbo glasses.

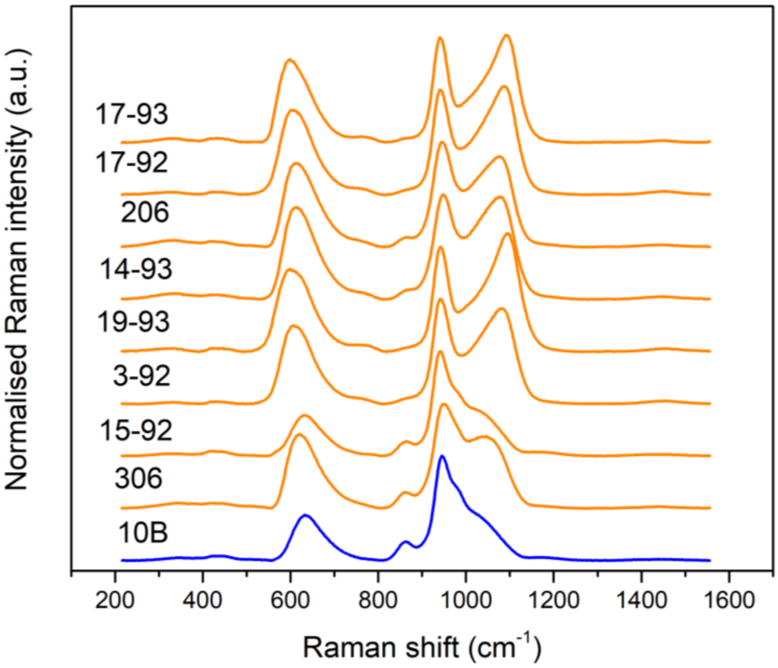

Figure A 5: Raman spectra of the highly bioactive Åbo glasses.

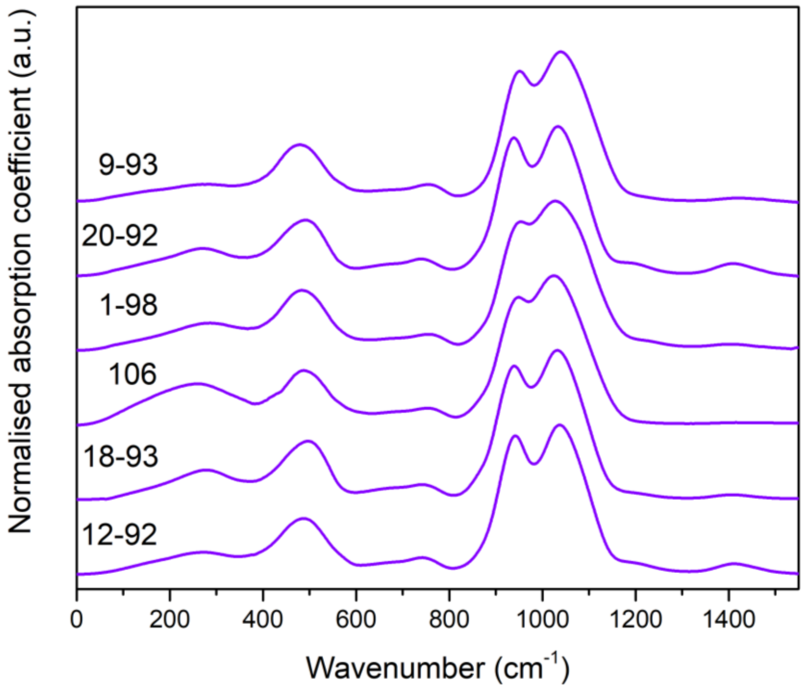

Figure A 6: FTIR spectra of the medium bioactive Åbo glasses.

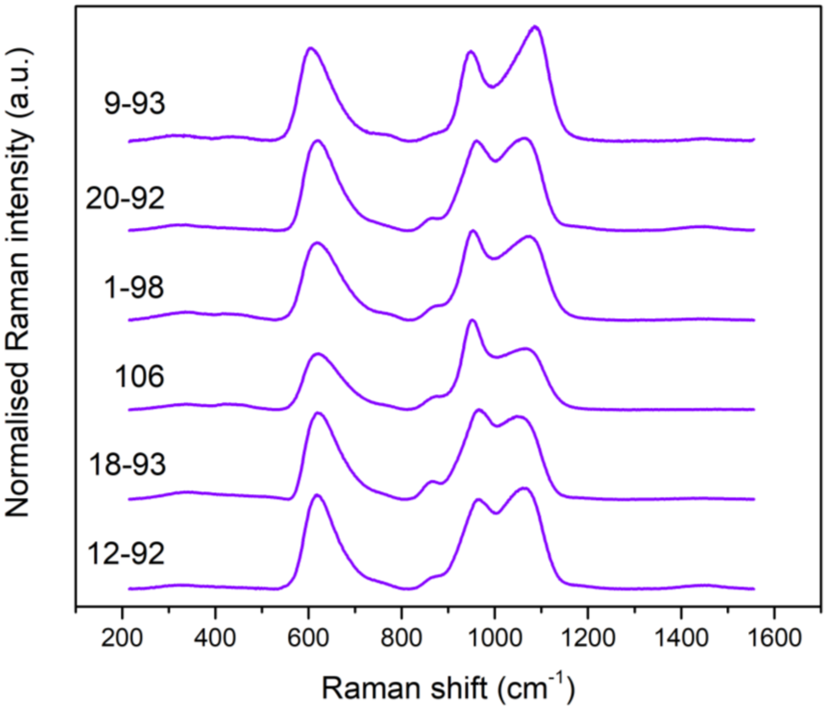

Figure A 7: Raman spectra of the medium bioactive Åbo glasses.

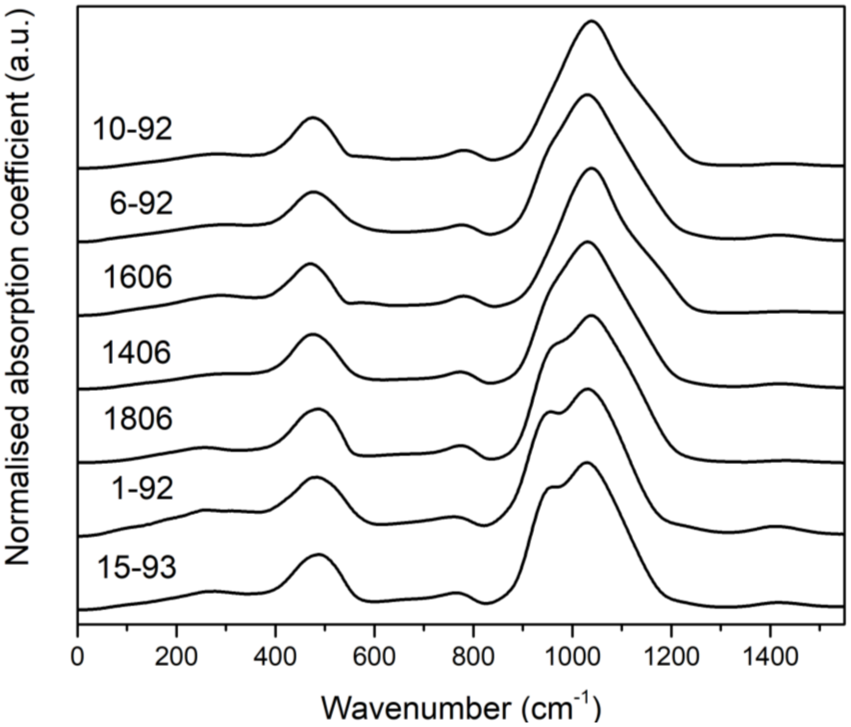

Figure A 8: FTIR spectra of the inert Åbo glasses

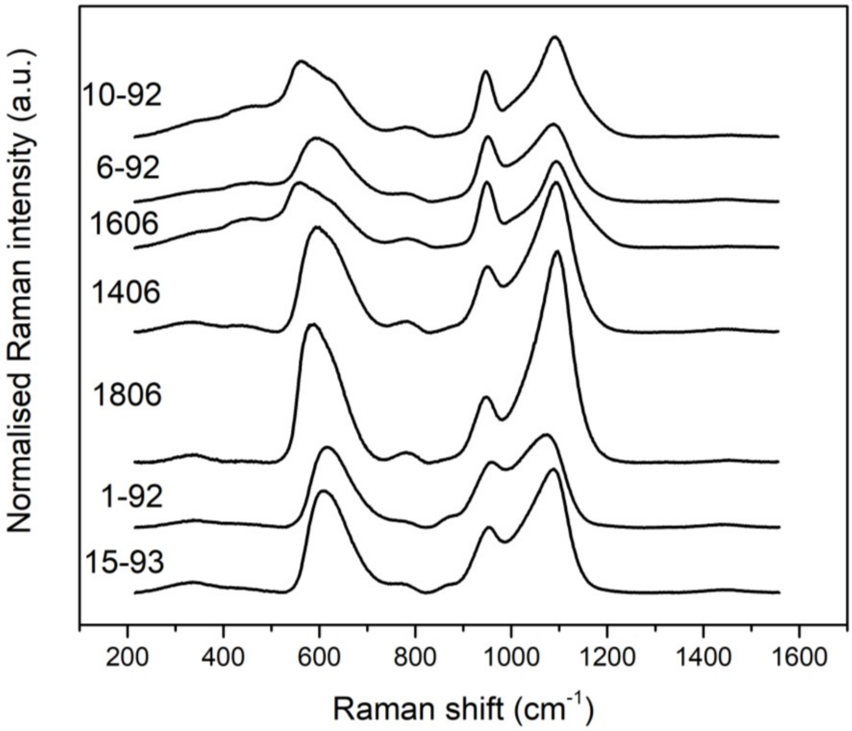

Figure A 9: Raman spectra of the inert Åbo glasses.

4.2.3. Dynamic dissolution tests (Åbo Glasses)

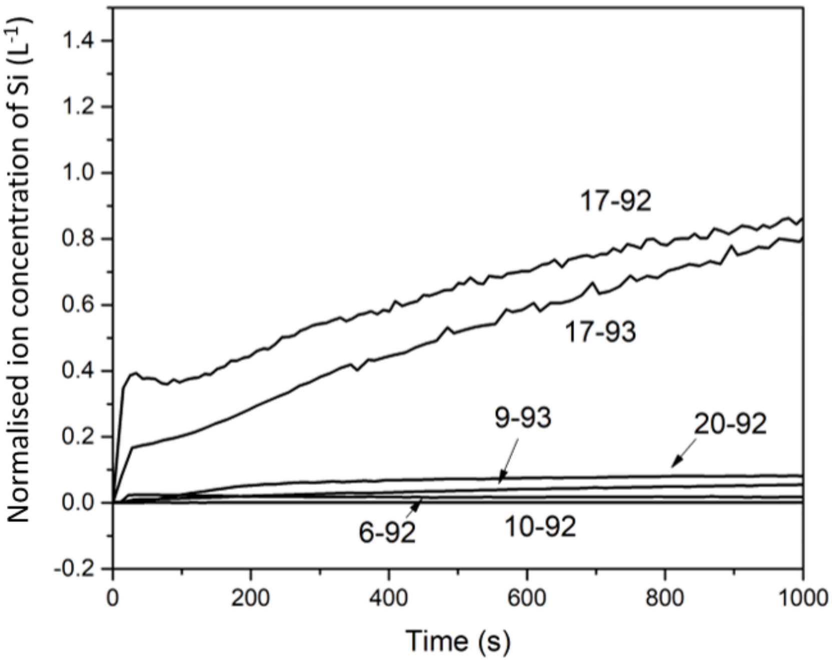

Figure A 10: Normalised ion concentration of silicon (Si) versus time plotted for the glasses 17-93, 17-92, 9-93, 20-92, 10-92 and 6-92.

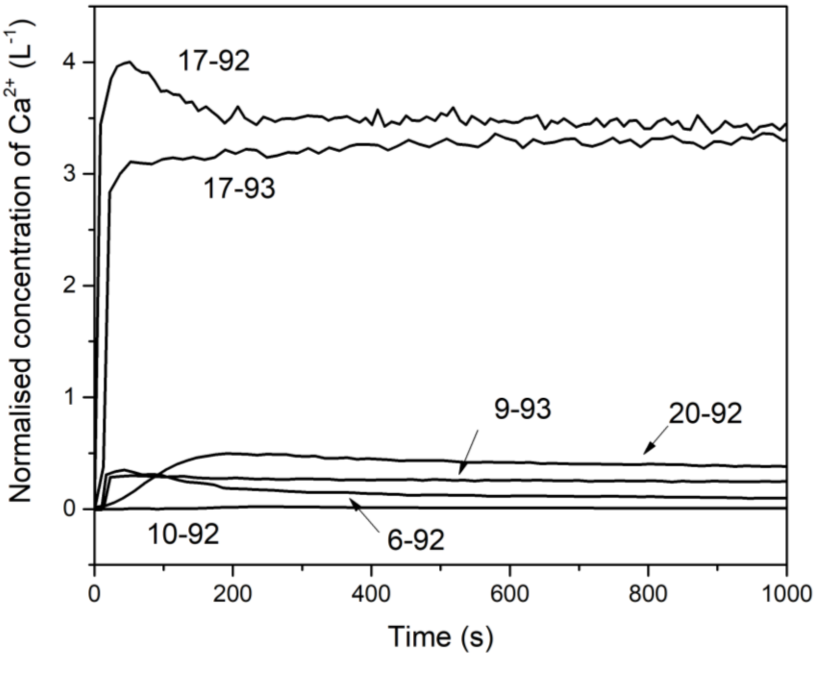

Figure A 11: Normalised ion concentration of calcium (Ca^{+}) versus time plotted for the glasses 17-93, 17-92, 9-93, 20-92, 10-92 and 6-92.

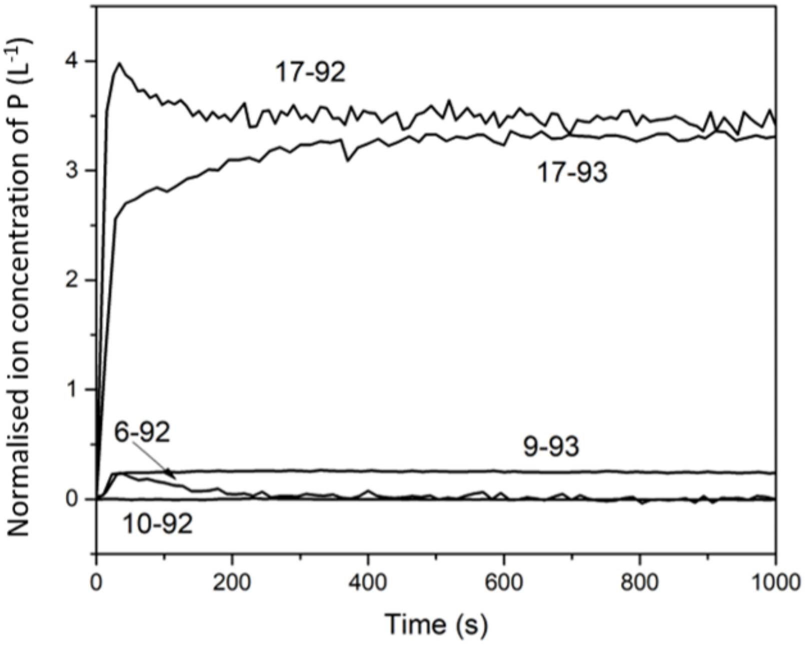

Figure A 12: Normalised ion concentration of phosphorous (P) versus time plotted for the glasses 17-93, 17-92, 9-93, 10-92 and 6-92. Glass 20-92 does not contain P.

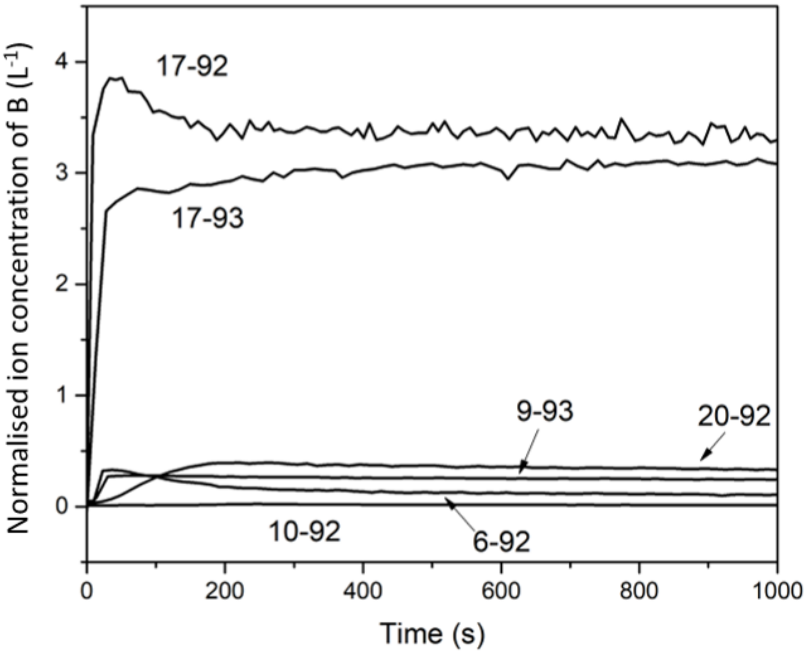

Figure A 13: Normalised ion concentration of boron (B) versus time plotted for the glasses 17-93, 17-92, 9-93, 20-92, 10-92 and 6-92.

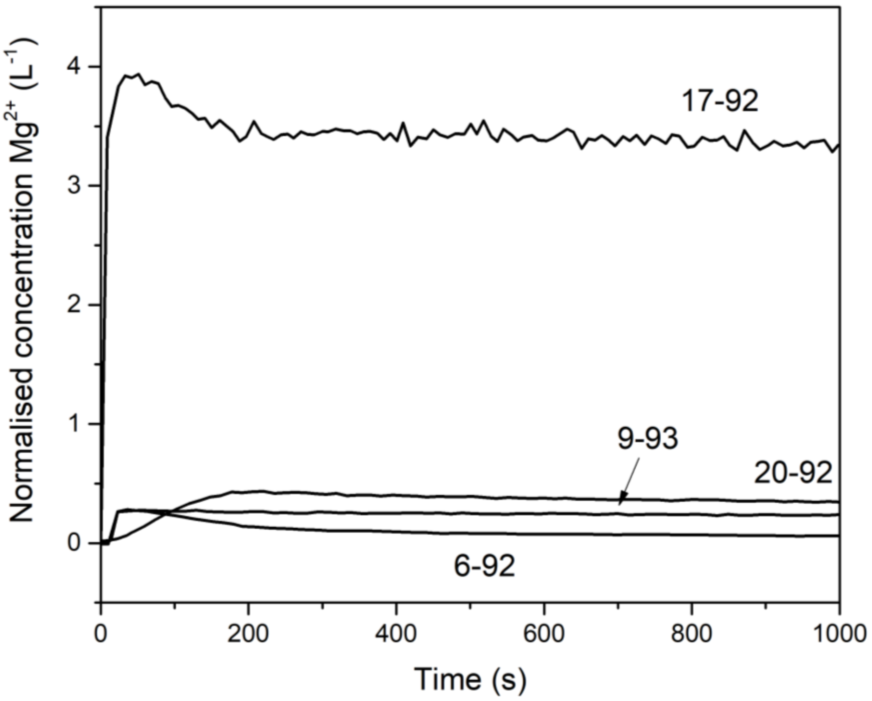

Figure A 14: Normalised ion concentration of magnesium (Mg^{2+}) versus time plotted for the glasses 17-92, 9-93, 20-92 and 6-92. Glass 17-93 and 10-92 do not contain Mg.

11. Acknowledgements

First, I would like to express many thanks to my superior Prof. Delia S. Brauer for excellent supervision during the whole working period of this dissertation. I thank Assoc. Prof. Jonathan Massera and his whole group for great working conditions during ten weeks research stay in Tampere in 2016 and 2017. Furthermore, I would like to thank our cooperation partners, which provided devices and tools associated with this thesis, see the chapter “Experimental Procedure”.

Especially I thank,

Prof. Leena Hupa for giving me the opportunity to carry out dynamic dissolution experiments during a short research stay in Turku in 2015

Gabriele Möller for the glass cutting, grinding and polishing

Dr Ekarat Meechoowas for the XRF investigations

Nadja Buchert for the XRD and Steffi Ebbinghaus for XRD as well as dilatometry measurements

Dr habil. Doris Möncke, Dr Kristin Griebenow, Felix Lind and Nagia Tagiara for the bulk FTIR investigations

Dr Sabari Venkatachalam for ^{31}P and ^{11}B MAS NMR and Dahiana Avila for ^{29}Si MAS NMR measurements

Dr Thomas Bocklitz for the calculation of the Fisher discriminant ratio and Pearson´s coefficient of correlation

Claudia Siedler for her help regarding replica sample preparation and the TEM investigations

Atsuhiro Miura, who carried out the dissolution tests on the glass powder of series 45S5-B, see chapter 4.1.3.

Nico Blaubach for the ICP-OES measurements

Dr Christian Bocker for the SEM and EDX investigations

Carsten Blaess for the heat microscopy measurements related to the crystallisation mechanism study, see chapter 4.1.5.

Luise Böhme for her support regarding glass processing of the glass series 45S5-B, the density measurement and the solubility tests of the glass discs (she wrote her master thesis about a part of the 45S5-B series in 2016)

Volker Seybold for the XRM investigations

Ayush Mishra for the DSC measurements of the 45S5-B series <38 µm, see chapter 4.1.4

Roland Wetzel for FTIR investigations of powder samples and particle size distribution measurements as well as Thilo Grammes and Nuttawan Sawangboon for some Raman measurements.

Thanks to all colleagues and friends for valuable discussions and well cooperative work, especially to Nuttawan Sawangbooon, Gloria Kirste, Roland Wetzel and Thilo Grammes, Jörg Schneider, Caroline Tschirpke, Neele van Laaten as well as to Dr Doris Möncke, Dr Kristin Griebenow, Dr Theresia Palenta, Felix Lind and Dr Thomas Bocklitz. Colleagues and co-workers at the Otto Schott Institute of Materials Research, which contributed to the success of the dissertation by support in everyday work, I would like to thank, especially Dr Ute Böttger, Corinna Seelheim, Lutz Preißer, Angelika Hacker, Christian Zeidler, Thomas Kittel and Dietmar Güttler. Thanks to Marlen Mannsfeld and Klara Schmidt for proof-reading.

I would particularly like to thank my husband Jan and my children for their great patience with my absence caused by working on the dissertation and for their constructive distraction in all-day life. Furthermore, I thank the teachers at the “Akonpuiston Päiväkoti”, German Kindergarten in Tampere, Finland for forwarding care of my daughter during my research stays, our nanny Klara and Christiane Nüsslein-Volhard Foundation for financial support.

12. Deutschsprachige Zusammenfassung (German Summary)

Die steigende Lebenserwartung von Menschen führt zu einer wachsenden Nachfrage nach Implantaten, um die Lebensqualität bei Senioren aufrecht zu erhalten. Bioglass® hat genaktivierende Eigenschaften, wodurch der Knochenwiederaufbau angeregt wird und es war das erste Material, welches in der Lage war an menschlichen Knochen anzubinden [1]. Bis heute werden bioaktive Gläser kommerziell als Granulat oder Pulver eingesetzt, um die Gewebsregeneration in Knochendefekten zu unterstützen [2]. Komplexe Strukturen, die Formgebung bei erhöhten Temperaturen erfordern, sind schwierig herzustellen, da bioaktive Gläser eine ausgeprägte Kristallisationstendenz aufweisen. Es wird die vollständige Auflösung im menschlichen Körper angestrebt, jedoch löst sich das bioaktive Glas Bonalive® sogar nach 14 Jahren Verweildauer nicht vollständig auf [3]. Das Element Bor spielt eine Rolle im Metabolismus von gesunden Knochen [4-6]. In Zelltests unterstützen Borosilikatgläser das Zellwachstum, die Adhäsion und die Differenzierung von Zellen [7] und in-vivo Ergebnisse zeigen eine gesteigerte Knochenneubildung [8]. Des Weiteren führt ein erhöhter Borgehalt im Glas zu einem schnelleren und vollständigeren Auflösungsprozess, wodurch die zeitigere Bildung der anorganischen Knochensubstanz, Hydroxylapatit ermöglicht wird [9, 10].

In der Dissertation wurde der Einfluss von Bor auf Struktur, Löslichkeit und Kristallisationsverhalten von bioaktiven Gläsern untersucht. Ausgehend von Bioglass® 45S5 wurde in der Glasserie 45S5-B Silizium systematisch durch Bor ausgetauscht. Die Strukturuntersuchungen haben gezeigt, dass die Siliziumatome mehrheitlich über zwei Sauerstoffatome mit den benachbarten Siliziumatomen verbunden sind (Q^2 Gruppen), was zu einer kettenartigen Struktur führt. Des Weiteren liegt Bor für die ganze Serie überwiegend (>80%) dreifach koordiniert vor. Orthophosphat ist die hauptsächlich vorliegende P-spezies für alle Gläser, welches leicht aus dem Glas herausgelöst werden kann und damit die Bildung von Apatit unterstützt. Der Austausch von Bor gegen Silizium führte zu einer weniger vernetzten Struktur (verminderte Netzwerkpolymerisation). Weitere Ergebnisse zeigten, dass es möglich ist das Löslichkeitsverhalten mittels des Borgehaltes zu kontrollieren. Ein erhöhter Borgehalt im Glas führte zu einer zeitigeren Apatitbildung.

Für die feinen Glaspulver wurde mit steigendem Boranteil eine geringfügige Abnahme der Kristallisationstendenz gefunden, wobei die Kristallisationstendenz der Glasserie 45S5-B im Vergleich zu anderen Glassystemen generell hoch ist. Für die feinen Glaspulver wird vorherrschend Oberflächenkristallisation angenommen, während für die groben Glaspulver eine komplexe Kristallisation, die in Verbindung zur Phasenseparation des Glases steht, vorgeschlagen wird. Interessanterweise war Glas 25B sogar nach teilweiser Kristallisation durch Wärmebehandlung in der Lage Apatit zu bilden.

Die Strukturuntersuchung der Åbo-Gläser zeigten ein kompakteres Netzwerk für die inerten Gläser im Vergleich zu den hoch- und mittelmäßig bioaktiven Gläsern. Wie für die inerten Gläser erwartet, wurde der Glasübergang bei höheren Temperaturen detektiert und der thermische Ausdehnungskoeffizient war im Vergleich zu den anderen Gläsern niedriger. Die reduzierte Kristallisationstendenz, die für die Mehrheit der Åbo-Gläser vorlag und einen substanziellen Vorteil bietet, ist wahrscheinlich verursacht durch die Präsenz von K_2O und MgO [11].

In weiteren systematischen Untersuchungen könnte der Einfluss von Kalium und Magnesium im Glassystem 45S5-B untersucht werden, um eine Glaszusammensetzung zu erhalten, die Heißformgebung durch reduzierte Kristallisationstendenz ermöglicht. Interessante nächste Schritte an der geeigneten Glaszusammensetzung wäre die Herstellung von 3D Scaffolds, die Durchführung von Zelltests und in-vivo Studien an lebenden Organismen.

1. Hench, L.L., *The story of Bioglass®.* Journal of Materials Science-Materials in Medicine, 2006. **17**(11): p. 967-978.
2. Boccaccini, A.R., D.S. Brauer, and L. Hupa, *Bioactive Glasses*. 2017, Cambridge, UK Royal Society of Chemistry
3. Fabert, M., et al., *Crystallization and sintering of borosilicate bioactive glasses for application in tissue engineering.* Journal of Materials Chemistry B, 2017. **5**(23): p. 4514-4525.
4. Nielsen, F.H., *Studies on the relationship between boron and magnesium which possibly affects the formation and maintenance of bones.* Magnesium and trace elements, 1990. **v.9** (no. 2): p. pp. 61-69.
5. Beattie, J.H. and H.S. Peace, *The Influence of a Low-Boron Diet and Boron Supplementation on Bone, Major Mineral and Sex Steroid-Metabolism in Postmenopausal Women.* British Journal of Nutrition, 1993. **69**(3): p. 871-884.

6. Newnham, R.E., *Essentiality of boron for healthy bones and joints.* Environ Health Perspect, 1994. **102 Suppl 7**: p. 83-5.
7. Fu, Q.A., et al., *Silicate, borosilicate, and borate bioactive glass scaffolds with controllable degradation rate for bone tissue engineering applications. II. In vitro and in vivo biological evaluation.* Journal of Biomedical Materials Research Part A, 2010. **95a**(1): p. 172-179.
8. Gorustovich, A.A., et al., *Biological performance of boron-modified bioactive glass particles implanted in rat tibia bone marrow.* Biomedical Materials, 2006. **1**(3): p. 100-5.
9. Huang, W., et al., *Kinetics and mechanisms of the conversion of silicate (45S5), borate, and borosilicate glasses to hydroxyapatite in dilute phosphate solutions.* Journal of Materials Science: Materials in Medicine 2006. **17**(7): p. 583-96.
10. Yao, A.H., et al., *In vitro bioactive characteristics of borate-based glasses with controllable degradation behavior.* Journal of the American Ceramic Society, 2007. **90**(1): p. 303-306.
11. Hupa, L. and K.H. Karlsson, *Tailoring of Bioactive Glasses*, in *Bioactive Glasses*, A.R. Boccaccini, D.S. Brauer, and L. Hupa, Editors. 2017, The Royal Society of Chemistry: Cambridge.

Selbstständigkeitserklärung

Ich erkläre, dass ich die vorliegende Arbeit selbstständig und unter Verwendung der angegebenen Hilfsmittel, persönlichen Mitteilungen und Quellen angefertigt habe.

J. Brandt - Slowik

Jena, 02.04.2020

Juliane Brandt-Slowik